Seman Bobulska, Dana (2022) *Doubly charmed baryon searches at the LHCb experiment.* PhD thesis.

https://theses.gla.ac.uk/83205/

Doubly charmed baryon searches at the LHCb experiment

Dana Seman Bobulska
of the College of Science and Engineering

A dissertation submitted to the University of Glasgow
for the degree of Doctor of Philosophy

June 2022

Abstract

The main analysis presented in this thesis is a search for the doubly charmed baryon Ξ_{cc}^{+} in the $\Xi_{c}^{+}\pi^{-}\pi^{+}$ final state, where the Ξ_{c}^{+} baryon is reconstructed in the $pK^{-}\pi^{+}$ final state. The search is based on the data collected at the LHCb experiment in 2016–2018 at a centre-of-mass energy of 13 TeV, corresponding to about $5.4\,\text{fb}^{-1}$ of integrated luminosity. Since the Ξ_{cc}^{+} baryon has previously not been observed and this analysis presents the first search for this baryon in the $\Xi_{c}^{+}\pi^{-}\pi^{+}$ final state, the $\Xi_{c}^{+}\pi^{+}\pi^{-}$ invariant-mass region from 3.3 to $3.8\,\text{GeV}/c^2$ was not examined until the full analysis was finalised in order to avoid any bias of the decisions made during the analysis.

No significant signal for the Ξ_{cc}^{+} baryon is observed in the invariant-mass range from 3.4 to $3.8\,\text{GeV}/c^2$, therefore upper limits are set on the ratio of production cross-section times branching fraction with respect to the already observed $\Xi_{cc}^{++} \rightarrow (\Xi_{c}^{+} \rightarrow pK^{-}\pi^{+})\pi^{+}$ decay, as a function of the assumed Ξ_{cc}^{+} mass for different Ξ_{cc}^{+} lifetime hypotheses, in the rapidity range from 2.0 to 4.5 and the transverse momentum range from 2.5 to $25\,\text{GeV}/c$. For the Ξ_{cc}^{+} lifetime hypothesis of 80 fs, the evaluated upper limit on the ratio of production cross-section times branching fraction with respect to the $\Xi_{cc}^{++} \rightarrow (\Xi_{c}^{+} \rightarrow pK^{-}\pi^{+})\pi^{+}$ decay varies between 2 and 5 at 95% confidence level in the invariant-mass range from 3.4 to $3.8\,\text{GeV}/c^2$.

The results are combined with the previously published search for the Ξ_{cc}^{+} baryon in the $\Lambda_{c}^{+}K^{-}\pi^{+}$ final state at LHCb. A maximum local significances of 4.0 standard deviations, including systematic uncertainties, is found for the combination of the two decay channels around the mass of $3623\,\text{MeV}/c^2$. Taking into account the look-elsewhere effect in the invariant-mass range from 3.5 to $3.7\,\text{GeV}/c^2$,

the combined global significance is 2.9 standard deviations, including systematic uncertainties.

A detector performance study described in this thesis is devoted to hit-resolution corrections of the VELO detector in the simulation, in order to improve the agreement with the corresponding resolutions measured in data. The method uses the hit resolutions in data to generate the hit uncertainties in simulation. A significant improvement in the resolutions of 2 and 3-strip clusters between the corrected simulation and data is achieved. As the method is not applicable on 1-strip clusters, a strategy to correct the 1-strip clusters is developed, in order to improve the agreement for the 1-strip clusters in the future.

Lastly, an inclusive software trigger line is developed for the Ξ_c^0 baryon based on the multivariate selection, which was implemented for the 2018 data taking at the LHCb experiment. The developed selection is aimed to be efficient for the $\Xi_c^0 \rightarrow pK^-K^-\pi^+$ decay, independent of the origin of the Ξ_c^0 baryon. The efficiency of the developed trigger line is improved with respect to the corresponding existing cut-based trigger line for the Ξ_c^0 baryon, in particular for the $\Xi_{cc}^+ \rightarrow \Xi_c^0\pi^+$ decay, which is important for future searches and studies of the doubly charmed baryon Ξ_{cc}^+.

Declaration

This dissertation is the result of my own work, except where explicit reference is made to the work of others, and has not been submitted for another qualification to this or any other university.

Dana Seman Bobulska

Acknowledgements

As far as we know, there are four fundamental forces in nature - the strong force, the electromagnetic force, the weak force, and the gravitational force. Like all interactions in nature are due to these forces, there are corresponding forces that are responsible for the existence of this thesis. I would like to introduce them and express my gratitude to their mediators. Just to note, the relative strengths of the individual forces in this personal theory do not correspond to those found in nature. There are surely people I missed to mention in the following, and I apologise for that, as I am thankful to everyone I met along the way, you all helped me to be where I am now.

Firstly, the gravitational force responsible that my centre-of-gravity over the last four years was particle physics, was carried out mainly by my supervisors, Lars and Paul, and all of my colleagues in Glasgow and at LHCb. Lars, thank you for your time, wisdom, countless interesting discussions about physics and life, your patience, and great advice whenever I needed it. Paul, I could not wish for a better second supervisor, thank you so much for your support, guidance, and patience during my studies. Many thanks to all of my LHCb Glasgow colleagues, namely the post-doctoral researchers and academics: Manuel, thank you for our interesting chats about physics and VELO, mainly while we were both based at CERN; Michael, thank you for always being helpful, and for your immense support and help during our VELO hit resolution study, I am very grateful for the opportunity to work with you and to learn from you; Patrick, thank you for your wisdom and advice, in particular on charm physics and doubly charmed baryons, I am looking forward to the future doubly charmed baryon results where you will surely contribute; Sneha, thank you for your always interesting updates on the VELO electronics, and good luck with the future upgrades; and last but not least, thanks to Lucia and Mark, our newest group members, for your interesting inputs and fresh air you brought to the Glasgow LHCb group, I wish you all the best in the future. Many thanks to my fellow PhD students at LHCb in Glasgow: Sara, Cameron, Murdo, Iain, and Lauren, as well as Patrik, a neutrino PhD student, all of you were there for me when I started and taught me so much during

my first year, I was very lucky to have you all around. Murdo, special thanks to you, as you introduced me to the doubly charmed baryon studies, and taught me many things that made my future work easier. Thank you David and Niall, the current LHCb PhD students in Glasgow, you are both great physicists, it was a pleasure to learn from you and share an office with you, it is unfortunate that it was interrupted by the pandemic. I wish you all the best with your analyses and theses, I am sure they will be excellent. I would like to thank to all members of the Glasgow particle physics experiment and theory groups: Christoph, Jill, John, Stephen, and Tony, to name a few, as you helped me whenever needed and made my PhD studies in Glasgow enjoyable and exciting, I will be forever thankful for the opportunity to study a PhD at the University of Glasgow. My special thanks to Andy, thank you for all your work as the local director of the CDT, for your advice whenever I needed it, and for preparing a very nice and helpful LaTeX class, *hepthesis*, on which this thesis is based. I would also like to thank the former and current conveners of the Charm working group at LHCb, Mark, Michael, Marianna, and Dominik, thank you for your time, support, and help during the review process of the Ξ_{cc}^{+} analysis. Also many thanks to the whole Charm working group and the Ξ_{cc} group, and everyone who helped me to improve the analyses presented in this thesis, in particular Ao, Jibo, and Jingyi, thank you for many interesting discussions and your advice over the years. I am also very thankful to the review committee of the Ξ_{cc}^{+} analysis, Yiming and Giovanni, thank you for a very helpful and efficient review process, and also to the editorial board and the main paper reviewer, Sergey, thank you for your tireless effort to improve the paper. Also, many thanks to Alexander, Michal, and Roman, who supported me during my Master studies, thank you for your encouragement to pursue doctoral studies. Last but not least, many thanks to the FCDO data science team I worked with during my industrial placement, namely Sarah, Alistair, and Rebecca, thank you for your time, help, and kindness, it was a pleasure to work with you and to learn from you.

My lovely friends represent mediators of the weak force, which is not weak by any means - mainly thanks to you I was able to (at least from time to time) disengage from the gravitational force pulling me into physics, and to enjoy other joys of life. Thank you to my friends (not only, but mainly) from Slovakia: Betka, Mišo and Milko, Katka, Kuzmix and Florian, Majka and Viťo, and Tinka, thank you all for your support and friendship, I am very lucky to have you all in my life. Many thanks to my *Lunch bunch* folks, who made my stay at CERN enjoyable and filled with funny memories, namely (in alphabetic order) Aaron, Adam, Bruno, Candice, Jake, Jakub, Jonathan, Laurynas, Maty, Melissa, Neil, Peter, Savannah, and also to Arnau, Martha, Stefano, many thanks to all of you. Special thanks to my close friends in Glasgow, Neil and Jonathan (also members of the Lunch bunch), thank you for your continuous support, help, and for always having a great time together.

The electromagnetic force is closely related to the weak force, and it is therefore represented by my family. As my friends, you are also the main reason why I did not go crazy (or did I?) over the years of my PhD studies. Many thanks to all of my close and extended family, I am immensely thankful to have you all. Thank you, dad, for making me believe in myself because you always believed in me, supported me, and was there for me, and many thanks to my late mum, who gave me so much love that I can still feel it, many years after she is gone. Thank you, Janka and Lenka, my dearest sisters, always holding my back, supporting me, and cheering for me. Thank you, Patrick, Daniel, Klara and Milo, you know how to cheer me up and fill my life with joy and love. Many thanks to all of my husband's family, which became also my family during my PhD, I am very lucky to have you.

The mediator of the strong force is my husband, Peter. The strong force in nature is what holds it all together, and it is not different in my life as well. Thank you, love, for always being there for me, for supporting me and encouraging me, for your love and care, no matter what. I hope you know that I could not have done it without you.

Preface

This thesis describes my main research activities, together with a theoretical introduction and description of the experimental setup of the LHCb detector, providing a background to the discussed studies.

Firstly, the theoretical aspects relevant to the presented analyses are discussed in Chapter 1, in order to give the reader an overview of the current status of the field. In particular, the Standard Model of particle physics is described, as well as the Quark Model and theoretical techniques used in hadron spectroscopy to calculate predictions of various properties of the doubly charmed baryons. An overview of the experimental status of the doubly charmed baryon studies is also given in Chapter 1.

The LHCb experiment is discussed in Chapter 2, as the data used in all studies described in this thesis were collected at the LHCb detector. The role and main goals of the LHCb experiment are discussed, as well as a detailed description of its individual detectors. The aim of this chapter is to provide sufficient background knowledge of the data used for the analyses described in the following chapters, as well as to convince the reader that the LHCb experiment is well suited for the search of the doubly charmed baryons due to the high production cross-section of charmed hadrons at LHCb, its excellent tracking, particle identification and secondary vertex resolution, as well as an efficient trigger system.

A software related study is described in Chapter 3, which is devoted to the development of the software-trigger selection for the $\Xi_c^0 \to pK^-K^-\pi^+$ decay based on multivariate techniques, independent of the origin of the Ξ_c^0 baryon. The described study was performed by me, but since the developed trigger line was implemented as part of the new set of the inclusive-trigger lines for charmed baryons for the 2018 data taking at LHCb, a close collaboration was maintained during the duration of this study with the analysts working on similar trigger lines, namely for the Ξ_c^+, Λ_c^+, and Ω_c^0 baryons.

Chapter 4 describes a detector performance study devoted to correcting the VELO hit resolution in the simulation, in order to improve the agreement between data and simulation. The study was performed in a collaboration with Michael Alexander, who worked closely with me mainly on the integration of the developed algorithm with the LHCb software.

The main analysis described in this thesis, which is devoted to a search for the $\Xi_{cc}^{+} \to \Xi_{c}^{+} \pi^{-} \pi^{+}$ decay, is introduced in Chapter 5. The analysis introduction is followed by the detailed presentation of the analysis strategy, since the analysis is prepared for observation and non-observation of the Ξ_{cc}^{+} baryon prior to unblinding of the studied invariant-mass spectrum from 3.3 to 3.8 GeV/c^2. Chapter 6 then describes the selection developed to search for the Ξ_{cc}^{+} baryon, which is used in the studies described in the following two chapters. The mass fit to the invariant-mass spectrum, evaluation of a significance, and combination with the $\Xi_{cc}^{+} \to \Lambda_{c}^{+} K^{-} \pi^{+}$ decay is described in Chapter 7. A determination of the upper limits on the ratio of production cross-sections times the ratio of branching fractions between the signal and normalisation channel $\Xi_{cc}^{++} \to \Xi_{c}^{+} \pi^{+}$, which are evaluated as a function of the assumed Ξ_{cc}^{+} mass and for different Ξ_{cc}^{+} lifetime hypotheses, is described in Chapter 8. This analysis was performed and completed by me from the start until its publication in JHEP [1], under the supervision of Lars Eklund and Paul Soler, with regular feedback from members of the Ξ_{cc} and Charm groups at LHCb.

Lastly, all studies described in this thesis are summarised in Chapter 9, with a discussion of future prospects for the presented studies.

It might sound a little bit odd to dedicate a thesis to a country. A country that is not even my homeland. However, Ukraine is where my heart was during substantial period of writing of this thesis, and where my heart will be until the war is over.

"For Ukraine and all Ukrainian people who fight for their future, freedom, for all of us."

Picture by Olga Shtonda,
an illustrator based in Kharkiv, Ukraine

Contents

Chapter 1.

Theoretical introduction to doubly charmed baryons

"Mankind has made giant steps forward. However, what we know is really very, very little compared to what we still have to know."
— Fabiola Gianotti

As the title of this thesis suggests, the main research project is devoted to a search for the doubly charmed baryon Ξ_{cc}^{+}, which is discussed in detail in Chapters 5, 6, 7, and 8.[1] This chapter aims to provide a theoretical background to the corresponding analysis, as well as a description of the experimental status of related studies. Moreover, the chapter gives an overview of the current status of the field, as it relates to all chapters presented in this thesis. Each of the topics discussed in this chapter could easily form a lengthy book, as they actually often do. It is therefore important to note that their description in the chapter is far from being exhaustive. The references for further study of the discussed topics are provided to equip the reader in case a deeper understanding is desired.

Firstly, the Standard Model (SM) of particle physics is discussed in Section 1.1, as it is currently the most important and relevant set of theories in particle physics. Section 1.2 then describes quark spectroscopy, which is relevant in particular to the studies of doubly charmed baryons. The doubly charmed baryons are subsequently discussed in Section 1.3 from a theoretical perspective, followed by an overview of

---

[1] Charge conjugation, which is a replacement of particles with their corresponding anti-particles (and vice versa), is implied throughout this document.

their historical and current experimental status. Finally, the chapter is summarised in Section 1.4.

1.1. The Standard Model

The Standard Model (SM) of particle physics is well known not only among all particle physicists, but its basic concepts are often known to non-physicists with an interest in the latest discoveries in particle physics. There is no surprise that the SM is so commonly mentioned - it represents a set of theories that describes our current understanding of the fundamental pieces of our universe: quarks and leptons as the elementary building blocks of all matter, and the fundamental forces[2] represented by the carrier particles exchanged between the particles of matter. Most importantly, not only does it describe these fundamental pieces, it describes them extremely well - the vast majority of the experimental results are compatible with the SM predictions.

The SM was not created overnight. It is a complex model based on a collection of theories that were developed over decades starting in the 1960s. The following Sections 1.1.1, 1.1.2 and 1.1.3 discuss the formalism of the SM and its individual pieces: the elementary particles, the fundamental forces, and the Higgs boson, which are summarised in Figure 1.1. Two topics of the SM that are closely related to the doubly-charmed-baryon studies, the theory of strong interactions and hadronic weak decays, are discussed in more detail in Sections 1.1.4 and 1.1.5, respectively.

Even though the SM is currently the most successful set of theories, with countless confirmations by experimental results, its description would not be complete if its limitations were not mentioned, which are summarised in Section 1.1.6. The limitations do not imply that the SM is an incorrect theory, but rather that it is incomplete. Therefore a lot of effort is dedicated to search for physics beyond the SM, including many direct and indirect searches for its effects at the Large Hardon Collider, which is introduced in the next chapter. There are a few exciting experimental results that, if confirmed, can present the first hints of physics beyond the SM, which are briefly discussed in Section 1.1.7.

---

[2] Except for gravity.

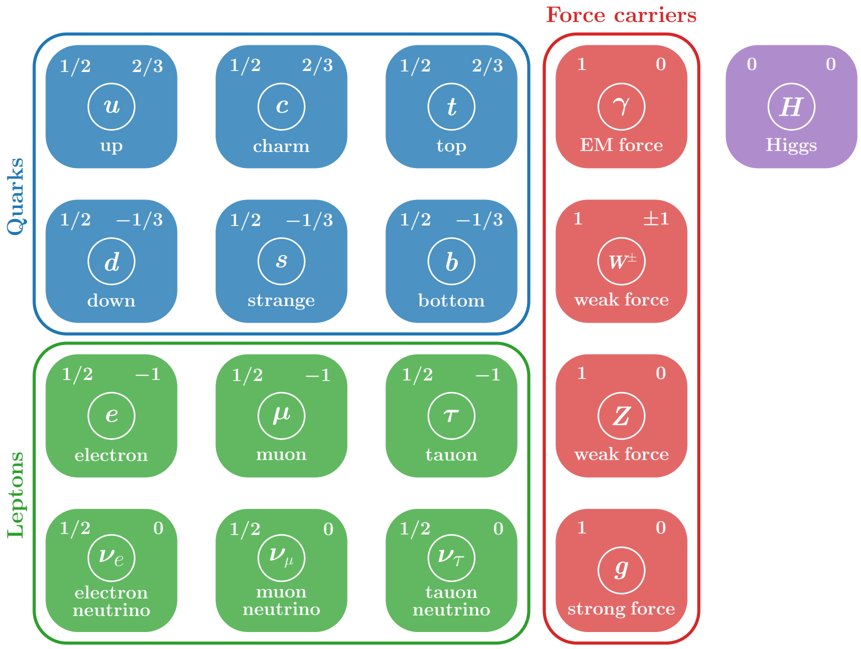

Figure 1.1.: Building blocks of the SM: the elementary particles - quarks (blue) and leptons (green); the force carriers of the fundamental forces (red); and the Higgs boson (purple). The numbers in the upper-left and upper-right corners represent the spin (intrinsic angular momentum) and the electric charge (in units of the electron charge), respectively.

1.1.1. Formalism

The SM is a gauge quantum field theory (QFT), which can be described by the gauge group SU(3) × SU(2) × U(1), so it is invariant under local gauge transformations. The SU(3) group describes the quantum chromodynamics (QCD) sector of the SM, and SU(2) × U(1) its electroweak sector.

Firstly, let us introduce the Lagrangian formalism as it is an important concept in a formulation of QFT. The Lagrangian function L was introduced by Joseph–Louis Lagrange in 1788 to describe the dynamics of a classical system using only one scalar function

$$L = T - V, \tag{1.1}$$

where T and V are the kinetic and potential energy of the system, respectively. The Lagrangian density $\mathcal{L}$ is the density of the Lagrangian function L, hence $L = \int \mathrm{d}^3x\, \mathcal{L}$. For quantum fields, the Lagrangian density $\mathcal{L}$ describes the dynamics of the quantum system. Due to a common use of the Lagrangian density, it is often called and referred to simply as the *Lagrangian*. To obtain the equations of motion, the principle of least action is used, where the action S is defined as the integration over space-time of the Lagrangian as

$$S = \int \mathrm{d}^4 x \mathcal{L}(\psi, \partial_\mu \psi), \tag{1.2}$$

where ψ and $\partial_\mu \psi$ represent a field and its partial derivative, respectively. The corresponding Euler-Lagrange equations of motion based on minimising the action for a relativistic field ψ are therefore

$$\partial_\mu \left(\frac{\partial \mathcal{L}}{\partial(\partial_\mu \psi)} \right) - \frac{\partial \mathcal{L}}{\partial \psi} = 0. \tag{1.3}$$

The Lagrangian is connected to another important concept of QFT, which is Noether's theorem that states that any transformation that leaves the Lagrangian unchanged implies a conserved quantity.[3] All conservation laws mentioned in the following are therefore caused by some SM symmetries.

Since the SM is a quantum field theory, its fundamental objects - matter particles and force carriers - are represented by quantum fields. The fermion fields that account for all matter particles are described in Section 1.1.2 in more detail, the electroweak boson fields, the gluon field, and the Higgs field, are together described in Section 1.1.3. Here, $\mathcal{O}(\text{many})$ steps are skipped in order not to exhaust a reader, and because this is not a book on QFT.[4] The Lagrangian of the SM can be simply expressed as the sum of the Lagrangians accounting for the particles and their interactions as

$$\mathcal{L} = \mathcal{L}_{\text{kin. (bosons)}} + \mathcal{L}_{\text{kin. (fermions)}} + \mathcal{L}_{\text{Higgs}} + \mathcal{L}_{\text{Yukawa}}. \tag{1.4}$$

The $\mathcal{L}_{\text{kin. (bosons)}}$ Lagrangian represents the kinetic term for gauge boson fields associated with the $\mathrm{U}(1)_Y$ group of weak hypercharge, the $\mathrm{SU}(2)_L$ group of weak isospin, and the $\mathrm{SU}(3)_C$ group representation of colour charge. The $\mathcal{L}_{\text{kin. (fermions)}}$ term is the kinetic term for fermion fields, which also includes their coupling to gauge bosons. The $\mathcal{L}_{\text{Higgs}}$ term in Equation 1.4 includes the terms associated with the Higgs field,

---

[3] In its weaker form, the Lagrangian function or the action are unchanged by the corresponding transformation.

[4] However, it is all very interesting, so in case more details are desired, *The Quantum Theory of Fields* by S. Weinberg [2] or *An Introduction To Quantum Field Theory* by D. Peskin and M. Schroeder [3] provide a comprehensive and excellent description of QFT.

which introduces a gauge invariance via spontaneous symmetry breaking by a scalar field with a non-zero vacuum expectation value, resulting in masses for (some) force carriers. The last term in Equation 1.4, $\mathcal{L}_{\text{Yukawa}}$, is the Lagrangian for the Yukawa sector of the SM, which contains the couplings of the Higgs field to fermions to generate their masses after electroweak symmetry breaking.

Equation 1.4 is, of course, a very simplified representation of the SM Lagrangian, a proper description of every term would fill several pages. However, Equation 1.4 gives a flavour of the fundamental pieces of the SM, which are further described in the following sections.

1.1.2. Elementary particles

All visible matter is made of two types of elementary particles: quarks, which are of type *up* (u), *down* (d), *charm* (c), *strange* (s), *top* (t), *bottom* (b)[5]; and leptons, namely electron (e), muon (μ), and tauon (τ), which are associated with their corresponding neutrino: ν_e, ν_μ, and ν_τ. The elementary particles can be arranged in three generations consisting of a pair of quarks, and a lepton with its corresponding neutrino. The masses of particles between generations are very different - the first generation is the lightest, whereas the heaviest particles are in the third generation, therefore they were discovered last. Only the elementary particles from the first generation form the visible matter, as the heavier particles from higher generations quickly decay to lighter particles. Neutrinos were thought to be massless in the SM, however the observation of neutrino oscillations [4,5] directly implies their non-zero mass, therefore their masses were later incorporated into the SM. The neutrino masses are however very small (at the level of a fraction of an electronvolt) so it is experimentally extremely challenging to measure them and so-far only upper limits on their mass have been experimentally determined [6–8]. The lepton generations have an associated corresponding lepton number, which is conserved in all interactions in the SM, except in neutrino oscillations.

All of the described particles have an anti-particle, which has the same mass, but opposite quantum numbers to their corresponding particle. However, the situation is still not clear for neutrinos, as they might be their own anti-particle, or may also have a corresponding anti-matter counterpart. Many current neutrino experiments try to resolve this outstanding ambiguity. The elementary particles are fermions with a

---

[5] Commonly also known as a *beauty* quark.

spin (which represents an intrinsic angular momentum) of $1/2$, therefore they obey the Pauli exclusion principle which says that only one fermion can be in a given quantum state within a quantum system. Leptons interact via the electromagnetic and weak force, and neutrinos only via the weak force. The electric charge[6] of leptons is -1, whereas their corresponding neutrinos are, as their name suggest, neutral, so their electric charge is zero. The u, c and t quarks have an electric charge of $+2/3$, the d, s and b quarks have an electric charge of $-1/3$. Apart from interacting via electromagnetic and weak forces, the quarks have also a colour charge, therefore they also interact via the strong force. Due to the properties of the strong interaction, which are described in Section 1.1.4 in more detail, it is not possible to observe free quarks, but only confined in *colourless* objects called hadrons: the three-quark (or three-antiquark) combinations qqq are known as baryons, which have half-integer spin; or quark-antiquark $q\bar{q}$ pairs known as mesons, which have integer spin.[7]

1.1.3. Fundamental forces

There are four fundamental forces observed in the universe: the weak, strong, gravitational, and electromagnetic force. They all differ by their corresponding strength, range, and on which elementary particles they act on. The main differences and the carrier of the corresponding forces are summarised in Table 1.1. Gravity is the only fundamental force that is not described by the SM, as there is no quantum theory for this interaction.[8] But as one can see from Table 1.1, the gravitational force is very weak with respect to other fundamental forces, so it can be neglected at the scale of particle physics.

The fundamental forces that are described by the SM are mediated by force carriers, the so-called gauge bosons. Gauge bosons are exchanged between elementary particles, described above, during their interactions. The W^-, W^+ and Z bosons are the carriers of the weak force, the photon (γ) acts as a carrier of the electromagnetic force, and the strong force is carried by the gluons. The electromagnetic and weak interactions

---

[6] Electric charge is given in units of the electron charge throughout this document.

[7] It is also possible to combine quarks as pentaquarks $qqqq\bar{q}$, or tetraquarks $q\bar{q}q\bar{q}$, or any other combination following the rules of the quark model described in 1.2.1, but they are considered to be *exotic hadrons* due to their rare and unusual nature.

[8] Yet. It is not known if a quantum description of gravity is possible, but nevertheless, there are ongoing efforts in the theory community to develop a theory that would incorporate all fundamental forces.

Force	Carriers	Range [m]	Strength
Strong	gluons	10^{-15}	10^{38}
Electromagnetic	photons	infinite	10^{36}
Weak	$W^{\pm}$ and Z	10^{-18}	10^{25}
Gravitational	?	infinite	1

Table 1.1.: Fundamental forces in nature and their carriers with the corresponding range and approximate relative strength of their effect, felt by a proton–proton pair, with respect to the gravitational force.

are unified into one theory, the so-called electroweak theory. The theory of the strong interaction, QCD, is described in Section 1.1.4 in more detail. Before that, one more important concept in the SM should be introduced. It is interesting that not all gauge bosons have a mass - the photon and gluons are massless, whereas the $W^{\pm}$ and Z boson have a non-zero mass. This is not a natural consequence of the SM, as all of the force carriers come massless without the introduction of some additional mechanism. This issue is solved with spontaneous symmetry breaking by the Higgs mechanism, where the fields representing the electroweak interaction mix and create physically observable states with non-zero masses, the $W^{\pm}$ and Z bosons, while still keeping the SM a renormalisable theory.[9] Moreover, a consequence of the interaction of the Higgs field with itself is the Higgs boson H with zero spin, which was the last piece of the SM to be found.[10]

1.1.4. Quantum chromodynamics

Quantum chromodynamics (QCD) is the gauge theory of strong interactions, which describes the interactions between particles carrying a colour charge. A simplified Lagrangian of QCD is

$$\mathcal{L}_{\mathrm{QCD}} = \overline{\psi}(i\gamma^{\mu}D_{\mu} - m)\psi - \frac{1}{4}G^{a}_{\mu\nu}G^{\mu\nu}_{a}, \tag{1.5}$$

---

[9] A *renormalisable theory* is a theory that does not involve an infinite amount of divergent terms, so by binding together finite number of divergencies into some non-constrained parameters, the theory can make quantitative predictions once those parameters are experimentally determined. A simple addition of the masses for the $W^{\pm}$ and Z bosons would break the renormalisation of the electroweak theory, hence making the SM unusable.

[10] The next chapter will reveal when and where the Higgs boson was discovered.

where γ^{μ} are the Dirac γ-matrices, $\psi(x)$ represents a quark field with mass m, the gluon field strength tensor is represented by G^{a}_{μ}, and D_{μ} is the gauge covariant derivative. The covariant derivative in QCD is $D_{\mu} = \partial_{\mu} - ig_s T_a G^{a}_{\mu}$, where T_a are eight generators of the SU(3) group, represented by the gauge bosons acting as mediators of the strong interaction, which are the massless spin-1 gluons, and g_s is the QCD coupling constant[11], which is one of the fundamental parameters of QCD and it determines the strength of an interaction between the particles with a colour charge. Index a in the previous definitions runs from 1 to 8 and denotes eight different gluon fields. The quarks are described by quark fields ψ associated with a colour charge (which can be red (R), green (G), or blue (B), but it has nothing to do with colours as we know them in our macro world) with a fundamental representation as a triplet

$$\psi(x) = \begin{pmatrix} \psi_R(x) \\ \psi_G(x) \\ \psi_B(x) \end{pmatrix} \tag{1.6}$$

that transforms so that the QCD Lagrangian is invariant under local transformations.

Interestingly, the gluon field strength tensor $G^{\mu\nu}_{a}$ contains a self-interacting part, which means that the gluons can couple to each other, directly implying that the interaction between two colour particles is stronger with increasing distance. At short distances (or equivalently at large energies), the strength of the strong interaction, represented by the effective coupling between quarks, is weak and the quarks and gluons are free, which is called *asymptotic freedom*. In this regime, the QCD calculation of the scattering cross-sections between quarks and gluons can be performed using perturbation calculations.[12] However, at large distances, the coupling is large and the calculations enter a non-perturbative regime, where the use of more sophisticated methods is needed in order to make any predictive quantitative calculations, some of which are discussed in Section 1.2.2. This effect causes that the quarks and gluons are bound together inside hadrons, called *colour confinement*, which is the reason why it is not possible to observe free quarks or gluons. Any hadron should therefore be considered as a system of valence quarks (qqq for baryons and $q\bar{q}$ for mesons) and an infinite *sea* of virtual quarks and gluons. An approximate energy scale at which

---

[11] The QCD coupling constant is strictly speaking not a constant as it varies as a function of the transferred momentum. But at a fixed energy scale, it is a constant.

[12] More on perturbation calculations is discussed in Section 1.2.2.

the transition between the regimes of asymptotic freedom and confinement occurs is about 200 MeV, denoted as Λ_{QCD}.

1.1.5. Hadronic weak decays

Since quarks have a non-zero weak isospin, the interactions between quark generations can occur via the flavour-changing weak interactions through $W^{\pm}$ boson exchange.[13] Only left-handed particles interact via the weak charged-current interactions, as the charged weak bosons do not couple to right-handed fermions. The right-handed particles have their spin vector projection aligned with their momentum vector, whereas for the left-handed particles the two quantities are anti-parallel. The neutral weak boson Z interacts with both right-handed and left-handed particles.

As the quark flavours are not conserved in the weak interactions, the weak-interaction eigenstates (d', s', b') are different to the flavour eigenstates (d, s, b). A transformation between the two eigenstates can be represented as

$$\begin{pmatrix} d' \\ s' \\ b' \end{pmatrix} = V_{\mathrm{CKM}} \begin{pmatrix} d \\ s \\ b \end{pmatrix} = \begin{pmatrix} V_{ud} & V_{us} & V_{ub} \\ V_{cd} & V_{cs} & V_{cb} \\ V_{td} & V_{ts} & V_{tb} \end{pmatrix} \begin{pmatrix} d \\ s \\ b \end{pmatrix},$$

where V_{CKM} is a unitary matrix called the Cabibbo–Kobayashi–Maskawa (CKM) matrix [9, 10], which represents mixing between the flavour eigenstates. As the CKM matrix represents how much of a flavour eigenstate there is for a weak eigenstate to interact with, the individual elements of the CKM matrix give the effective strength of the weak interaction on a particular flavour i quark to a flavour j quark transition.

Based on its unitarity and the arbitrariness of some internal complex phases, the CKM matrix has four independent parameters, which can be parametrised with the three real parameters as a representation of the mixing angles between the quark generations, and one complex parameter commonly known as a complex phase [10]. A consequence of the non-reducible complex phase is that some of the elements are

---

[13] As the weak isospin of the Z boson is zero, flavour-changing neutral currents are not allowed in the SM.

complex, which provides a mechanism for the violation of the combined charge (C) and parity (P) symmetry, the so-called CP violation in the weak interactions [10].[14]

The magnitudes of the CKM elements are determined from a combination of various experimental results [11] as

$$\begin{pmatrix} |V_{ud}| & |V_{us}| & |V_{ub}| \\ |V_{cd}| & |V_{cs}| & |V_{cb}| \\ |V_{td}| & |V_{ts}| & |V_{tb}| \end{pmatrix} = \begin{pmatrix} 0.97401 \pm 0.00011 & 0.22650 \pm 0.00048 & 0.00361^{+0.00011}_{-0.00009} \\ 0.22636 \pm 0.00048 & 0.97320 \pm 0.00011 & 0.04053^{+0.00083}_{-0.00061} \\ 0.00854^{+0.00023}_{-0.00016} & 0.03978^{+0.00082}_{-0.00060} & 0.999172^{+0.000024}_{-0.000035} \end{pmatrix}.$$

The probability of a transition from flavour j quark into flavour i quark is proportional to $|V_{ij}|^2$. The unitarity of the CKM matrix gives unitarity relations between its elements, namely $\sum_i V_{ij}V^*_{ik} = \delta_{jk}$ and $\sum_j V_{ij}V^*_{kj} = \delta_{ik}$. Experimentally, the most commonly used unitarity relation out of the six vanishing combinations is $V_{ud}V^*_{ub} + V_{cd}V^*_{cb} + V_{td}V^*_{tb} = 0$, since it can be represented as a triangle in the complex plane with sides of a similar size.

1.1.6. Limitations of the SM

The SM model provides a very good description of the microscopic world, as its predictions are confirmed by thousands of measurements with great precision. However, it is clear that the SM does not give a complete picture of the subatomic world. To list a few examples:

- Dark matter and dark energy, which together make up about 95% of the mass-energy content of the universe, are not incorporated in the SM.
- The SM does not provide a sufficient explanation of the observed matter-antimatter asymmetry in the universe as there is not enough CP violation in the SM weak interactions to explain it.
- Neutrino oscillations are also not possible to explain by the SM.

---

[14] The charge symmetry is invariant under the transformation of a particle to its anti-particle, and the parity symmetry is invariant under a mirror reflection of the spatial coordinates. The combined CP symmetry is invariant under both of these changes simultaneously. The strong and electromagnetic interactions are invariant under the CP symmetry, but not the weak interactions.

- As was already mentioned, one of the fundamental forces, gravity, is not incorporated in the SM. It is possible (even though still not clear) that the fundamental forces unify at some scale.
- The SM does not explain some of its observed qualities, such as why there are three generations of the fundamental particles and the structure of their observed masses, the CKM matrix, or fine tuning of some of its free parameters.

These and other open questions directly suggest that some new physics beyond the SM is still to be understood and observed. A lot of effort is therefore dedicated to search for such predictive theories, and to search for the corresponding observables in various experiments. With the current sophisticated particle experiments, advanced theoretical and experimental methods, and brilliant minds working on these peculiar problems, we are hopefully not far from a significant breakthrough in this area.

1.1.7. Experimental discrepancies with the SM predictions

A careful reader surely noticed the use of a specifically chosen word combination in the last sentence of the first paragraph in Section 1.1, namely *"the vast majority of the experimental results are compatible with the SM predictions"*. The vast majority is not all, exactly. There are a few exceptions that might be the first signs of physics beyond the SM, if confirmed in the future. This section summarises the three areas where large deviations with respect to the SM predictions are seen.

Firstly, a long-standing discrepancy is a measurement of the anomalous magnetic dipole moment of a muon, which currently provides one of the largest tensions with the SM predictions.[15] A new result from the g-2 experiment in Fermilab was announced in 2021 [12], where its combination with a result from the g-2 experiment in Brookhaven [13] from 2006 gives a tension with the SM prediction at the level of 4.2 standard deviations. Currently, more data collected by the g-2 experiment are being analysed, therefore a measurement with improved precision is expected in the near future.

A set of anomalies has been reported over the last decade in the b-physics sector, for example angular observables in the $b \to s\ell^+\ell^-$ transitions, measurements of lepton

---

[15] Interestingly, the experimental results for the anomalous magnetic dipole moment of an electron provide the most accurate prediction of the SM - the measured value agrees with its theoretical prediction to more than 10 significant digits!

flavour universality, or the branching ratios of the $B_s^0 \to \mu^+\mu^-$ and $B^0 \to \mu^+\mu^-$ decays. A global fit of the observed anomalies deviates from the SM at the level of up to 4.7 standard deviations [14]. The single measurement with the largest deviation from the SM in this sector is a result reported by the LHCb collaboration measuring the ratio of branching fractions for the $B^+ \to K^+\mu^+\mu^-$ and $B^+ \to K^+e^+e^-$ decays, resulting in a deviation from the SM prediction at 3.1 standard deviations [15]. These results combined form so far the most striking anomalies as they were measured in different decays and by different experiments, including BaBar, Belle, CMS, ATLAS and most precisely by LHCb. However, more data are needed to confirm if the observed results are a demonstration of physics beyond the SM and not only a statistical fluctuation.

The most recent striking result was announced in April 2022, when the CDF collaboration reported the most precise measurement of the W-boson mass to date [16] with a discrepancy of 7 standard deviations from the SM prediction. Interestingly, the measured value also deviates from the previous results on the W-boson mass from other experiments, for example D0 II [17], a combination of the results from the LEP experiments [18], ATLAS [19], LHCb [20], with a descrepancy of the CDF result from their combined average [11] at the level of about 3.9 standard deviations. There is no question it is an exciting result of what is a very complex measurement, but the discrepancy with the previous world average should be understood in the first place.

All of these results, if confirmed, would be the first hints of physics beyond the SM. The mediators of these new effects remain unknown, even though there are countless theory models that try to interpret the observed anomalies. Since the research described in the following chapters is not relevant to searches for physics beyond the SM, it is not discussed in more detail. Nevertheless, it is important to note that this is an exciting time for particle physics as there is still a lot to be discovered.

1.2. Quark and hadron spectroscopy

Quark and hadron spectroscopy deals with a description of properties of strongly interacting particles. Based on QCD, hadrons are known to be the bound states of quarks and gluons, as introduced in Section 1.1.4. The quantum numbers of hadrons are given by the intrinsic quantum numbers of quarks, as the gluons carry only colour charge. Quarks are fermions with spin 1/2 and positive parity[16]. There are more

---

[16] Consequently, the anti-quarks have negative parity

intrinsic quantum numbers that can be used to classify hadrons, which are introduced in the following sections, where the quark model is described. As there are tens of quark combinations to form various hadronic states, the quark model provides a useful framework to classify hadrons and to understand relations between various states.

1.2.1. The Quark Model

As was described earlier in this chapter, quarks are bound together by the strong interaction into composite particles called hadrons. As it is not possible to observe quarks and gluons freely due to their confinement, hadrons play an important role in particle physics because they provide an environment to study QCD.

The quark model provides a useful classification and prediction scheme for hadrons. It was first introduced by Gell-Mann [21], and independently by Zweig [22], in 1964. The quark model predicts the existence of multiplets of baryon and meson states with a structure determined by the symmetry properties of the hadron wavefunctions. At the time of its establishment, the quark model provided a classification scheme for hadrons made from the three lightest quarks - u, d, and s quarks. However, it was successfully extended to accommodate the rest of the observed quark flavours.[17]

The excited hadron states, called *resonances*, are unstable states that decay to lighter hadrons by the strong or electromagnetic interaction. The quantum numbers associated with a quark flavour are conserved in both of these interactions. For the strong interaction, a typical time scale of a decay is about 10^{-23} s, whereas for the electromagnetic interaction it is typically in a range from 10^{-16} to 10^{-21} s. The ground states decay to lighter hadrons via the weak force, in which a quark flavour is not conserved, as described by the CKM matrix discussed in Section 1.1.5. The lifetimes of weak decays are substantially longer than for the strong decays, usually in a range from 10^{-6} to 10^{-14} s, and they depend on the energy released in the decay, the so-called Q value.

---

[17] It is important to note that there are no hadrons containing a t quark as its lifetime is too short to form hadron-bound states.

1.2.1.1. Isospin symmetry

An approximate symmetry between u and d quarks is a useful characteristic to provide a relationship between hadrons that have the u (d) quark instead of the d (u) quark. It is not an exact symmetry as the masses and electric charges of the u and d quarks are not the same. However, as the electromagnetic force is weak with respect to the strong force and the mass difference between the u and d quarks is very small compared to Λ_{QCD}, it allows for a symmetry approximation, called the *isospin symmetry*. Using the isospin symmetry, particles can be related into isospin multiplets.

Firstly, let us introduce some additional intrinsic quantum numbers for quarks and hadrons, which are connected to the mentioned isospin symmetry. As was already mentioned, quark flavours are conserved in the strong interactions. The additive quantum numbers associated with the quark flavours are strangeness $S = -1$ for the s quark, charm $C = 1$ for the c quark, bottom $\widetilde{B} = -1$ for the b quark, and top $T = 1$ for the t quark. Together with the additive baryon quantum number B, which is $B = 1/3$ for quarks and $B = -1/3$ for anti-quarks (therefore $B = 1$ for baryons, $B = -1$ for anti-baryons, and $B = 0$ for mesons), the quantum numbers for quark flavours can be combined into the so-called hypercharge Y, which can be defined[18] as

$$Y = B + S - \frac{C - \widetilde{B} + T}{3}. \tag{1.7}$$

The hypercharge Y given by Equation 1.7 is $1/3$ for the u and d quark, $-2/3$ for the s quark, and zero for all other quarks. The hypercharge is not a useful quantum number per se, but it can be used to classify hadrons in a given multiplet as it forms equidistant planes with the same Y, as shown in the next section. To classify individual hadrons in isospin multiplets, the quantum number I_3 is defined as the third component of the isospin I, which relates to the electric charge Q, the baryon number B, and the flavour quantum numbers through the generalised Gell-Mann-Nishijima formula as

$$I_3 = Q - \frac{B + S + C + \widetilde{B} + T}{2}. \tag{1.8}$$

---

[18] The concept of hypercharge was first introduced only for the three lightest quarks. It can be extended to six-quark flavours as given by Equation 1.7, so that Equation 1.8 also holds for six-quark flavours. However, it is only one of the possible extensions and other conventions are also used, for example a sum of the baryon number and flavour quantum numbers $Y = B + S + C + \widetilde{B} + T$.

The values of I_3 can run from $I, I-1, \dots, -I$, where I is the maximum value of I_3 in a given multiplet. As other intrinsic quantum numbers, the isospin is also conserved in the strong interactions. From these rules, one can deduce that $I_3 = -1/2$ for a d quark and $I_3 = 1/2$ for an u quark, whereas $I_3 = 0$ for the remaining quark flavours. We can therefore assign u and d quarks into an isospin doublet with $I = 1/2$.

Isospins for composite hadrons follow simple addition rules, where the isospin can run from their sum to their difference in steps of 1, and its third component of the isospin is just the sum of the individual values of I_3. For the simplest case of the lightest baryons, proton and neutron, it is clear they form an isospin doublet. In case of the lightest mesons, the pions, an isospin triplet is formed where π^+, π^0, and π^- have I_3 of $+1$, 0, and -1, respectively. This principle can be further extended to heavier hadrons, as we will see in the next section for doubly charmed baryons. It is expected, and experimentally confirmed for many hadrons, that a mass difference between the hadrons from the same isospin multiplet is very small, at the level of a few MeV/c^2.

1.2.1.2. Baryons in flavour SU(4) symmetry

As was mentioned earlier, quarks are fermions, so they have to obey the Pauli exclusion principle. Therefore, a wavefunction of the three-quark system $|qqq\rangle$ must be antisymmetric under interchange of any two quarks. The baryon wavefunction $|qqq\rangle$ can be expressed as

$$|qqq\rangle_A = |\text{colour}\rangle_A \times |\text{space, spin, flavour}\rangle_S, \tag{1.9}$$

where the A and S labels represent symmetry and antisymmetry of the corresponding wavefunctions, respectively. Since a color-singlet representation $|\text{colour}\rangle$ is antisymmetric, the wavefunction with respect to space, spin and flavour has to be symmetric in order to have an overall antisymmetric baryon wavefunction. The ground-state baryons have the orbital angular momentum $L = 0$, therefore their corresponding spatial wavefunction $|\text{space}\rangle$, given by $(-1)^L$, is symmetric. This implies a constraint on the product of the spin and flavour wavefunctions, $|\text{spin}\rangle \times |\text{flavour}\rangle$, to be symmetric for all ground-state baryons. A total angular momentum J, commonly referred to as the total spin, is given by the orbital angular momentum L of the qqq state as $|L-S| \leq J \leq |L+S|$, where S is the intrinsic angular momentum, which in case of baryons is 1/2 or 3/2, depending on the alignment of spin of the individual quarks. As for the ground-state baryons $L = 0$, their total spin J can be either $1/2$ or $3/2$ and it is given only by the alignment of the spin of the individual quarks in a baryon. The corresponding wavefunction $|\text{spin}\rangle$ for spin $3/2$ combinations is completely symmetric, whereas for spin $1/2$ combinations it is of a mixed symmetry. The flavour states can be classified as either symmetric, antisymmetric, or mixed combinations. Therefore to get the symmetric product $|\text{spin}\rangle \times |\text{flavour}\rangle$, symmetric states with $3/2$ spin have to be combined with symmetric representations of the flavour states, and the spin $1/2$ states with mixed symmetry have to be combined with mixed representations of the flavour states, in order to form a fully symmetric product.

The baryons containing u, d, s and c quarks can be embedded into an approximate flavour SU(4) symmetry. Due to the much heavier mass of the c quark compared to the three lightest quarks, this symmetry is heavily broken, however it provides a good classification scheme under the SU(4) $\rightarrow$ SU(3) $\times$ U(1)$_{\text{charm}}$ decomposition for multiples of baryons containing a three-baryon combination of the u, d, s and c quarks [11]. The flavour SU(4) tensor product of the three quarks in the baryon is $4 \times 4 \times 4 = \overline{4}_A + 20_S + 20_M + 20_M$ [23], where A, S and M subscripts label the antisymmetric, symmetric, and mixed representation, respectively. Since the spin-flavour representation of ground-state baryons has to be fully symmetric, the ground-state baryons belong to the 20_S with total spin J and parity P of $J^P = \frac{3}{2}^+$, and a single combination of the two 20_M with $J^P = \frac{1}{2}^+$ [11].[19] Figure 1.2 shows three-dimensional illustrations of these 20-plets, where the vertical level represents different charm quantum numbers C, and in a plane of the individual levels with different C, the x-direction represent I_3 and the y-direction the Y quantum numbers described in the previous section. The bottom levels are therefore the SU(3) light-baryon decuplet and octet with charm quantum number equal to zero.

The excited states can be constructed from higher orbital angular momentum states. They represent an important part of hadron spectroscopy as they provide an extensive way of testing the QCD predictions for higher orbital angular momentum, for which many states are predicted. However, they are not discussed further as they go beyond the extent of this introduction and are not relevant for the studies of the doubly charmed baryons presented in this thesis.

The baryon multiples can be further extended to include b quarks based on flavour SU(5) symmetry. Since the main emphasis in this thesis is given to the doubly charmed

---

[19] The states from $\overline{4}_A$ cannot be constructed as it is fully antisymmetric, as well as the antisymmetric combination of the two 20_M. They can however describe the states with a higher angular momentum.

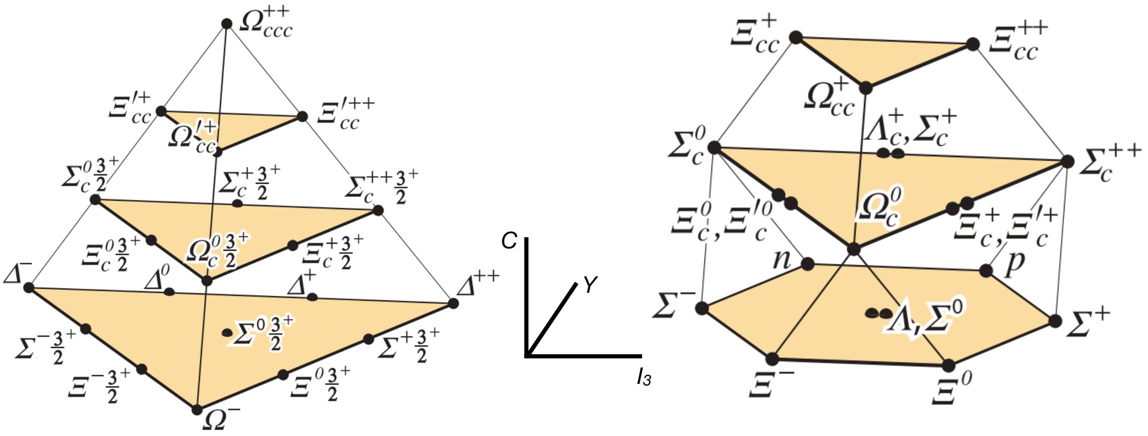

Figure 1.2.: Ground-state baryon 20-plets with $J^P = \frac{3}{2}^+$ (left) and $J^P = \frac{1}{2}^+$ (right) [11]. The individual shaded levels represent a different charm quantum number (from bottom 0, 1, 2 and 3 for the 20-plet on the left; 0, 1, and 2 for the 20-plet on the right). The axes in the centre indicate the quantum numbers for each of the three dimensions.

states, a further description of the hadrons containing b quarks is not presented. However, they also represent an important environment to test QCD predictions.

All ground states of the charmless and singly-charmed baryons from the SU(4) 20-plets, shown in Figure 1.2, have been discovered, together with many of their excited states [11]. Of the doubly or triply charmed baryons, only the Ξ_{cc}^{++} baryon has been unambiguously discovered, as discussed in Section 1.3 in more detail.

1.2.2. Calculation techniques

One of the main goals of QCD is to predict the mass spectrum of hadrons. As shown in the following sections, where some of the methods are discussed, it is not an easy task. One of the most used techniques in QFT (and more generally in quantum mechanics) is perturbation theory in order to calculate predictions for complicated systems using small perturbing terms as corrections to some simpler, solvable system. The key in the perturbation calculations is that these corrections are small compared to the calculated quantities. The main obstacle in QCD is that it is not possible to use perturbation methods at larger distances where the hadronisation occurs, as the strong coupling is large in this region, as was already mentioned when QCD was introduced in Section 1.1.4. Therefore to study physics at the hadronic level, one enters the region of non-perturbative QCD. Three commonly used QCD calculation techniques are therefore presented in the next sections to give an overview of how the various quantitative and qualitative predictions of hadron properties, such as hadronic matrix elements, form factors, weak decay constants, or hadron masses, are calculated.

As one can expect, all of the methods are complex mathematical techniques as they are trying to solve one of the most complicated areas of the SM - the non-perturbative region of QCD. What follows is therefore only an overview of the calculation techniques, not their precise description, as this is beyond the scope of this theoretical introduction and beyond the skills of the author, a non-theoretical physicist.

1.2.2.1. Lattice QCD

Lattice QCD is the only method that uses first principles for its calculations, using finite dimensional path integrals in QCD. Lattice QCD was first introduced by K. Wilson in 1974 [24]. The name of this method is highly descriptive as it uses a lattice in the space-time coordinates in a finite volume with small spacing usually on a hypercubic lattice, where the links between sites represent gauge fields, and quark fields are placed on the sites [11]. In the limit of vanishing lattice spacing, the continuum theory is recovered. It is a complex method that uses Monte Carlo simulations to generate random samples of all possible configurations of the quark and gluon fields, and therefore requires a lot of computational resources, as well as efficient algorithms, to obtain a required precision.

As with every theoretical computational technique, there are systematic uncertainties that need to be considered. The uncertainties related to lattice QCD predictions mainly arise from finite lattice spacing that needs to be extrapolated to the continuum limit, which depends on the choice of fitting function. Further uncertainties are due to the finite simulation volume, or the use of the u and d quark masses to be heavier than their experimental values in simulations where virtual quark-antiquark pairs are included, and the need to extrapolate their masses [11].

Nevertheless, lattice QCD represents a state-of-the-art theoretical framework for (not only) spectroscopy calculations. It is mainly due to huge advances in computational resources and more efficient algorithms over the last decade, which allow to perform lattice QCD calculations with a high precision.

1.2.2.2. Heavy quark effective theory

Heavy quark effective theory (HQET) provides a systematic framework using effective field theory (EFT)[20] for heavy-quark systems [25–29]. The masses of c and b quarks are much larger than the QCD energy scale Λ_{QCD}, therefore the EFT provides a good approximation at the heavy-quark scale, where the heavy quarks acts like a static colour source resulting in the simplified QCD interactions. The scale of heavy-quark physics can be then treated perturbatively due to their short-distance nature. The long-distance effects arising from confinement of the strong interaction are treated using expansions in the inverse powers of a heavy-quark mass.

The HQET calculations provides successful predictions for properties of hadrons containing c and b quarks. The doubly heavy-baryon systems provide a different environment for the corresponding calculations than systems with only one heavy quark. The systems with two heavy quarks are often treated as a static diquark with one lighter quark orbiting around it, which simplifies the associated calculations. The experimental results on doubly heavy baryons will help to confront the predictions from HQET, especially for these specific systems.

1.2.2.3. QCD sum rules

A method called QCD sum rules introduced in 1979 by M. Shifman, A. Vainshtein and V. Zakharov [30] is also often used to calculate properties of the heavy-quark systems, but also more widely in hadron spectroscopy. Good agreement with the experimental data for various hadron observables is often achieved. In this method, the correlation functions of interpolating quark currents, which represent the hadrons, are treated using operator product expansion (OPE).[21] The short-distance interactions are calculated perturbatively, whereas nonperturbative long-distance effects are parametrized as corrections in the inverse powers of a heavy-quark mass using OPE. A sum over hadronic states is then calculated via a dispersion relation from the results of these long and short-distance contributions, where the current correlators are related to spectral densities [31].

---

[20] Effective field theories present a framework that operates at a given length scale, which signficantly simplifies the calculations of realistic quantum field theories, which cannot be solved exactly.

[21] The operator product expansion is used in QFT by defining the product of fields as a sum over the fields in order to allow for non-perturbative calculations.

The limitations and uncertainties of the method arise from the approximations in the OPE and due to complicated structures of the hadronic dispersion integrals. A comprehensive overview of QCD sum rules is presented in reference [32] which is recommended for further reading.

1.3. Doubly charmed baryons

The two baryon 20-plets shown in Figure 1.2 on page 17 were introduced in Section 1.2.1.2 for the baryons containing a combination of the u, d, s and c quarks. Each of these multiplets contains a triplet with two charm quarks – a $\Xi_{cc}^{+(+)}$ isodoublet ($I = 1/2$), with a quark content of ccu for the Ξ_{cc}^{++} state and ccd for the Ξ_{cc}^{+} state, and an Ω_{cc}^{+} isosinglet ($I = 0$) with a quark content of ccs. The states with $J^P = \frac{3}{2}^+$ are expected to decay to $J^P = \frac{1}{2}^+$ states via the strong or electromagnetic interaction. The $J^P = \frac{1}{2}^+$ ground states decay weakly with a c quark transformed to a lighter quark, as shown in Figure 1.3, predominately via the $c \rightarrow sW^{*+} \rightarrow su\overline{d}$ decay, but also through the Cabibbo suppressed decays $c \rightarrow dW^{*+} \rightarrow du\overline{d}$ or $c \rightarrow sW^{*+} \rightarrow su\overline{s}$, where W^{*+} denotes exchange of a positive, virtual W boson.

In general, hadron spectroscopy is an important area to understand dynamics between quarks and gluons and the interactions of hadrons to improve our knowledge about the non-perturbative sector of QCD. As the doubly charmed baryons contain two heavy quarks, they provide a different environment to study QCD than the light-quark systems. The following Section 1.3.1 and its subsections provide an overview of the theoretical predictions for the properties of the doubly charmed baryons. The theoretical predictions can be subsequently compared to experimental results, once the doubly charmed baryons are observed and their properties are precisely measured. The current experimental overview of doubly charmed baryons is therefore discussed in Section 1.3.2.

1.3.1. Theoretical predictions

There are numerous predictions for the fundamental properties of the doubly charmed baryons based on QCD calculation techniques, some of which were introduced in Section 1.2.2. In the following discussion, mainly ground states of doubly charmed baryons with $J^P = \frac{1}{2}^+$ are discussed, as it is experimentally easier to observe the ground states before their excited states can be observed and studied. The theoretical predictions of the main properties, namely production, mass, lifetime, and decay modes, are discussed in the following corresponding sections.

1.3.1.1. Production

The theoretical predictions of the production of doubly charmed baryons at hadron colliders is an important input to their experimental studies, as it is crucial to understand if it is feasible to search for these states at the given experimental conditions. The production mechanisms are also an important input to simulate the production of the doubly charmed baryons, as the simulation samples are used in many experimental studies.

A calculation of the production of doubly charmed baryons is in general treated in two steps: production of a cc pair via short-distance processes, and hadronisation of the produced diquark with a light quark via long-distance interactions forming a doubly charmed baryon [33–40]. The first step can be calculated at the perturbative QCD level, since it involves only heavy quarks and hard interactions [33]. Some

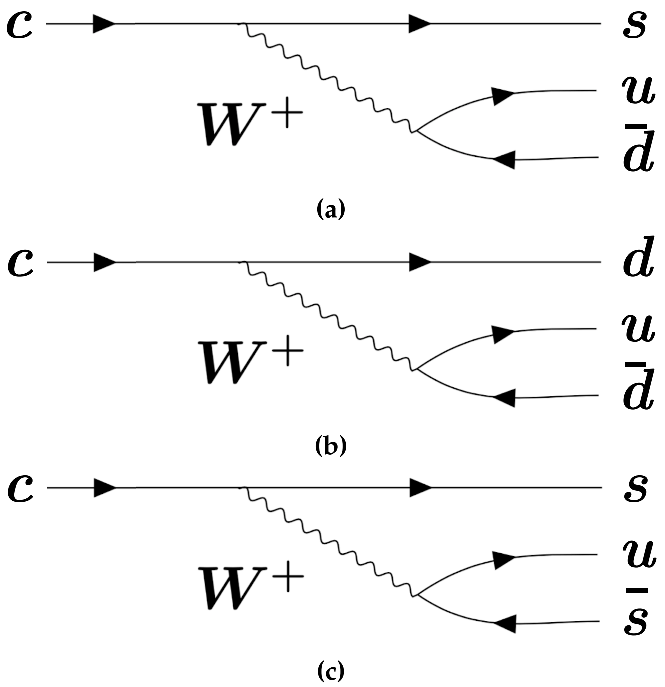

(c)

Figure 1.3.: Examples of the (a) Cabibbo favoured $c \to sW^{*+} \to su\bar{d}$ and the Cabibbo suppressed (b) $c \to dW^{*+} \to du\bar{d}$ and (c) $c \to sW^{*+} \to su\bar{s}$ weak transitions relevant for the decays of doubly charmed baryons.

possible Feynman diagrams contributing to the production of the cc diquark via gluon-gluon fusion and quark-antiquark interactions, which are used in the calculations, are shown in Figure 1.4. Although gluon-gluon fusion is the dominant mechanism of the doubly charmed baryon production at hadron colliders, the contributions from quark-antiquark interactions and collisions of a quark and a gluon inside the colliding hadrons can be also large, as shown in reference [38], therefore they should be also considered in the calculations. For the second step, the non-relativistic QCD framework [41] is commonly used to calculate the corresponding matrix elements of the non-perturbative regime.

Since the first step is identical for all doubly charmed baryons, their relative production cross-section, which is a measure of the production rate, depends only on long-distance interactions and hadronisation with a light quark. For the isospin doublet of Ξ_{cc}^{++} and Ξ_{cc}^{+} baryons, where either an u or d quark is required, it is expected the production is the same for both states, as hadronisation with the u or d quark should occur with nearly the same probability [38]. For the Ω_{cc}^{+} baryon, where an s quark is required, its production cross-section is expected to be about $1/3$ of the production cross-section of the $\Xi_{cc}^{+(+)}$ isodoublet due to a different fragmentation with the s quark [42].

The calculations often come with large theoretical uncertainties arising from non-perturbative calculations, and they depend on several input parameters, such as the mass of the c quark or the value of the strong coupling constant. For example, a cross-section σ of the doubly charmed baryon $\Xi_{cc}^{+(+)}$ in proton-proton (pp) collisions at a centre-of-mass energy 13 TeV is calculated to be $\sigma_{\Xi_{cc}^{+(+)}} = 1800\,\text{nb}$ in reference [37], whereas it is $\sigma_{\Xi_{cc}^{+(+)}} = 122\,\text{nb}$ in reference [35], which is about 15 times smaller. The main reason for the observed differences between the results is the sensitivity of these predictions to values of input parameters. Nevertheless, a sizable production rate of the doubly charmed baryons in pp collisions is expected, as it is predicted to be in the range from 60 to 1800 nb [34,35,37–40].

The cross-sections depend on the initial process, and they are calculated not only for the pp collisions mentioned above, but also for other processes, such as ep, e^+e^- or $\gamma\gamma$ collisions [33,35–37]. However, the following chapters are devoted to the search for the doubly charmed baryon using data from pp collisions, therefore other production mechanisms are not discussed further in this overview.

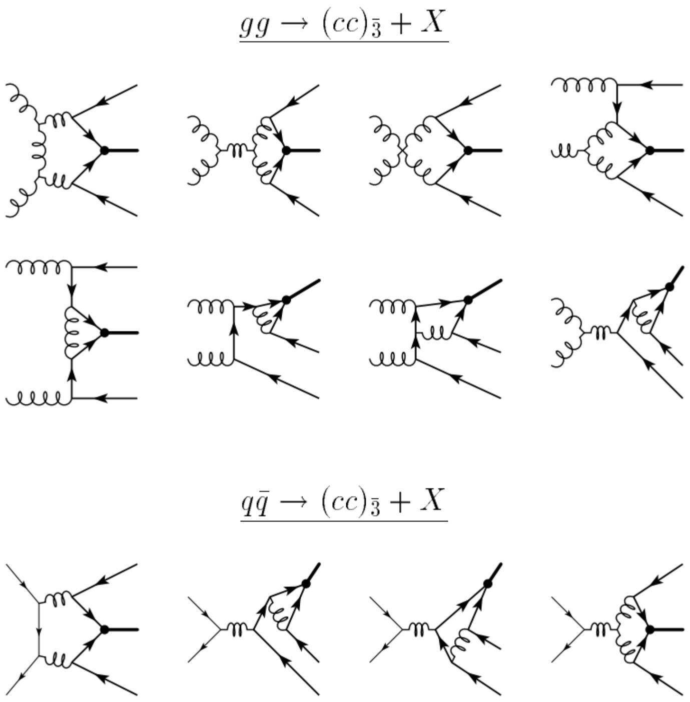

Figure 1.4.: Examples of Feynman diagrams for the gluon-gluon $gg \to cc + X$ (first two lines) and quark-antiquark $q\bar{q} \to cc + X$ (bottom line) production, reproduced from reference [35]. The helical lines are gluon propagators, the thin solid lines represent the initial quarks, and the final cc diquarks are denoted by the bold solid lines.

1.3.1.2. Mass

Many theoretical methods, such as lattice QCD [43–51], models using one light quark and two heavy quarks [52], QCD sum rules [53–57], heavy quark effective theory [58], the bag model [59] or the relativistic quark model [60], have been applied to determine masses of the ground and excited states of the doubly charmed baryons. The largest number of theoretical predictions for the masses of the $\Xi_{cc}^{+(+)}$ ground states are in the range from 3.5 to 3.7 GeV/c^2, depending on the theoretical model used [35,43,44,46–74], as shown in Figure 1.5. The mass splitting between singly and doubly charged $\Xi_{cc}^{+(+)}$ baryons is predicted to be small, a few MeV/c^2 [75–77], due to isospin symmetry, which was discussed in Section 1.2.1.1. For the Ω_{cc}^{+} baryon, it is predicted that its mass is about 100 MeV/c^2 higher than that of the $\Xi_{cc}^{+(+)}$ isodoublet.

Figure 1.6 shows a summary of the lattice QCD results, which were briefly introduced in Section 1.2.2.1, for the masses of the doubly and triply charmed baryons [11]. A horizontal line for the $\Xi_{cc}^{+(+)}$ state represent the measured mass of the Ξ_{cc}^{++} baryon

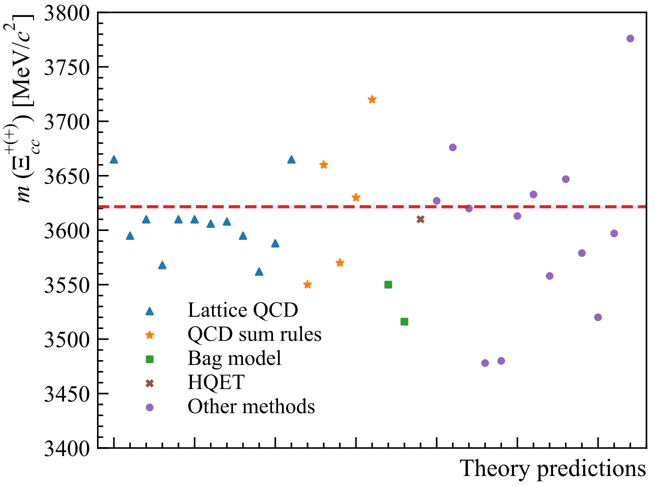

Figure 1.5.: Predicted central values for masses of the $\Xi_{cc}^{+(+)}$ ground states [35,43,44,46–74] for various theoretical calculations with the red dashed horizontal line representing the mass of the Ξ_{cc}^{++} baryon measured by the LHCb collaboration [78].

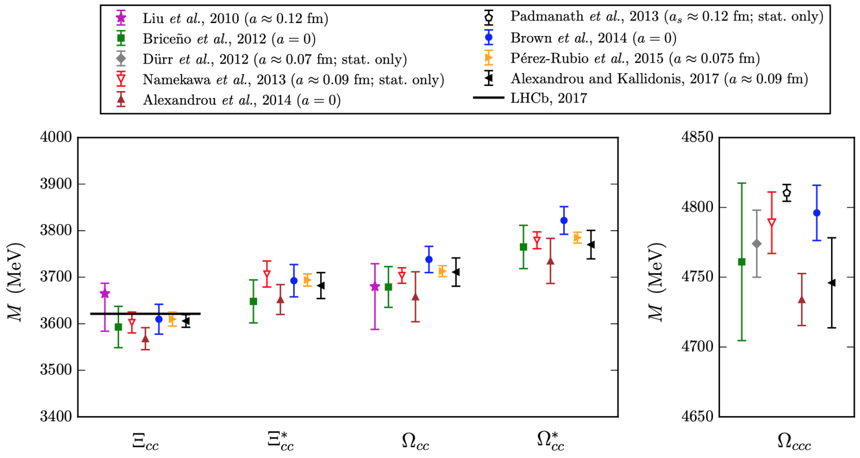

Figure 1.6.: Summary of the lattice QCD results [43–51] for the masses of the doubly and triply charmed baryons, reproduced from reference [11]. A horizontal line for the $\Xi_{cc}^{+(+)}$ state represents the measured mass of the Ξ_{cc}^{++} baryon observed by the LHCb collaboration [79] after these predictions were published.

observed by the LHCb collaboration in 2017 [79], which is described in Section 1.3.2 in more detail. One can see that the lattice QCD results provided an excellent prediction for the mass of this newly observed baryon.

1.3.1.3. Lifetime

There are many theoretical predictions for the lifetimes of the doubly charmed states. Many of these predictions vary significantly. They are mostly determined using the optical theorem to obtain the total width by calculating the absorptive part of the forward-scattering amplitude [80]. The OPE technique is usually used in calculations to determine nonperturbative contributions [81–84]. Most of the theoretical predictions for the lifetime of the Ξ_{cc}^{++} state are in a range from 200 to 700 fs [35, 52, 61, 81–86]. A wide range of the theoretical predictions is again caused by the initial parameters used in the calculations, and due to various methods used to calculate non-perturbative effects. However, a common feature in most of the predictions is the expectation that the doubly charged state Ξ_{cc}^{++} has about 2–4 times longer lifetime than the singly charged state Ξ_{cc}^{+} due to the effect of the destructive Pauli interference of the c-quark decay products and the valence u quark in the initial state. The Pauli interference occurs when there is a transition of the heavy quark in a hadron into an identical flavour of the spectator light quark in the hadron [87–89]. This effect impacts the decay rates, which are increased for the d and s spectator quarks, and decreased for the u spectator quarks [88], therefore there is a destructive interference for the Ξ_{cc}^{++} baryon. The Ξ_{cc}^{+} lifetime is further shortened due to the transition $cd \to su$, which is not present in the Ξ_{cc}^{++} decays, as they only proceed via the transition $c \to su\overline{d}$ [35, 82, 83, 85, 86]. Figure 1.7 shows these effects for all three doubly charmed baryons. Considering predictions for the ratio of $\Xi_{cc}^{+(+)}$ lifetimes, most of the lifetime predictions for the Ξ_{cc}^{+} baryon are in a range from 40 to 250 fs.

The lifetime of the Ω_{cc}^{+} state is predicted to be somewhere in between the $\Xi_{cc}^{+(+)}$ isodoublet states, with a value closer to the singly charged state and in an approximate range from 75 to 180 fs [35, 82, 83, 85]. The shorter lifetime of the Ξ_{cc}^{+} baryon than that of the doubly charged state by a factor of about 2–4 makes searches for the singly charged state and the Ω_{cc}^{+} baryon experimentally more challenging, as the longer lifetimes provide a higher efficiency to reject combinatorial background, especially in the environment of hadron colliders.

1.3.1.4. Decay modes and branching fractions

The decay properties are of key importance for any experimental search of unobserved hadrons. In general, it is rather challenging to find the decay mode with a significantly

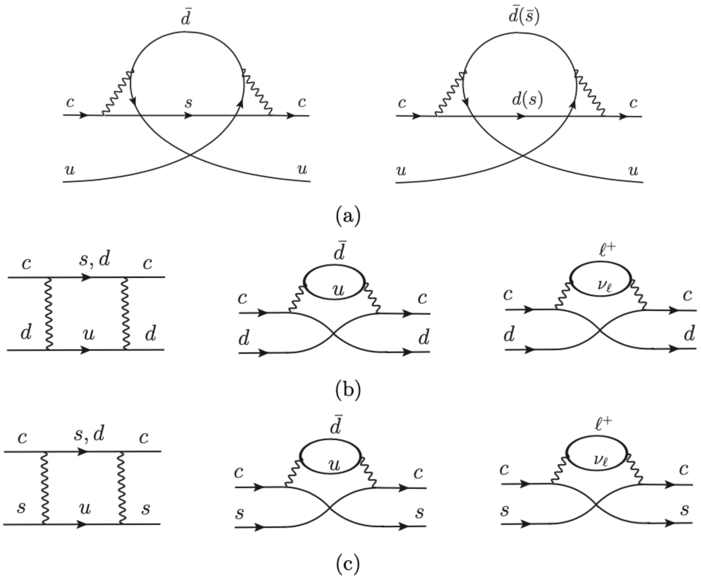

Figure 1.7.: Examples of spectator effects in decays of the doubly charmed baryons, reproduced from reference [86], for (a) destructive Pauli interference in Ξ_{cc}^{++} decays, and (left for (b) and (c)) W-boson exchange and (middle and right for (b) and (c)) constructive Pauli interference in (b) Ξ_{cc}^{+} and (c) Ω_{cc}^{+} decays.

high branching fraction for the doubly charmed baryons, therefore an experimental exploration of many decay modes is needed in order to increase the possibility of their observation. The lifetimes of the $\Xi_{cc}^{+(+)}$ baryons are important inputs for the predictions of their branching fractions (BFs). Since the lifetime of the Ξ_{cc}^{+} baryon is *a priori* unknown and there is a large uncertainty in predictions for the ratio between the lifetime of the Ξ_{cc}^{+} baryon and its isospin partner, the Ξ_{cc}^{++} baryon, it is difficult to make precise theoretical predictions for the BFs due to the associated uncertainties.

The BFs are usually calculated for two-body decays. As the multibody decays often proceed through some intermediate resonances, some multibody final states can be associated with theoretical predictions for two-body decays. The ratios of BFs are often predicted rather than their absolute values, since many theoretical uncertainties cancel in the ratio. If they are calculated as absolute BFs, they are usually associated with large systematic uncertainties. It is also important to note that for the interest of searches for these decays at hadron colliders, the final states that can be reconstructed in fully hadronic charged states are preferred, as they have a significantly higher reconstruction efficiency than decays that can be reconstructed only partially. Therefore the following review is focused only on fully hadronic decay modes of the doubly charmed baryons.

Regarding the Ξ_{cc}^{+} baryon, which is the main interest of the research described in this thesis, the $\Xi_{cc}^{+} \to \Lambda_c^{+} \overline{K}^{*0}$ resonant decay, leading to the $\Lambda_c^{+} K^{-} \pi^{+}$ final state, is generally considered to have a large BF among fully hadronic charged decays at a level of a few percent [90]. According to reference [91], where the predictions for the $\Xi_{cc}^{+(+)}$ BFs are calculated as the relative branching fractions, the BF for the $\Xi_{cc}^{+} \to \Lambda_c^{+} \overline{K}^{*0}$ decay is estimated to be approximately 5 times larger than for the $\Xi_{cc}^{+} \to \Xi_c^{+} \rho^{0}$ decay. The $\Xi_{cc}^{+} \to \Xi_c^{+} \rho^{0}$ decay, which can be reconstructed in the $\Xi_c^{+} \pi^{-} \pi^{+}$ final state, is indicated as one of the most promising modes to search for the Ξ_{cc}^{+} baryon in a fully hadronic state with its BF prediction of up to 2.5% [92,93]. The theoretical calculations indicate enhanced BF also for the $\Xi_{cc}^{+} \to \Xi_c^{0} \pi^{+}$ decay due to flavour dependence [35,94] at a few tens of percent level, or at least at the level of 4%, as calculated in [94].

For the doubly charged state Ξ_{cc}^{++}, the $\Xi_{cc}^{++} \to \Lambda_c^{+} K^{-} \pi^{+} \pi^{+}$ and $\Xi_{cc}^{++} \to \Xi_c^{+} \pi^{+}$ decays are considered to be the most favourable decay modes at a level of a few percent [91]. The Ω_{cc}^{+} decays that are favoured by the theory predictions, and which could be also considered for experimental studies, are the $\Omega_{cc}^{+} \to \Xi_c^{+} K^{-} \pi^{+}$ and $\Omega_{cc}^{+} \to \Omega_c^{0} \pi^{+}$ decays [93].

1.3.2. Experimental status

All of the predicted baryon ground states that contain zero or one valence charmed quarks have already been discovered [11], as was already discussed in Section 1.2.1.2. However, the experimental observation of the doubly charmed states has shown to be rather challenging, as shown in the following overview.

The first published evidence of the doubly charmed baryon was reported by the SELEX collaboration in 2002, when they announced an observation of the Ξ_{cc}^{+} baryon in $\Xi_{cc}^{+} \to \Lambda_c^{+} K^{-} \pi^{+}$ decays [95], later followed by reported evidence in the $pD^{+}K^{-}$ decay mode [96]. The reported state was measured with a mass of $3518.7 \pm 1.7\,\mathrm{MeV}/c^2$, local significance of 6.3 standard deviations for the $\Lambda_c^{+} K^{-} \pi^{+}$ and 4.8 standard deviations for the $pD^{+}K^{-}$ final states, and an upper limit on its lifetime was determined to be 33 fs at the 90% confidence level. These results were unexpected for the theory community, since the measured value is not consistent with the expectation for a lifetime of a weak decay. Moreover, the measured Ξ_{cc}^{+} mass was below almost all theoretical predictions, and the reported production rate was several orders of magnitude larger than theoretical predictions for the collisions of the hyperon beam with a fixed target.

In short, the SELEX observations could not be explained by any known mechanism of the strong interaction [76]. Subsequent searches for the Ξ_{cc}^{+} state by other experiments did not confirm the SELEX result. There were searches performed by the BaBar [97], Belle [98] and FOCUS [99] experiments but none of them showed any evidence of the reported doubly charmed baryon. The LHCb collaboration also performed a search for the singly charged state Ξ_{cc}^{+} in $\Lambda_c^+ K^- \pi^+$ decays using 0.65 fb^{-1} of the 2011 data, but saw no evidence of the decay [100]. However due to the limited sensitivity of LHCb to search for particles with very short lifetimes and different production environments of the two experiments, this non-observation is not directly inconsistent with the SELEX result. A recent additional search for the Ξ_{cc}^{+} baryon in the $\Lambda_c^+ K^- \pi^+$ decay channel by the LHCb experiment using combined Run 1 and Run 2 datasets [101] again reported no significant signal observed. The largest local significance, corresponding to 2.7 standard deviations, occurs around 3620 MeV/c^2, however the global significance evaluated in the invariant-mass range from 3.5 to 3.7 GeV/c^2 was found to be only 1.7 standard deviations. The upper limits on the ratio of production cross-section times branching fraction with respect to the Λ_c^+ and Ξ_{cc}^{++} baryons has been set as a function of the Ξ_{cc}^{+} mass and for different Ξ_{cc}^{+} lifetime hypotheses.

In 2017, the LHCb collaboration reported the first observation of the doubly charmed baryon Ξ_{cc}^{++}, which was found in the invariant-mass spectrum of the $\Lambda_c^+ K^- \pi^+ \pi^+$ final state, where the Λ_c^+ baryon was reconstructed in the $pK^-\pi^+$ final state [79]. The analysis was based on data from pp collisions collected by the LHCb experiment at the centre-of-mass energy ($\sqrt{s}$) 13 TeV taken in 2016, confirmed by a cross-check based on the independent 2012 dataset collected at $\sqrt{s} = 8$ TeV. The local significance of the Ξ_{cc}^{++} peak was 12 standard deviations, and the measured mass $3621.40 \pm 0.72\,(\mathrm{stat}) \pm 0.27\,(\mathrm{syst}) \pm 0.14\,(\Lambda_c^+)$ MeV/c^2. Figure 1.8 shows the invariant-mass distribution of the $\Lambda_c^+ K^- \pi^+ \pi^+$ candidates reported by LHCb.

In a subsequent analysis, the lifetime of the Ξ_{cc}^{++} baryon was measured to be $0.256^{+0.024}_{-0.022}\,(\mathrm{stat}) \pm 0.014\,(\mathrm{syst})$ ps [102], which is in agreement with the expectation for a weak decay. Based on the measured lifetime of the Ξ_{cc}^{++} baryon and the theoretical predictions discussed in Section 1.3.1.3 that suggest about 2–4 times shorter lifetime of the Ξ_{cc}^{+} baryon with respect to its isospin partner, the expectations for the lifetime of the Ξ_{cc}^{+} baryon are in the range from 40 to 160 fs.

Subsequently, the Ξ_{cc}^{++} baryon was confirmed in the $\Xi_{cc}^{++} \to \Xi_c^+ \pi^+$ decay reported by the LHCb collaboration [103], where the mass of the Ξ_{cc}^{++} baryon was measured to be $3620.6 \pm 1.5\,(\mathrm{stat}) \pm 0.4\,(\mathrm{syst}) \pm 0.3\,(\Xi_c^+)$ MeV/c^2, a value consistent

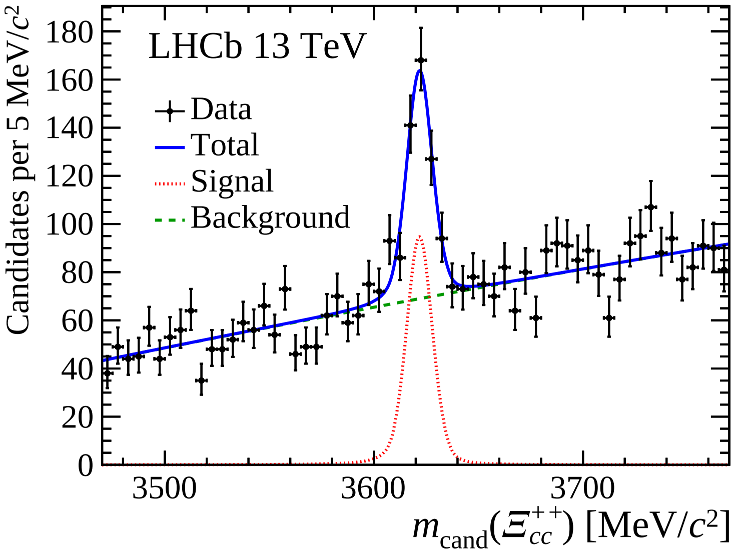

Figure 1.8.: Fitted invariant-mass distribution of the $\Lambda_c^+ K^- \pi^+ \pi^+$ candidates [79].

with the previous measurement. No significant signal was observed in a search for the $\Xi_{cc}^{++} \to D^+ p K^- \pi^+$ decay mode [104], therefore an upper limit on the ratio of branching fractions with respect to the $\Xi_{cc}^{++} \to \Lambda_c^+ K^- \pi^+ \pi^+$ decay was measured to be $< 1.7(2.1) \times 10^{-2}$ at the 90% (95%) confidence level at the known mass and lifetime of the Ξ_{cc}^{++} baryon.

Recent LHCb results on the Ξ_{cc}^{++} baryon include also its production measurement [105] and precision mass measurement [78]. The ratio of the Ξ_{cc}^{++} production cross-section times the branching fraction of the $\Xi_{cc}^{++} \to \Lambda_c^+ K^- \pi^+ \pi^+$ decay relative to the prompt Λ_c^+ production cross-section is measured to be $(2.22 \pm 0.27\,(\mathrm{stat}) \pm 0.29\,(\mathrm{syst})) \times 10^{-4}$ at $\sqrt{s}$ =13 TeV and at the central value of the measured Ξ_{cc}^{++} lifetime. The Ξ_{cc}^{++} production was evaluated in the fiducial region of the transverse-momentum range from 4 to 15 GeV and the rapidity range from 2.0 to 4.5. A precise mass measurement, which used 2016–2018 data collected by the LHCb experiment and a combination of both observed Ξ_{cc}^{++} decay channels, reported the mass of the Ξ_{cc}^{++} baryon to be $3621.55 \pm 0.23\,(\mathrm{stat}) \pm 0.30\,(\mathrm{syst})\,\mathrm{MeV}/c^2$.

The Ξ_{cc}^{+} state reported by SELEX has a mass that is 103 MeV/c^2 smaller than the mass of the Ξ_{cc}^{++} state observed by the LHCb collaboration. This result is inconsistent with the assumption that these two observed states are isospin partners. Although there were some attempts for a theoretical explanation for such a large mass difference of these two states [106], it still remains unclear if the state reported by the SELEX is indeed the Ξ_{cc}^{+} baryon. Other confirmations or refutations of the SELEX result are therefore of a crucial interest.

To complete this overview of the experimental status of doubly charmed baryons, it is important to mention the first search for the Ω_{cc}^{+} baryon, which was performed only recently at the LHCb experiment [107]. A search for the Ω_{cc}^{+} baryon was performed in the $\Xi_{c}^{+}K^{-}\pi^{+}$ final state. No significant signal has been observed in the invariant-mass range from 3.6 to 4.0 GeV/c^2, therefore upper limits on the ratio of the production cross-sections times the BFs with respect to the $\Xi_{cc}^{++} \to \Lambda_c^{+}K^{-}\pi^{+}\pi^{+}$ decay were set.

The experimental study of doubly heavy baryons in general is of key importance in completing the charmed baryon spectrum and shedding light on perturbative and non-perturbative QCD dynamics [91]. The LHCb detector is well suited for the search of doubly charmed baryons due to the high production cross-section of charmed hadrons, its strong tracking and PID capabilities, excellent secondary vertex resolution, and efficient trigger system, as discussed in detail in Chapter 2 devoted to describing the LHCb experiment. Also, it is expected that the doubly charmed baryons have sizeable production cross-sections at hadron colliders [34,35,37–40], as described in Section 1.3.1.1. The first observation of the doubly charmed baryon Ξ_{cc}^{++} by the LHCb collaboration makes searches for its isospin partner at the LHCb experiment even more promising.

1.4. Summary

This chapter discussed theoretical aspects and gave an experimental overview relevant to the doubly charmed baryons in order to provide a background for the studies described in the following chapters. The aim of this chapter was also to give a brief introduction to the field of particle physics, which was mainly discussed in Section 1.1 by introducing the SM of particle physics, so the topics discussed in the rest of this thesis may be easier to comprehend.

All theoretical papers discussing various calculations of the properties of the doubly charmed baryons unanimously state the importance of the baryon system with two heavy quarks, as they provide a different environment than light-quark systems to study non-perturbative QCD. It is therefore important to experimentally observe and study these states, in order to confront the experimental results with the corresponding theoretical predictions.

As was shown in Section 1.3.2, the first doubly charmed baryon, the Ξ_{cc}^{++} state, was unambiguously observed only recently. Observation of the Ξ_{cc}^{+} and Ω_{cc}^{+} states seems rather challenging, primarily due to their short lifetime compared to that of the Ξ_{cc}^{++} baryon, and suppressed production of the Ω_{cc}^{+} baryon with respect to the $\Xi_{cc}^{+(+)}$ isodoublet. So far, the only evidence for the Ξ_{cc}^{+} baryon was provided by the SELEX experiment in 2002, but given the measured properties which were inconsistent with the theoretical predictions and a large difference between the measured mass and the mass of its isospin partner Ξ_{cc}^{++} observed by LHCb, it is generally accepted that more results on the Ξ_{cc}^{+} baryon are needed in order to establish its existence and precisely measure its properties.

Since there is not one golden decay channel to search for these states, an interplay between theoretical predictions and consideration of what final states are experimentally efficient needs to be carefully evaluated. The first search for the Ξ_{cc}^{+} baryon at LHCb was therefore performed in the $\Lambda_c^+ K^- \pi^+$ final state, as it is theoretically predicted to have a BF at the level of a few percent, and it can directly confront the SELEX result, which claimed to observe the Ξ_{cc}^{+} baryon in the same final state. Since no significant signal of the Ξ_{cc}^{+} baryon was observed in the $\Lambda_c^+ K^- \pi^+$ final state, more decay channels can be explored using the large data sample collected by the LHCb experiment with efficient triggers aimed to select decays of the doubly charmed baryons. Based on theoretical predictions, the next search for the Ξ_{cc}^{+} baryon at LHCb is performed in the $\Xi_c^+ \pi^- \pi^+$ final state, which was recently published [1] and is the main topic of this thesis. The corresponding analysis is introduced in Chapter 5, with a detailed description of the analysis and its results presented in Chapters 6, 7, and 8. Before we get there, let us first introduce the LHCb experiment in the next chapter to describe its various aspects and understand why it is a suitable experiment to search for doubly charmed baryons.

Chapter 2.

The LHCb experiment

"The LHC accelerates the protons and the lead,
and the things that it discovers will rock you in the head."
— Katherine McAlpine (aka Alpinekat) in her *Large Hadron Rap*

In this chapter, the LHCb experiment is discussed in detail. Firstly, the Large Hadron Collider (LHC) is described in Section 2.1 to discuss the role of the LHCb experiment within the LHC and to explain what happens before the beams are collided at the LHCb interaction point. Section 2.2 then describes the overview of the LHCb experiment, its physics case and the running conditions, with the following Sections 2.3–2.12 where the individual LHCb sub-detectors, its trigger system, data processing and simulation, are discussed. The chapter is then summarised in Section 2.13.

The main goal of this chapter is to provide relevant information for the understanding of the LHCb experiment and its data flow to better comprehend the studies described in the following chapters.

2.1. The LHC

The Large Hadron Collider (LHC) [108] is a 26.7 km long circular particle accelerator at the European Laboratory for Particle Physics (CERN) located in Geneva, Switzerland.[1,2] The LHC was built in the same tunnel as the Large Electron-Positron (LEP) collider [109], which was in operation from 1989. Construction of the LHC commenced after the LEP was closed down in 2000, with the first beam circulating in 2008 and the first collisions taking place in 2010.

At the LHC, two high-intensity and high-energy beams accelerated in opposite directions are collided at four interaction points along the LHC ring, where four large experiments are located - A Toroidal LHC ApparatuS (ATLAS) [110], A Large Ion Collider Experiment (ALICE) [111], Compact Muon Solenoid (CMS) [112] and LHC-beauty (LHCb) [113]. The accelerated beams consist of protons, with occasional collisions of heavy ions, namely proton-lead (p-Pb), lead-lead (Pb-Pb), or Xenon-Xenon (Xe-Xe). The ATLAS and CMS are general-purpose and high-luminosity experiments constructed mainly for precise measurements of the SM and searches for any signs of physics beyond. These two experiments announced a discovery of the Higgs boson in 2012 [114, 115], at the time the last missing fundamental particle of the SM, and they have continued to work on precise studies of its properties and decays since then. The ALICE experiment is a dedicated experiment to study the quark-gluon plasma and QCD thermodynamics in heavy-ion collisions. The LHCb experiment, which is discussed in the rest of this chapter in more detail, is dedicated to flavour physics. It is important to emphasise that, to this day, all four experiments have produced many intriguing results far beyond their main physics programme.[3] There are also four smaller experiments located along the LHC ring, namely TOTEM [116], LHCf [117], MoEDAL [118] and FASER [119].

Before the beams are accelerated and collided in the LHC, they go through four accelerators in order to achieve the desired energy to enter the LHC. The schematic picture of a full CERN accelerator chain is shown in Figure 2.1. In case of the proton beam, the source of the protons is a bottle of gaseous hydrogen. An electric field is used to strip atoms of hydrogen from electrons to leave only protons to be accelerated.

---

[1] The CERN acronym originally stands for “Conseil Européen pour la Recherche Nucléaire” in French, which can be translated as the “European Organization for Nuclear Research”. At the time of the CERN establishment, pure physics research concentrated on the understanding of the inside of the atom, therefore the word “nuclear” was used in its name. However, it is not very accurate to describe its research as nuclear since very soon the work at the laboratory went beyond the study of the atomic nucleus. For that reason, CERN is often referred to as the “European Laboratory for Particle Physics”.

[2] One can also argue that “European” is quite misleading these days as well. Historically, the laboratory was established as a European organisation. However, currently it is an international laboratory associated with institutions in more than 70 countries around the world. But it is still located in Europe, so let’s not argue about that.

[3] It will be shown what it means specifically for the LHCb experiment in the following section.

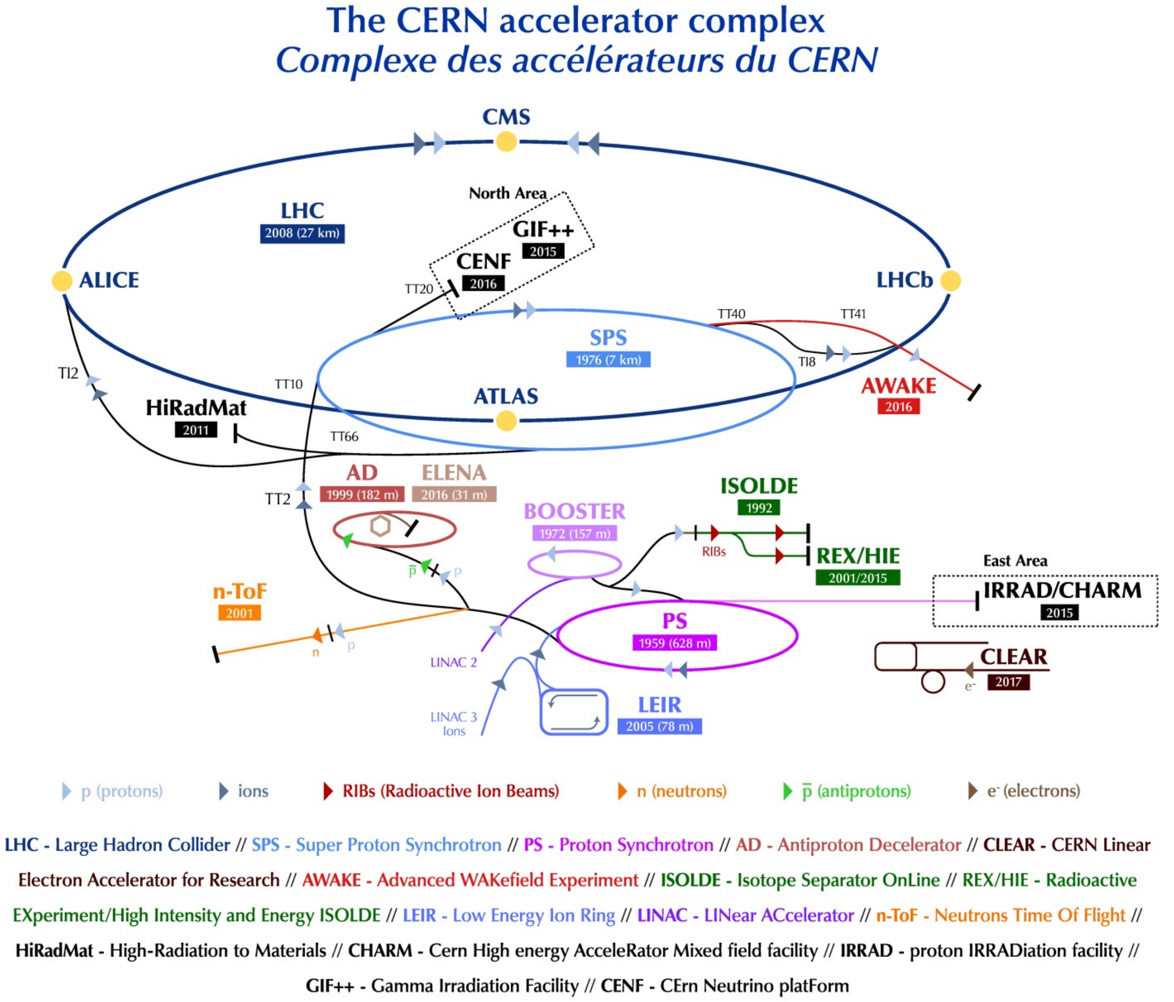

Figure 2.1.: CERN accelarator complex as of 2018 [120].

The first accelerator in the chain is a linear collider called LINAC 2, where the protons are accelerated to the energy of 50 MeV. After LINAC 2, the proton beams are subsequently injected into three synchrotron accelerators - firstly the Proton Synchrotron Booster (BOOSTER), where the proton beam is accelerated up to 1.4 GeV, followed by the Proton Synchrotron (PS), which accelerates the beam up to 25 GeV, and finally the Super Proton Synchrotron (SPS) accelerating protons up to 450 GeV. The proton beam is then split into two beams, which are injected into the LHC in opposite directions in separated beryllium beam pipes kept at ultra-high vacuum, where they are accelerated to the maximum desired energy. The proton beams consist of up to 2808 bunches per beam at their full intensity, with each bunch containing more than 10^{11} protons.

The journey of the heavy-ion beam is similar to the proton beam, however it starts differently due to a different source needed to produce the heavy ions and due to their different mass. The source of the heavy atoms (for example vaporized lead in case of lead ions) is located at one end of LINAC 3, a linear collider that is the first accelerating point for the heavy-ion beam used in the LHC. To produce the heavy-ions beam that is subsequently accelerated in LINAC 3, electrons are removed from the atoms inside a plasma. After LINAC 3, the beam is injected, accelerated and split into bunches in the Low Energy Ion Ring (LEIR). From there, the heavy-ion beam follows the same journey as the proton beam described above.

A strong magnetic field produced by 1232 main dipole superconducting magnets is used to bend the beams in a circular orbit of the LHC. In addition, 392 main quadrupole superconducting magnets are used to provide the force to focus the beams. Many other magnets supporting the optics design of the LHC are positioned around the beam pipe, resulting in more than 6500 magnets in total. All magnets are cooled down to 1.9 K by liquid helium to have superconducting properties. As was mentioned, the proton beams enter the LHC from the SPS with the energy of 450 GeV. In order to accelerate the beams to the desired energy, 16 radiofrequency (RF) accelerating cavities are used, which are all placed in one of the LHC sectors. The RF cavities are metallic chambers working in a superconducting state and containing an electromagnetic field to bring the energy of the beams from 450 GeV up to 6.5 TeV.

The high energies of the collided beams are essential to produce heavy particles, in order to study their properties and to discover so-far unobserved species and decays. However, it is also vital for beams to reach high luminosities in order to look for very rare events and to be able to collect enough data to make statistically valid conclusions. Therefore an important quantity that describes any accelerator is the luminosity. The instantaneous luminosity $\mathcal{L}$ is defined as

$$\mathcal{L} = \frac{N}{\sigma}, \tag{2.1}$$

where N is a rate of a particular process per second and σ is the cross-section of that process. The instantaneous luminosity therefore represents the number of events that can be produced per cm^2 and per s. An integrated luminosity (often denoted as L) is the integral of the delivered instantaneous luminosity $\mathcal{L}$ over time

$$L = \int \mathcal{L} \mathrm{d}t. \tag{2.2}$$

It is usually reported in units of inverted cross-section, i.e. fb^{-1} (inverse femtobarn[4]) or pb^{-1} (inverse picobarn). The integrated luminosity describes the performance of an accelerator or detector as it measures how much data were delivered by the accelerator or recorded by the detector in a certain period of time.

The operation of the LHC is divided in time into so-called running periods. Between these periods, major upgrades, which are planned and prepared a long time before, are performed to the detectors of the individual experiments, accelerators and their technologies, such as radiofrequency cavities, superconducting magnets, beam vacuum, and other aspects of the accelerator complex. The very first run (referred to as Run 1) was conducted between the late 2009 and early 2013, where the LHC collided protons at a centre-of-mass energy of 7 TeV and 8 TeV and a bunch crossing rate of 20 MHz. One block of lead-ions collisions was carried out for a period of four weeks at the end of 2010, with Pb-Pb collisions at a centre-of-mass energy of 2.76 TeV per nucleon pair and one month of p-Pb collisions at a centre-of-mass energy of 5.02 TeV per nucleon pair. The second running period, Run 2, commenced in early 2015 and lasted until the end of 2018. During this period, the protons were collided at a centre-of-mass energy up to 13 TeV with a bunch crossing rate of 40 MHz. During Run 2, p-Pb and Pb-Pb collisions also took place during a few weeks, at a centre-of-mass energy of 8.16 TeV and 5.02 per nucleon pair, respectively. Moreover, the first Xe-Xe collisions took place at a centre-of-mass energy of 5.44 TeV. Currently, the LHC, the CERN accelerator complex and all large (and also smaller) experiments are being maintained and upgraded in a preparation for Run 3, which is planned to start its operation in 2022 and continue until the end of 2025, when the LHC shuts down once again for another two-year major upgrade from 2026 for the high-luminosity LHC with the luminosity of the beams significantly increased.

2.2. Overview of the LHCb experiment

The Large Hadron Collider beauty (LHCb) experiment [113,121] is one of the four main experiments at the LHC. Figure 2.2 shows the layout of the LHCb detector system. The LHCb detector is a single-arm spectrometer with a forward pseudorapidity (η)

---

[4] A barn (b) is a unit of area equal to $10^{-28}\,\text{m}^2$.

coverage of $2 < \eta < 5$ with η defined as

$$\eta \equiv -\ln\left[\tan\left(\frac{\theta}{2}\right)\right], \tag{2.3}$$

where θ is the angle between the particle momentum p and the positive direction of the beam axis. The individual detectors of the LHCb experiment are discussed in more details in the following sections. The LHCb experiment is a dedicated heavy flavour physics experiment. Design of the LHCb detector to cover the forward region rather than to have full 4π coverage similar to ATLAS, CMS and ALICE, was chosen based on its main physics goals. The $c\bar{c}$ and $b\bar{b}$ pairs are predominantly produced in the forward (and backward) region as the main production mechanism of the heavy flavour quarks at the LHC is via gluon-gluon fusion. Moreover, the produced long-lived hadrons are highly boosted, so they fly several millimetres in the detector before they decay weakly.

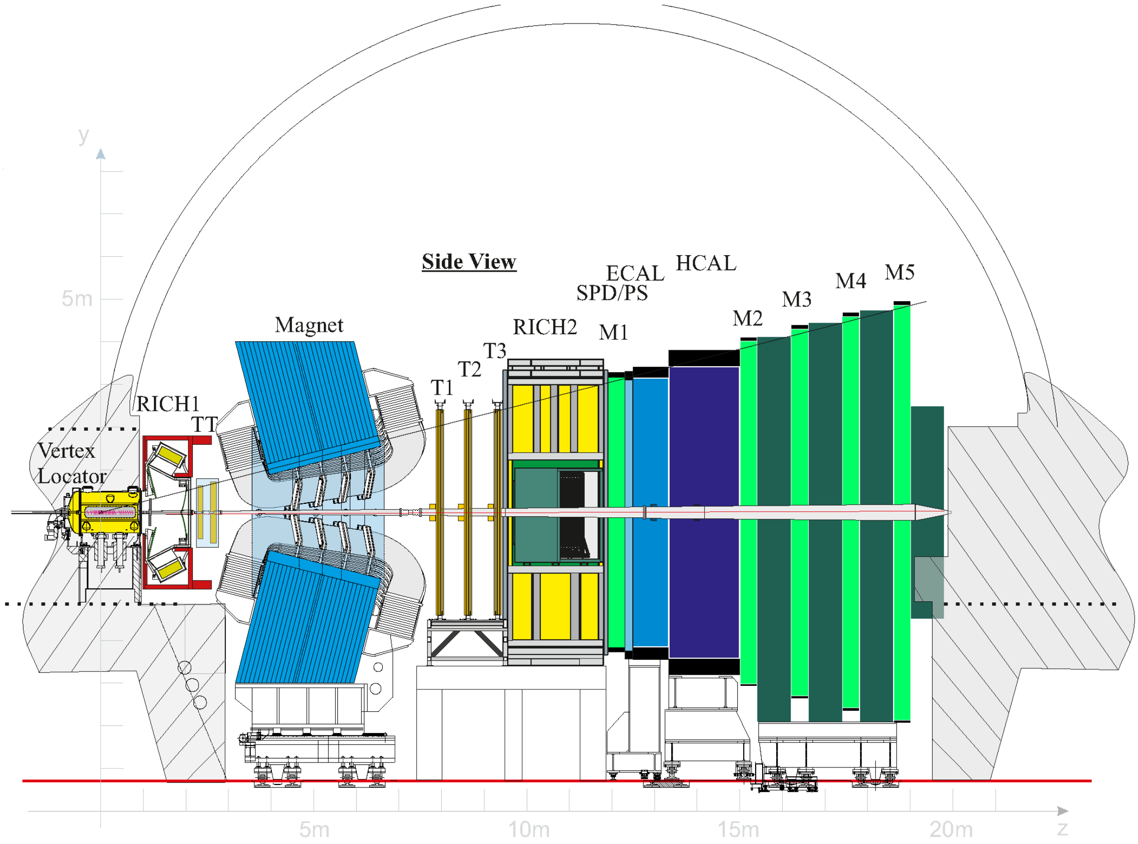

Figure 2.2.: Side view of the LHCb detector [122].

As was already mentioned in Chapter 1, many effects of the models of physics beyond the SM could be seen in heavy flavour decays, for example the contributions that change the expectations of the *CP* violating phases, or in loop-suppressed rare decays from contributions modifying branching fractions or angular distributions of these decays. Precise measurements of the *CP* violation and rare decays of beauty and charm hadrons is therefore one of the main goals of the LHCb experiment.

Recent highlights of *CP* violation measurements from LHCb include the first observation of time-dependent *CP* violation in B_s^0 decays [123], or precise measurements of the *CP* violating phase ϕ_s [124, 125]. Besides these and many other world-leading results on CP violation in b-mesons, there are many searches for *CP* violation in charm decays at LHCb. A large breakthrough in charm physics came with the first observation of the *CP* violation of D^0 mesons decaying into K^+K^- or $\pi^+\pi^-$ pairs [126].

Many searches for rare decays are performed at LHCb in order to measure their branching fraction and decay properties so they can be compared with the SM predictions. An improved measurement of the $B_s^0 \to \mu^+\mu^-$ decay properties and search for the $B^0 \to \mu^+\mu^-$ and $B_s^0 \to \mu^+\mu^-\gamma$ decays was recently performed [127], where no significant signals for the search decays were found and upper limits on the corresponding branching fractions have been determined. The most precise measurement of the branching fraction of the rare $B_s^0 \to \phi\mu^+\mu^-$ decay to date reported a result that is 3.6 standard deviations below its SM prediction [128]. There is also a set of intriguing results from searches for lepton flavour violation, where the LHCb collaboration reported several anomalies in b-meson decays that could suggest first hints of physics beyond the SM. The most precise and notable is the measurement of the ratio $\mathrm{R_K}$, which is the ratio of the branching fractions of $B^+ \to K^+\mu^+\mu^-$ and $B^+ \to K^+e^+e^-$ decays, determined using the full Run 1 and Run 2 data sample collected by the LHCb experiment. The ratio $\mathrm{R_K}$ was measured to be $0.846^{+0.044}_{-0.041}$ [15], which is in tension with the SM prediction with a statistical significance of 3.1 standard deviations, hence providing the first evidence for lepton universality violation.

The LHCb experiment has also a rich heavy-hadron-spectroscopy programme. To mention just some of the recent interesting results reported by the LHCb collaboration: the first observation of the doubly charmed baryon Ξ_{cc}^{++} [79] already described in Chapter 1, the first observation of five narrow Ω_c^0 states [129], as well as other observations of many new excited states and resonances. Figure 2.3 shows all observed hadrons at the LHCb experiment as of March 2021 [130]. All of these measurements

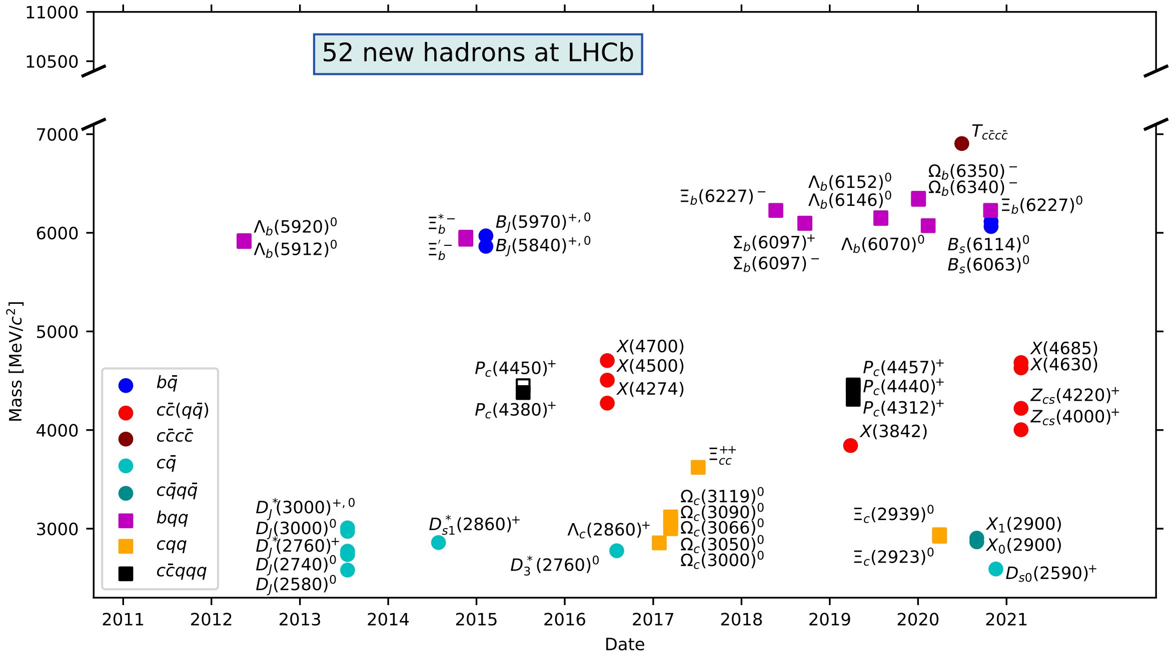

Figure 2.3.: All observed hadrons at the LHCb experiment as of March 2021 [130].

are important tests of QCD as well as a valuable contribution to the knowledge of the properties of known and newly observed hadrons.

In addition to traditional hadronic states, the LHCb experiment is one of a few current experiments where exotic hadrons are observed and precisely studied. In July 2015, the LHCb collaboration announced the first observation of two states $P_c(4380)^+$ and $P_c(4450)^+$ in $\Lambda_b^0 \to P_c^+ K^- \to J/\psi K^- p$ decays consistent with the five quark content $c\bar{c}uud$ [131]. In a recent update of the analysis where a larger data sample was studied, the additional narrow pentaquark state was observed, $P_c(4312)^+$, and a two-peak structure of the previously observed state $P_c(4450)^+$ was seen [132]. The LHCb collaboration also observed several tetraquark candidates, for example the first observation of exotic states with a quark content $c\bar{c}u\bar{s}$ [133], or the recent observation of a doubly charmed tetraquark T_{cc}^+ [134].

Apart from the mentioned *CP* violation, rare decays and spectroscopy results, other studied topics at LHCb include measurements of the electroweak gauge bosons in the forward region, top quark production, or various heavy ion physics studies. The physics output of the LHCb experiment clearly extends beyond its original core programme.

During Run 2, the LHCb experiment collected data from the proton-proton (pp) collisions at a centre-of-mass energy of 13 TeV and operated at the average instantaneous luminosity of $4 \times 10^{32}\,\mathrm{cm}^{-2}\,\mathrm{s}^{-1}$ with a non-empty bunch crossing frequency of up to 26 MHz. The rate of beauty and charm hadrons produced at these conditions is extremely high. The cross-section of the b-quark production in the LHCb detector acceptance at a centre-of-mass energy of 13 TeV was measured to be $154.3 \pm 1.5\,(\mathrm{stat}) \pm 14.3\,(\mathrm{syst})\,\mu\mathrm{b}$ [135], which given the average instantaneous luminosity corresponds to a $b\bar{b}$ pair production of about 60 kHz. The charm production at LHCb at a centre-of-mass energy of 13 TeV is $2369 \pm 3\,(\mathrm{stat}) \pm 152\,(\mathrm{syst}) \pm 118\,(\mathrm{frag})\,\mu\mathrm{b}$ [136], corresponding to the $c\bar{c}$ pair production in Run 2 of almost 1 MHz. Due to the high rates of beauty and charm hadrons, the LHCb experiment operates at a continuous luminosity that is lower than the two general-purpose detectors ATLAS and CMS, which in practice means that the colliding beams are displaced with respect to each other and gradually brought closer to head on collisions by the LHC machine operators as the proton concentration decreases.[5] On average, the rate of visible interactions per bunch crossing in Run 2 was set to $\mu = 1.1$. This set-up brings an advantage of the operational stability and constant trigger rates over a long period of time. A pp collision data sample collected with the LHCb detector during Run 1 and Run 2 corresponds to a total integrated luminosity of about $9\,\mathrm{fb}^{-1}$. Figure 2.4 shows the integrated luminosity of the recorded pp collisions over time for each year of data taking at the LHCb experiment. One can see that the LHCb experiment recorded almost twice as much data during Run 2 than in Run 1.

2.3. Vertex locator

The Vertex Locator (VELO) [138, 139] is the LHCb detector located closest to the interaction point. It was designed for the precise determination of the primary and secondary vertices, which is crucial for the LHCb physics programme. The VELO detector, which was used during Run 1 and Run 2, is a silicon strip detector situated inside a vacuum tank. The silicon sensors have a semi-circular shape and are patterned either with azimuthal or radial strips in order to measure the ϕ or R coordinates, respectively. There are 21 detector modules in each detector half. Each module consists of a ϕ-sensor on one side and an R-sensor on the other side of the module. Each module therefore provides a single R-ϕ space point which is then used in the reconstruction.

---

[5] This is commonly referred to as *luminosity levelling*.

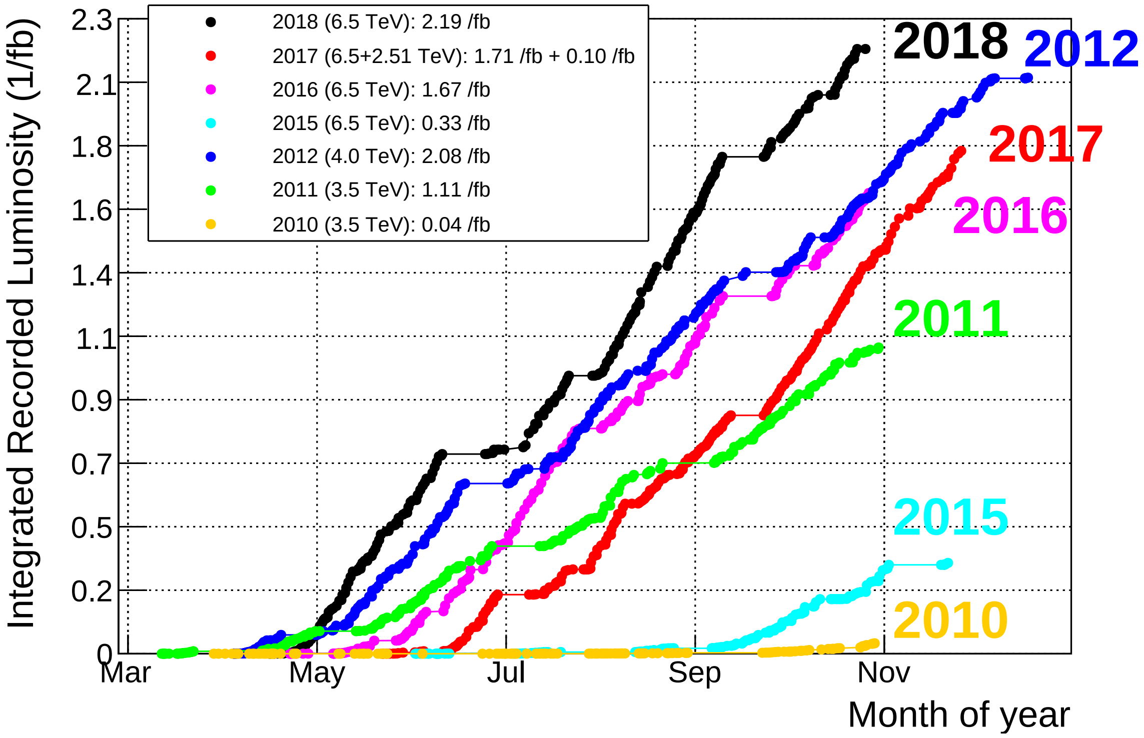

Figure 2.4.: Integrated recorded luminosity of the pp collisions over time at LHCb during Run 1 and Run 2 data taking [137]. The values of the integrated luminosity for Run 2 are not precisely determined yet, therefore they can vary within 10% from the values published in the future.

The n-in-n silicon sensors with a thickness of 300 µm and a strip pitch of 38–100 µm are used for both types of sensors. The strip pitch, which is the distance between adjacent strips, varies to balance the occupancy across the sensors to optimise the hit resolution. The finest pitch is used for the strips in the innermost region of the sensors close to the beam axis, where the track density is the highest. Figure 2.5 shows an illustration of the VELO sensor geometry. The R-sensors are divided into four 45° regions to reduce the strip occupancy. The pitch size in the region closest to the beam pipe is 38 µm, increasing linearly up to about 100 µm at the outermost radius. The ϕ-sensor are divided into two regions: an inner region that goes up to a radius of 17.25 mm with the pitch of about 38–78 µm, and an outer region with the pitch of about 39–100 µm. The ϕ-sensor has a skew design of the strips to improve pattern recognition [113]. The signal from the VELO detector is read out by 170k channels using the analogue Beetle ASIC chip [140].

An important quantity measured using the VELO detector is the impact parameter (IP), which is defined as the minimum distance between a track and a primary pp collision vertex (PV). The IP is measured with a resolution of $(15 + 29/p_{\mathrm{T}})$ µm, where p_{T} is the transverse component of the p with respect to the beam axis given in GeV/c [141]. The average decay time resolution of the VELO detector in Run 2 is about 45 fs for a four-track vertex [141].

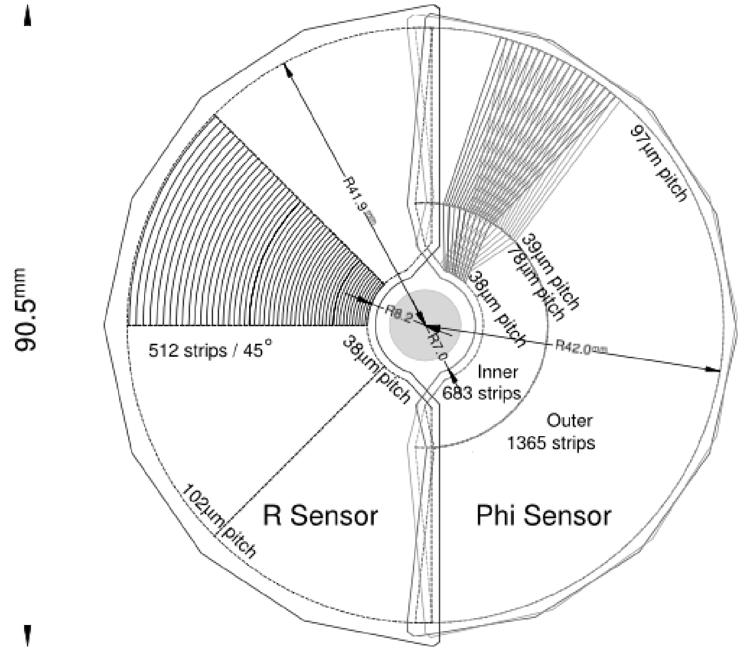

Figure 2.5.: Illustration of the VELO sensor geometry, with only a portion of the strips sketched for clarity [113].

To reach the required precision of the IP measurement, the strips closest to the interaction point are located only 8.2 mm from the beam. However, it is a smaller distance than the aperture required by the LHC during injection of the beam, therefore the VELO detector consists of two moveable halves perpendicular to the incoming beam. They are retracted by 29 mm during the beam injection, and are subsequently closed around the beam once stable beams are declared. The cabling between the modules and the detector has to be flexible enough in order to absorb the movement every time new beams are injected. Once the VELO is closed, the two detector halves (which are shifted in the z direction with respect to each other by 1.5 cm) overlap in order to cover the full azimuthal acceptance and to allow a proper detector alignment.

The cooling of the VELO is provided by evaporative CO_2, which circulates in stainless steel pipes. Cooling blocks are clamped to the base of the module during their assembly. Since the VELO has to be operated in a separate vacuum to the beam vacuum, a 300 µm thin radio frequency (RF) aluminium foil is shaped around each module. The RF foil also provides RF shielding from the beam and allows the passage of the mirror currents of the bunched proton beams.

2.4. Ring imaging Cherenkov detectors

The two Ring Imaging Cherenkov detectors (RICH) [142, 143] are essential for the particle identification (PID) at the LHCb experiment, mainly to distinguish between pions, kaons and protons over a wide momentum range. The RICH detectors use Cherenkov radiation [144] emitted by charged particles that travel through a medium with a higher velocity than the phase velocity of light in that medium. The Cherenkov radiation is emitted as a cone of light centred around the particle trajectory with a half opening angle θ_C such as

$$\cos\theta_C = \frac{1}{n\beta}, \tag{2.4}$$

where β is defined as particle velocity v divided by the speed of light in vacuum c, and n is the refractive index of the medium. The threshold velocity β_{th} for Cherenkov light to be emitted is therefore $\beta_{th} = 1/n$. The Cherenkov angle θ_C and hence β of the passing particle are determined by measuring the radius of the imaged rings. Combining the β information with a momentum known from the tracking system, RICH provides essential information to determine the mass hypothesis of an incident particle.

The medium of the detectors is chosen based on its refractive index n to match the desired momentum range. The upstream detector, RICH1, uses C_4F_{10} (with additional aerogel used during Run 1) as a radiator and covers the low momentum range from about 2 to 40 GeV/c. It is located directly after the VELO detector. The downstream detector, RICH2, uses CF_4 and covers the high momentum range from about 15 to more than 100 GeV/c [143]. Both RICH detectors use a system of spherical mirrors that focus the Cherenkov rings and also transport the Cherenkov photons for their detection outside of the detector acceptance to achieve low material budget inside the acceptance in order to avoid multiple scatterings of tracks, impacting the invariant mass resolution. A set of secondary flat mirrors in each RICH detector is used to reflect the image from the spherical mirrors onto the photon detectors in order to shorten the length of the detectors along the beam direction. Figure 2.6 shows the schematic layout of RICH1 where the individual parts of the detector are displayed.

The RICH2 detector is positioned after the magnet and the tracking stations described in the following sections. The location of the individual RICH detectors is important as it determines what materials can be used for their mirrors as the amount of scattering has to be reduced before a particle enters the tracking system in RICH1, but it is less critical for RICH2. Therefore RICH1 uses four lightweight spherical mirrors built from a carbon-fibre reinforced polymer, whereas RICH2 uses glass spherical mirrors.

To detect the Cherenkov photons emitted by a particle and reflected by the mirrors, pixel hybrid photon detectors [145] are used. They provide single-photon detection with good spatial resolution and a large active area in order to disentangle rings originating from different tracks.

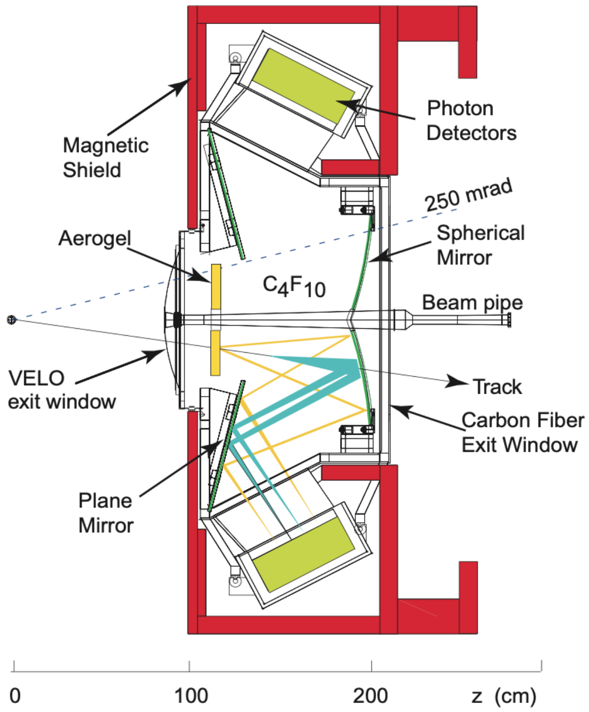

Figure 2.6.: Side view layout of the RICH1 detector [113].

2.5. Tracking stations

There are four planar tracking stations at the LHCb experiment [146–150]. One of them, the Tracker Turicensis (TT) detector, is located upstream of the dipole magnet just after RICH1, whereas three other tracking stations, T1-T3, are located downstream of the magnet before RICH2. Figure 2.7 shows the illustration of the arrangements of the tracking stations. All tracking stations are used to precisely measure the position of the tracks of the charged hadrons. Using the information from the magnet bending power, it allows to determine the charge and momentum of the passing charged particles.

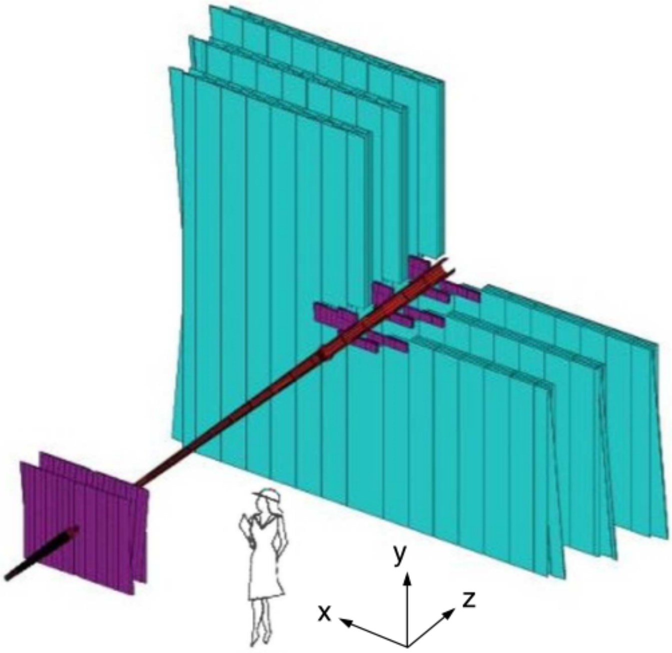

Figure 2.7.: Illustration of the arrangements of the LHCb tracking stations, where the TT detector is located on the left side of the picture and the T1-T3 stations are located downstream. The TT detector and the inner parts of T1-T3 (highlighted in purple) use silicon sensors, the outer parts of T1-T3 (turquoise) use drift straw tubes [113].

The TT station consists of silicon microstrip sensors with a pitch size of about 180 µm. There are four silicon planes in TT that are arranged in two pairs separated by around 27 cm along the beam axis. The downstream tracker stations, T1-T3, use two different technologies - one is often referred to as the inner tracker and the other one the outer tracker. The inner tracker is the cross-shaped region of the T1-T3 stations around the beam pipe, as shown in Figure 2.7. The inner tracker also uses silicon microstrip sensors with a pitch size of about 200 μm in order to achieve a good spatial resolution in a region of the highest track density. The outer parts of the T1-T3 detectors represent the outer tracker. The outer tracker uses drift straw tubes, where the ionisation of the gas molecules by a passing particle creates a signal in the detector. Each station of the outer tracker contains four layers built from separate modules containing straw tubes filled with 70% of argon and 30% of carbon dioxide gas. In total, about 55000 single straw-tube channels are used in all outer tracker stations.

2.6. Magnet system

A non-superconducting dipole magnet [151] is located between the TT and T1-T3 tracking stations described in the previous section. The magnet consists of two trapezoidal coils providing an integrated magnetic field of about 4 Tm in order to bend the tracks of charged particles to allow the determination of their electric charge and momentum. The magnet is designed not to interfere with the beam orbit of the colliding proton bunches. The coils are constructed from 15 'pancakes' arranged in triplets wound from almost 3000 m of aluminium conductor, weighing about 27 tonnes each. They are mounted inside a steel yoke frame with a total weight of 1500 tonnes.

The polarity of the magnet is reversed a few times per year of data taking in order to study and correct for detector induced asymmetries impacting the precise *CP* violation measurements, and hence to minimise the systematic effects arising from any residual detection asymmetry by averaging over the two polarities. A size of the magnetic field is chosen to sufficiently (but not excessively) bend the tracks to achieve the required momentum resolution in the desired momentum range. The three components of the magnetic field were measured using Hall probe arrays mapping the magnetic field from the interaction point up to RICH2 with a relative precision of about 4×10^{-4} [113].

The combination of the information from the tracking detectors with the magnet bending power and the precise measurement of its magnetic field, the LHCb tracking system provides the measurement of p of charged particles with a relative uncertainty of 0.5% for low momentum tracks up to 1% for tracks with a p of 200 GeV/c [121].

2.7. Calorimeter system

The LHCb calorimeter system [152, 153] consists of a scintillating pad detector (SPD), a preshower (PS), an electromagnetic calorimeter (ECAL) and a hadronic calorimeter (HCAL). The calorimeter system is used to measure the energy and position of charged and neutral particles and is also one of the detectors used for the candidate selections in a hardware trigger based on their high transverse energy. The calorimeters also provide a crucial input for the particle identification, as they can distinguish photons, leptons (e and μ) and hadrons (π, K and p) based on their energy deposits in the calorimeters. In particular, the calorimeters are crucial to identify neutral particles, such as photons and neutral pions, as they enter the calorimeters undetected by any of the other LHCb detectors.

The calorimeter system uses sampling technology, where layers of absorber material are alternating with layers of active scintillators. The thickness of the individual layers is designed so that particles are stopped in the detector volume and therefore their energy can be measured. The scintillating light created by the particle shower in the active detector layers is collected by wavelength-shifting fibres and transported to the photomultiplier tubes where the light is transformed to an electrical signal. The individual detectors are laterally segmented to take into account different hit density with respect to the beam pipe.

The SPD detector provides information whether the passing particle is charged or neutral, whereas the PS detector determines the electromagnetic character of the particle based on its shower created in the detector and thus helps to separate electrons, photons and neutral pions. Both SPD and PS use one layer of scintillating pads as an active material with lead foil located between them acting as an absorber. The ECAL detector measures the energy of photons, electrons and neutral pions. The energy of the neutral pions is measured through their decay to two photons, which are detected by their showers deposited close to each other in the ECAL cells and have a combined invariant mass close to that of the π^0 meson. The ECAL detector uses 4 mm thick scintillating plates alternating with 2 mm plates of lead and 120 μm thick white reflecting TYVEK paper [113]. There are 66 layers in total in the ECAL detector. The relative energy resolution $\sigma(E)/E$ of ECAL is parametrised as $(9.0 \pm 0.5)\%/\sqrt{E} \oplus (0.8 \pm 0.2)\% \oplus 0.003/(E\ \sin\theta)$ [153]. The identification of hadrons and the measurement of their energy is provided by HCAL. It consists of iron plates alternating with scintillating tiles oriented parallel to the beam pipe. The relative energy resolution of HCAL is $(67 \pm 5)\%/\sqrt{E} \oplus (9 \pm 2)\%$ [153].

2.8. Muon stations

The last part of the LHCb detector is the muon station [154, 155]. It provides muon identification and also crucial information for the hardware trigger. It consists of five rectangular stations gradually increasing in size: M1 located upstream of the calorimeter station, and M2-M5 forming the last section of the original LHCb detector.[6] Between the individual M2-M5 stations, there are 80 cm thick iron-absorber walls so the highly energetic hadrons that were not stopped in the HCAL are stopped and thus distinguished from muons, which are not stopped by the iron blocks.

Multi wire proportional chambers (MWPC) are used in the M2-M5 stations and in the outer region of the M1 station. Triple gas electron multiplier (GEM) detectors are used in the inner region of the M1 station due to high occupancy, since MWPCs would be insufficient in such conditions. The first three muon stations are used to precisely measure the p_{T} of muons for the hardware trigger, therefore they have a higher granularity than the last two stations, which are mainly used for muon identification. The p_{T} resolution of muons used in the hardware trigger is improved from about 35% to 25% using the information from all muon stations with respect to only using the four downstream stations [155].

There are almost 1400 MWPCs in the muon station with a gas mixture of $\mathrm{Ar/CO_2/CF_4}$ with a ratio of 40:55:5. The GEM detectors consist of three GEM foils layered between anode and cathode planes with a gas mixture of $\mathrm{Ar/CO_2/CF_4}$ (45:15:40) [155]. The gas mixture used provides a very good time resolution, which in combination with an optimized charge-collection geometry of the muon stations is essential for a high hardware trigger efficiency of at least 95% within a time window smaller than the LHC bunch spacing window of 25 ns [155].

---

[6] The HERSCHEL detector was added for Run 2, see the next section for more details.

2.9. HERSCHEL

For completeness, the High Rapidity Shower Counters for LHCb (HERSCHEL) detector [156] is also described, even though it was not part of the original LHCb experiment design as it was installed only in 2015 for Run 2. The data from HERSCHEL are used only for specific studies of diffractive physics at LHCb. The HERSCHEL detector is located close to the beam pipe in order to detect shower activity at a higher rapidity than the coverage of the other LHCb detectors. The information from HERSCHEL is therefore useful to detect and classify Central Exclusive Production (CEP) candidates [157].

The HERSCHEL detector consists of a system of plastic scintillators that are located in the LHC accelerator tunnel on both sides of the LHCb experiment. Three stations are placed on the opposite side from the interaction region than the LHCb detector in the so-called backward direction, and two stations are placed downstream of the muon station (forward direction). The closest station is located about 7.5 m from the interaction point in the backward direction and the most distant stations are at a distance of about 114 m where there is already a separated vacuum pipe for each of the two beams. Each station is formed from four 20 mm thick rectangular plastic scintillator plates with hole(s) to allow space for the beam pipe(s). Each scintillator plate is read out by a separate photo multiplier. From 2016, the information from HERSCHEL is also used in the software trigger for the selection of the CEP candidates.

2.10. Trigger system

In order to suppress the rate of events that are read out by the detector and saved on disk to a reasonably low level and to distinguish numerous different charm and beauty decays of interest from background, LHCb uses a trigger system [141, 158]. It consists of two main parts: the L0 trigger implemented in hardware, which is described in the following Section 2.10.1; and the high level trigger (HLT) implemented in software, described in Section 2.10.2. The trigger system used in Run 1 [158] was substantially different from the one used in Run 2 [141]. The Run 1 trigger system lacked the use of low-momentum particles and full particle identification, which was in particular limiting for charm physics [141]. Therefore the LHCb trigger system and data processing framework were redesigned during the long shut-down between

Run 1 and Run 2 to perform the full offline event reconstruction at the trigger level and to enable detector alignment and calibration in real time. Figure 2.8 shows the schematic representation of the LHCb trigger architecture in Run 2 [141]. The following sections describe the trigger system used in Run 2, as the data used for the studies described in the following chapters of this thesis use only a subset of the Run 2 data.

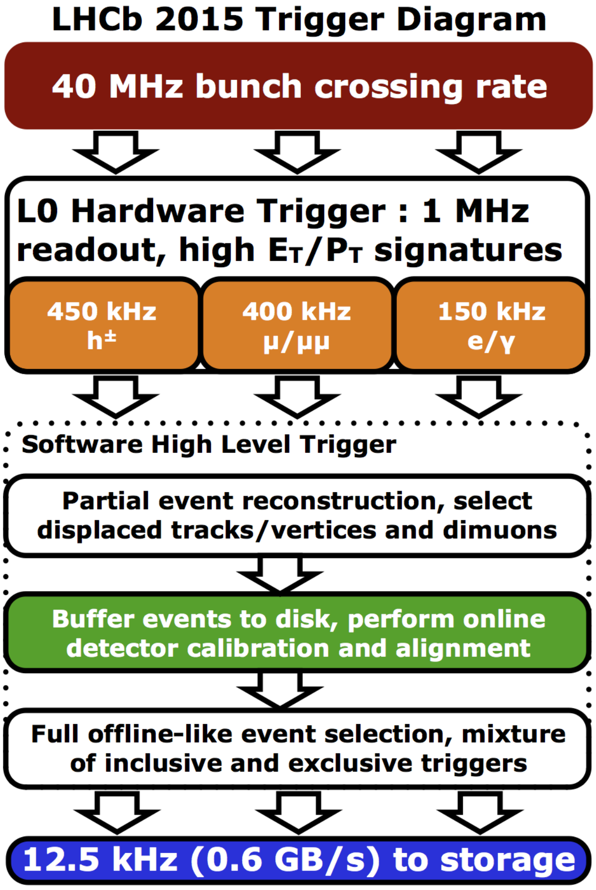

Figure 2.8.: Schematic overview of the LHCb trigger system used in Run 2 [159].

A sequence of selection and classification algorithms in L0 or HLT, which returns either an accept or reject decision, is called a trigger line. The trigger consists of a set of numerous pre-defined trigger lines. The event is accepted only if it passes at least one of the trigger lines at each stage. The signal candidates reconstructed offline via a specific decay chain can be associated with a trigger decision. There are two main categories of the offline signal candidates selected by the trigger: the candidates selected at the trigger level based on the information from their decay products, the so-called *triggered on signal* (TOS); or the candidates selected independently of their reconstructed decay, the so-called *triggered independently of signal* (TIS).

The configuration of the L0 trigger and the thresholds used in the L0 trigger lines varied during the data taking in response to changing LHC conditions. The HLT trigger configuration was kept more stable. Apart from a few exceptions, the changes were often introduced during the end-of-year technical stops, so the trigger conditions are easily reproduced in a simulation, which is tuned separately for each year of data taking.

2.10.1. Hardware trigger

The L0 trigger implemented in hardware uses the information read out at 40 MHz event rate from the calorimeter and muon stations. The decisions are determined by a system of field-programmable gate arrays of the front-end detector boards with a fixed latency of 4 μs. The L0 trigger is required to reduce the rate to 1 MHz [141, 158] before the events are processed by the software stage of the trigger.

The L0 calorimeter system uses the information from the SPD, PS, ECAL and HCAL detectors and computes the transverse energy deposited in clusters of ECAL and HCAL. Three types of candidates are then formed from the clusters: a hadron candidate using the highest E_{T} in the HCAL cluster; a photon candidate from the highest E_{T} in the ECAL cluster with one to four PS cells hit(s) in front of ECAL and no hit in the corresponding SPD cells; and an electron candidate using the same requirements as for a photon candidate with at least one SPD hit in front of the corresponding PS cell(s) [158]. The event is retained only if it contains at least one candidate with the E_{T} larger than the fixed L0 threshold. An additional requirement on the number of the SPD hits is used in many L0 trigger lines in order to enable a faster reconstruction at the subsequent software stage [141].

The L0 muon system uses the quadrants of the muon stations, which are connected to a separate L0 processor. Each of the four L0 muon processors identifies two muon tracks with the largest p_{T} [158]. The event is then retained if at least one of the eight muon candidates passes the required p_{T} threshold, which is the so-called L0 Muon trigger line, or the product of the two largest p_{T} of the muon candidates is above the certain fixed threshold (L0 DiMuon trigger line).

Table 2.1 shows the corresponding E_{T} thresholds for the L0 calorimeter triggers, the p_{T} thresholds for the muon triggers, and the maximum number of SPD hits which were used during the majority of the data taking in 2015, 2016 and 2017 [141].

L0 trigger	E_T or p_T threshold			SPD hits
	2015	2016	2017	
Hadron	$> 3.6\,\text{GeV}$	$> 3.7\,\text{GeV}$	$> 3.46\,\text{GeV}$	< 450
Photon	$> 2.7\,\text{GeV}$	$> 2.78\,\text{GeV}$	$> 2.47\,\text{GeV}$	< 450
Electron	$> 2.7\,\text{GeV}$	$> 2.4\,\text{GeV}$	$> 2.11\,\text{GeV}$	< 450
Muon	$> 2.8\,\text{GeV}$	$> 1.8\,\text{GeV}$	$> 1.35\,\text{GeV}$	< 450
Muon high p_T	$> 6.0\,\text{GeV}$	$> 6.0\,\text{GeV}$	$> 6.0\,\text{GeV}$	none
Dimuon	$> 1.69\,\text{GeV}^2$	$> 2.25\,\text{GeV}^2$	$> 1.69\,\text{GeV}^2$	< 900

Table 2.1.: Thresholds used in the L0 trigger for the different trigger lines that were predominantly used in 2015, 2016 and 2017 [141].

2.10.2. Software trigger

The software stage of the LHCb trigger system is the so-called high level trigger (HLT), which consists of two stages: HLT1 and HLT2 [141]. The HLT is a program written in C++ that runs on a large online processing farm. The output rate from the HLT which is put into storage for offline processing, analysis and detector calibration is about 12.5 kHz (3 kHz) in Run 2 (Run 1).

The HLT1 stage processes the full L0 output rate to reduce the rate to about 110 kHz before it goes into HLT2 for the full event reconstruction. It uses the information from the VELO detector and the tracking stations. Decisions in HLT1 are based on the requirements for some simple inclusive kinematic selections of one or two reconstructed tracks, the presence of displaced tracks or vertices, and dimuon combinations in the event [141]. The events are then buffered to a disk storage in order to perform an online detector calibration and alignment, so the events are fully calibrated once they enter the HLT2 stage. Most physics analyses at LHCb use the inclusive HLT1 lines, which also represent almost all of the HLT1 bandwidth. There are two inclusive HLT1 lines used for hadronic decays of heavy-flavour hadrons: one line selecting a displaced track with a high p_T; and one line selecting a displaced two-track vertex with a high p_T and passing a MatrixNet classifier [160] pre-trained on tracks p_T and vertex information [141]. The requirements of the two inclusive HLT1 lines are described in more detail in Section 3.3.1 as they are used in the analysis selection described in Chapter 3.

The HLT2 stage is based on more complex algorithms which allow an implementation of advanced multivariate discriminants or reconstruction algorithms. The HLT2 trigger used in Run 2 is asynchronous and uses fully aligned and calibrated detector information, so the reconstructed objects in HLT2 are identical to those produced offline. Therefore in 2015 a new stream called Turbo was introduced [161], to run alongside the existing full stream. The Turbo stream makes a selection of candidates in HLT2 and the output is saved to a disk and used directly by the analysts, so no further offline reconstruction is necessary, which significantly saves the offline computing resources. It also reduces the disk space usage due to the fact that only a part of the event, containing the relevant information about the candidates that is interesting for the corresponding analysis, is saved. During Run 2, more than 500 trigger lines were used at the HLT2 stage, of which around half were Turbo. In 2018, 29% of the trigger rate came from the Turbo lines, but it acounted for only 17% of the bandwidth as the Turbo event size is about half of a full stream event [162], so it is a highly effective way of selecting and storing data. However, one needs to be very cautious since there is no turning back – the Turbo stream cannot be re-reconstructed because the information needed to do that is thrown away.

There are various inclusive and exclusive trigger lines used in HLT2. The inclusive lines are mostly used for the b-hadron decays, often referred to as the topological trigger lines [163]. The exclusive selections are mainly implemented as the Turbo lines as they are dedicated to some specific decay of interest and therefore storing the full event information is not necessary. This is particularly useful for the c-hadron decays due to the very high charm production rate at LHCb.

Additionally, in 2016 the Turbo++ lines and in 2017 the so-called TurboSP (where SP stands for *selective persistence*) lines were added in HLT2 [164] as a compromise for selections for which Turbo is too restrictive. In addition to the objects saved in a standard Turbo line, the TurboSP lines save some additional objects not involved in the trigger decision. These objects are pre-defined for each TurboSP line prior to the data taking. The Turbo++ lines allow to save all reconstructed objects in HLT2. For example, there are some dedicated Turbo++ lines to trigger for the hadronic decays of the singly charm baryons, independent on their production origin. The analysis can be done on the TurboSP and Turbo++ trigger output in the same way as for the standard (exclusive) Turbo line.

2.11. Tracking

The previously described tracking detectors, namely the VELO and the tracking stations, provide essential information for the reconstruction and track determination of long-lived charged particles. The track determination allows to estimate the particle's place of origin, as well as the particle's momentum, which is evaluated from the track curvature in the magnetic field present before the tracking stations. Figure 2.9 shows an illustration of the various types of tracks at LHCb, depending on which input detector information that is used for the track determination. Long tracks are most commonly used in physics analyses, as they provide the best momentum and spatial resolution [165]. The search for doubly charmed baryons presented in this thesis also uses long tracks.

To build tracks from hits left by a particle in the tracking detectors, tracking algorithms are used. There are two main parts of the LHCb tracking – track identification, often referred to as *pattern recognition*, and *track fitting*. The pattern recognition aims to find all possible tracks associated with the hits in the detector, whereas the track fitting is designed to provide the best parameter estimates of the found tracks.

Pattern recognition for the VELO detector [166] builds the tracks from hits compatible with a straight line extrapolation, since VELO is placed before the magnetic field. Firstly, two-dimensional tracks are built in the Rz-projection using hits in the R-sensors, with a subsequent addition of the compatible hits in the ϕ-sensors to build three-dimensional VELO tracks. A least square fit is then performed to find good tracks and to discard fake tracks. The main algorithm to find long tracks is the forward

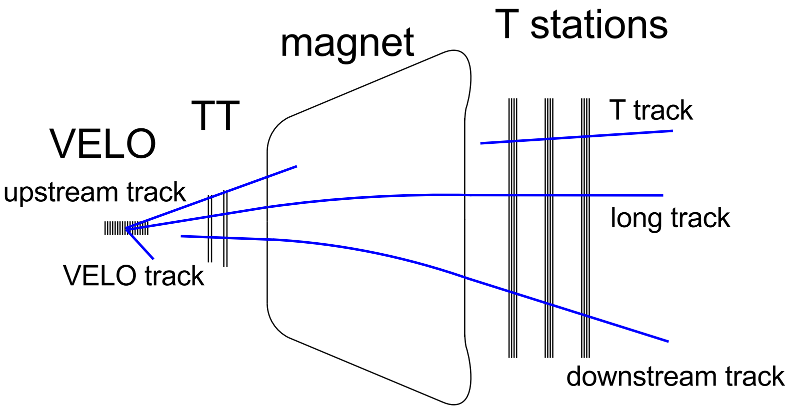

Figure 2.9.: Illustration of types of tracks at LHCb in Run 1 and 2 [165].

tracking [167], which uses the propagation of the VELO tracks to the three downstream tracking stations. The hits in the tracking stations are searched in a window around their expected position based on the track parameters evaluated from the VELO tracks. All hits from within a search window are collected into a common plane and fitted with a third order polynomial. The fit is repeated until χ^2 of the fit is minimised. The best tracks are then selected on the quality variable, which is often the χ^2 of the fit per degrees of freedom. Afterwards, if the hits in the TT detector are close enough to the tracks found in the VELO detector and the tracking stations, they are associated with the corresponding long tracks. One other method used at LHCb to find the long tracks is track matching [168, 169], which finds tracks in the tracking stations using an independent algorithm [170], and then combines the tracks found in the tracking stations with the VELO tracks by extrapolating the two sets of tracks to the magnet plane to determine if they belong together.

The track parameters and their uncertainties are then determined with precision using track fitting. The track fitting is also used to identify and discard fake tracks. At LHCb, a Kalman filter [171, 172] is used. It is an iterative process when the information is propagated to the next detector plane. The starting point for the fitting are the estimates of the track parameters determined from the pattern recognition. The track fit using a Kalman filter has three main steps: prediction, filtering and smoothing. The prediction of the measurement at a given layer is an extrapolation of the estimated measurement from the previous layer, using the transport matrix. The covariance matrix with the information on the track uncertainties is also transported and increased with additional uncertainties arising from the interactions of the particle with the detector material, mainly taking into account multiple scattering and energy loss. The next step is filtering, which is a calculation of the weighted average between the measured hit and its prediction at the given layer to give the filtered estimate, which is then propagated to the next plane and the process is repeated until the last hit of for the given track is reached. Since the Kalman filter provides the best estimates at the last detector plane, the information gained has to be propagated by performing the first two steps in the reverse direction, which is called smoothing. The weighted average of both results at each layer gives the final track measurement. The calculated χ^2 of the track fit per degree of freedom is then used also offline to determine the track quality and to filter good-quality tracks in physics analyses.

In Run 2, an identical estimation of the best track parameters was achieved online and offline, which allowed the use of data reconstructed by the software trigger directly in physics analyses using the Turbo stream, as mentioned in the previous section. The track-reconstruction efficiency in Run 2, determined using $J/\psi \to \mu^+\mu^-$ decays, was above 95% in a wide momentum range [173].

2.12. Data processing and simulation

In order to create a data sample that is suitable for an offline analysis, the data recorded by the LHCb detector need to be pre-processed and saved to a disk storage in a suitable format where they can be accessed by the analysts. The data processing at LHCb is described in Section 2.12.1.

In addition to the real data recorded by the LHCb detector, the simulated data are used in many physics and performance analyses. The overview of the simulation used at LHCb is presented in Section 2.12.2.

2.12.1. Data processing

As was described already in Section 2.10, the events recorded by the LHCb detector are processed by the trigger system before they are put into permanent storage. The application responsible for the HLT software is called MOORE. From Run 2, the data processed as the HLT2 Turbo stream are sent directly to the disk storage since the reconstructed Turbo data are of the same quality as they would be if they were re-processed offline.

To transform the hits in the detector to reconstructed objects for triggered non-Turbo data, the BRUNEL application is used. The reconstructed objects are however not directly accessible for the offline analysis. The files containing reconstructed objects by BRUNEL need to be processed by the DAVINCI application to filter through the recorded events in order to build up the selection of interest for a specific analysis. This step is usually done by the central productions using a set of pre-defined selections called *stripping*. The (re-)stripping campaigns for a data set however run only every few years and they therefore require a thorough preparation, since it is a highly CPU intensive process. As discussed earlier, there is no need to apply stripping on the Turbo data as the selection is already applied at the trigger stage so the data can be used for the analysis directly.

After the data are pre-selected by the stripping or at the Turbo trigger level, the final files, which are used by the analysts, are created using again the DaVinci application, resulting in files in the ROOT [174] format. This stage is highly customisable by using an option file defining the event and candidate selection criteria and the required physics information to be stored in the final ROOT file. Only this final stage is usually run by the analysts, although the so-called *analysis productions*, which run these selections centrally, can also be used as they provide a useful framework for data preservation and efficient data processing. The other stages of the data processing mentioned above are normally run centrally in order to save computing resources.

2.12.2. Simulation

The simulation is an essential tool for many high-energy-physics analyses. It is used to model various detector effects and its impact on the analyses, optimise the candidate selections, compute acceptance, trigger and selection efficiencies, or to perform detector performance studies.

The software framework responsible for the simulation at LHCb is called Gauss [175]. It runs multiple stages of the simulation process in order to create a final sample that can be used by the analysts. The LHCb simulation consists of three main steps: the generation of the pp[7] events; decay of the produced short-lived particles; and the interactions of the created particles at the collisions and their decay products with the detector material.

The first step is done by the high-energy-physics event generators using Monte Carlo methods. At LHCb, Pythia [176,177] with a specific LHCb configuration [178] is used to generate the pp collisions. There are also other generators dedicated to specific processes, for example the generators customised for a precise simulation of soft or hard processes. The GenXicc2.0 [179] generator, which is dedicated to the doubly heavy baryon production, is used to produce the simulation samples used for the studies described in Chapters 6, 7 and 8. Once the signal candidates are produced, the output of the GenXicc2.0 generator is passed through Pythia for further hadronization and integration with the underlying event.

The next step is a description of the decays of the produced unstable particles and the signal candidate to the desired final state, which is done by EvtGen [180],

---

[7] Or any other colliding particles.

in which generation of the final-state radiation is done by PHOTOS [181]. The signal candidates or its decay products might be required to pass some generator-level cuts, which are specified in the simulation option files, so only the particles with properties that are used for the final analysis are propagated to the next stage of the simulation process.

The most CPU intensive step is the simulation of the propagation of particles through the detector, where the interactions of particles with the detector material need to be evaluated. For this purpose, the GEANT4 toolkit [182, 183] is used, with the specific application to LHCb as described in reference [175].

A digitalisation of the simulated hits in the detector into the detector signal is performed using the BOOLE application. The simulated data then follow the same processing chain as the real data (beginning with the MOORE application) described in the previous section. The simulation samples contain the information from the reconstruction stage, but also the *truth* values of the observables from the generator level.

During Run 2, a lot of effort was dedicated to speed-up the LHCb simulation as many analyses require large simulation samples to reduce their systematic uncertainties. Some dedicated tools are now available to produce more events while saving the overall simulation CPU time. For example, ReDecay [184] is used to generate uniquely only the signal candidate and its decays, while re-using the rest of the event multiple times. However, a careful treatment of the statistical uncertainties needs to be considered as the ReDecay events are by definition correlated.

Even though the simulation is a very useful tool and the essential part of almost every analysis, it is important to be aware of its limitations in order to correct and account for them. For instance, the simulation often does not correctly reproduce the occupancies near the beam pipe, ageing of some parts of the detector are difficult to model precisely, or the η and p_{T} spectra of light particles are often not reproduced accurately. Moreover, the trigger conditions and selections vary during the year, so they are often not precisely reflected in the simulation. In general, data-driven methods are used to correct for these effects, so the simulation matches the real data more closely. For any residual discrepancy and also limitations of the methods used for the corrections, a systematic uncertainty needs to be assigned to a measured quantity. More details on the calibration applied to the simulation samples used in the analysis of the doubly charmed baryons are described in the corresponding sections of Chapter 6.

2.13. Summary

This chapter described all relevant parts of the LHCb experiment in order to provide a sufficient background knowledge of the data used for the analyses described in the following chapters.

To understand the LHCb experiment and its position within CERN, the LHC and overview of LHCb and its physics programme were firstly briefly discussed. The individual LHCb detectors and systems were subsequently described, followed by the description of its trigger system, data processing and simulation, in order to understand the LHCb data flow from the signal formed in the detector until the data are ready to be used in the physics and performance analyses.

During Run 1 and Run 2, the LHCb experiment produced numerous fruitful results and extended its physics programme far beyond its original goals. Currently, the LHCb detector is being upgraded [185] for Run 3, which is planned to commence in 2022. More than 90% of the detector channels used in Run 2 have been replaced, with the accommodation of a fully software-based trigger [186] as the hardware trigger would be a limiting factor to fully exploit high-luminosity Run 3 data due to the saturation in yield for many hadronic final states [187]. There has been a huge effort in the detector construction and software development to cope with five times higher instantaneous luminosity and about two times more efficient trigger. One can therefore expect plenty of precise and exciting results to come from the newly upgraded LHCb experiment in the upcoming years.

Chapter 3.

Trigger development for charmed baryons

"To make progress in understanding, we must remain modest and allow that we do not know. Nothing is certain or proved beyond all doubt. You investigate for curiosity, because it is unknown, not because you know the answer."

— Richard P. Feynman

This chapter describes the development of the software-trigger selection for the $\Xi_c^0 \to pK^-K^-\pi^+$ decay, which was done as part of the new inclusive set of the charm-baryon-trigger lines implemented for the 2018 data taking at LHCb. In addition to the trigger line developed for the Ξ_c^0 baryon discussed in this chapter, other similar trigger lines were prepared for the Ξ_c^+, Λ_c^+ and Ω_c^0 baryons.

Firstly, the analysis is introduced in Section 3.1, followed by Section 3.2 where the data and simulation samples are presented and the analysis method is discussed. Section 3.3 describes the event-selection method developed for the trigger line, where the individual stages of the selection are discussed in detail. The results and performance of the developed trigger line are presented in Section 3.4. The chapter is then summarised in Section 3.5.

3.1. Introduction and motivation

As was mentioned in Chapter 2, the $c\bar{c}$ pair production at LHCb in Run 2 is almost 1 MHz [136], resulting in vast production of charmed hadrons, including charm baryons. The charm baryons are produced either directly in pp collisions, which is often referred to as *prompt production*, but also as the decay products of the heavier baryons created at pp collisions, the so-called *secondary production*. An efficient inclusive-trigger selection can cover many sources of charmed baryons, which creates a flexible framework for analyses that require a charmed baryon in their final state.

As was already described in Section 2.10.2, the Turbo++ trigger lines were added to the LHCb software-trigger configuration in 2016. This configuration allows to implement the inclusive selection for various types of decays as the information about all reconstructed objects in HLT2 is saved, not only the information about the candidate and its decay products as for the standard Turbo lines. However, it means that the event size is considerably larger – the average size of Turbo events is 15 kbytes, whereas for Turbo++ events it is about 70 kbytes. Therefore not every selection can and should be implemented as an inclusive selection. Preferably, it should be used to cover for many different final states and also to provide an opportunity for future analyses of unanticipated decays not covered by the exclusive trigger selections.

In 2016, the inclusive trigger selections for the $\Xi_c^0 \to pK^-K^-\pi^+$, $\Xi_c^+ \to pK^-\pi^+$, $\Lambda_c^+ \to pK^-\pi^+$ and $\Omega_c^0 \to pK^-K^-\pi^+$ decays were implemented in Turbo++. A common selection was developed for the Ξ_c^0 and Ω_c^0 baryons, as their final state particles are the same. Separate selections were implemented for the Ξ_c^+ and Λ_c^+ baryons even though they share the final state, but their selections were, in any case, very similar. All of these selections used rectangular requirements with low signal purity. Therefore this was the motivation to develop the new Turbo++ lines based on multivariate analysis (MVA) techniques for these charmed-baryon decays before 2018 data taking. The main goal of the new inclusive trigger lines is to use the MVA-based selection to improve the signal efficiency and increase the signal purity for charmed baryons, independent of their origin.

The following sections of this chapter describe the procedure, development, and performance tests of the MVA-based inclusive Turbo++ trigger line implementation for the $\Xi_c^0 \to pK^-K^-\pi^+$ decay.

3.2. Procedure and data samples

The key objective is to develop a multi-purpose Turbo++ line for the $\Xi_c^0 \to pK^-K^-\pi^+$ decay which would be efficient on different sources of the Ξ_c^0 baryon, namely the promptly produced Ξ_c^0 baryons, the Ξ_c^0 baryons produced in the doubly-charmed-baryon decays as well as in various b-hadron decays. Therefore it is important not to include any pointing and angular variables in the selection, since these variables have a strong correlation with the source of a charmed baryon. The Turbo++ selection is implemented in two stages:

- The first stage has an improved cut-based pre-selection with respect to the already implemented corresponding cut-based trigger line. The pre-selection requirements are applied in order to suppress the combinatorial background and to control the CPU requirements of the HLT2 throughput, but the pre-selection is kept loose enough in order not to introduce any bias towards a particular decay mode;
- The second stage has an efficient MVA-based selection using the variables with good discriminating power between the signal and background, with the exception of using any lifetime-biasing variables to preserve the inclusive nature of the trigger line.

The following three different simulation samples produced for 2016 are used in order to optimise the selection, to train the MVA classifier and to evaluate the signal efficiency for various sources of the Ξ_c^0 baryon:

- Promptly produced Ξ_c^0 baryons;
- Ξ_c^0 baryons produced in $\Xi_{cc}^+ \to \Xi_c^0\pi^+$ decays, where the mass of the Ξ_{cc}^+ baryon is set to $3621.4\,\text{MeV}/c^2$ and its lifetime to 80 fs;
- Ξ_c^0 baryons produced in $\Xi_{cb}^0 \to \Xi_c^0 J/\psi$ decays, where the mass of the Ξ_{cb}^0 baryon is set to $6900\,\text{MeV}/c^2$ and its lifetime to 400 fs.

A higher priority in the training is given to the prompt and Ξ_{cc}^+ samples than to the Ξ_{cb}^0 sample since the trigger is in general more efficient to baryons with a higher lifetime, therefore the listed simulation samples are weighted as 2:2:1 in the MVA training. Reconstructed simulation candidates are matched using the truth matching identification numbers (TRUE ID) shown in Table 3.1 to have pure samples of the required decays. The truth matching ensures to reject combinatorial background and other partially reconstructed decays that could mimic the signal candidates.

As a background proxy, the wrong-sign (WS) combinations of the final-state particles, either the $pK^-K^-\pi^-$ or $pK^+K^+\pi^+$ combinations, are used for the optimisation of the selection. The WS data are obtained from the 2016 minimum-bias data sample.

Particle	abs(ID)	abs(parent ID)
Ξ_c^0 (prompt)	4132	4
Ξ_c^0 (from Ξ_{cc}^+)	4132	4412
Ξ_c^0 (from Ξ_{cb}^0)	4132	5142
p	2212	4132
K	321	4132
π	211	4132

Table 3.1.: Simulation TRUE ID requirements [188] used to match the $\Xi_c^0 \to pK^-K^-\pi^+$ decay.

3.3. Selection

To implement an efficient inclusive selection for the Ξ_c^0 baryons, several steps are implemented in a selection sequence. Firstly, the candidates are selected by simple trigger requirements. Subsequently, two stages of the offline selection are implemented - a cut-based and an MVA-based selection. The following sections describe the individual stages in more detail.

3.3.1. Trigger selection

There are no specific L0 trigger requirements for both the simulation and the WS background data other than passing the global L0 decision.

For the HLT1 stage, the Ξ_c^0 candidates are required to pass either the HLT1 one-track (Hlt1TrackMVA) or the two-track (Hlt1TwoTrackMVA) trigger line. The Hlt1TrackMVA trigger line selects a good-quality track displaced from a primary vertex, with high p_{T}, and with a low probability of being a ghost track (P_{ghost}) [141]. A good track quality is based on low χ^2 per degree of freedom (χ^2/ndf) of the track fit. A track displacement is evaluated based on χ^2_{IP} with respect to any PV, where χ^2_{IP} is the difference in χ^2 of the vertex fit reconstructed with and without the considered track. The Hlt1TwoTrackMVA line in addition requires two tracks to originate from a good-quality vertex with a large invariant mass corrected with respect to its flight direction ($M_{\mathrm{corrected}}$) and to pass a MatrixNet classifier [160] trained on the scalar sum of the p_{T}, quality of the vertex fit, and the displacement of the vertex and tracks [141]. A good-quality vertex is based on low χ^2 of the vertex fit (χ^2_{vtx}). The HLT1 selection requirements are summarised in Table 3.2. One can notice a peculiar requirement in the Hlt1TrackMVA selection, which is based on a hyperbolic requirement in two-dimensional plane of the track displacement and p_{T} [141]. Figure 3.1 shows this requirement in track displacement versus p_{T} to better visualise a region of its acceptance.

Trigger line	Requirement
Hlt1TrackMVA	$\chi^2/\mathrm{ndf} < 2.5$
	$P_{\mathrm{ghost}} < 0.2$
	$\{1\,\mathrm{GeV}/c < p_{\mathrm{T}} < 25\,\mathrm{GeV}/c$
	and $\log\chi^2_{\mathrm{IP}} > (\frac{1}{(p_{\mathrm{T}}-1)^2} + \frac{1.1\times(25-p_{\mathrm{T}})}{25} + \log(7.4))\}$
	or $\{p_{\mathrm{T}} > 25\,\mathrm{GeV}/c$ and $\chi^2_{\mathrm{IP}} > 7.4\}$
Hlt1TwoTrackMVA	$p > 5\,\mathrm{GeV}/c$
	$p_{\mathrm{T}} > 500\,\mathrm{MeV}/c$
	$\chi^2/\mathrm{ndf} < 2.5$
	$\chi^2_{\mathrm{IP}} > 4$
	$\chi^2_{\mathrm{vtx}} < 10$
	$M_{\mathrm{corrected}} > 1\,\mathrm{GeV}/c^2$
	MatrixNet threshold > 0.95

Table 3.2.: Trigger requirements used for the HLT1 selection of the Ξ_c^0 candidates. The p_{T} variable used in the given inequality represents a numerical value of p_{T} given in GeV/c. The given inequality for $\log\chi^2_{\mathrm{IP}}$ at $1\,\mathrm{GeV}/c < p_{\mathrm{T}} < 25\,\mathrm{MeV}/c$ is visualised in Figure 3.1.

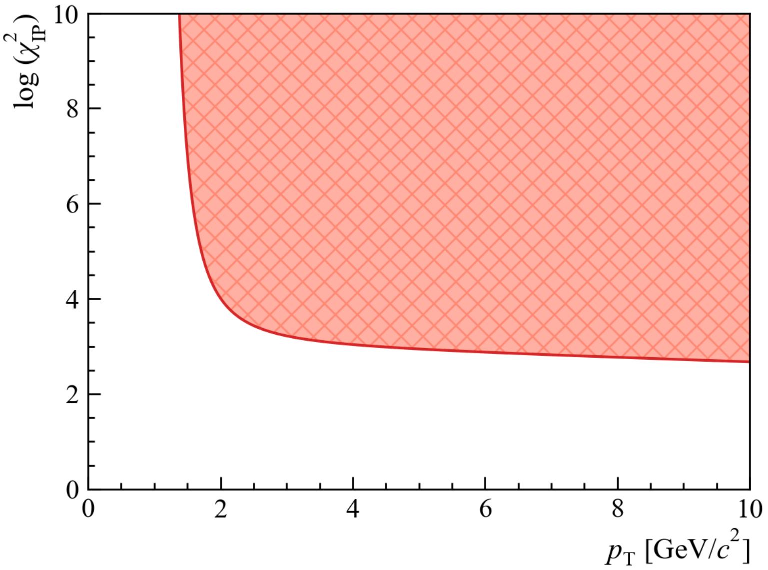

Figure 3.1.: Visualisation of a hyperbolic requirement used in the Hlt1TrackMVA trigger in a two-dimensional plane of the track displacement and p_{T}. The red dashed coloured region represents the region of acceptance for the corresponding requirement.

3.3.2. Pre-selection

The first stage of the implementation of the new trigger line is the cut-based pre-selection with the loose sequential requirements to suppress the combinatorial background before the MVA selection.

The pre-selection is based on tests of the signal efficiency and background retention for different combinations of the rectangular requirements. The starting point of the pre-selection requirements was the current cut-based trigger line, with subsequent tests of the overall signal efficiency and background retention for a combination of looser requirements. No figure of merit was adopted at this point, the aim was to only suppress the combinatorial background before the next stage of the selection to control the CPU requirements of the HLT2 throughput. Table 3.3 summarises the final pre-selection requirements that are used as the first stage of the Ξ_c^0 Turbo++ line implementation. The events are mainly selected based on high p_{T} of the Ξ_c^0 baryon and p_{T} and p of its decay products, as well as a good quality of the vertex and individual tracks. Only the Ξ_c^0 candidates with an invariant mass $m(\Xi_c^0)$ between 2380 MeV/c^2 and 2550 MeV/c^2 are retained. The invariant mass is computed from the particle four-momentum as $(\sqrt{E^2 - \vec{p}^2c^2})/c^2$, where E is the energy and $\vec{p}$ momentum vector of the Ξ_c^0 baryon. There are also some loose PID requirements applied to the final state particles. The thresholds are applied to the $\mathrm{DLL}_{X\pi}$ variable, which represents the difference in the log likelihoods between the pion hypothesis and the particle X under consideration, where X can be either a proton, a kaon, an electron or a muon [189]. The likelihoods are based on the information from the RICH detectors, the calorimeter system, and the muon stations. The number of events passing the trigger and pre-selection requirements is shown in Table 3.4, as well as the efficiency of all pre-selection cuts with respect to all reconstructed candidates selected by the trigger. These events are used in the subsequent MVA training described in the following section.

$2380\,\mathrm{MeV}/c^2 < m(\Xi_c^0) < 2550\,\mathrm{MeV}/c^2$		
p_T of Ξ_c^0	$>$	$1000\,\mathrm{MeV}/c$
$\chi^2_\mathrm{vtx}/\mathrm{ndf}$ of Ξ_c^0	$<$	50
sum of p_T of Ξ_c^0 decay products	$>$	$1000\,\mathrm{MeV}/c$
p_T of all Ξ_c^0 decay products	$>$	$250\,\mathrm{MeV}/c$
p of proton	$>$	$5000\,\mathrm{MeV}/c$
p of kaon	$>$	$1000\,\mathrm{MeV}/c$
p of pion	$>$	$1000\,\mathrm{MeV}/c$
χ^2/ndf of all tracks	$<$	2
$\mathrm{DLL}_{p\pi}$ & ($\mathrm{DLL}_{p\pi}$-$\mathrm{DLL}_{K\pi}$) for proton	$>$	5
$\mathrm{DLL}_{K\pi}$ for kaon	$>$	5
$\mathrm{DLL}_{K\pi}$ for pion	$<$	5

Table 3.3.: Pre-selection cuts for the new Turbo++ line for the Ξ_c^0 baryon.

Simulation/data sample	Number of events	Efficiency (%)
Ξ_c^0 (prompt)	3434	40.58 ± 0.53
Ξ_c^0 (from Ξ_{cc}^+)	64523	52.81 ± 0.14
Ξ_c^0 (from Ξ_{cb}^0)	16572	41.47 ± 0.25
WS1 ($pK^-K^-\pi^-$)	14933	24.78 ± 0.18
WS2 ($pK^+K^+\pi^+$)	12917	24.58 ± 0.19

Table 3.4.: Number of simulation and background events passing the trigger and pre-selection cuts used in the subsequent MVA training and testing, with the corresponding pre-selection efficiencies with respect to the trigger selection, for the various sources of the Ξ_c^0 baryon.

3.3.3. MVA selection

For the MVA training, the TMVA package version 4.2.1 [190] with the ROOT version 6.12.04 [174] is used. Based on the performance comparison of the different MVA methods using a receiver operating characteristic (ROC) curve, the BDT [191] method is chosen as the optimal method to use. The BDT method is however complex and it takes a long time to evaluate its response. Therefore, to meet the HLT2 timing constraints, discretised input variables for the BDT are employed, using a method called the Bonsai Boosted Decision Tree (BBDT) algorithm [192]. Since the input variables are discretised, the BBDT response is evaluated for every possible region of the phase space and converted into a simple one dimensional look-up table. Due to the limitation of computing resources, one needs to be careful about the size of the look-up table which scales with the number of input variables and bins. Therefore a coarse binning scheme and a minimum set of uncorrelated variables are used. Several different combinations of the input variable sets for the MVA training are tested, with a use of 5–8 variables with 3–7 bins for each of them. The variables are ranked according to their separation power $\langle S^2 \rangle$, which for a classifier y is defined as

$$\langle S^2 \rangle = \frac{1}{2} \int \frac{(\hat{y}_S(y) - \hat{y}_B(y))^2}{\hat{y}_S(y) + \hat{y}_B(y)} dy, \tag{3.1}$$

where $\hat{y}_S$ and $\hat{y}_B$ are the signal and background distributions of y, normalised to unity. Only the variables with a correlation smaller than 70% are used in the MVA training, where the variables are discarded based on their separation power defined by Equation 3.1. In the end, the following seven variables are used in the MVA training: the $\chi^2_{\text{vtx}}/\text{ndf}$ of the Ξ_c^0 candidate; the maximum distance of closest approach (DOCA) between any pair of the Ξ_c^0 decay products; the scalar sum of the p_{T} of the Ξ_c^0 decay products; the minimum p_{T} of the Ξ_c^0 decay products; the logarithm of the sum of the χ^2_{IP} of the Ξ_c^0 decay products; the logarithm of the minimum of the χ^2_{IP} of the Ξ_c^0 decay products; and the logarithm of the χ^2 of the Ξ_c^0 flight distance (FD). The MVA variables together with their chosen binning scheme are summarised in Table 3.5. The lower edges of the first bins are chosen based on the minimum value of the corresponding variable.

Figure 3.2 shows the comparison of the signal and background input variables used in the MVA. Figure 3.3 shows the overtraining check using the BBDT method with 800 decision trees, which is used in the implementation. There is no indication of overtraining in the performed BDT training based on the Kolmogorov–Smirnov test [193], which evaluates whether two samples are drawn from the same continuous probability distribution.

Variable	Bin edges								
$\chi^2_{\text{vtx}}/\text{ndf}$ of Ξ_c^0	0	1	2	5	10	∞			
Ξ_c^0 maximum DOCA [mm]	0	0.1	0.2	0.5	∞				
sum of p_{T} of Ξ_c^0 decay products	1	2	2.5	3.5	4.5	6.5	∞		
min of p_{T} of Ξ_c^0 decay products	0.2	0.3	0.4	0.55	0.7	1	∞		
log (sum of χ^2_{IP} of Ξ_c^0 decay products)	–5	1	2	3	4	6	∞		
log (min of χ^2_{IP} of Ξ_c^0 decay products)	–10	–3	–2	–1	0	1	3	∞	
log (χ^2_{FD} of Ξ_c^0)	–6	0	1	2	3	4	5	7	∞

Table 3.5.: Bin edges of the input variables used in the MVA selection. The p_{T} variable is given in units of GeV/c.

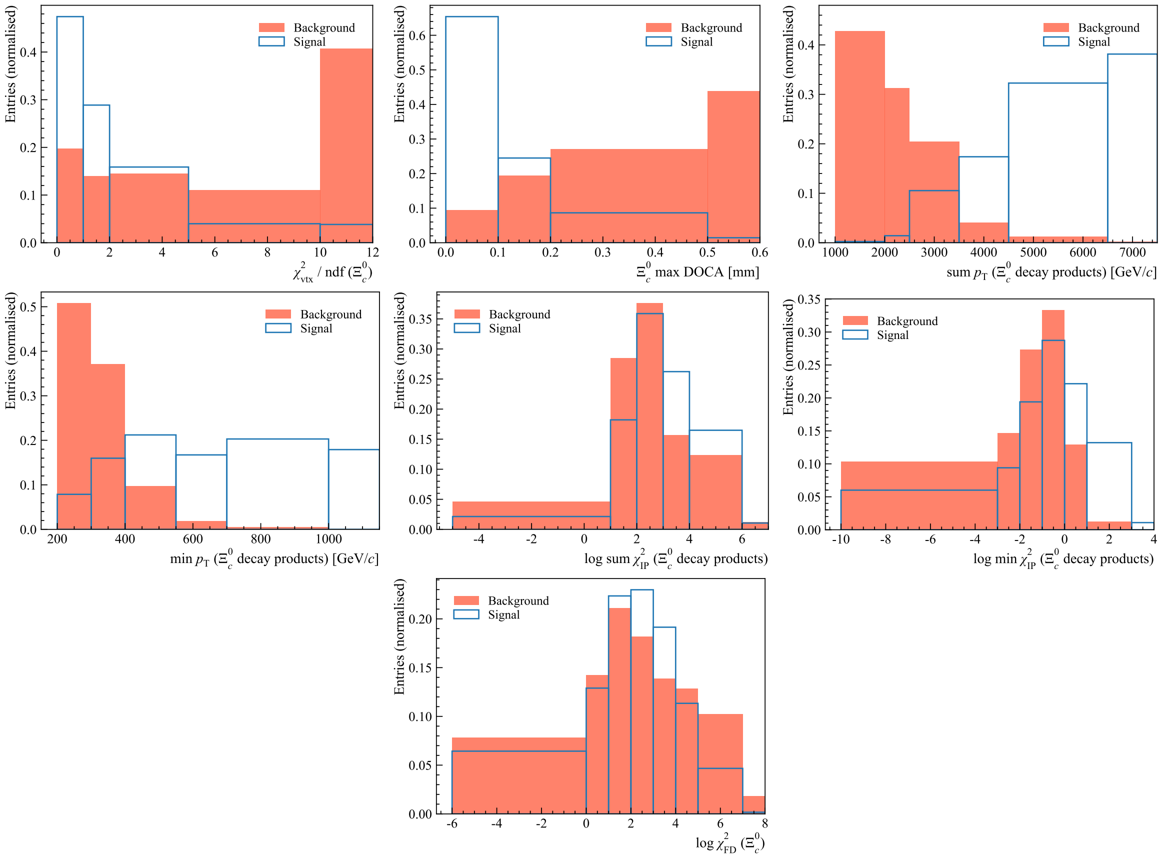

Figure 3.2.: Distribution of the discretised signal (blue line) and background (red fill) variables used in the MVA training.

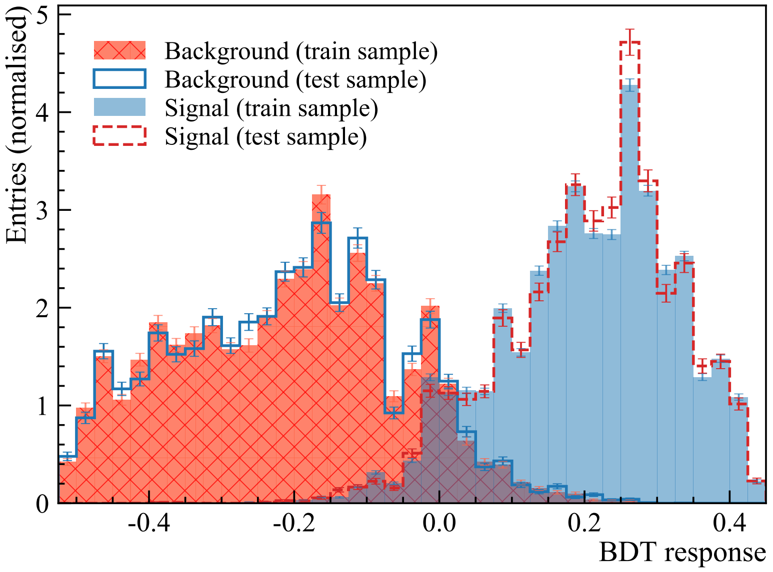

Figure 3.3.: Overtraining check for the background (red dashed fill for the training and the blue solid line for the testing sample) and the signal (blue solid fill for the training and the red dashed line for the testing sample).

3.4. Performance and results

The estimation of the signal efficiencies is performed using 20k simulated events for the different sources of the Ξ_c^0 baryon. The rate and the CPU usage of the implemented line is measured using 50k HLT1 accepted events with the HLT1 rate of 110 kHz. Table 3.6 shows the results for the signal efficiency of the combined HLT2 selection with respect to the events accepted by HLT1, and the trigger rate for different thresholds of the BDT response. The preferred working point for the BDT threshold is chosen to be 0.2 since the rate of around 30 Hz is reasonably low for the inclusive HLT2 trigger line. The measured CPU time for the new trigger line is 2.78 ms per event. The estimated efficiency of the new MVA based Turbo++ line is significantly improved with respect to the existing cut-based trigger line. In particular, the efficiency for the Ξ_{cc}^+ sample is improved by a factor of about 27 using the preferred working point.

Turbo line	ε (%) prompt Ξ_c^0	ε (%) Ξ_c^0 from Ξ_b^-	ε (%) Ξ_c^0 from Ξ_{cc}^+	Rate [Hz]
Existing cut-based line	0.14 ± 0.04	0.45 ± 0.06	0.04 ± 0.02	0.00 ± 0.00
New line, BDT > 0.27	0.62 ± 0.09	2.85 ± 0.15	0.62 ± 0.08	6.60 ± 3.81
New line, BDT > 0.25	0.73 ± 0.09	3.09 ± 0.16	0.87 ± 0.10	14.55 ± 6.43
New line, BDT > 0.20	0.94 ± 0.11	3.61 ± 0.17	1.10 ± 0.11	30.80 ± 8.23
New line, BDT > 0.18	0.99 ± 0.11	3.76 ± 0.17	1.24 ± 0.12	55.00 ± 11.00

Table 3.6.: Measured rates and efficiencies of the HLT2 selection with respect to the HLT1 accepted candidates for the different sources of the Ξ_c^0 baryon and various BDT thresholds. The line with a highlighted text corresponds to the preferred working point implemented in HLT2.

3.5. Summary

This chapter described the development of the MVA-based inclusive Turbo++ trigger line for the Ξ_c^0 baryon implemented for the 2018 data taking. The trigger selection aimed to be efficient on the $\Xi_c^0 \to pK^-K^-\pi^+$ decay, independently of the origin of the Ξ_c^0 baryon. Based on the simulation samples, it is estimated that the efficiency of the newly developed MVA-based Turbo++ line is improved with respect to the existing cut-based trigger line, especially for the $\Xi_{cc}^{+} \to \Xi_{c}^{0}\pi^{+}$ decay. At this point it is not possible to evaluate this outcome for the $\Xi_{cc}^{+} \to \Xi_{c}^{0}\pi^{+}$ decay since the Ξ_{cc}^{+} baryon has not been observed and therefore all searches for its final states are kept blinded until the corresponding analyses are completed. However, the studies are ongoing to search for the $\Xi_{cc}^{+} \to \Xi_{c}^{0}\pi^{+}$ decay, so the relevant checks can be performed once the analyses are unblinded.

For Run 3, where a fully software based trigger [186] will be implemented at LHCb, almost all of the trigger selections need to be performed as Turbo, TurboSP, or Turbo++ as there will not be sufficient bandwidth to save all reconstructed events. This study is also considered as a preparation for the Run 3 Turbo++ selections to evaluate how much bandwidth these selections require in real data-taking conditions, as some of the HLT2 trigger lines (including the lines for the charmed baryons) are required to be implemented as Turbo++ lines. The studies are still ongoing and the final decisions on the implementation of the HLT2 trigger selections for the charmed baryons will be made in the near future.

Chapter 4.

VELO hit resolution study

“Admitting something is wrong is always the first step towards fixing it.”
— Sylvia Earle

“The only question that really counts, must be this one: are things getting better or are they getting worse?”
— Erlend Loe in his book *Naiv. Super*

This chapter describes a study that was performed to correct for discrepancies in the VELO hit resolution observed between the data and Monte Carlo (MC) simulation.[1] An introduction to the study and its motivation are discussed in Section 4.1, followed by a description of the method used to correct for the observed discrepancies in Section 4.2. The results are discussed and the chapter is summarised in Sections 4.3 and 4.4, respectively.

4.1. Introduction and motivation

The importance of the VELO detector was already described in Section 2.3. As it is the detector located closest to the interaction point, it is used for a precise determination of the primary and secondary vertices [139]. Moreover, the VELO is crucial to determine a track displacement, which is used in many analyses to evaluate if a given track

---

[1] The simulation data shown in plots are labelled as *MC* throughout this document.

originates from the decay of a long lived particle. To achieve a desired performance in the track reconstruction, the reconstructed tracks need to be found and fitted precisely using a Kalman filter [171, 172], for which the uncertainties on the hit positions need to be accurately evaluated. A correct estimation of the uncertainties on the position of VELO hits is therefore of a crucial importance for the tracking and reconstruction, as well as in the subsequent calculation of the track related variables. If the uncertainties are not estimated properly, the fitting procedure is not optimal and the total χ^2 of the fit is incorrect, which also impacts the corresponding track quantities.

The estimation of the VELO hit uncertainties is based on the error parametrisation of the hit residuals, which are defined as a distance between the hit measurement and the extrapolated point of the fitted track to the corresponding sensor [139]. In Run 1, this parametrisation was based on studies of the simulation, which was tuned on the results obtained from measurements of the VELO sensors using beam tests before the first start of the data taking at LHCb. The parametrisation was obtained as a function of the projected angle and strip pitch, separately for R and ϕ sensors. The projected angle is calculated by projecting the track onto the plane perpendicular to the strip, and then taking the angle between the projection and the vector perpendicular to the sensor plane [139]. The same parametrisation was used during Run 1 and 2015–2016 data taking and for the corresponding simulation samples.

When a particle traverses a silicon sensor, free charge carriers are released, which are subsequently collected by the strips. If the collected charge passes a certain threshold, a signal is detected. The cluster size is the number of adjacent strips (between 1 and 4) that have the collected charge above an inclusion threshold in the VELO reconstruction algorithm. Since larger projected angle and smaller pitch give a higher probability of charge being collected by more than one strip, the parametrisation of the VELO hit uncertainties is done as a function of strip pitch and projected angle, as already mentioned. The cluster centre, which represents the measured hit position, is calculated as the charge-weighted average of the positions of each strip in the cluster. Due to the radiation damage of the VELO detector, the average cluster size in the data increased over time. The increased average cluster size in the data caused overestimation of the corresponding hit uncertainties on the position of the VELO hits from 2012 onwards. Therefore, in 2017, the parametrisation in data was updated based on data collected at the end of 2016, as a function of the projected angle, strip pitch, cluster size, and sensor type. The parametrisation that was used to update the data is described in detail in reference [194]. As the ageing of the VELO detector is however not precisely modelled in simulation, the VELO hit resolution differs between the data and simulation, so they require different error parametrisations to achieve an optimal performance. Therefore only the parametrisation in the data was updated, as the parametrisation in the simulation gave a good description of the hit resolution. As a consequence of the updated parametrisation in data that better describes the state of the ageing detector, the agreement between the reconstructed data and simulation in track and vertex χ^2 has improved.

However, a disagreement between the data and simulation for 2017 and 2018 samples was observed for some variables. Since the data and simulation use different parametrisations from 2017 onwards, the variables that require the error estimates to be the same between the data and simulation were impacted. These variables measure displacement significance given the errors, such as χ^2_{IP} for displaced tracks, or χ^2 of the flight distance. For example, evaluation of χ^2_{IP} uses the uncertainty on the IP, which comes from the extrapolation of the track back to a PV, with the propagation of the uncertainties on the track trajectory, which are derived from the VELO hit uncertainties. Since the estimation of the hit uncertainties is different in the data and simulation, a different value of χ^2_{IP} is obtained for the same particle kinematics. The disagreement has a direct impact on many analyses using these variables, in particular the analyses that rely on the simulation for a precise evaluation of the efficiencies as a function of a decay time, since its impact varies with the reconstructed decay time of the corresponding particle.

Finding a suitable solution to this issue is not a simple task. Ideally, the simulation should be tuned to have the same VELO hit resolutions as in the data, so the same error parametrisation can be used for both. In practice, it is a complex task. As was mentioned above, the cluster size is impacted by the radiation damage. The charge sharing varies with operational bias voltage, which had to be changed over the years due to the radiation damage in the VELO. The charge deposits in the VELO sensors have therefore a wider spread in data than in simulation. The smaller size of the clusters in simulation leads to worse resolution, since it is not possible to interpolate between strips in 1-strip clusters. Moreover, the radiation damage is not uniform, as it depends on the distance of the sensor from the interaction point. As all sensors behave identically in the simulation, it presents another complication in tuning the simulation. Figure 4.1 shows the mean cluster size as a function of the strip pitch and projected angle for R and ϕ sensors for the 2018 data and simulation samples. One can see that the mean cluster size in data is larger than in the simulation.

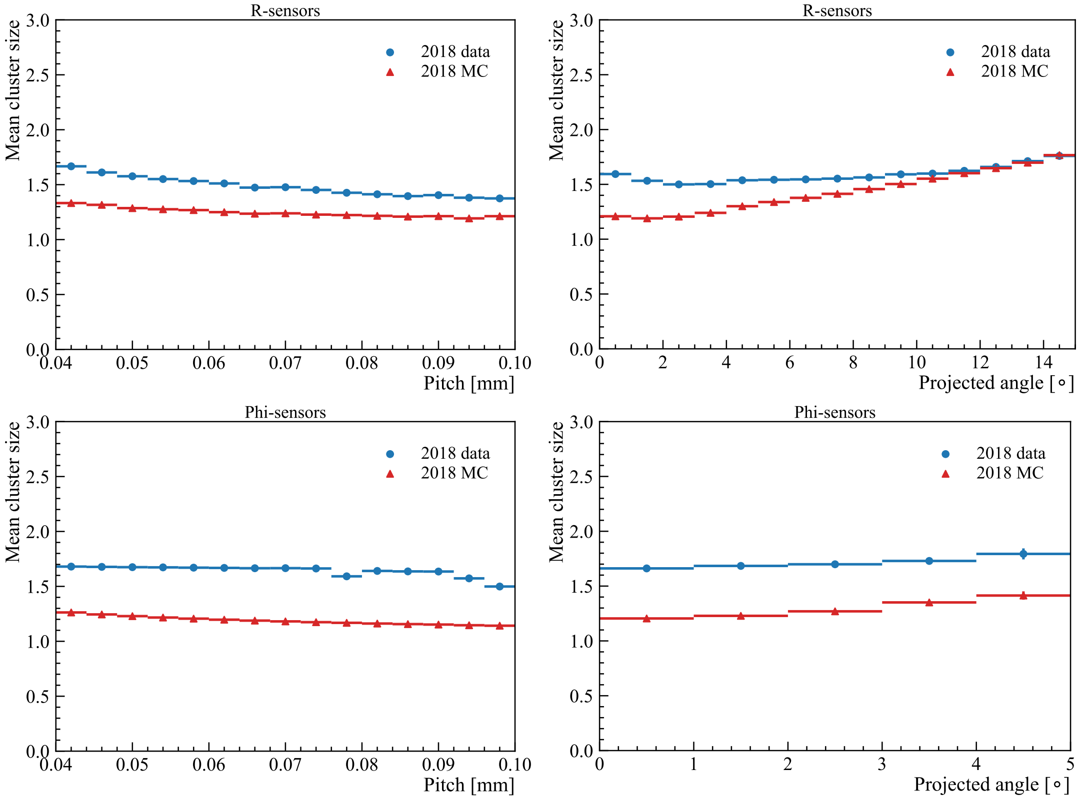

Figure 4.1.: Mean cluster size as a function of the strip pitch (left) and projected angle (right) for R (upper) and ϕ (bottom) sensors for the 2018 data (red circles) and simulation (blue triangles).

The cluster size is impacted by the amount of charge that is deposited and how it is distributed in the silicon material, as well as by the efficiency of the individual strips, which declines with radiation damage. There were several attempts to tune these effects in the simulation in order to match its hit resolution to that in the data, however only with a limited success. For example, the cluster sizes in the simulation were tuned using different values of capacitive coupling and charge diffusion width, which are used to calculate the charge on each strip. None of these efforts demonstrated satisfactory conclusions.

To illustrate the complexity of the issue further, Figure 4.2 shows the mean cluster size as a function of the strip pitch and projected angle for R and ϕ sensors, but for the 2017 data and simulation, for which an updated version of the simulation version was used, which contains a tuning of some low-level VELO parameters related to the radiation damage as mentioned above. One can see that the agreement is better than for the 2018 data and simulation using the older simulation version, but the cluster size is on average larger in the simulations than in the data, which demonstrates a

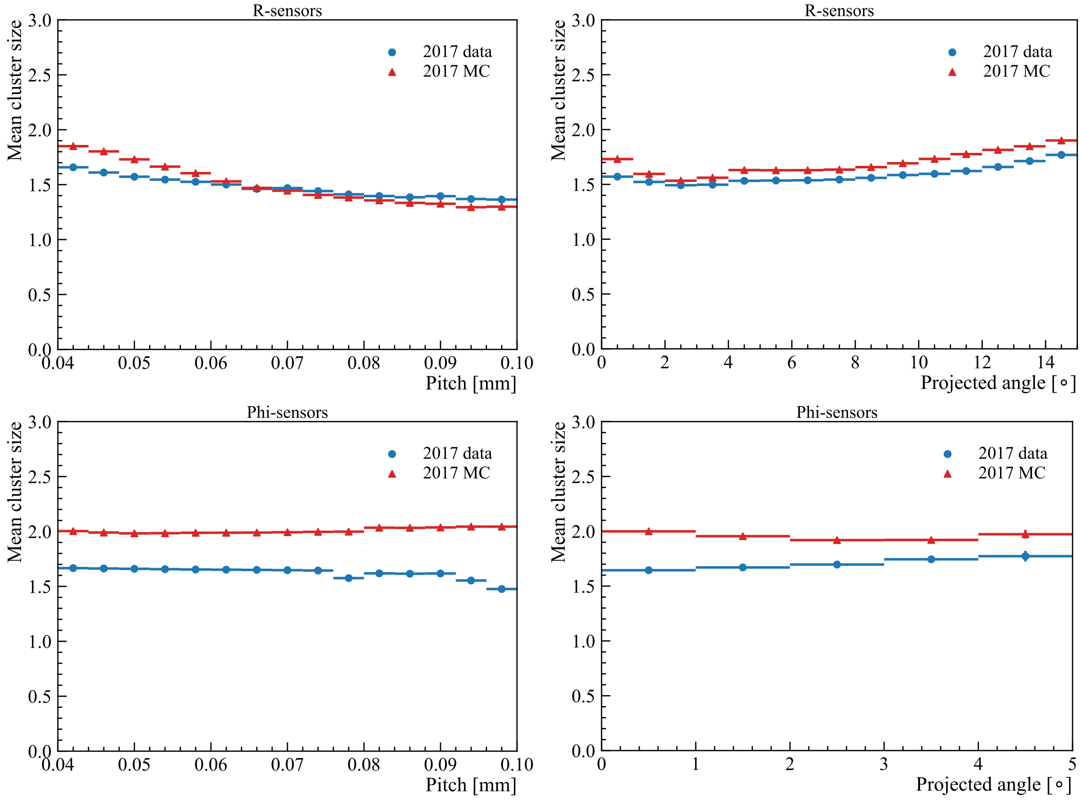

Figure 4.2.: Mean cluster size as a function of the strip pitch (left) and projected angle (right) for R (upper) and ϕ (bottom) sensors for the 2017 data (red circles) and simulation (blue triangles) using an updated simulation version.

difficulty of finding a suitable correction. Hence, the corresponding hit resolutions are still significantly different between the data and simulation even after the simulation version update, as shown in Figure 4.3 for one bin of the projected angle and strip pitch.

This study uses a different approach to overcome the described issue. Rather than tuning the low-level VELO parameters in the simulation, which was shown to be unsuitable to accurately reproduce the hit resolutions seen in the data, the hit resolutions from the data are used to generate the hit residuals in the simulation. The method to perform this correction is described in Section 4.2, with the corresponding results and suggestions for further improvements discussed in Section 4.3.

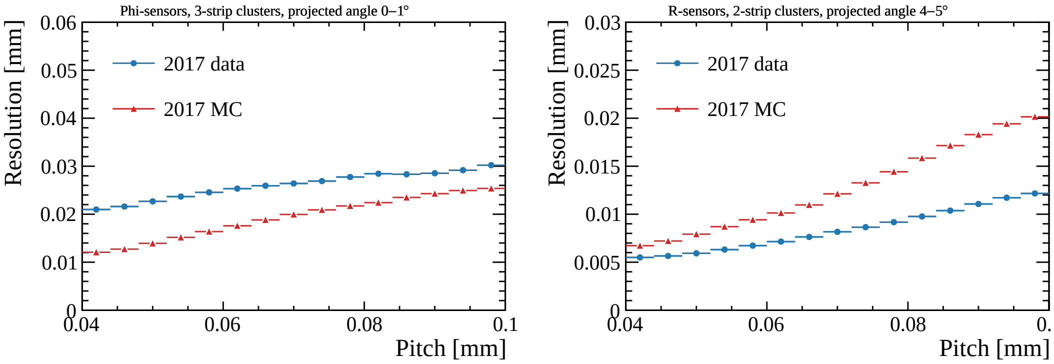

Figure 4.3.: Hit resolution as a function of strip pitch for (a) 3-strip clusters of ϕ sensors and (b) 2-strip clusters of R sensors for one-degree bins of the projected angle.

4.1.1. VELO hit error parametrisation

As a parametrisation of the VELO hit uncertainties is used in this study, this section briefly describes how it is performed. As was mentioned above, the hit residual is defined as a distance between the hit measurement and the extrapolated point of the fitted track to the corresponding sensor [139]. As including the sensor under consideration in the Kalman track fit biases the corresponding residual, the hit residual has a correction factor applied, which is $\sigma_{\text{hit}}/\sigma_{\text{residual}}$ [195], where σ_{hit} is the estimated error on the hit position represented by the cluster centre, and σ_{residual} is the estimated error on the residual from the Kalman-filter fit. For each bin of strip pitch and projected angle, the resolution is determined as the standard deviation of the residual distribution. Figure 4.4 shows the distribution of the track residual in the data and simulation, as well as the true residual based on the truth information from the simulation. The true residual is based on the difference between the true hit and its measured position. One can also consider to fit the corresponding distributions with a Gaussian function and estimate the resolution based on its width, however, it is preferred to use the standard deviation as it is independent of the binning scheme, and it does not bias a result even if the shape is not exactly a Gaussian, such as the true residual shown in Figure 4.4. As shown in reference [194] and tested for this study as well, both approaches give consistent results for well populated bins.

The estimated resolutions based on the standard deviation of the residual distributions are evaluated in bins of strip pitch and projected angle, separately for R and ϕ sensors and 1-, 2- and 3-strip clusters. The estimated resolutions are parametrised using one-degree bins of projection angle as a function of the strip pitch, which approximately follows a linear dependence, as shown in Figure 4.3. For each bin of the projected angle, the slope and offset of the linear function that best fits the distribution are evaluated. In the reconstruction, the estimates of the projected angle and strip pitch are used to obtain the hit uncertainty based on a given VELO hit parametrisation. The evaluated uncertainty is then used in the track fit and computation of the related track variables.

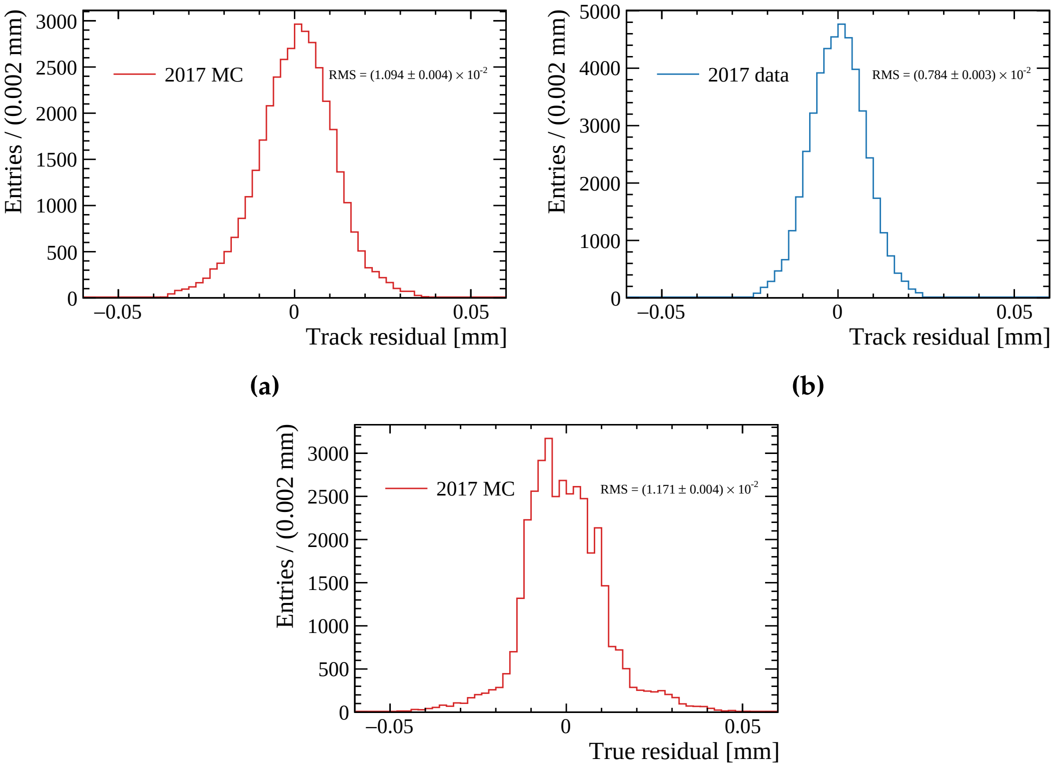

(a) (b) (c)

Figure 4.4.: Distribution of the track residuals in the 2017 (a) simulation and (b) data, and the (c) true residual in the simulation, for 2-strip clusters of R sensors for one pitch bin of 4 μm size and one-degree bins of the projected angle.

4.2. Method

As was already described in the introduction of this chapter, the main goal of this study is to adjust the hit residuals in the simulation so that the resolution in the simulation matches the resolution in the data. To achieve this, the hit residuals in the simulation are generated based on the parametrisation of the resolution in the data. The study is performed on 200k events from the 2017 data and simulation, since the only available minimum-bias simulation samples, which are in a suitable LHCb data format to perform required modifications, are for the 2017 data taking. Only 1-, 2- and 3-strip clusters are considered, since the corresponding parametrisation only applies to those. Since the 4-strip clusters account for about 1% of the used data and simulation samples, they can be safely neglected.

To ensure that only good-quality tracks are used for the study, some minimal requirements are applied to the reconstructed tracks to evaluate the resolutions. Only the tracks that are reconstructed by the VELO detector and all tracking stations are considered. The tracks are required to have χ^2/ndf less than 5, p of more than 5 GeV/c, and at least 10 reconstructed hits in the VELO detector. The VELO sensors that are located more than 75 cm from a PV in the direction along the beam pipe are excluded. The first and last hits of each track are not included in order not to bias the result, as the track fit using the Kalman filter would not have a hit to extrapolate to at one side and could therefore return a larger residual than its true value.

As was mentioned above, the cluster centre is calculated as the charge-weighted average of the positions of each strip in the cluster. The study described in this chapter uses this relation from the other way around, using the low-level simulation of particle interactions in the VELO sensors that have the cluster size and its total charge already determined. Firstly, the residual is randomly generated from a Gaussian distribution, with its width given by the resolution parametrisation of the 2017 data, based on the strip pitch, projected angle, sensor type and cluster size of the corresponding hit. Subsequently, the total charge of the cluster is redistributed to the corresponding strips of the clusters, so that the cluster centre matches the generated position, which is given by the simulated hit position plus the generated residual. The next section describes how the charge redistribution is performed. This approach clearly only works for the clusters with more than 1 strip, therefore the initial focus is given to the correction of 2- and 3-strip clusters, leaving 1-strip clusters unchanged. The strategy for 1-strip clusters is discussed in Section 4.3.1.

4.2.1. Charge distribution adjustment

The redistribution of the total charge in each cluster to its corresponding strips, so that it gives the generated resolution, is as follows. If the generated cluster position is given with respect to the first strip in the cluster, the interstrip position f can be calculated as

$$f = \frac{\sum_{i=0}^{n-1} i c_i}{\sum_{i=0}^{n-1} c_i}, \tag{4.1}$$

where c_i are the individual charges on strip i in the cluster. The value of f is from the interval $[0, n-1]$, where n is the corresponding cluster size. The value of f is evaluated as the sum of the true position of the hit and the generated residual, which is generated from a Gaussian with a zero mean and the width given by the resolution parametrisation.

To redistribute the total charge c_{tot} given f, the individual charges on each strip in 2- and 3-strip clusters are calculated using Equation 4.1. For 2-strip clusters, the charge of the first strip in the cluster is

$$c_0 = (1-f)c_{\text{tot}}, \tag{4.2}$$

and the charge of the second strip is

$$c_1 = f c_{\text{tot}}. \tag{4.3}$$

For 3-strip clusters, the system given by Equation 4.1 is under-determined, therefore a random value for the central strip is chosen from the interval from zero to $f c_{\text{tot}}$. For $f \leq 1$, the charge of the last cluster is then calculated as

$$c_2 = \frac{1}{2}(f c_{\text{tot}} - c_1), \tag{4.4}$$

and the charge of the first cluster as the remaining value out of the total charge. If $f > 1$, then $f \rightarrow (2-f)$ and the values computed for the first and last strip described above are swapped. The adjusted charge distribution is then used in the reconstruction, where the same resolution parametrisation is used as for the generated residuals, which is based on the parametrisation of the 2017 data.

4.3. Results and discussion

After the correction of the residuals described in Section 4.2, the agreement in the resolutions for 2- and 3-strip clusters between the data and simulation is significantly improved. Figure 4.5 shows resolutions for one bin of projected angle for 2- and 3-strip clusters for R and ϕ sensors, where the improvement after the correction is clearly visible. There are regions for which the agreement is improved less significantly, but all bins of projected angle for 2- and 3-strip clusters are improved with respect to the resolution in the simulation before the correction.

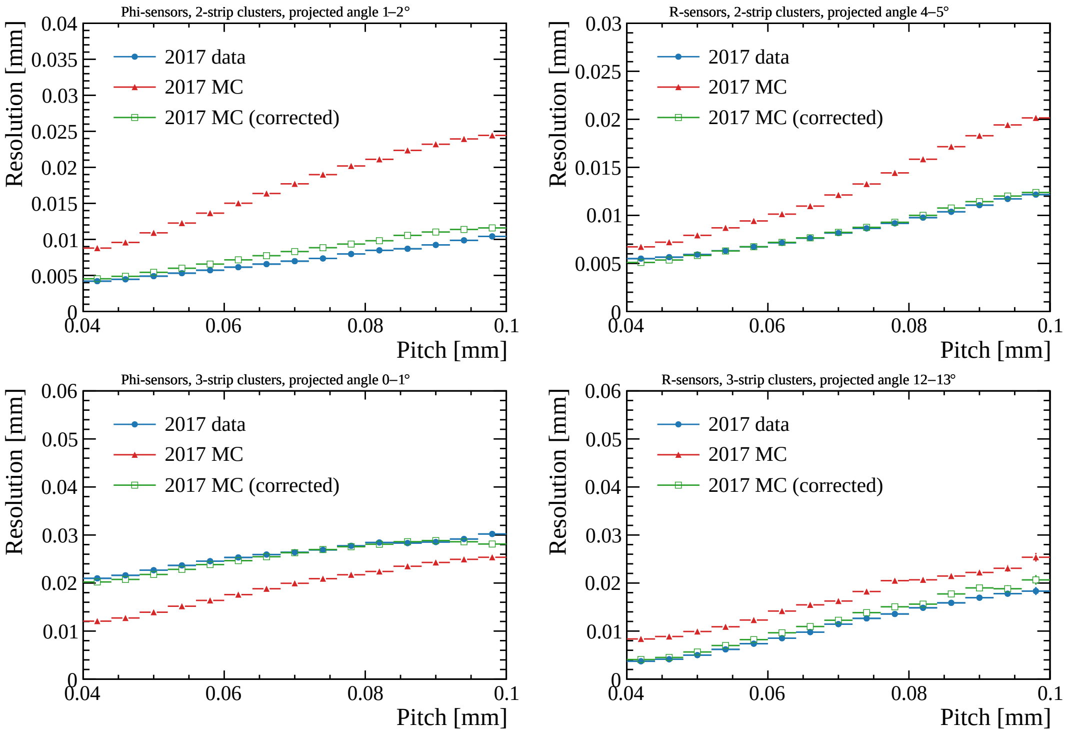

Figure 4.5.: Hit resolution as a function of strip pitch for ϕ sensors (left) and R sensors (right) for 2-strip clusters (upper) and 3-strip clusters (bottom) for one-degree bins of the projected angle before and after the residual correction in the simulation.

To check the impact of the corrected residuals on the χ^2_{IP} distribution, the reconstructed muon tracks from the 2017 minimum-bias 2017 data and simulation samples are used. Since only the minimum-bias sample is available for this study, there is a negligible number of tracks that are displaced from a PV, which would be more suitable for the comparison. Figure 4.6 shows the χ^2_{IP} distribution of the muon tracks before and after the correction described in the previous section is applied. One can see that a further improvement is desirable in order to improve the agreement between the data and simulation, namely the correction of the resolution for 1-strip clusters. As it is beyond the scope of this study, only the corresponding strategy is outlined in the following section.

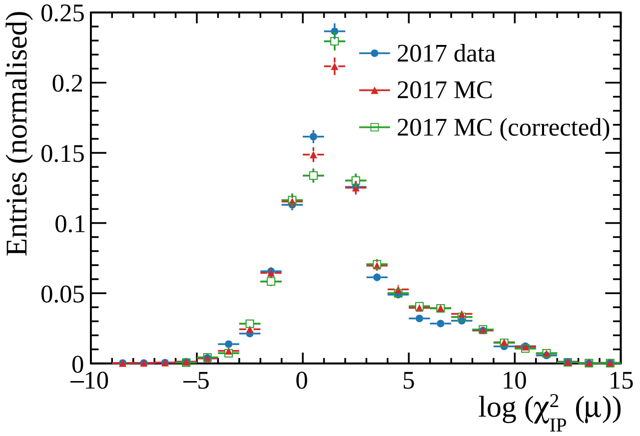

Figure 4.6.: Distribution of χ^2_{IP} for muon tracks in the minimum bias data and simulation, before and after the residuals are corrected in the simulation.

4.3.1. Future improvements

The remaining issue and the discrepancies observed for χ^2_{IP} shown in Figure 4.6 are mainly due to the uncorrected 1-strip clusters, since it is not possible to tune their residuals by modifying the corresponding charge. Figure 4.7 shows resolutions for one bin of projected angle for 1-strip clusters for R and ϕ sensors, where it is clearly visible that no improvement was achieved for 1-strip clusters after the correction described in Section 4.2 was applied. Since the 1-strip clusters form about 40% of all clusters, it is important to improve the agreement between the data and simulation for their corresponding residuals as well. The resolution of 1-strip clusters is well defined and given by the strip pitch divided by $\sqrt{12}$, corresponding to the expected resolution for hits uniformly distributed on the strips. However, there is a difference in fraction of 1-strip clusters between data and simulation, and hence a difference in average cluster size and resolution.

To correct the fractions of the individual cluster sizes, the normalised frequency of n-strip clusters f_n can be calculated for each cluster size as a fraction of n-strip clusters in bins of strip pitch, projected angle, and distance from the nearest strip, separately for R and ϕ sensors. A consideration of the distance from the nearest strip is important as the resolution of the 1-strip clusters is determined by the distance of the corresponding hit from the strip. If the distance is large, then 2 or 3-strip clusters are created. To match the size of the clusters in simulation to those in the data, the following transformation procedure to add or remove strips in simulation with a certain probability can be

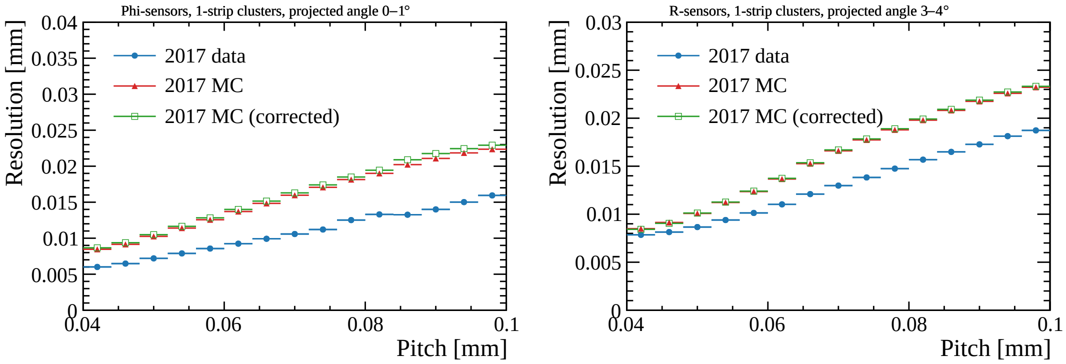

Figure 4.7.: Hit resolution as a function of strip pitch for ϕ sensors (left) and R sensors (right) for 1-strip clusters for one-degree bins of the projected angle before and after the residual correction in the simulation.

considered. The corresponding probabilities can be calculated as

$$\begin{pmatrix} P(f_1^{\mathrm{MC}} \to f_1^{\mathrm{D}}) & P(f_2^{\mathrm{MC}} \to f_1^{\mathrm{D}}) & P(f_3^{\mathrm{MC}} \to f_1^{\mathrm{D}}) \\ P(f_1^{\mathrm{MC}} \to f_2^{\mathrm{D}}) & P(f_2^{\mathrm{MC}} \to f_2^{\mathrm{D}}) & P(f_3^{\mathrm{MC}} \to f_2^{\mathrm{D}}) \\ P(f_1^{\mathrm{MC}} \to f_3^{\mathrm{D}}) & P(f_2^{\mathrm{MC}} \to f_3^{\mathrm{D}}) & P(f_3^{\mathrm{MC}} \to f_3^{\mathrm{D}}) \end{pmatrix} \begin{pmatrix} f_1^{\mathrm{MC}} \\ f_2^{\mathrm{MC}} \\ f_3^{\mathrm{MC}} \end{pmatrix} = \begin{pmatrix} f_1^{\mathrm{D}} \\ f_2^{\mathrm{D}} \\ f_3^{\mathrm{D}} \end{pmatrix}, \qquad (4.5)$$

where f_n^{MC} and f_n^{D} are the normalised frequencies of n-strip clusters in the simulation and data, respectively. The 3×3 matrix on the left side of Equation 4.5 is a transformation matrix, where $P(f_i^{\mathrm{MC}} \to f_j^{\mathrm{D}})$ denotes a probability to transform an i-strip cluster into a j-strip cluster in the simulation. The transformation matrix is calculated for each bin of strip pitch, projected angle, and distance between the hit and the nearest strip.

Since the transformation matrix contains probabilities, it directly implies that the sum over the individual columns has to be one. However, there is no single solution for the transformation matrix, as the system of equations given by Equation 4.5 is underdetermined, because it contains more unknown variables than equations. Therefore, a minimisation based on the minimal transformation is applied, using the following steps:

- If f_n^{MC} is smaller than f_n^{D}, the corresponding clusters size is under-represented in the simulation in that bin, therefore $P(f_n^{\mathrm{MC}} \to f_n^{\mathrm{D}})$ equals to 1, and $P(f_n^{\mathrm{MC}} \to f_i^{\mathrm{D}})$ is zero for i not equal to n.
- If f_n^{MC} is larger than f_n^{D}, then only a fraction of hits in that bin should have the corresponding size in the simulation, therefore $P(f_n^{\mathrm{MC}} \to f_n^{\mathrm{D}})$ is $f_n^{\mathrm{D}}/f_n^{\mathrm{MC}}$.

- What remains is to re-distribute the excess $(1 - f_n^{\mathrm{D}} / f_n^{\mathrm{MC}})$ from the second case to probabilities that are missing for the first case.

Using the described algorithm, at most five elements have a non-zero value, since $\sum_{n=1}^{3} f_n = 1$ for both data and simulation, and therefore only one or two values of f_n^{MC} can be larger than the corresponding frequencies for n-strip clusters in the data.

The new cluster size in the simulation is then randomly generated based on the corresponding probabilities. If the new cluster size is different to the original cluster size, the new strips are removed or added to the cluster based on their distance with respect to the true hit position. The furthest strips are removed in case the new cluster size is smaller, and the closest strips are added in case it is larger.

To demonstrate the proposed cluster size transformation, the transformation matrix given in Equation 4.5 is calculated using the 2017 data and simulation samples in bins of strip pitch and projected angle. The distance of the hit to the nearest strip is not included in this demonstration, as more aspects have to be considered in that case, which are outlined below for completeness. Figure 4.8 shows the mean cluster size in the data and simulation after the cluster size transformation is applied, as well as the residual correction of 2- and 3-strip clusters described in Section 4.2. One can see much better agreement between the transformed simulation and data than for the uncorrected simulation. The next step would be to include also bins of distance of the reconstructed hit position to the nearest strip. Subsequently, a simulation correction in bins of distance would be done using a smeared truth distance so it matches the corresponding reconstructed distance. It is expected that the correct number of 1-strip clusters as a function of distance to the nearest strip would yield the correct resolutions. The procedure for the redistribution of charge on 2-strip and 3-strip clusters, described in Section 4.2.1, would follow the cluster size transformation. Since it is beyond the scope of this study, it remains to be implemented as a future improvement of the performed study.

4.4. Summary

This chapter discussed a study to improve the agreement between the VELO hit resolution in the data and simulation. The presented method uses the hit resolutions from the data to generate the hit residuals in the simulation, with a subsequent

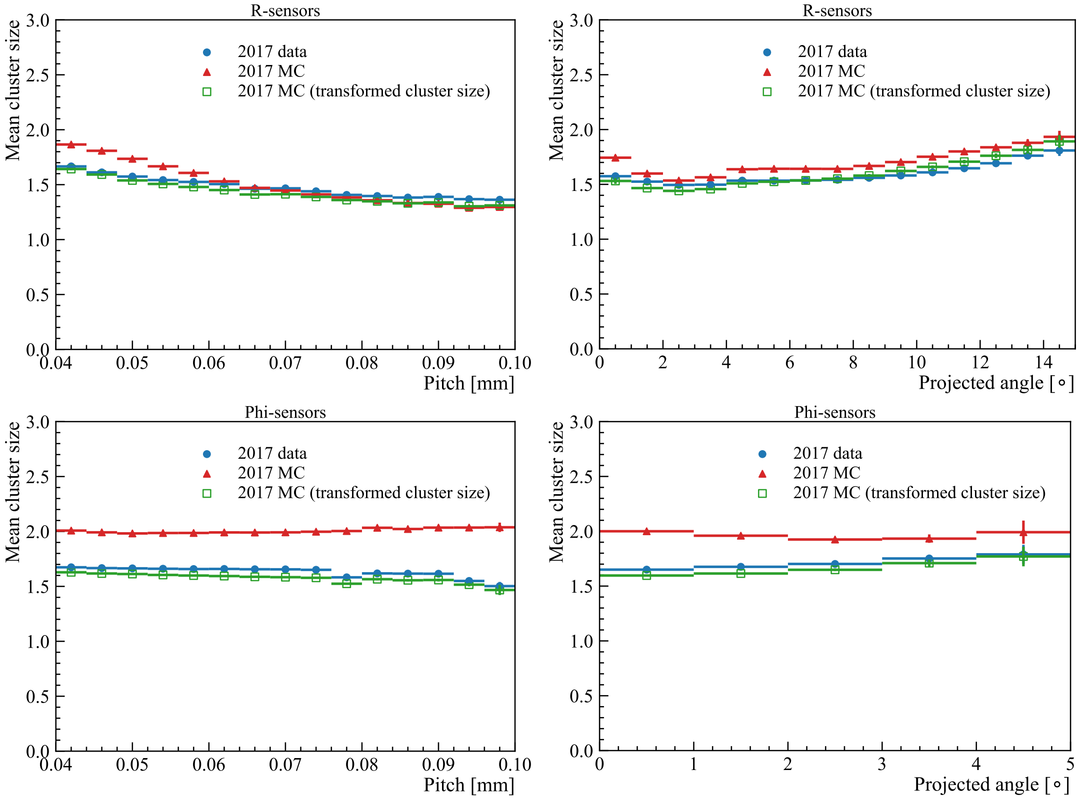

Figure 4.8.: Mean cluster size as a function of the strip pitch (left) and projected angle (right) for R (upper) and ϕ (bottom) sensors for the 2017 data (blue circles), simulation (red triangles) and the simulation after the cluster size correction (green squares).

adjustment of the charge on the strips to match the generated residual. The resolutions of the 2- and 3-strip clusters are clearly improved as they match the data well after the correction, however, 1-strip clusters are not improved as the proposed method is not applicable to them.

A strategy to correct 1-strip clusters as a function of the distance between the hit and the nearest strip is presented, in order to improve the agreement for 1-strip clusters in the future. However, as it is beyond the scope of this study, the method is only outlined and the preliminary checks of the proposed approach are presented. It is expected that the proposed correction of 1-strip clusters would improve the agreement between χ^2_{IP} and other related variables, which are impacted by the difference in resolution between the data and simulation. A large simulation sample would be needed for validation to check the effect of the correction on these variables, which was not available at the time of the study. Further studies of its impact, once the simulation samples are available, are therefore required.

Chapter 5.

Introduction to the search for the doubly charmed baryon Ξ_{cc}^{+}

"Let's think the unthinkable, let's do the undoable. Let us prepare to grapple with the ineffable itself, and see if we may not eff it after all."
— Douglas Adams in his book *Dirk Gently's Holistic Detective Agency*

This chapter introduces the studies related to the search for the $\Xi_{cc}^{+} \to \Xi_{c}^{+}\pi^{-}\pi^{+}$ decays (and their charge conjugates; the conjugate channels are implied throughout this document). Firstly, the analysis and the studied decay mode are introduced in Section 5.1. The analysis strategy related to the work that is discussed in the following three chapters is described in detail in Section 5.2. The chapter is then summarised in Section 5.3.

5.1. Analysis introduction

As was already introduced in Section 1.3.2, the Ξ_{cc}^{+} baryon has never been unambiguously observed. This analysis presents the search for this baryon using the $\Xi_{cc}^{+} \to \Xi_{c}^{+}\pi^{-}\pi^{+}$ decays, which is the first search for the Ξ_{cc}^{+} baryon in this final state. Figure 5.1 shows the dominant decay diagrams for the $\Xi_{cc}^{+} \to \Xi_{c}^{+}\pi^{-}\pi^{+}$ decay mode. This analysis is based on the data collected in 2016–2018 with the LHCb detector at a centre-of-mass energy of 13 TeV, corresponding to about 5.4 fb^{-1} of integrated

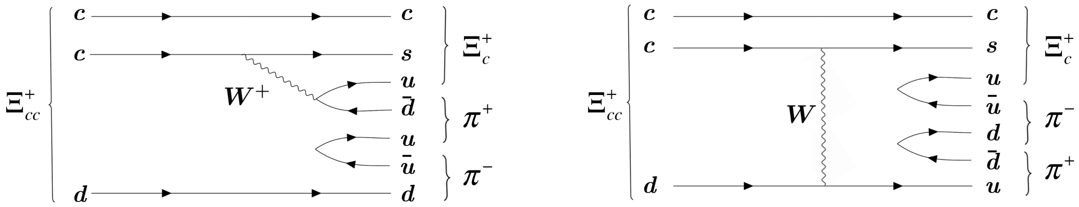

Figure 5.1.: Examples of decay diagrams for the $\Xi_{cc}^{+}\to \Xi_c^{+}\pi^{-}\pi^{+}$ decay channel.

luminosity. The data from Run 1 and 2015 cannot be easily included as there are no dedicated trigger or stripping lines for this decay mode, therefore only 2016–2018 data is used.

The multibody decays often proceed through some intermediate resonances. In case of the $\Xi_{cc}^{+}\to \Xi_c^{+}\pi^{-}\pi^{+}$ decay, the final state can proceed via the $\Xi_{cc}^{+}\to \Xi_c^{+}(\rho^{0}\to \pi^{-}\pi^{+})$ or $\Xi_{cc}^{+}\to (\Xi_c(2645)^{0}\to \Xi_c^{+}\pi^{-})\pi^{+}$ decay chains. Since the final state is identical between the studied decay mode and the two resonant modes, both of these resonant decays are included in this analysis and the same baseline selection criteria are applied in all cases. The ρ^{0} meson present in the $\Xi_{cc}^{+}\to \Xi_c^{+}(\rho^{0}\to \pi^{-}\pi^{+})$ decay is a broad resonance, therefore a restriction on the $\pi^{+}\pi^{-}$ invariant mass would not be very efficient to further suppress the combinatorial background. However, the combinatorial background for the $\Xi_{cc}^{+}\to (\Xi_c(2645)^{0}\to \Xi_c^{+}\pi^{-})\pi^{+}$ decay mode can be reduced by restricting the invariant-mass window around the $\Xi_c(2645)^{0}$ baryon in order to increase the sensitivity to this resonant decay mode. Therefore this resonant decay chain is considered as an additional cross-check after unblinding, in which case a restriction on the $\Xi_c^{+}\pi^{-}$ invariant mass is applied and the statistical significance of the $\Xi_c(2645)^{0}\pi^{+}$ invariant-mass spectrum is evaluated. More details on this cross-check can be found in Section 5.2.2.

The Ξ_c^{+} candidates are reconstructed through their decays to the $pK^{-}\pi^{+}$ final state. The absolute branching fraction (BF) for the $\Xi_c^{+}\to pK^{-}\pi^{+}$ decay has been recently measured by the LHCb collaboration [196] to be $(1.135 \pm 0.002\,(\text{stat}) \pm 0.387\,(\text{syst}))\%$ and by the Belle experiment [197] to be $(0.45 \pm 0.21\,(\text{stat}) \pm 0.07\,(\text{syst}))\%$. As these results come from different experiments and are therefore uncorrelated, one can calculate the inverse-variance weighted mean of these two measurements resulting in $(0.62 \pm 0.19)\%$. Even though this decay mode of the Ξ_c^{+} baryon is Cabibbo suppressed, its reconstruction efficiency is significantly larger than for the Cabibbo-favoured decays due to its hadronic nature, which makes it the most suitable decay mode to reconstruct the Ξ_{c}^{+} baryon at the LHCb experiment.

As the number of already observed Ξ_{cc}^{++} candidates in the $\Xi_{cc}^{++} \to \Lambda_{c}^{+} K^{-} \pi^{+} \pi^{+}$ and $\Xi_{cc}^{++} \to \Xi_{c}^{+} \pi^{+}$ decays in the 2016–2018 dataset is relatively small [78], the contamination from the secondary decays from the (so far never observed) doubly beauty baryons for both the Ξ_{cc}^{+} and Ξ_{cc}^{++} baryons can be safely neglected.

5.2. Analysis strategy

In order to build a solid and unbiased study, this analysis was treated as a blinded analysis until all of its aspects were completed and a green light for unblinding from the analysis review committee was received. All of the possible outcomes from the search for the Ξ_{cc}^{+} baryon and the corresponding measurements were defined and studied prior to unblinding, and they are described in detail in this chapter, and Chapters 6, 7 and 8, alongside the already unblinded results. The $\Xi_{c}^{+} \pi^{-} \pi^{+}$ invariant mass that was not examined before unblinding was from 3.3 to 3.8 GeV/c^2. This wide invariant-mass window covers both the SELEX result of $m(\Xi_{cc}^{+}) = 3518.7 \pm 1.7\,\text{MeV}/c^2$ [95] and the mass of the Ξ_{cc}^{++} baryon measured by the LHCb experiment, which is $m(\Xi_{cc}^{++}) = 3621.55 \pm 0.23\,(\text{stat}) \pm 0.30\,(\text{syst})\,\text{MeV}/c^2$ [78]. The majority of the studies described in this and the following chapters were performed before unblinding, unless stated otherwise.

The analysis selection is built on the knowledge of the simulated events, which represent the signal candidates, and the real data with an unphysical combination of the final-state tracks, namely the wrong-signed minus (WSM) for the combinations of the Ξ_{c}^{+} baryons with two negative pions ($\Xi_{c}^{+} \pi^{-} \pi^{-}$) and the wrong-signed plus (WSP) for the $\Xi_{c}^{+} \pi^{+} \pi^{+}$ combinations, as the combinatorial background representation in the signal region. The upper side-band (SB) of the right-signed (RS) candidates in the $\Xi_{c}^{+} \pi^{-} \pi^{+}$ invariant-mass region from 3.8 to 4.0 GeV/c^2 is also considered for the background studies as a complementary sample to the WSM and WSP combinations.

The analysis strategy developed and implemented before unblinding is as follows. There are two possible outcomes of which only one would be relevant for this analysis after unblinding. The first case would be if a significant peaking structure consistent with the Ξ_{cc}^{+} baryon would be observed, in which case the Ξ_{cc}^{+} mass would be measured and the relative production cross-section multiplied by the branching fraction of the studied decay with respect to the normalisation channel $\Xi_{cc}^{++} \to \Xi_c^+ \pi^+$ defined as

$$R = \frac{\sigma(\Xi_{cc}^{+}) \times \mathcal{B}(\Xi_{cc}^{+} \to \Xi_c^+ \pi^- \pi^+)}{\sigma(\Xi_{cc}^{++}) \times \mathcal{B}(\Xi_{cc}^{++} \to \Xi_c^+ \pi^+)} \tag{5.1}$$

would be determined, where $\sigma(\Xi_{cc}^{+})$ and $\sigma(\Xi_{cc}^{+})$ represent the production cross-sections of the Ξ_{cc}^{+} and Ξ_{cc}^{++} baryons, respectively, which are expected to be the same [38], and $\mathcal{B}$ represents the corresponding branching fractions. The second case would be when no significant structure would be observed, in which case an upper limit (UL) on R would be set for four different lifetime hypotheses: 40, 80, 120 and 160 fs. Figure 5.2 shows the decision tree for this analysis where the decisions to discriminate between the significant and non-significant observations are based on the evaluated local and global significances, evaluation of which is described in the dedicated Section 7.2.

Two sets of triggers were used in this analysis, where one set is chosen to allow for a precise determination of the relative efficiencies, and the second one to maximise the significance of the signal. A detailed description of the used trigger requirements can be found in the dedicated Section 6.2.1. In summary, the two trigger sets are based on the following criteria:

- The Ξ_{cc}^{+} candidates which are triggered independently of signal (TIS) with respect to a collection of all L0 lines (hadron, electron, photon, muon, and di-muon). Moreover, an inclusive HLT2 line for the Ξ_c^+ baryon was used, where the Ξ_c^+ candidates were reconstructed through their decay to the $pK^-\pi^+$ final state and were subsequently combined with two companion, oppositely charged, pions. This trigger combination is referred to as the *default trigger set* throughout this document.

- The Ξ_c^+ candidates which are triggered on signal (TOS) with respect to the L0 hadron selection or TIS on the Ξ_{cc}^{+} candidates with respect to a collection of all L0 lines. In addition to the inclusive HLT2 line used in the default trigger set which is in common for all studied years, an exclusive HLT2 line for the $\Xi_{cc}^{+} \to \Xi_c^+ \pi^- \pi^+$ decay implemented in 2017, and an additional MVA-based inclusive HLT2 line for the Ξ_c^+ baryon available in 2018 were used. This trigger combination is referred to as the *extended trigger set* throughout this document.

The default trigger set is used in a selection to evaluate the significance after unblinding and to measure the UL on R since it allows a precise evaluation of the

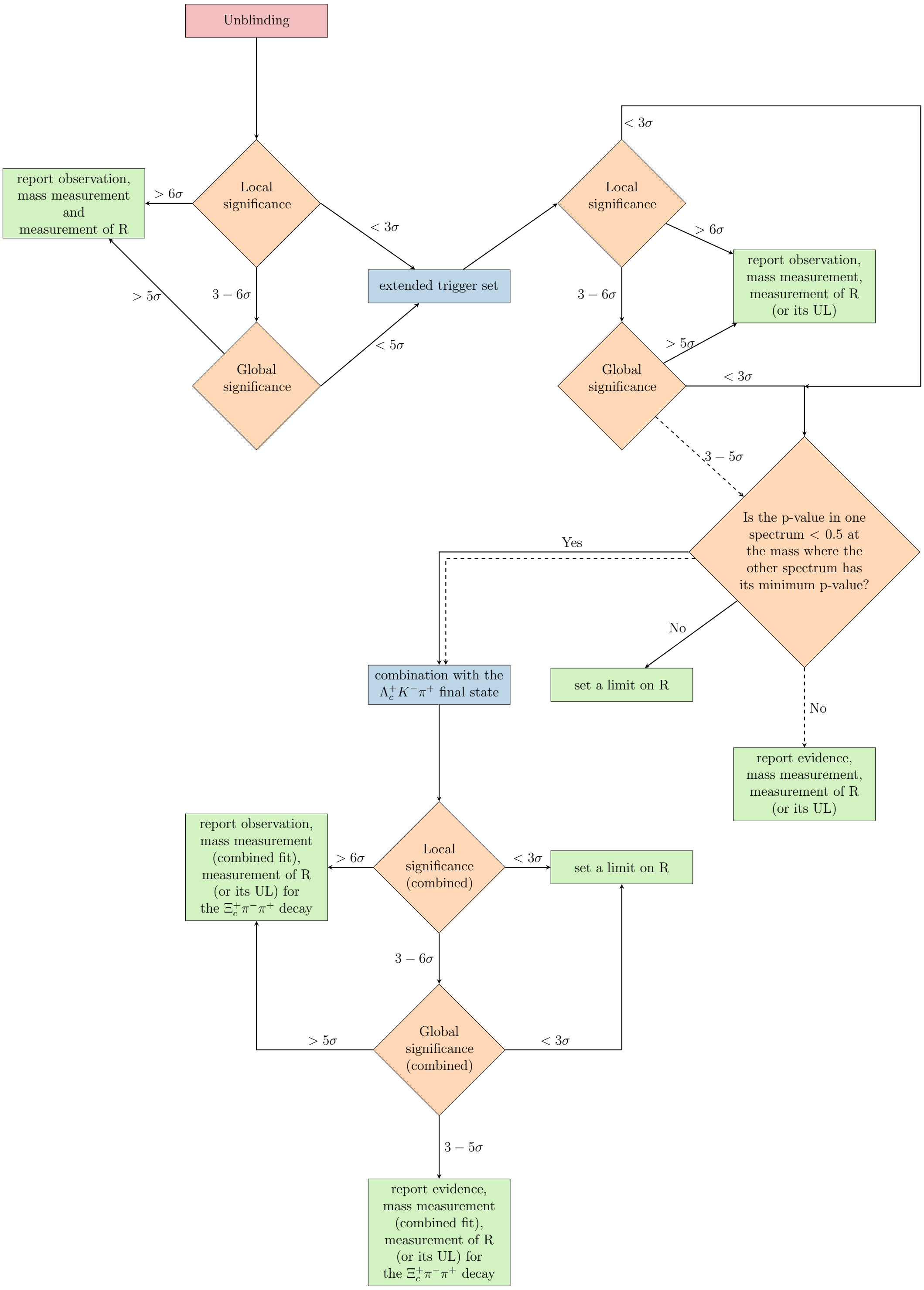

Figure 5.2.: Decision tree based on the evaluated local and global significances and additional criteria for the combination with the $\Xi_{cc}^{+} \to \Lambda_c^+ K^- \pi^+$ decay channel. The dashed and solid lines indicate different paths out of the decision node depending on the path into it.

efficiencies needed for the determination of the UL. The extended trigger set is used in the case that an evaluated significance in the default trigger set would not reach the level required for observation, as shown in Figure 5.2, in order to enhance the possibility of the signal observation. In case the evaluated significance in the default trigger set would be sufficient to claim observation, the significance would be also evaluated using the extended trigger set as an additional cross-check. In case the evaluated significance would be larger in the extended trigger set than in the default trigger set, the significances and yields from both trigger sets would be reported in the published analysis paper.

The extended trigger set, however, is not used for the determination of R (or its UL) in any case, since the evaluation of the L0 efficiency introduces additional systematic uncertainties which are expected to be large with respect to other systematic uncertainties. Moreover, the extended trigger set includes an additional MVA-based inclusive HLT2 line for the Ξ_{c}^{+} baryon, which was introduced only for 2018 data taking. This trigger line was developed in a similar way as the trigger line for the Ξ_{c}^{0} baryon described in Chapter 3. As there are PID requirements implemented in the MVA-based HLT2 line, in order to evaluate the PID efficiency correctly, one needs to apply the HLT2 selection offline (without the PID requirements), which is more difficult for the MVA-based trigger line due to the application of the MVA selection used in the trigger. Additionally, there was a bug in the mentioned HLT2 MVA-based trigger line which was fixed only during the first technical stop in June 2018, therefore the 2018 dataset would be inconsistent between different trigger lines used in this analysis. Last but not least, it is not possible to use more HLT2 Turbo lines for the determination of R as there is no procedure to estimate an overlap between the HLT2 lines in the real data with 100% precision due to the unavailability of TIS and TOS information for the Turbo HLT2 lines. The overlap between the different HLT2 lines in the extended trigger set is removed if the $\Xi_{cc}^{+(+)}$ candidates in different HLT2 lines share the same run and event numbers and their masses are within $1\,\mathrm{MeV}/c^2$, in order to conservatively take into account possible differences in computing of the properties of the final states, so it is certain that no candidate is counted twice. This method can be safely used for the evaluation of the statistical significance as it is clear that all possible candidates selected by more than one HLT2 line are removed, but it is not suitable for the determination of R as there is no way to retrieve the missing HLT2 information for a precise evaluation of the corresponding efficiencies.

The normalisation channel for this analysis is the already observed decay of the Ξ_{cc}^{++} baryon with the Ξ_{c}^{+} baryon in its final state, namely the $\Xi_{cc}^{++} \to \Xi_{c}^{+}\pi^{+}$ decay mode. Since the Ξ_{c}^{+} baryon is an intermediate particle reconstructed in the same final state in both cases, its BF to the $pK^{-}\pi^{+}$ final state cancels in the ratio. As already mentioned, a recent search for the Ξ_{cc}^{+} baryon at LHCb in the $\Xi_{cc}^{+} \to \Lambda_{c}^{+}K^{-}\pi^{+}$ decay channel using Run 1 and Run 2 data [101] showed no significant signal, therefore it was not considered as a normalisation channel for this analysis.

5.2.1. Decisions after unblinding

As already mentioned, the procedures for both the observation and non-observation of the signal were established prior to unblinding. They are described in this and the following chapters as they are an inherent part of this analysis. Figure 5.2 shows all possible outcomes after unblinding and established decisions based on them defined prior to unblinding, which are described as follows. A measurement of R would be performed only for the $\Xi_{cc}^{+} \to \Xi_{c}^{+}\pi^{-}\pi^{+}$ decay channel at the mass where the highest local significance would be found, whereas an UL on R would be measured as a function of the Ξ_{cc}^{+} mass in the invariant-mass region from 3400 to 3800 MeV/c^{2}.

A combination with the $\Xi_{cc}^{+} \to \Lambda_{c}^{+}K^{-}\pi^{+}$ decay mode would be performed only if the p-value in the $\Lambda_{c}^{+}K^{-}\pi^{+}$ ($\Xi_{c}^{+}\pi^{+}\pi^{-}$) spectrum would be < 0.5 for the mass at which the $\Xi_{c}^{+}\pi^{+}\pi^{-}$ ($\Lambda_{c}^{+}K^{-}\pi^{+}$) spectrum would have its minimum p-value. The $\Xi_{cc}^{+} \to \Lambda_{c}^{+}K^{-}\pi^{+}$ selection used for the combined fit is that from the recently published $\Xi_{cc}^{+} \to \Lambda_{c}^{+}K^{-}\pi^{+}$ search referred to as Selection B in the corresponding reference [101], which uses a restricted set of triggers and has a lower background level. In case a significant signal would be observed after the combination with the $\Lambda_{c}^{+}K^{-}\pi^{+}$ final state, a measurement of R would be performed if the local significance for the $\Xi_{c}^{+}\pi^{+}\pi^{-}$ final state would be larger than 3 standard deviations (σ) and it would align with the maximum local significance of the combined fit, otherwise an UL on R would be set at the mass of the maximum significance in the combined fit.

If a significant signal would be observed for the extended trigger set, a measurement of R would be performed if the local significance for the $\Xi_{c}^{+}\pi^{+}\pi^{-}$ final state would be larger than $3\,\sigma$ in the spectrum using the default trigger set and its position would align with the maximum local significance in the extended trigger set, otherwise the UL on R would be set at the mass of the maximum significance in the spectrum for the extended trigger set. In case a significant signal would be observed for the extended trigger set, the mass would be measured for the spectrum that gives the smallest overall uncertainty on the mass. If a significant signal would be observed after the combination with the $\Lambda_c^+ K^- \pi^+$ final state, the mass would be measured for the combined spectrum since the overall uncertainty would be lower due to the dominant statistical component of the overall uncertainty.

5.2.2. Planned cross-checks before and after unblinding

In order to ensure the stability of the result, several cross-checks were established to be performed as the last step before unblinding, namely a blinded fitted yield of the signal to be compared with the data, split by:

- Baryon charge: Ξ_{cc}^{+} vs. Ξ_{cc}^{-};
- Year of data taking: 2016, 2017 and 2018;
- Trigger category: default vs. extended trigger set;
- L0 trigger category: TIS vs. TOS (with full set of the HLT2 triggers);
- Magnet polarity: up and down.

The yield-consistency checks are performed at the mass where the mass fit converges. The fit is designed in a way that only the information about the compatibility between the categories from the fit is revealed, the information about the yields or their uncertainty is discarded. To perform the check, firstly the p-value scan is performed in the invariant-mass range from 3400 to 3800 MeV/c^2 using the full data sample in order to find the global minimum which is used as the initial value for the subsequent mass fits for the subsets of data in the different categories, as specified above. The compatibility between the yields is computed and saved to an output file, all other output files (p-value scan, mass and fit information) are deleted before the check is finalised. The check of the signal yields would be repeated after unblinding in case a significant signal would be observed, so the number of signal candidates in each category could be reported.

The consistency check of the fitted mass between the categories listed above would be performed only after unblinding if a significant signal would be observed. The reason is that if there would not be a significant peak in the data, the mass fit would converge on the mass with the largest local significance, depending on the background fluctuations, which does not have to be the same for the different categories. Therefore a significantly inconsistent blinded mass check would indicate that there is no signal peak present in the dataset, which would indirectly unblind the result.

Another check, which would be performed in case an evidence or an observation of the Ξ_{cc}^{+} baryon would be reported after unblinding, is the evaluation of its compatibility with a weak decay. A decay time requirement of 5 times the decay time resolution would be applied to check if the peak still remains.

As an additional cross-check after unblinding, the $\Xi_{c}^{+}\pi^{-}$ invariant-mass window would be restricted to (2635, 2660) MeV/c^2, corresponding to about twice the mass resolution around the mass of the $\Xi_c(2645)^0$ resonance [188], in order to evaluate a statistical significance for the resonant decay $\Xi_{cc}^{+}\to(\Xi_c(2645)^0\to\Xi_c^{+}\pi^{-})\pi^{+}$. The type of measurement performed for the $\Xi_{cc}^{+}\to\Xi_c(2645)^0\pi^{+}$ decay would depend on the evaluated significance and on the final result for the $\Xi_{cc}^{+}\to\Xi_c^{+}\pi^{-}\pi^{+}$ decay channel:

- If there would be an observation of the $\Xi_{cc}^{+}\to\Xi_c^{+}\pi^{-}\pi^{+}$ decay, the local significance for the $\Xi_{cc}^{+}\to\Xi_c(2645)^0\pi^{+}$ mode would be evaluated at that mass. Based on the result of the evaluated significance, observation (if the significance $> 5\,\sigma$), evidence (if the significance 3–5 σ) or no significant signal (if the significance $< 3\,\sigma$) for the $\Xi_{cc}^{+}\to\Xi_c(2645)^0\pi^{+}$ decay would be reported.

- If there would be an evidence for the $\Xi_{cc}^{+}\to\Xi_c^{+}\pi^{-}\pi^{+}$ decay, firstly the local significance for the $\Xi_{cc}^{+}\to\Xi_c(2645)^0\pi^{+}$ mode would be evaluated at that mass. Based on the result of the evaluated significance, evidence for the $\Xi_{cc}^{+}\to\Xi_c(2645)^0\pi^{+}$ decay would be reported as well if the local significance would be at least $3\,\sigma$. The global significance would be also evaluated, and in case it would be larger than $5\,\sigma$, observation of the $\Xi_{cc}^{+}\to\Xi_c(2645)^0\pi^{+}$ decay would be claimed. If the local significance would be below $3\,\sigma$, no significant signal would be reported.

- If there would be no significant signal seen in the $\Xi_{cc}^{+}\to\Xi_c^{+}\pi^{-}\pi^{+}$ mode, the local significance of the $\Xi_c(2645)^0\pi^{+}$ invariant-mass spectrum would be evaluated. Based on the result of the evaluated local significance, observation would be reported if the significance would be $> 6\,\sigma$. If the local significance would be below $6\,\sigma$, the decisions based on the same criteria as described in the second case would be executed.

In addition, in case there would be an evidence or observation for the $\Xi_{cc}^{+} \to \Xi_{c}(2645)^{0}\pi^{+}$ decay, the signal yield would be reported and the mass and its R with respect to the normalisation channel would be measured by re-evaluation of the corresponding efficiency ratio for the simulated candidates in that particular invariant-mass window. If there would be no signal candidates observed in the $\Xi_{cc}^{+} \to \Xi_{c}(2645)^{0}\pi^{+}$ mode but an evidence or observation for the $\Xi_{cc}^{+} \to \Xi_{c}^{+}\pi^{-}\pi^{+}$ decay, an upper limit on R would be set for the $\Xi_{cc}^{+} \to \Xi_{c}(2645)^{0}\pi^{+}$ decay at the mass where the Ξ_{cc}^{+} signal would be seen.

All of the performed cross-checks described above which are relevant to the case after unblinding are presented in the dedicated Section 7.3.4.

5.3. Summary

This chapter discussed the introduction to and the strategy for a search for the doubly charmed baryon Ξ_{cc}^{+} in the $\Xi_{cc}^{+} \to \Xi_{c}^{+}\pi^{-}\pi^{+}$ decay mode. Since the doubly charmed baryon Ξ_{cc}^{+} has not been observed yet, the complete analysis is developed without the examination of the final invariant mass from 3.3 to 3.8 GeV until the finalisation of the corresponding procedures and methods.

The analysis strategy described in this chapter aims to provide an introduction and the overall analysis approach for the studies described in the following three chapters. Firstly, Chapter 6 describes the candidate and event selection for the $\Xi_{cc}^{+} \to \Xi_{c}^{+}\pi^{-}\pi^{+}$ decay, as well as the selection for the normalisation channel $\Xi_{cc}^{++} \to \Xi_{c}^{+}\pi^{+}$ and various checks for stability of the developed selection. Chapter 7 then discusses a mass fit, a significance evaluation, and a combination of the studied decay with the $\Lambda_{c}^{+}K^{-}\pi^{+}$ final state. Lastly, the determination of the UL on R and evaluation of the corresponding systematic uncertainties relevant for the UL determination are described in detail in Chapter 8.

Chapter 6.

Event selection for the search for the doubly charmed baryon Ξ_{cc}^{+}

"There is no certainty or predictability. There is no fate. There is a choice.
My choice and yours, in each moment that demands it."
— Maria Alyokhina in her book *Riot days*

This chapter describes the event and candidate selection developed for a search for the doubly charmed baryon Ξ_{cc}^{+} in the $\Xi_{c}^{+}\pi^{-}\pi^{+}$ final state, where the Ξ_{c}^{+} candidates are reconstructed through their decay to the $pK^{-}\pi^{+}$ final state.

Firstly, the data and simulation samples used in the analysis are described in Section 6.1, followed by Section 6.2 with a detailed description of the analysis selection for the signal decay and Section 6.3 discussing the selection for the normalisation channel. A comparison of the variables for the Ξ_{cc}^{++} and Ξ_{c}^{+} baryons in the data and simulation is discussed in Section 6.4. The final remarks are summarised in Section 6.5. The selection described in this chapter is an input for the related analyses of the $\Xi_{cc}^{+}\to\Xi_{c}^{+}\pi^{-}\pi^{+}$ decay discussed in Chapters 7 and 8.

6.1. Data and simulation samples

As already mentioned in the previous section, the data collected in 2016–2018, corresponding to a total integrated luminosity of about 5.4 fb^{-1}, are used in this analysis for both the signal and the normalisation channels. The following sections describe the used data and simulation samples for the signal and normalisation modes in detail.

6.1.1. Signal channel data

A common HLT2 selection for all years is the inclusive Turbo++, where the Ξ_c^+ candidates are reconstructed in the $pK^-\pi^+$ final state. The Ξ_c^+ candidates are then combined with two companion, oppositely charged, pions. Only this HLT2 selection is included in the default trigger set. In addition, there is an exclusive Turbo line for the $\Xi_{cc}^+ \to \Xi_c^+ \pi^- \pi^+$ decay implemented in 2017 and additional MVA-based inclusive Turbo++ line for the $\Xi_c^+ \to pK^-\pi^+$ decay available in 2018. A study on the simulated data showed that the fraction of the candidates in the default set with respect to the extended trigger set is about 66% for the signal mode, and about 59% for the normalisation mode.

For the inclusive HLT2 trigger line, the WSM and WSP combinations are selected in the same way as for the signal decay using the Ξ_c^+ candidates combined with two companion pions, since the Ξ_c^+ baryon is present in all combinations and only charges of the companion pions are altered for the wrong-signed background combinations. For the exclusive HLT2 trigger line, there is a dedicated exclusive HLT2 Turbo line for the WSM combinations for the 2017–2018 data taking, but there is no corresponding trigger line for the WSP combinations, therefore the WSP samples are not considered for the background studies of the extended trigger set.

The invariant-mass distribution and the kinematic variables of the three background samples (WSM, WSP and SB) are investigated and shown to be shaped very similarly, as discussed in Sections 6.2.5 and 6.2.2. The WSM data are used as a default sample for the background studies and the MVA training, other background samples are used for cross-checks where needed.

6.1.2. Simulation for the signal channel

In the simulation, a dedicated generator GENXICC2.0 is used to produce the initial hard process leading to the $\Xi_{cc}^{+(+)}$ baryon production [179]. The GENXICC2.0 generator produces the $\Xi_{cc}^{+(+)}$ events via gluon-gluon fusion, gluon-charm collisions and charm-charm collisions based on the non-relativistic QCD framework [41]. There is only one $\Xi_{cc}^{+(+)}$ candidate per event produced in the simulation.

The mass and the lifetime of the Ξ_{cc}^{+} baryon in the simulation are set to $3621.4\,\mathrm{MeV}/c^2$ and 80 fs, respectively, based on the measured mass and lifetime of the Ξ_{cc}^{++} baryon and the theoretical predictions that suggest a similar mass and about 2–4 times shorter lifetime for its isospin partner Ξ_{cc}^{+} [35, 82, 83, 85]. The decay products of the Ξ_{cc}^{+} baryon are distributed uniformly in phase space, whereas the decays of the Ξ_{c}^{+} baryon are distributed according to a resonant model in which 55% of the Ξ_{c}^{+} decays proceed via the resonant decay $p\bar{K}^{*}(892)^{0}$ followed by the decay of the $\bar{K}^{*}(892)^{0}$ meson to the $K^{-}\pi^{+}$ final state [188]. Generator-level requirements are applied to enhance the simulation efficiency: the p_{T} of the Ξ_{cc}^{+} baryon is required to be larger than $2.5\,\mathrm{GeV}/c$, the p_{T} of all final state particles to be larger than $200\,\mathrm{MeV}/c$, and a requirement for all decay products to be in the LHCb acceptance.

The 2016 simulation sample is generated in two steps - firstly, the simulation with non-resonant Ξ_{c}^{+} decays (event type 26165851) is generated, namely 5M events are generated for each magnet polarity. However, mainly to simulate the phase space more precisely and also to be consistent with the normalisation channel $\Xi_{cc}^{++} \to \Xi_{c}^{+}\pi^{+}$ where the Ξ_{c}^{+} decays contain the resonant decay $p\bar{K}^{*}(892)^{0}$, an additional simulation sample (event type 26165854) is generated with also 5M events for each magnet polarity. This simulation sample contains the Ξ_{c}^{+} baryons that decay only via the $p\bar{K}^{*}(892)^{0}$ resonance. Those two samples are subsequently combined with the $p\bar{K}^{*}(892)^{0}$ contribution of 55% to match the value reported by the PDG [188]. Both 2017 and 2018 simulation samples are generated using event type 26165855, where both resonant and non-resonant decays with a ratio of 55:45 are included, with 5M events generated for each magnet polarity and each year. Table 6.1 summarises the event types and $p\bar{K}^{*}(892)^{0}$ resonance contribution used for the production of the simulation samples for both signal and normalisation modes.

The truth matching is done using the TRUE ID values, where each track is required to have the correct ID for its mass hypothesis and origin from the correct corresponding particle. The TRUE ID requirements used to match the $\Xi_{cc}^{+} \to (\Xi_{c}^{+} \to pK^{-}\pi^{+})\pi^{-}\pi^{+}$ decay are shown in Table 6.2. The invariant-mass distributions for different background categories for all events passing the truth-matching requirement are shown in Figure 6.1 for the 2017 simulation sample. For the candidates selected by the truth matching described in Table 6.2, only three signal and background categories

Decay mode	Year	Event type	$p\bar{K}^{*}(892)^{0}$ resonance	Number of events
$\Xi_{cc}^{+} \to \Xi_{c}^{+}\pi^{-}\pi^{+}$	2016	26165851	0%	10M
$\Xi_{cc}^{+} \to \Xi_{c}^{+}\pi^{-}\pi^{+}$	2016	26165854	100%	10M
$\Xi_{cc}^{+} \to \Xi_{c}^{+}\pi^{-}\pi^{+}$	2017	26165855	55%	10.1M
$\Xi_{cc}^{+} \to \Xi_{c}^{+}\pi^{-}\pi^{+}$	2018	26165855	55%	13.3M
$\Xi_{cc}^{++} \to \Xi_{c}^{+}\pi^{+}$	2016	26264053	55%	4M
$\Xi_{cc}^{++} \to \Xi_{c}^{+}\pi^{+}$	2017	26264053	55%	10M
$\Xi_{cc}^{++} \to \Xi_{c}^{+}\pi^{+}$	2018	26264053	55%	10M

Table 6.1.: Summary of the event types and corresponding $p\bar{K}^{*}(892)^{0}$ resonance contribution with the number of generated events for both signal and normalisation modes.

are present: the signal candidates without any intermediate resonances, the signal candidates with the intermediate resonances, and the candidates classified as low-mass background candidates. These candidates correspond to the candidates for which not all final state particles in the simulation truth decay are matched to the final state particles of the reconstructed decay and the mass of the truth parent particle is approximately $100\,\mathrm{MeV}/c^{2}$ smaller than the average mass of the candidate particle. The candidates from this category correspond to only about 3.4% of all truth-matched candidates. All three mentioned categories are included in the signal sample used to develop the event selection and to study the signal efficiencies. There is a truth-matching inefficiency related to the truth matching described above, since the matching by definition associates the reconstructed particle to the simulation particle if there is an overlap of more than 70% between their hits. As the threshold of 70% is somehow arbitrary, it introduces an inefficiency that needs to be corrected. A detailed procedure for the evaluation of this inefficiency for both the signal and normalisation modes is described in Section 8.1.8.

All mentioned simulation samples for the signal channel are used for the selection studies, however the 2016 simulation sample with the $p\bar{K}^{*}(892)^{0}$ resonance (event type 26165854) is removed from the efficiency evaluation required to determine the UL on R for the following reason. The 2016 simulation sample for the signal channel that contains the $p\bar{K}^{*}(892)^{0}$ resonance was produced with a different simulation version than the 2016 simulation for the normalisation channel. The simulation version for the signal channel simulation sample contains an incorrect description of wide resonances impacting event multiplicity and therefore the trigger response and its efficiency.

Particle	abs(ID)	abs(parent ID)
Ξ_{cc}^{+}	4412	
Ξ_{c}^{+}	4232	4412
π from Ξ_{cc}^{+}	211	4412
p from Ξ_{c}^{+}	2212	4232
K from Ξ_{c}^{+}	321	4232 or 313
π from Ξ_{c}^{+}	211	4232 or 313

Table 6.2.: Requirements for the TRUE ID values [188] in the simulation to match the $\Xi_{cc}^{+} \to \Xi_{c}^{+}\pi^{-}\pi^{+}$ decay mode.

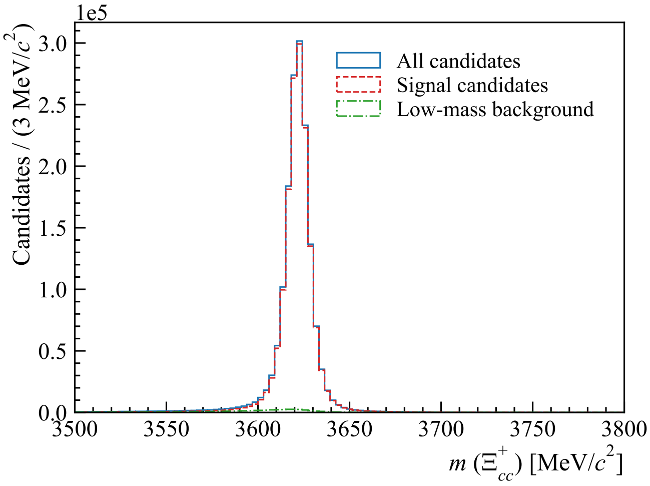

Figure 6.1.: Invariant-mass distribution of the Ξ_{cc}^{+} candidates in the 2017 simulation sample that pass the truth-matching requirements described in Table 6.2 (blue solid line), where the signal candidates (with and without any intermediate resonances) are represented by the red dashed line and the low-mass background candidates by the green dash-dotted line.

Hence the ratio of efficiencies using different simulation version for the signal and normalisation channels would be a measure of the difference between the simulation versions rather than the difference between the two modes. To have a consistent phase space model in the 2016 signal simulation sample, the invariant-mass distribution of the $K^{-}\pi^{+}$ originating from the Ξ_{c}^{+} baryon is weighted to match the $K^{-}\pi^{+}$ invariant-mass distribution of the normalisation decay mode.

6.1.3. Normalisation channel data

Regarding the normalisation channel $\Xi_{cc}^{++} \to \Xi_{c}^{+} \pi^{+}$, the reconstruction strategy for the final candidates is very similar to the signal channel described in the previous section. The Ξ_{c}^{+} candidates reconstructed in the $pK^{-}\pi^{+}$ final state are triggered either by the inclusive Turbo++ lines and are subsequently combined with one positively charged pion, or from a dedicated exclusive line for the $\Xi_{cc}^{++} \to \Xi_{c}^{+} \pi^{+}$ decay for the 2017 and 2018 data. The MVA-based inclusive line and the exclusive line for the normalisation channel are used only to cross-check the signal yield to see a potential gain of the extended trigger set, but only the Ξ_{cc}^{++} candidates passing the default trigger set requirements are used for the measurement of R to be consistent with the selection of the signal decay mode.

The wrong-signed background sample for the normalisation channel is a combination of the Ξ_{c}^{+} candidates with one negatively charged pion, referred to as the normalisation channel WSM sample. The upper side-band invariant-mass window of the right-signed candidates from 3.8 to 4.0 GeV/c^2 is the same as for the signal channel.

6.1.4. Simulation for the normalisation channel

As for the Ξ_{cc}^{+} baryon, the simulation events containing the Ξ_{cc}^{++} baryon are also produced using the GENXICC2.0 generator. The simulation samples for the $\Xi_{cc}^{++} \to \Xi_{c}^{+} \pi^{+}$ decay (event type 26264053) are generated with a lifetime of 333 fs and with a mass of 3598.97 MeV/c^2 in the 2016 sample and 3621.4 MeV/c^2 in the 2017 and 2018 samples. The lifetime of the Ξ_{cc}^{++} baryon is weighted to its measured value of 256 fs. As for the signal mode, the decay products of the Ξ_{cc}^{++} baryon are distributed uniformly in phase space, whereas the decays of the Ξ_{c}^{+} baryon are distributed according to a resonant model. Some loose requirements are placed already at the generator level in order to speed up the simulation production as in the case of the Ξ_{cc}^{+} baryon, namely all decay products are required to be in the LHCb acceptance and the minimum p_{T} of the Ξ_{cc}^{++} baryon is required to be 2 GeV. The number of generated events for each magnet polarity for 2016 is 2M, and 5M for 2017 and 2018 data samples, as summarised in Table 6.1.

The truth matching is done using TRUE ID values in the same manner as for the signal mode, the corresponding TRUE ID requirements are summarised in Table 6.3.

The same three signal and background categories as for the signal channel are present in the simulation samples for the normalisation channel after the truth matching is applied. The candidates identified as the low-mass background present about 3% of all simulation events after the truth matching, which is in good agreement with the simulation samples used for the Ξ_{cc}^{+} baryon. All three mentioned background categories are included in the signal sample used to develop the event selection and to study the selection efficiencies.

Particle	abs(ID)	abs(parent ID)
Ξ_{cc}^{++}	4422	
Ξ_{c}^{+}	4232	4422
π from Ξ_{cc}^{+}	211	4422
p from Ξ_{c}^{+}	2212	4232
K from Ξ_{c}^{+}	321	4232 or 313
π from Ξ_{c}^{+}	211	4232 or 313

Table 6.3.: Requirements for the TRUE ID values [188] in the simulation to match the $\Xi_{cc}^{++} \to \Xi_{c}^{+}\pi^{+}$ decay mode.

6.2. Event and candidate selection for the $\Xi_{cc}^{+} \to \Xi_{c}^{+}\pi^{-}\pi^{+}$ decay

The event selection in this analysis is based on four main steps: a trigger selection, an offline cut-based pre-selection, an MVA-based selection and a removal of multiple candidates.

As already mentioned, all selection studies are performed as a blinded analysis, the signal region is not saved in any used data files in order to avoid an unintentional unblinding of the signal data. The removal of multiple candidates is studied on the WSM data prior to unblinding. The same same approach is then applied to the right-signed data after unblinding. The selection is developed with the combined 2016–2018 simulation and data samples, which significantly increases the available simulation statistics for a training of the MVA classifiers. The selection for the signal channel is described in detail in Sections 6.2.1–6.2.7, whereas the selection for the normalization channel is summarised in Section 6.3.

6.2.1. Trigger selection

As described in Section 2.10, the LHCb trigger system in Run 2 consisted of the L0 trigger implemented in hardware, and two stages of the software trigger: HLT1 and HLT2. The selections applied at the individual stages of the trigger systems are discussed in the following sections.

6.2.1.1. L0 trigger

As already described in Section 5.2, there are two different trigger selections used in this analysis, namely the default and extended trigger sets, where different L0 requirements are applied.

In the extended trigger-set selection, only minimal L0 trigger requirements are applied in order to get a maximum significance of the potentially observed signal decays. The Ξ_{c}^{+} candidates have to be either triggered on signal (TOS) with respect to the L0 hadron selection, or the Ξ_{cc}^{+} candidates have to be triggered independently of signal (TIS) with respect to a collection of L0 channels (L0 hadron, muon, dimuon, electron, and photon). For the WSM sample in the invariant-mass range from 3.5 to $3.7\,\text{GeV}/c^2$, the fraction of events in the TIS category is $(77.02 \pm 0.92)\%$ and in the TOS category it is $(44.34 \pm 0.69)\%$ after the full selection is applied. These fractions were checked with the right-signed data in the invariant-mass range from 3.5 to $3.7\,\text{GeV}/c^2$ post-unblinding, where the fractions of events after the full selection in the TIS and TOS categories are $(76.15 \pm 0.29)\%$ and $(45.14 \pm 0.22)\%$, respectively.

Therefore the baseline L0 trigger selection used in the default trigger set for the first data unblinding and also for the determination of the UL on R is to consider the Ξ_{cc}^{+} candidates from the TIS category. The decision to choose only one L0 trigger category is to avoid non-trivial evaluation of their overlap in the evaluation of the associated efficiencies for the ratios between the signal and normalisation modes, since TIS and TOS are by definition not independent. The fraction of events in the L0 TIS, TOS and TIS-TOS overlap categories for the WSM, upper side-band, right-signed, and simulation data samples after all selection is applied can be found in Table 6.4. The

Sample	TIS only (%)	TIS & TOS overlap (%)	TOS only (%)
WSM (3.5–3.7 GeV/c^2)	55.66 ± 0.78	21.36 ± 0.48	22.98 ± 0.50
Upper-mass SB	59.16 ± 0.49	19.40 ± 0.28	21.44 ± 0.30
Simulation	55.21 ± 0.42	22.19 ± 0.27	22.60 ± 0.27
Right-signed (3.5–3.7 GeV/c^2)	54.86 ± 0.25	21.30 ± 0.15	23.85 ± 0.16

Table 6.4.: Fractions of candidates in the L0 TIS only, TOS only and TIS-TOS overlap categories for different samples after the full selection is applied. The three trigger categories are independent, therefore the sum of the individual fractions for each sample is 100%.

numbers for the signal region in the right-signed data were added to Table 6.4 only after unblinding. The fractions for the WSM, right-signed, and simulation samples agree with each other within their statistical uncertainties.

6.2.1.2. HLT1 trigger

The Ξ_c^+ candidates are required to be TOS with respect to the HLT1 one-track or the two-track trigger line. The detailed selection requirements of these HLT1 trigger lines are summarised in Section 3.3.1 in Table 3.2. The fractions of events in the HLT1 one-track only and two-track only categories and in their overlap for the WSM, upper SB, right-signed and simulation data after all selection is applied can be found in Table 6.5. The fractions for the signal region in the right-signed data were added to the corresponding table only after unblinding. Some non-negligible discrepancies between the fractions in the simulation and data are observed. Therefore a simulation correction to improve the agreement between the individual categories in the simulation and SB data is considered for the efficiency studies discussed in Chapter 8, which is described in detail in the dedicated Section 8.2.3.

Sample	One-track only (%)	One-track & Two-track overlap (%)	Two-track only (%)
WSM (3.5–3.7 GeV/c^2)	5.59 ± 0.25	64.33 ± 0.84	30.08 ± 0.57
Upper-mass SB	5.88 ± 0.16	61.33 ± 0.50	32.78 ± 0.37
Simulation	3.77 ± 0.11	74.04 ± 0.49	22.19 ± 0.27
Right-signed (3.5–3.7 GeV/c^2)	5.63 ± 0.08	63.67 ± 0.27	30.70 ± 0.18

Table 6.5.: Fractions of events in the HLT one-track only and two-track only categories and in their overlap for different samples after the full selection is applied. The three trigger categories are independent, therefore the sum of the individual fractions for each sample is 100%.

6.2.1.3. HLT2 trigger

As already mentioned in Section 6.1, there are three different HLT2 Turbo lines which are used in this analysis for the significance evaluation and mass measurement after the full selection is developed:

- inclusive Turbo++ line for the $\Xi_c^+ \to pK^-\pi^+$ decay used for the 2016–2018 data;
- exclusive Turbo line for the $\Xi_{cc}^+ \to \Xi_c^+\pi^-\pi^+$ decay used for the 2017 and 2018 data;
- inclusive MVA-based Turbo++ line for the $\Xi_c^+ \to pK^-\pi^+$ decay used for a subset of 2018 data.

However, for the first significance evaluation after unblinding and for the efficiency studies used for the determination of the UL on R, only events triggered by the inclusive Turbo++ line for the $\Xi_c^+ \to pK^-\pi^+$ decay are considered in order to properly evaluate the HLT2 selection efficiencies. The requirements of this Turbo++ line can be summarised as follows:

- $\Xi_c^+ \to pK^-\pi^+$ candidates are reconstructed from three tracks passing minimal p_{T}, PID and track quality requirements, with also kinematic requirements on the combinations of these tracks to further suppress a combinatorial background and promptly produced tracks;
- Ξ_c^+ candidates are also required to have a good vertex fit quality, be displaced from its PV, and point back to the PV evaluated by a minimum requirement on a direction angle (DIRA), which is the angle between the vector from the PV to the

decay vertex of the candidate and its momentum vector reconstructed from its decay products;

- Ξ_c^+ candidates are required to be inside the Ξ_c^+ invariant-mass window from 2390 to 2548 MeV/c^2.

All selection requirements for this HLT2 selection are summarised in Table 6.6. This trigger line was developed ahead of time and remained the same throughout the 2016–2018 data-taking period, therefore the same approach is followed for all studied years. This strategy is followed for both the right-signed and wrong-signed data for both the signal and normalisation channels used in this analysis.

The exclusive Turbo line for the $\Xi_{cc}^{+} \to \Xi_c^+ \pi^- \pi^+$ decay, which is used only in the extended trigger set, contains similar requirements for the Ξ_c^+ candidate as described for the inclusive line above. In addition, there are PID and kinematic requirements applied to two companion pions similar to the corresponding requirements used in the pre-selection described in the next section, which are however a bit tighter in the Turbo line than in the pre-selection, namely the p_{T} of the pions is required to be larger than 500 MeV/c. The only substantial difference with respect to the inclusive Turbo++ line is that there are no specific HLT1 requirements applied for the candidates selected by this exclusive Turbo line. The inclusive MVA-based Turbo++ line for the $\Xi_c^+ \to pK^-\pi^+$ was trained to identify the Ξ_c^+ candidates originating from any baryon decay, similarly to the Turbo++ line developed for the Ξ_c^0 baryon described in Chapter 3.

6.2.2. Cut-based pre-selection

The first stage of the offline selection is the cut-based pre-selection, which is a selection based on sequential requirements. The final pre-selection requirements are chosen based on a high signal efficiency and background rejection before the events are used in the MVA training, which is the next stage of the offline selection. Table 6.7 summarises all of the pre-selection requirements. The overall pre-selection efficiencies for the simulation data with respect to the HLT1 and HLT2 trigger selections in the default trigger set are $(88.92 \pm 0.12)\%$, $(89.33 \pm 0.14)\%$ and $(89.00 \pm 0.14)\%$ for 2016, 2017 and 2018 simulation samples, respectively (with the tracking, PID, η, p_{T} and nTracks corrections, which are considered for the efficiency evaluation and described in Section 8.1, applied). The WSM background rejection with respect to the HLT1 and

$2392\,\text{MeV}/c^2 < m(\Xi_c^+) < 2543\,\text{MeV}/c^2$		
proton, kaon, pion to have a signal in RICH		
p_{T} of proton, kaon, pion	$>$	$200\,\text{MeV}/c$
p of kaon, pion	$>$	$1000\,\text{MeV}/c$
p of proton	$>$	$10000\,\text{MeV}/c$
χ^2/ndf of proton, kaon, pion track	$<$	3
χ^2_{IP} of proton, kaon, pion	$>$	6
P_{ghost} of proton, kaon, pion track	$<$	0.4
χ^2_{vtx}/ndf of Ξ_c^+	$<$	10
DIRA of Ξ_c^+	$<$	10 mrad
lifetime of Ξ_c^+	$>$	0.00015 ns
sum of p_{T} of Ξ_c^+ decay products	$>$	$3000\,\text{MeV}/c$
p_{T} of at least one decay product of Ξ_c^+	$>$	$1000\,\text{MeV}/c$
p_{T} of at least two decay products of Ξ_c^+	$>$	$400\,\text{MeV}/c$
χ^2_{IP} of at least one decay product of Ξ_c^+	$>$	16
χ^2_{IP} of at least two decay products of Ξ_c^+	$>$	9
$\text{DLL}_{p\pi}$ & ($\text{DLL}_{p\pi}$-$\text{DLL}_{K\pi}$) for proton	$>$	5
$\text{DLL}_{K\pi}$ for pion	$<$	5
$\text{DLL}_{K\pi}$ for kaon	$>$	5

Table 6.6.: Trigger requirements for the HLT2 inclusive Turbo++ line for the $\Xi_c^+ \to pK^-\pi^+$ decay.

HLT2 trigger selection in both the default and extended trigger set is about 84% for all studied years. For both the simulation and background samples, the candidates are required to be inside the Ξ_c^+ invariant-mass window from 2450 to $2488\,\text{MeV}/c^2$, which corresponds to approximately $\pm 3\,\sigma$ region around its central PDG value of $2467.97 \pm 0.22\,\text{MeV}/c^2$ [198]. The fiducial region is defined in the same way for both the signal and normalisation modes: only the Ξ_{cc}^{+} and Ξ_{cc}^{++} candidates in the rapidity range from 2.0 to 4.5 and a p_{T} from 2.5 to $25\,\text{GeV}/c$ are considered.

The invariant-mass distributions of the Ξ_c^+ baryon in the WSM sample before and after the pre-selection requirements are applied are shown in Figure 6.2. The purity of the Ξ_c^+ signal candidates in the WSM 2017 sample in the invariant-mass window from 2450 to $2488\,\text{MeV}/c^2$ is 17.2% before and 27.6% after the pre-selection requirements are applied. However, the signal purity before the pre-selection is overestimated as

$2\,\mathrm{GeV}/c <$	p	$< 150\,\mathrm{GeV}/c$ for all tracks
$1.5 <$	η	< 5.0 for all tracks
$2.5\,\mathrm{GeV}/c <$	p_{T}	$< 25\,\mathrm{GeV}/c$ for Ξ_{cc}^{+}
$2.0 <$	η	< 4.5 for Ξ_{cc}^{+}
$2450\,\mathrm{MeV}/c^2 <$	$m(\Xi_c^+)$	$< 2488\,\mathrm{MeV}/c^2$
$\chi^2_{\mathrm{vtx}}/\mathrm{ndf}$ of Ξ_{cc}^{+}	$<$	25
χ^2_{IP} of Ξ_{cc}^{+}	$<$	25
p_{T} of Ξ_{cc}^{+}	$>$	$2500\,\mathrm{MeV}/c$
χ^2_{DTF} of Ξ_{cc}^{+}	$<$	50
p of pion from Ξ_{cc}^{+}	$>$	$2000\,\mathrm{MeV}/c$
p_{T} of pion from Ξ_{cc}^{+}	$>$	$200\,\mathrm{MeV}/c$
χ^2/ndf of pion track from Ξ_{cc}^{+}	$<$	3
ProbNN(ghost) of proton	$<$	0.9
ProbNN(ghost) of kaon	$<$	0.9
ProbNN(ghost) of pion	$<$	0.9
ProbNN(π) of pion from Ξ_{cc}^{+}	$>$	0.1
$\mathrm{DLL}_{K\pi}$ of pion from Ξ_{cc}^{+}	$<$	5

Table 6.7.: Pre-selection requirements for the $\Xi_{cc}^{+} \to \Xi_c^+ \pi^- \pi^+$ decay.

there are already a few pre-selection requirements applied at the production level of the corresponding data files so the final files are not unmanageably large.

There is one pre-selection requirement where the Decay Tree Fitter (DTF) is used [199], namely the χ^2 of a kinematic fit of the Ξ_{cc}^{+} decay chain to be less than 50. The DTF tool is used to refit the Ξ_{cc}^{+} candidates which are constrained to originate from the associated PV, which is a PV that best fits the flight direction of the reconstructed Ξ_{cc}^{+} candidate. An additional constraint on the Ξ_c^+ mass can be added to the DTF refit as it is used in one of the variables used in the MVA training described in Section 6.2.6.

The normalised invariant-mass distributions of the WSM samples for each year after the pre-selection requirements are applied are shown in Figure 6.3, where a good agreement between the years can be observed. Figure 6.4 shows the WSP, WSM and SB distributions for all studied years outside of the blinded region, which are also in

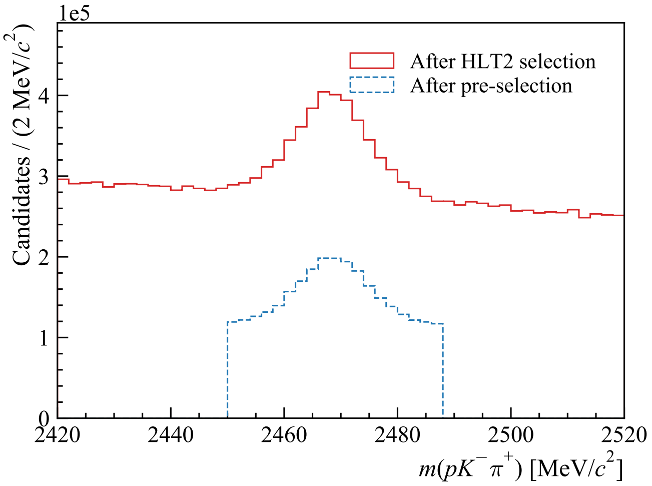

Figure 6.2.: Invariant-mass distribution of the Ξ_c^+ baryon in the 2017 WSM sample before (red solid line) and after (blue dashed line) the pre-selection requirements are applied.

good agreement. Moreover, no peaking structures are observed in any of the studied background samples after the pre-selection.

Apart from the use of the $\mathrm{DLL}_{X\pi}$ variables in the trigger and pre-selection already described in Chapter 3 on page 66, the PID requirements on the hadrons which are applied in the pre-selection include the ProbNN variables [200]. The ProbNN variables are based on a neural network trained to identify protons, kaons, pions, electrons, muons, and ghost tracks, using also information from the tracking stations in addition to the information from the RICH detectors, the calorimeters, and the muon stations. The restrictions on the ProbNN variables help to increase the purity of the signal as well as remove the ghost tracks.

All PID requirements that are applied in the pre-selection are directly applied for the data samples. However, the PID information is not well reproduced in the simulation, since it is difficult to precisely model the occupancy of the RICH detectors and also other conditions sensitively affecting the refractive index, for example the pressure or temperature. Therefore a data-driven calibration based on the LHCb software package PIDCalib [189, 201, 202] is used for the simulation samples to generate the efficiency weights for the corresponding PID requirements in order to make the PID variables in the simulation samples more similar to their distribution in the data. The obtained PID weights are used for the PID selection in the simulation instead of a direct application of the PID requirements, and also for a determination of the PID efficiencies discussed in Section 8.1.5. The PID corrections are determined in intervals of p and η from

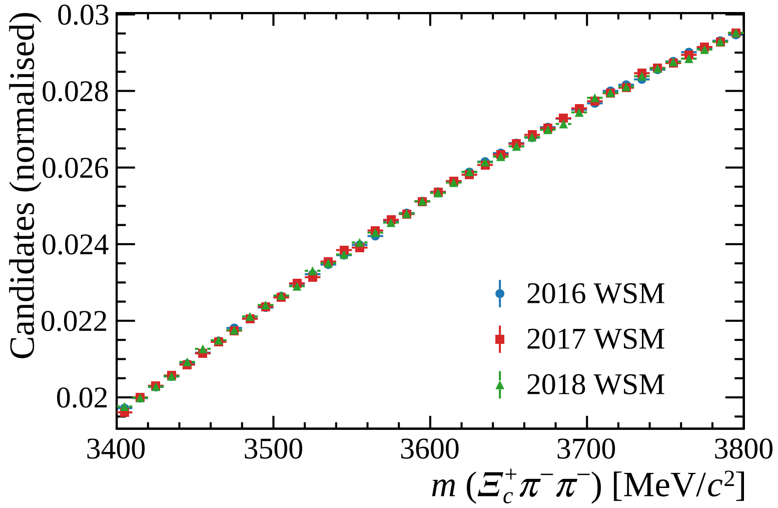

Figure 6.3.: Comparison of the normalised $\Xi_c^+\pi^-\pi^-$ invariant-mass distribution in 2016 (blue circles), 2017 (red squares) and 2018 (green triangles) WSM data samples after the pre-selection requirements are applied.

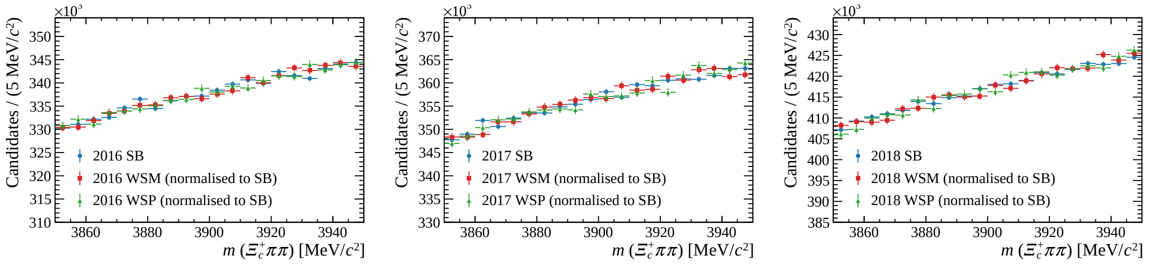

(a) **(b)** **(c)**

Figure 6.4.: Comparison of 20% of the signal SB (blue circles), WSM (red squares) and WSP (green triangles) invariant-mass distributions in the upper SB mass window for (a) 2016, (b) 2017 and (c) 2018 data after the pre-selection requirements are applied. The WSM and WSP distributions are normalised to the one of the SB.

calibration samples. Table 6.8 shows the binning schemes used to obtain the PID weights for both the signal and normalisation channels. All tracks are also required to have a momentum between 2 and 150 GeV and be in a pseudorapidity range from 1.5 to 5 in order to distinguish between signatures of different particle species in the RICH detector. Only very loose pre-selection PID requirements are chosen based on the tests of the signal efficiency. A tighter PID selection is studied after the MVA selection, as described in Sections 6.2.6.1 and 6.3.2.

Variable	Binning scheme
p [GeV/c]	(2.0; 5.6; 9.2; 12.8; 16.4; 20.0; 26.0; 32.0; 38.0; 44.0; 50.0; 56.0; 62.0; 68.0; 74.0; 80.0; 90.0; 100.0; 110.0; 120.0; 150.0)
η	(1.5; 2.25; 2.5; 2.75; 3; 3.25; 3.5; 3.75; 4.0; 4.5; 5)

Table 6.8.: Binning schemes for the PID variables in the p and η space used to obtain the PID efficiencies using the PIDCalib package.

6.2.3. Veto to remove misidentified background

After the pre-selection requirements are applied, the invariant-mass distributions of the final state particles originating from the Ξ_c^+ vertex with changed mass hypothesis are checked in the WSM data in order to recognise any misidentified particle species. In particular, the dominant misidentification (mis-ID) is found when the proton mass hypothesis is changed to be that of a pion or kaon. The re-calculated invariant-mass distributions for the 2017 WSM data after the mass hypothesis of the proton is changed is shown in Figure 6.5.

The dominant peak in the $K^-\pi^+\pi^+$ invariant-mass spectrum is the D^+ meson at 1870 MeV/c^2. In the $K^+K^-\pi^+$ spectrum, the dominant peak is the same peak of the D^+ meson, reflected under $p \to \pi^+ \to K^+$ mis-ID. This misidentified background can be easily removed by an explicit veto for rejecting all candidates in a tight mass window around the two main misidentified peaks in the $K^-\pi^+\pi^+$ and $K^+K^-\pi^+$ spectra for both the signal and normalisation modes. The veto removes around 20% of the background while keeping a high signal efficiency of around 95% to allow the next stage of the selection based on a multivariate selector to focus on more difficult backgrounds. Therefore the vetoes of (1850,1890) MeV/c^2 in the $K^-\pi^+\pi^+$ invariant-mass spectrum and (2025,2060) MeV/c^2 in the $K^+K^-\pi^+$ invariant-mass spectrum are applied before the MVA selection.

6.2.4. Correction of the kinematic variables in simulation

After the observation of the doubly charmed baryon Ξ_{cc}^{++} in the $\Xi_{cc}^{++} \to \Lambda_c^+ K^-\pi^+\pi^+$ decay, evaluation of the simulation samples produced using the GENXICC2.0 generator was performed. It was observed that the p_{T} and η distributions of the Ξ_{cc}^{++} baryon are not modelled well by the generator. The underlying reason for the ob-

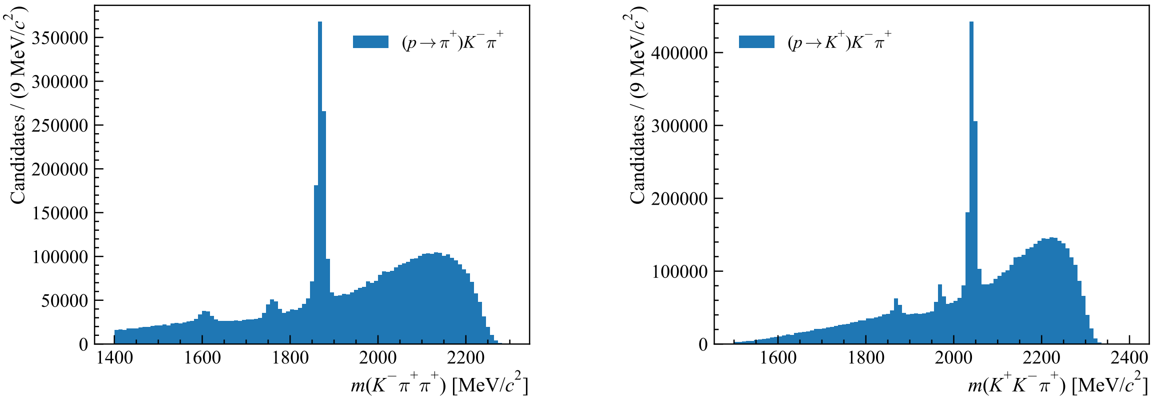

(a) **(b)**

Figure 6.5.: Invariant-mass distribution of the $pK^-\pi^+$ final state, where a proton mass hypothesis is changed for that of (a) a pion or (b) a kaon, for the signal channel 2017 WSM data after the pre-selection requirements are applied.

served discrepancy is not yet understood, even though it has been studied within LHCb. Moreover, the number of tracks (nTracks) is generally not well modelled in simulation, therefore a correction is needed for the corresponding distribution as well. Therefore a multidimensional weighting procedure is developed to simultaneously correct for discrepancies in the mentioned variables where a disagreement between the simulation and data is most visible, namely the p_{T}, η and nTracks distributions.

The weighting procedure is using the Gradient Boosted Reweighter (GBR) algorithm from the hep_ml package [203], which is based on an ensemble of regression trees, so it can be used for multidimensional weighting. The 2016–2018 simulation and s-weighted data [204] for the $\Xi_{cc}^{++}\rightarrow\Lambda_c^+K^-\pi^+\pi^+$ and $\Xi_{cc}^{++}\rightarrow\Xi_c^+\pi^+$ decay channels are used in order to train the GBR to match the distribution of variables in simulation to those in data. The technique of s-weights allows to discriminate between a signal and background distribution of the control variables given the signal and background candidates can be distinguished with some discriminant variable. The discriminant variable in this case is the invariant-mass distribution of the Ξ_{cc}^{++} candidates. Each candidate is assigned a corresponding s-weight based on the mass fit, and the s-weights are subsequently used to obtain the p_{T}, η and nTracks distributions of the signal candidates. The selection for the $\Xi_{cc}^{++}\rightarrow\Lambda_c^+K^-\pi^+\pi^+$ channel is the same as described in reference [78], where a precise measurement of the Ξ_{cc}^{++} mass is discussed. The selection for the $\Xi_{cc}^{++}\rightarrow\Xi_c^+\pi^+$ mode is the same as described in Section 6.3, only without the use of any kinematic correction. The parameters used to train the GBR can be found in Table 6.9. As the Ξ_{cc}^{++} and Ξ_{cc}^{+} baryons are isospin partners, they are

Parameter name	Description	Set value
n_estimators	number of trees	70
learning_rate	size of step	0.1
max_depth	maximal depth of trees	3
min_samples_leaf	minimal number of events in the leaf	80
loss_regularization	number of events that algorithm puts in each leaf	8
subsample	fraction of data to use on each stage	0.9

Table 6.9.: Parameters used in the GBR to simultaneously correct for discrepancies in the p_{T}, η and nTracks distributions between the simulation and data.

expected to have similar production p_{T} and η spectra, therefore the trained GBR is applied to all simulation samples for both the signal and normalisation decay modes to obtain the corresponding correction weights. Those weights are subsequently used in the MVA training described in Section 6.2.6 and also for the efficiency evaluation described in Chapter 8.

Figures 6.6, 6.7 and 6.8 show the normalised p_{T}, η and nTracks distributions for the 2016–2018 simulation samples before and after the GBR weighting and the s-weighted data for the combined $\Xi_{cc}^{++} \to \Lambda_c^{+} K^{-} \pi^{+} \pi^{+}$ and $\Xi_{cc}^{++} \to \Xi_c^{+} \pi^{+}$ decay channels. All distributions in the simulation agree with the corresponding distributions in data better after the weighting procedure. A comparison of ratios of data and simulation with their statistical uncertainties before and after the weights obtained from the GBR are applied in several p_{T}, η and nTracks bins can be found in Tables 6.10, 6.11 and 6.12, respectively. After the weighting procedure, all ratios are compatible with one within their statistical uncertainties.

p_{T} bin [MeV/c]	Data/simulation before weighting	Data/simulation after weighting
(2500, 5000)	1.34 ± 0.28	1.02 ± 0.21
[5000, 7000)	1.25 ± 0.12	1.03 ± 0.10
[7000, 9000)	1.14 ± 0.09	1.03 ± 0.08
[9000, 11000)	0.90 ± 0.09	0.93 ± 0.09
[11000, 13000)	0.80 ± 0.10	0.98 ± 0.12
[13000, 15000)	0.72 ± 0.12	0.93 ± 0.15
[15000, 19000)	0.63 ± 0.12	0.95 ± 0.18
[19000, 25000)	0.67 ± 0.21	1.17 ± 0.36

Table 6.10.: Ratios of data and simulation with their statistical uncertainties before and after the GBR weighting procedure in several p_{T} bins.

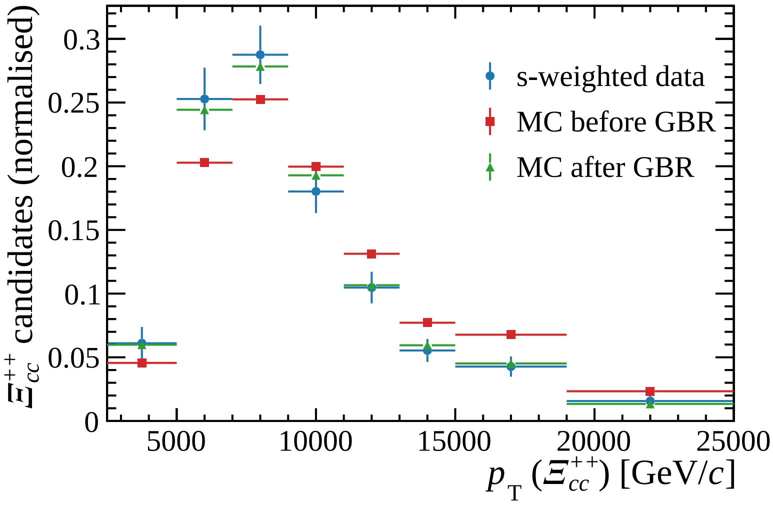

Figure 6.6.: Normalised p_{T} distribution for the s-weighted data (blue circles) from combined $\Xi_{cc}^{++} \to \Lambda_c^+ K^- \pi^+ \pi^+$ and $\Xi_{cc}^{++} \to \Xi_c^+ \pi^+$ decay channels and corresponding simulation data before (red squares) and after (green triangles) the weights obtained from the GBR are applied.

η bin	Data/simulation before weighting	Data/simulation after weighting
(2.0, 2.5)	0.60 $\pm$ 0.12	0.96 $\pm$ 0.19
[2.5, 3.0)	0.97 $\pm$ 0.07	0.99 $\pm$ 0.07
[3.0, 3.5)	1.08 $\pm$ 0.07	1.00 $\pm$ 0.06
[3.5, 4.5)	1.08 $\pm$ 0.11	1.03 $\pm$ 0.11

Table 6.11.: Ratios of data and simulation with their statistical uncertainties before and after the GBR weighting procedure in several η bins.

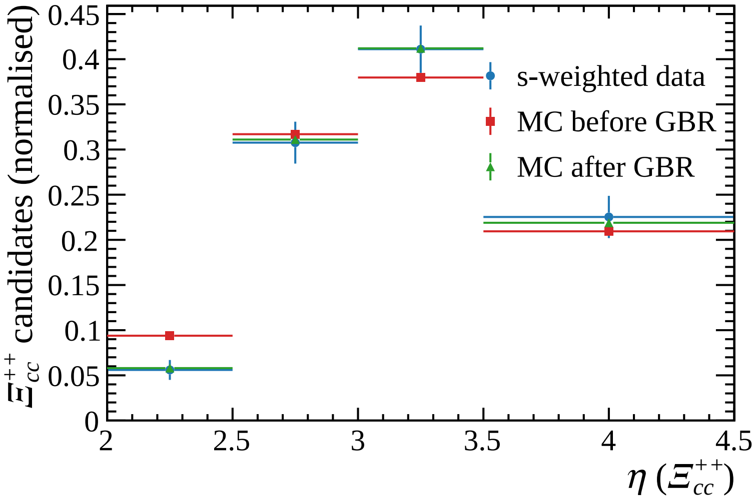

Figure 6.7.: Normalised η distribution for the s-weighted data (blue circles) from combined $\Xi_{cc}^{++} \to \Lambda_c^+ K^- \pi^+ \pi^+$ and $\Xi_{cc}^{++} \to \Xi_c^+ \pi^+$ decay channels and corresponding simulation data before (red squares) and after (green triangles) the weights obtained from the GBR are applied.

nTracks bin	Data/simulation before weighting	Data/simulation after weighting
(0, 25)	0.46 $\pm$ 0.09	0.99 $\pm$ 0.19
[25, 40)	0.77 $\pm$ 0.07	0.94 $\pm$ 0.09
[40, 55)	1.23 $\pm$ 0.09	1.01 $\pm$ 0.07
[55, 70)	1.38 $\pm$ 0.11	1.08 $\pm$ 0.09
[70, 85)	0.89 $\pm$ 0.14	0.92 $\pm$ 0.15
[85, 200)	0.69 $\pm$ 0.16	0.94 $\pm$ 0.21

Table 6.12.: Ratios of data and simulation with their statistical uncertainties before and after the GBR weighting procedure in several nTracks bins.

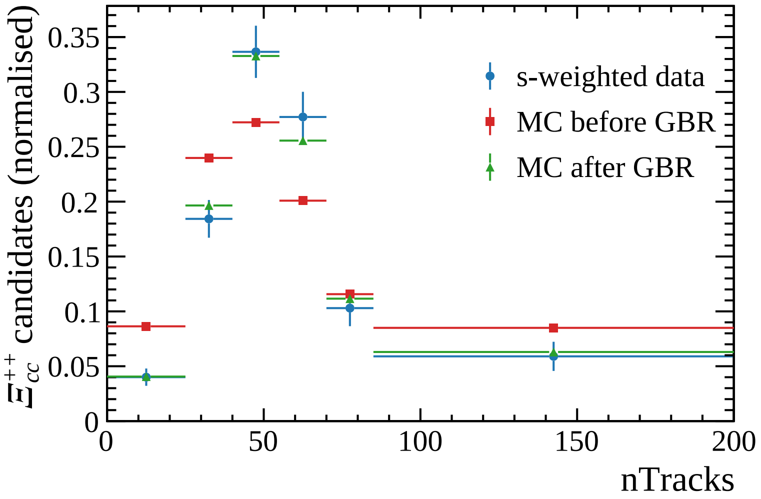

Figure 6.8.: Normalised nTracks distribution for the s-weighted data (blue circles) from combined $\Xi_{cc}^{++} \to \Lambda_c^+ K^- \pi^+ \pi^+$ and $\Xi_{cc}^{++} \to \Xi_c^+ \pi^+$ decay channels and corresponding simulation data before (red squares) and after (green triangles) the weights obtained from the GBR are applied.

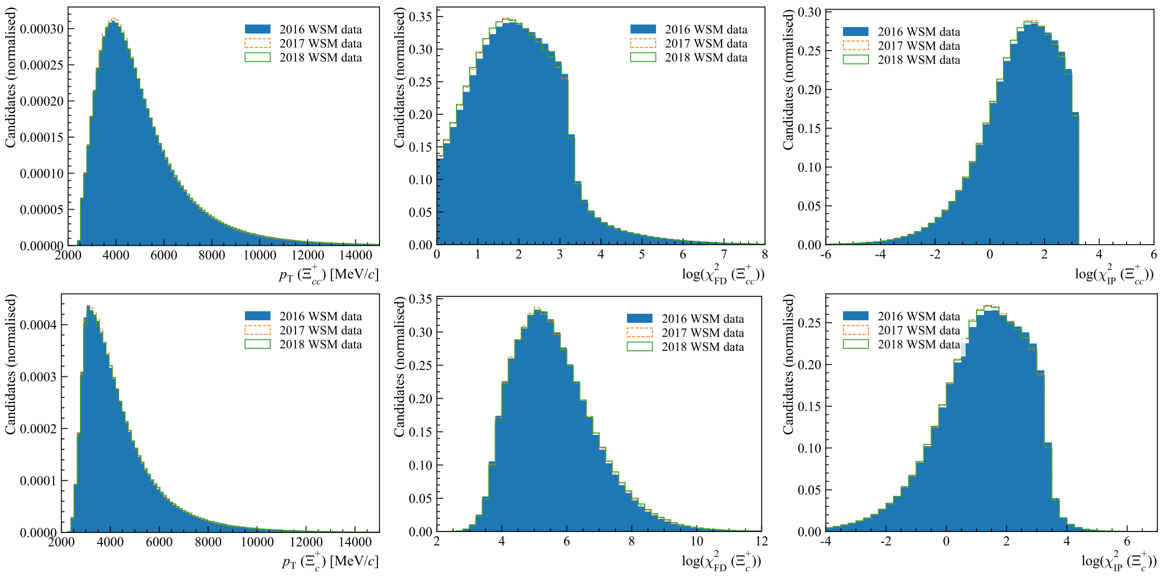

Figure 6.9.: Comparison of distributions for several kinematic variables for 2016 (blue area), 2017 (orange dashed line) and 2018 (green solid line) WSM data for the Ξ_{cc}^{+} (top) and Ξ_{c}^{+} (bottom) baryons from the $\Xi_{cc}^{+} \to \Xi_{c}^{+}\pi^{-}\pi^{+}$ decay after the HLT2 and pre-selections requirements are applied.

6.2.5. Comparison of 2016, 2017 and 2018 data and simulation

Since the HLT2 selection for the inclusive Turbo++ line which is used in the MVA training remained the same throughout the 2016–2018 data-taking period, the strategy for the $\Xi_{cc}^{+} \to \Xi_{c}^{+}\pi^{-}\pi^{+}$ selection is to combine all available signal simulation samples and train only one MVA with approximately three times more signal statistics than it would be in case each year was trained separately. This approach is beneficial for the MVA training as the overtraining risk is significantly lower when a higher number of events is available at the training stage, as well as an improved MVA performance can be expected with larger training samples. The data and simulation samples are therefore compared within the studied years to check for any potential discrepancies impacting the combination of the samples. Some distributions of the Ξ_{cc}^{+} and Ξ_{c}^{+} kinematic variables after the HLT1, HLT2 and pre-selection requirements applied to the WSM data can be found in Figure 6.9 and applied to the simulation samples are found in Figure 6.10. A comparison of more variables and also distributions for the WSP and SB samples can be found in Appendix A. A good agreement between all studied years is observed, therefore the joined strategy for all years, as described above, is followed.

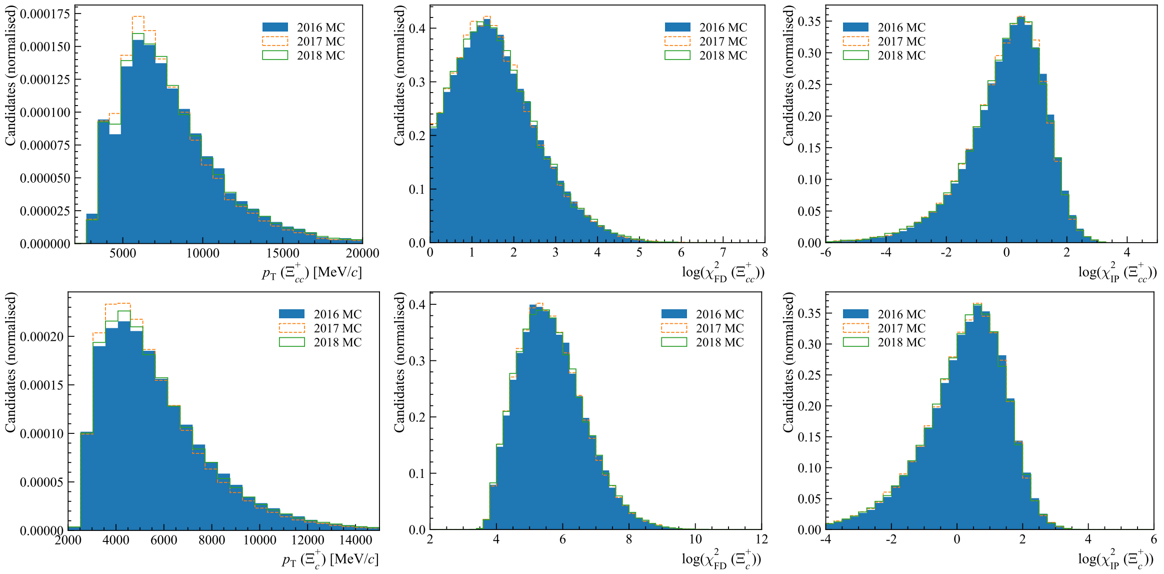

Figure 6.10.: Comparison of distributions for several kinematic variables for 2016 (blue area), 2017 (orange dashed line) and 2018 (green solid line) simulation data for the Ξ_{cc}^{+} (top) and Ξ_{c}^{+} (bottom) baryons from the $\Xi_{cc}^{+} \to \Xi_{c}^{+} \pi^{-} \pi^{+}$ decay after the HLT2 and pre-selections requirements are applied.

6.2.6. MVA based selection

In order to further suppress the combinatorial background and to get a higher signal purity, which is essential for a signal observation, the second step of the offline selection is an MVA based selection developed using the TMVA package [190] with ROOT version 6.16.00 [174]. To train the MVA classifier, the 2016–2018 simulation samples are used as a signal proxy. The MVA training is performed using the simulation samples after the momentum rescaling, the PIDCalib weighting and the kinematic weighting, which are applied subsequently in that order. A momentum-rescaling correction [205,206] is applied to the momentum of charged particles using $J/\psi \to \mu^{+}\mu^{-}$ and $B^{+} \to J/\psi K^{+}$ decays. To represent the background, the WSM combinations in the invariant-mass region from 3500 to 3700 MeV/c^2 are used. Due to the large data statistics, only a randomly chosen subset corresponding to 5% of the total WSM data sample for each year is used in the training. Only the candidates from the inclusive HLT2 Turbo++ trigger line which passed either the L0 TIS or TOS requirement described in Section 6.2.1.1 and all pre-selection requirements are used for the MVA training.

Both signal and background samples are randomly split into two sub-samples: two thirds of the events are used for training, and one third is used for testing of the trained MVA classifier. The number of signal events used in the MVA training and testing is about 258k and the number of WSM background events about 3.7M. Table 6.13 shows the number of events used in the MVA for both signal and normalisation modes for each year separately. The background events are automatically weighted down in the MVA to match the number of signal events in order to keep the same weight for the signal and background samples in the training. Several different combinations of the input variable sets for the MVA training were tested to evaluate the optimal set to use in the MVA selection. The variables were ranked according to their discriminating power and only the ones with a low correlation are used in the final MVA selection. Table 6.14 shows a list of the final set of 15 variables together with their separation power $\langle S^2 \rangle$, which for a classifier y is defined as

$$\langle S^2 \rangle = \frac{1}{2} \int \frac{(\hat{y}_S(y) - \hat{y}_B(y))^2}{\hat{y}_S(y) + \hat{y}_B(y)} dy, \tag{6.1}$$

where $\hat{y}_S$ and $\hat{y}_B$ are the signal and background distributions of y, normalised to unity. It is clear that the separation is zero for identical signal and background shapes, and it is one for shapes with no overlap. The distributions of the variables used in the MVA training for the signal and background are shown in Figure 6.11. The corresponding distributions after the optimal MVA threshold is applied can be found in Appendix B.2, where one can see that only background with a similar distribution to the signal passed the MVA threshold, as expected. The correlation matrices for the final set of variables are shown in Figure 6.12 for the signal events and in Figure 6.13 for the background events. One can see that only variables with either low correlation values or with different correlations between the signal and background samples are used.

Several different MVA classification algorithms are compared for the purpose of this analysis, *e.g.* Boosted Decision Trees (BDT) [191], Boosted Decision Trees with gradient boosting (BDTG) [207], Boosted Decision Trees with decorrelation and adaptive boost (BDTD) [208], Multilayer perceptron (MLP) [209], and Multilayer perceptron with Broyden-Fletcher-Goldfarb-Shanno training method and Bayesian regulator (MLPBNN) [209]. In addition, the gradient boosting algorithm from the Python library XGBoost [210] is used as an additional cross-check and complementary method to the TMVA package. The same set of variables and training samples are used. The overtraining checks for all used classifiers are shown in Figure 6.14. The MVA response of different classifiers for the signal channel samples for each year can be found in Appendix B.1.

	Simulation			WSM data		
	2016	2017	2018	2016	2017	2018
signal mode	108 401	72 162	77 763	1 131 855	1 191 757	1 383 382
normalisation mode	22 854	93 546	75 516	391 304	415 310	463 956

Table 6.13.: Number of simulation and WSM events used in the MVA training and testing for both the signal ($\Xi_{cc}^{+} \to \Xi_{c}^{+}\pi^{-}\pi^{+}$) and normalisation ($\Xi_{cc}^{++} \to \Xi_{c}^{+}\pi^{+}$) modes and for each year.

Variable	Separation
sum of p_{T} of pions from Ξ_{cc}^{+}	0.418
$\log(\chi^2_{\mathrm{vtx}}/\mathrm{ndf}$ of $\Xi_{cc}^{+})$ with Ξ_{c}^{+} mass and Ξ_{cc}^{+} PV constraints	0.317
(p_{T} of Ξ_{c}^{+}) / (sum of p_{T} of Ξ_{cc}^{+} decay products)	0.256
max DOCA between any pair of Ξ_{cc}^{+} decay products	0.222
$\log(\chi^2_{\mathrm{IP}}$ of $\Xi_{cc}^{+})$	0.219
$\log(\chi^2_{\mathrm{IP}}$ of $\Xi_{c}^{+})$	0.190
(χ^2_{IP} of Ξ_{c}^{+}) / (sum of χ^2_{IP} of Ξ_{cc}^{+} decay products)	0.130
max DOCA between any pair of Ξ_{c}^{+} decay products)	0.119
$\chi^2_{\mathrm{vtx}}/\mathrm{ndf}$ of Ξ_{c}^{+}	0.116
DIRA of Ξ_{cc}^{+}	0.106
sum of p_{T} of Ξ_{c}^{+} decay products	0.105
(p of proton from Ξ_{c}^{+}) / (sum of p of Ξ_{c}^{+} decay products)	0.100
$\log(\chi^2_{\mathrm{vtx}}/\mathrm{ndf}$ of $\Xi_{cc}^{+})$	0.050
$\log(\chi^2_{\mathrm{FD}}$ of $\Xi_{cc}^{+})$	0.048
$\log(\chi^2_{\mathrm{FD}}$ of $\Xi_{c}^{+})$	0.033

Table 6.14.: List of variables used in the MVA selection for the $\Xi_{cc}^{+} \to \Xi_{c}^{+}\pi^{-}\pi^{+}$ decay ordered by their separation power. The separation is one for shapes with no overlap, and it is zero for identical shapes.

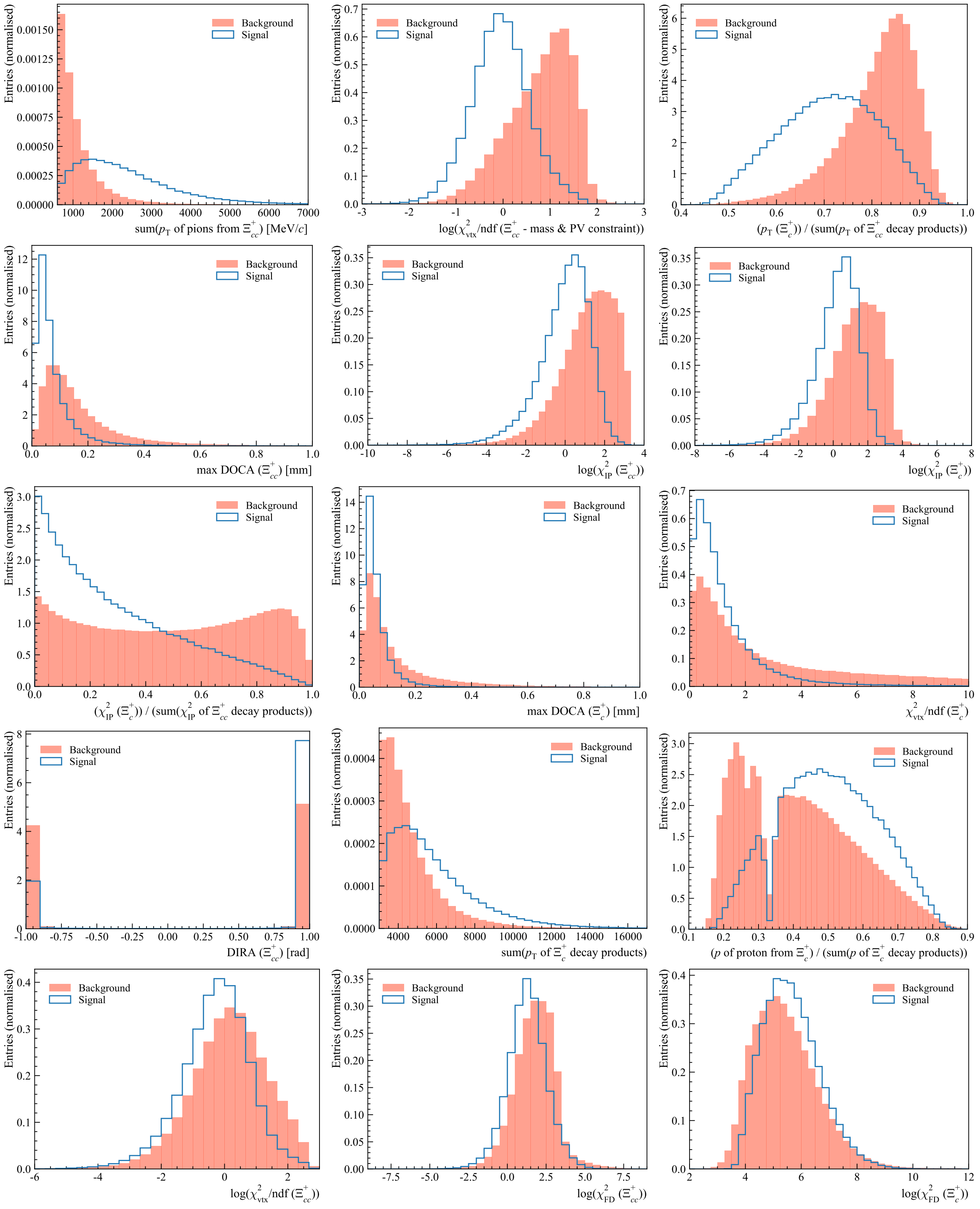

Figure 6.11.: Distributions of the final set of 15 variables used in the MVA training for the signal sample (blue line) and the background (red area) represented by the WSM sample, ordered by their separation power as shown in Table 6.14.

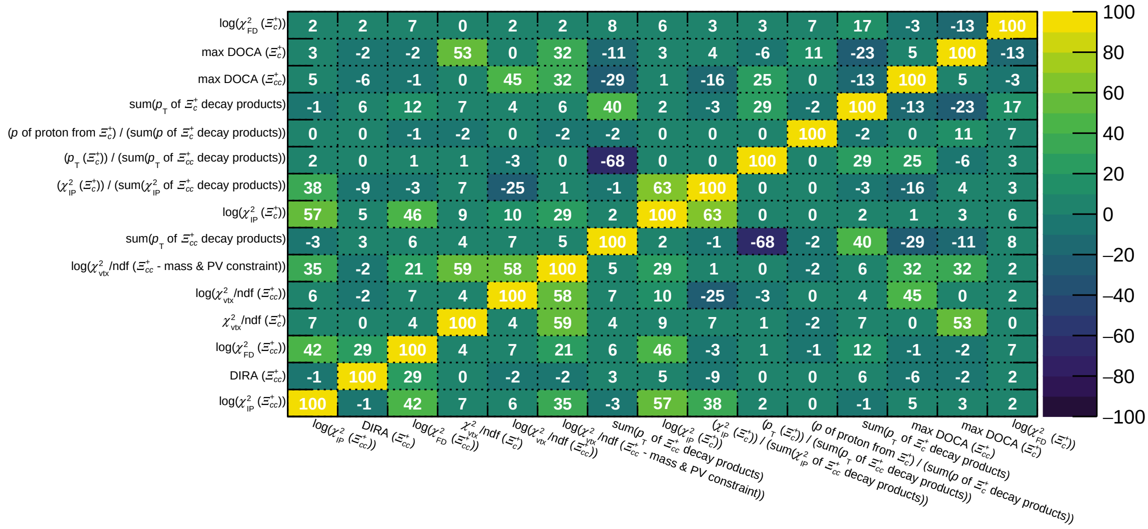

	log(χ^2_{IP} (Ξ_{cc}^+))	DIRA (Ξ_{cc}^+)	log(χ^2_{FD} (Ξ_{cc}^+))	χ^2_{vtx}/ndf (Ξ_c^+)	log(χ^2_{vtx}/ndf (Ξ_{cc}^+))	log(χ^2_{vtx}/ndf (Ξ_{cc}^+ - mass & PV constraint))	sum(p_{T} of Ξ_{cc}^+ decay products)	log(χ^2_{IP} (Ξ_c^+))	(χ^2_{IP} (Ξ_c^+)) / (sum(χ^2_{IP} of Ξ_{cc}^+ decay products))	(p_{T} (Ξ_c^+)) / (sum(p_{T} of Ξ_{cc}^+ decay products))	(p of proton from Ξ_c^+) / (sum(p of Ξ_c^+ decay products))	sum(p_{T} of Ξ_c^+ decay products)	max DOCA (Ξ_{cc}^+)	max DOCA (Ξ_c^+)	log(χ^2_{FD} (Ξ_c^+))
log(χ^2_{FD} (Ξ_c^+))	2	2	7	0	2	2	8	6	3	3	7	17	-3	-13	100
max DOCA (Ξ_c^+)	3	-2	-2	53	0	32	-11	3	4	-6	11	-23	5	100	-13
max DOCA (Ξ_{cc}^+)	5	-6	-1	0	45	32	-29	1	-16	25	0	-13	100	5	-3
sum(p_{T} of Ξ_c^+ decay products)	-1	6	12	7	4	6	40	2	-3	29	-2	100	-13	-23	17
(p of proton from Ξ_c^+) / (sum(p of Ξ_c^+ decay products))	0	0	-1	-2	0	-2	-2	0	0	0	100	-2	0	11	7
(p_{T} (Ξ_c^+)) / (sum(p_{T} of Ξ_{cc}^+ decay products))	2	0	1	1	-3	0	-68	0	0	100	0	29	25	-6	3
(χ^2_{IP} (Ξ_c^+)) / (sum(χ^2_{IP} of Ξ_{cc}^+ decay products))	38	-9	-3	7	-25	1	-1	63	100	0	0	-3	-16	4	3
log(χ^2_{IP} (Ξ_c^+))	57	5	46	9	10	29	2	100	63	0	0	2	1	3	6
sum(p_{T} of Ξ_{cc}^+ decay products)	-3	3	6	4	7	5	100	2	-1	-68	-2	40	-29	-11	8
log(χ^2_{vtx}/ndf (Ξ_{cc}^+ - mass & PV constraint))	35	-2	21	59	58	100	5	29	1	0	-2	6	32	32	2
log(χ^2_{vtx}/ndf (Ξ_{cc}^+))	6	-2	7	4	100	58	7	10	-25	-3	0	4	45	0	2
χ^2_{vtx}/ndf (Ξ_c^+)	7	0	4	100	4	59	4	9	7	1	-2	7	0	53	0
log(χ^2_{FD} (Ξ_{cc}^+))	42	29	100	4	7	21	6	46	-3	1	-1	12	-1	-2	7
DIRA (Ξ_{cc}^+)	-1	100	29	0	-2	-2	3	5	-9	0	0	6	-6	-2	2
log(χ^2_{IP} (Ξ_{cc}^+))	100	-1	42	7	6	35	-3	57	38	2	0	-1	5	3	2

Figure 6.12.: Correlation matrix for the MVA variables for the signal sample. The linear correlation coefficients in the matrix are given in %.

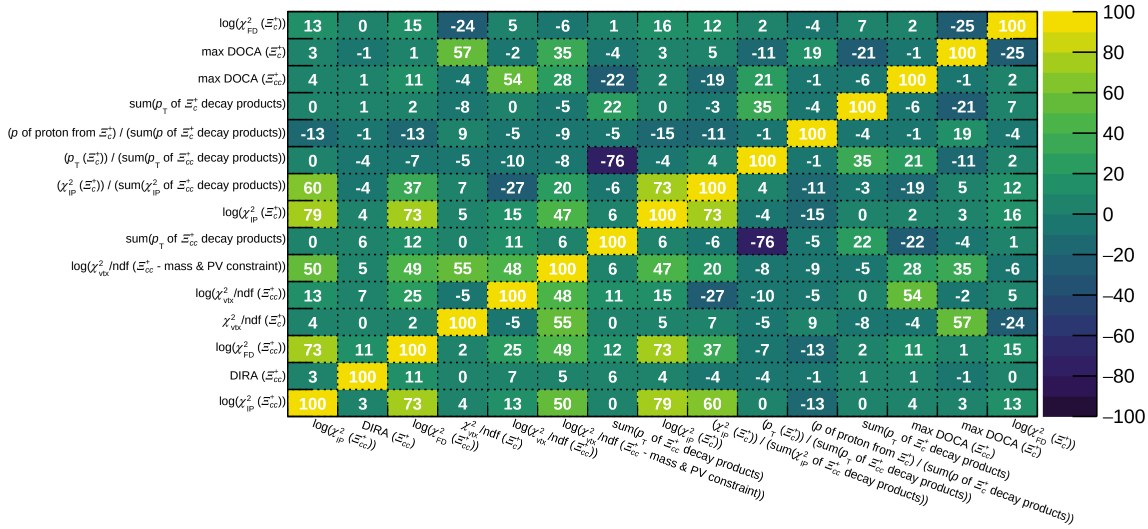

	log(χ^2_{IP} (Ξ_{cc}^+))	DIRA (Ξ_{cc}^+)	log(χ^2_{FD} (Ξ_{cc}^+))	χ^2_{vtx}/ndf (Ξ_c^+)	log(χ^2_{vtx}/ndf (Ξ_{cc}^+))	log(χ^2_{vtx}/ndf (Ξ_{cc}^+ - mass & PV constraint))	sum(p_{T} of Ξ_{cc}^+ decay products)	log(χ^2_{IP} (Ξ_c^+))	(χ^2_{IP} (Ξ_c^+)) / (sum(χ^2_{IP} of Ξ_{cc}^+ decay products))	(p_{T} (Ξ_c^+)) / (sum(p_{T} of Ξ_{cc}^+ decay products))	(p of proton from Ξ_c^+) / (sum(p of Ξ_c^+ decay products))	sum(p_{T} of Ξ_c^+ decay products)	max DOCA (Ξ_{cc}^+)	max DOCA (Ξ_c^+)	log(χ^2_{FD} (Ξ_c^+))
log(χ^2_{FD} (Ξ_c^+))	13	0	15	-24	5	-6	1	16	12	2	-4	7	2	-25	100
max DOCA (Ξ_c^+)	3	-1	1	57	-2	35	-4	3	5	-11	19	-21	-1	100	-25
max DOCA (Ξ_{cc}^+)	4	1	11	-4	54	28	-22	2	-19	21	-1	-6	100	-1	2
sum(p_{T} of Ξ_c^+ decay products)	0	1	2	-8	0	-5	22	0	-3	35	-4	100	-6	-21	7
(p of proton from Ξ_c^+) / (sum(p of Ξ_c^+ decay products))	-13	-1	-13	9	-5	-9	-5	-15	-11	-1	100	-4	-1	19	-4
(p_{T} (Ξ_c^+)) / (sum(p_{T} of Ξ_{cc}^+ decay products))	0	-4	-7	-5	-10	-8	-76	-4	4	100	-1	35	21	-11	2
(χ^2_{IP} (Ξ_c^+)) / (sum(χ^2_{IP} of Ξ_{cc}^+ decay products))	60	-4	37	7	-27	20	-6	73	100	4	-11	-3	-19	5	12
log(χ^2_{IP} (Ξ_c^+))	79	4	73	5	15	47	6	100	73	-4	-15	0	2	3	16
sum(p_{T} of Ξ_{cc}^+ decay products)	0	6	12	0	11	6	100	6	-6	-76	-5	22	-22	-4	1
log(χ^2_{vtx}/ndf (Ξ_{cc}^+ - mass & PV constraint))	50	5	49	55	48	100	6	47	20	-8	-9	-5	28	35	-6
log(χ^2_{vtx}/ndf (Ξ_{cc}^+))	13	7	25	-5	100	48	11	15	-27	-10	-5	0	54	-2	5
χ^2_{vtx}/ndf (Ξ_c^+)	4	0	2	100	-5	55	0	5	7	-5	9	-8	-4	57	-24
log(χ^2_{FD} (Ξ_{cc}^+))	73	11	100	2	25	49	12	73	37	-7	-13	2	11	1	15
DIRA (Ξ_{cc}^+)	3	100	11	0	7	5	6	4	-4	-4	-1	1	1	-1	0
log(χ^2_{IP} (Ξ_{cc}^+))	100	3	73	4	13	50	0	79	60	0	-13	0	4	3	13

Figure 6.13.: Correlation matrix for the MVA variables for the background sample. The linear correlation coefficients in the matrix are given in %.

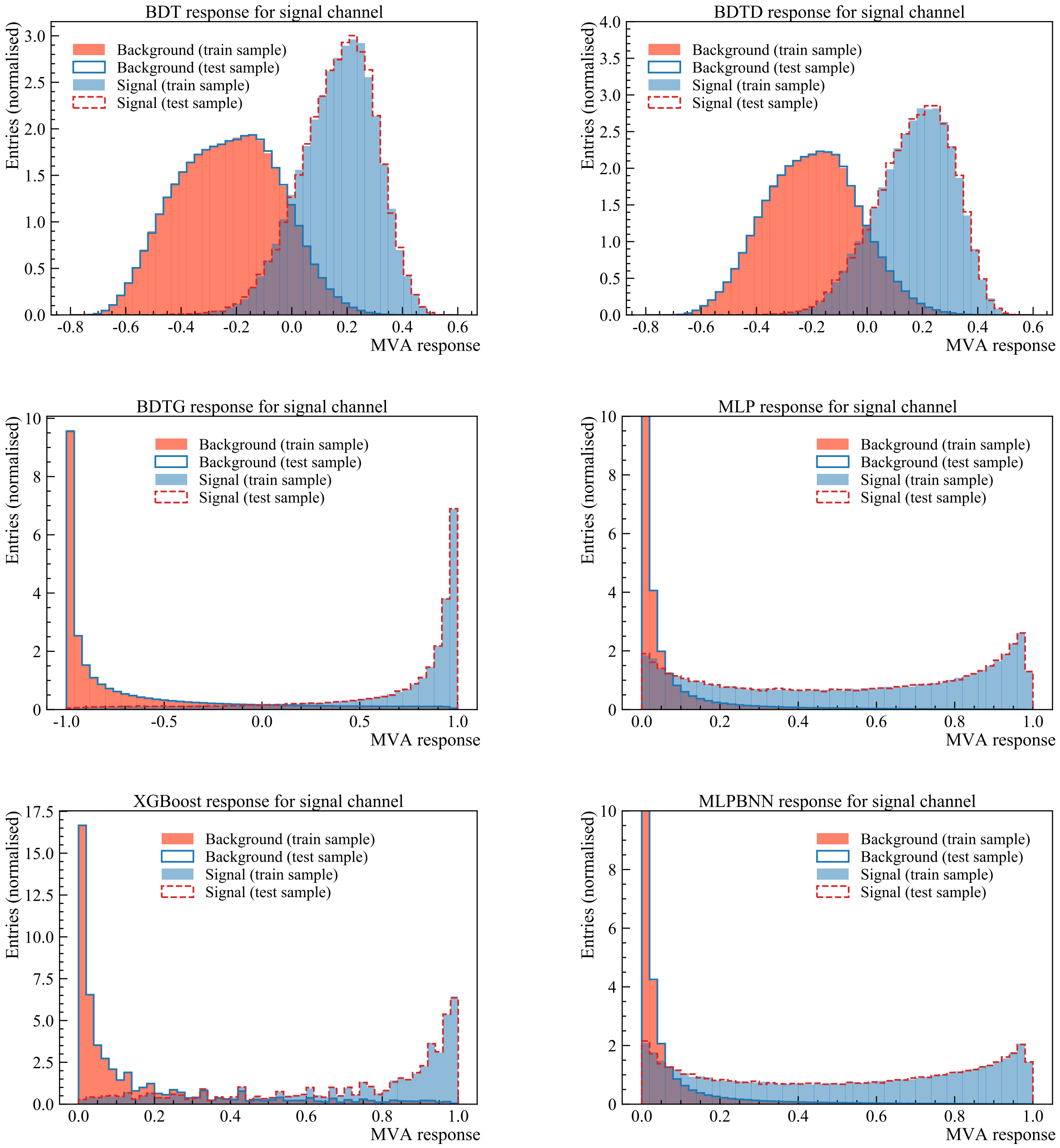

Figure 6.14.: Overtraining plots for different MVA classifiers.

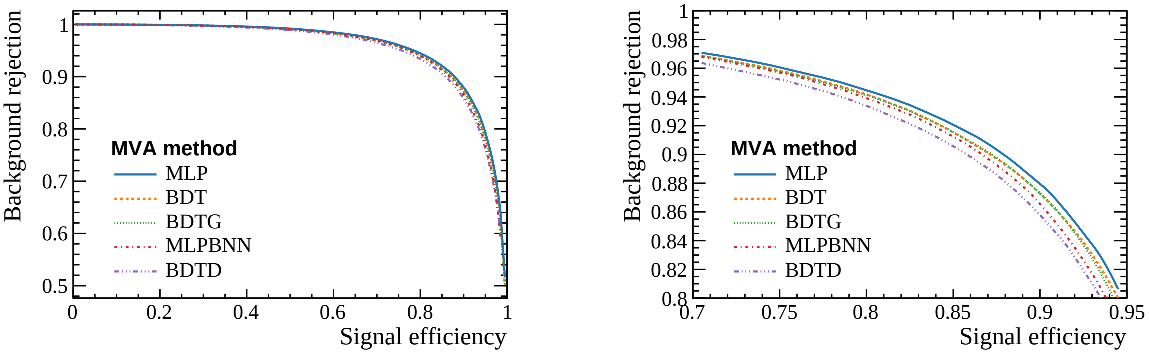

Figure 6.15.: ROC curve representing a background rejection versus signal efficiency for tested TMVA classifiers (zoomed on the right) or the signal channel.

A performance of the different classifiers can be compared based on a receiver operating characteristic (ROC) curve, which shows the classifier background rejection against signal efficiency at various response thresholds. Figure 6.15 shows the ROC curves for various TMVA methods used in this analysis, the area under the ROC curve for all tested MVA classifiers can be found in Table 6.15. The signal efficiencies for the background retention of 1% for various MVA classifiers are shown in Table 6.16 to compare the performance of the individual classifiers. All used methods have a very similar performance, with a minor dominance of the MLP method. One can also notice that the efficiency values are very similar for the testing and training samples, which is a good indication of the absence of overtraining. To perform an independent check of overtraining, the Kolmogorov–Smirnov test [193] is used. The Kolmogorov-Smirnov test for the MVA response distribution for training and testing samples is evaluated for each method and for both signal and background samples used in the MVA. The evaluated p-value is high for each method and both signal and background samples, which confirms no signs of overtraining for the studied MVA classifiers.

In addition to the ROC curve, the Punzi figure of merit (FoM) [211] is evaluated for all used MVA classifiers. The Punzi FoM is particularly useful for the optimisation of processes in which the expected number of signal events is *a priori* unknown. It is used to determine the optimal working point of the classification algorithms based on the equation

$$\mathrm{FoM} = \frac{\varepsilon(t)}{a/2 + \sqrt{B(t)}}, \tag{6.2}$$

MVA method	ROC area
MLP	0.959
BDT	0.957
BDTG	0.957
MLPBNN	0.954
BDTD	0.952
XGBoost	0.926

Table 6.15.: Area under the ROC curve for various MVA classifiers.

MVA method	Signal efficiency (%) for testing (training) sample
MLP	53.3 (53.5)
BDT	51.9 (52.1)
BDTG	51.2 (51.6)
MLPBNN	51.5 (51.6)
BDTD	48.6 (48.7)
XGBoost	38.6 (38.6)

Table 6.16.: Training and testing signal efficiencies for the background retention of 1% for various MVA classifiers.

where $\varepsilon(t)$ is the signal efficiency, $B(t)$ is the expected number of background events under the Ξ_{cc}^{+} mass peak for a given threshold t and $a = 5$ denotes a target significance level, which is set to $5\,\sigma$ for this analysis. The signal efficiency $\varepsilon(t)$ is calculated as the number of events passing the trigger selection, the pre-selection and a given MVA threshold divided by the number of all generated events. The expected number of background events $B(t)$ is evaluated as

$$B(t) = B_{\text{raw}} \times f_{\text{scale}} \times f_{\text{RS}}, \tag{6.3}$$

where B_{raw} is the number of events in the WSM sample passing the trigger selection, the pre-selection requirements and a given MVA threshold in a narrow Ξ_{cc}^{+} mass window from 3600 to 3640 MeV/c^2 corresponding to approximately $3\,\sigma$ around the Ξ_{cc}^{++} mass of 3621.4 MeV/c^2, $f_{\text{scale}} = 4.99$ is a correction factor for the use of only around 20% of the available WSM sample for the calculation of the Punzi FoM, and

$f_{\mathrm{RS}} = 1.97$ is a correction factor for the difference in number of events between the right-signed and WSM samples, which is calculated as a ratio of the right-signed and WSM events in the invariant-mass window from 3800 to 4000 MeV/c^2. Figures 6.16 and 6.17 show the values of the Punzi FoM for the trained MVA classifiers as a function of the MVA threshold for the default and extended trigger sets, respectively. A comparison of the optimal working points for the default trigger set based on the Punzi FoM for each year separately and also combined is shown in Table 6.17. The optimal points differ only marginally among the years - the ratio of the Punzi FoM values at the optimal point evaluated for each year separately and for all years combined is 1.05. Therefore an optimal threshold evaluated on all years combined is used as the optimal MVA point for all years to avoid different selection for each year. A summary of the optimal working points with the corresponding signal and background efficiencies for the different MVA classifiers can be found in Table 6.18.

Based on the performance comparison of the different methods using the Punzi FoM, both MLP and BDT are within their uncertainties the optimal methods. The MLP classifier is chosen as the baseline MVA method due to better stability around its optimal working point, with the optimal points of 0.905 for the default trigger set and 0.9 for the extended trigger set.

The invariant-mass distribution in the background samples for a chosen MVA method and its optimal working point is checked to ensure the MVA selection does not introduce any peaking structures in the WS samples. Figures 6.18 and 6.19 show the WSM invariant-mass distribution for the default and extended trigger sets, respectively, for each year separately after all pre-selection and MVA requirement are applied, together with the removal of multiple candidates discussed in Section 6.2.7, using about 20% of the full available statistics. No peaking structure is observed in any of the background samples. Comparison of the Ξ_{cc}^{+} invariant-mass distribution for the default trigger set in the upper side-band window for three different background samples (WSM, WSP and SB) for each year is shown in Figure 6.20. The invariant-mass distribution of the Ξ_{c}^{+} baryon in the WSM sample for the default trigger set before and after the optimal MVA requirement is applied is shown in Figure 6.21. One can see that the Ξ_{c}^{+} sample is very clean after the MVA selection. Figure 6.22 shows the fitted Ξ_{c}^{+} invariant-mass distribution after the full selection is applied, where practically only a signal component is present, which is represented by the sum of two Gaussian functions with a fraction of both components fixed based on a fit to the simulation

MVA method	Optimal MVA threshold			
	2016	2017	2018	Combined
MLP	0.905	0.905	0.9	0.905
MLPBNN	0.87	0.865	0.895	0.895
BDT	0.295	0.265	0.27	0.3
BDTG	0.97	0.975	0.965	0.97
BDTD	0.29	0.255	0.27	0.285
XGBoost	0.98	0.98	0.98	0.98

Table 6.17.: Optimal MVA working points based on the Punzi FoM evaluated separately for each year and for all studied years combined (last column) for the default trigger set.

MVA method	Optimal threshold	FoM ($\times 10^{-6}$)	ε_{sig} (%)	ε_{bkg} (%)
MLP	0.905	5.06 ± 0.04	17.33 ± 0.10	0.056 ± 0.001
MLPBNN	0.895	4.56 ± 0.03	15.98 ± 0.09	0.059 ± 0.001
BDT	0.3	4.72 ± 0.04	14.77 ± 0.09	0.047 ± 0.001
BDTG	0.97	4.54 ± 0.03	20.20 ± 0.10	0.095 ± 0.002
BDTD	0.285	3.88 ± 0.02	20.73 ± 0.10	0.138 ± 0.002
XGBoost	0.98	2.93 ± 0.02	12.91 ± 0.09	0.093 ± 0.002

Table 6.18.: Optimal MVA working points for the $\Xi_{cc}^{+} \to \Xi_{c}^{+}\pi^{-}\pi^{+}$ decay based on the Punzi FoM evaluated for all studied years combined and the corresponding MVA signal and background efficiencies for $\pm 3\,\sigma$ region around the Ξ_{cc}^{++} mass for the different MVA classifiers for the default trigger set.

data. The resolution σ is defined as

$$\sigma = \sqrt{f_1 \cdot \sigma_1^2 + f_2 \cdot \sigma_2^2}, \tag{6.4}$$

where f_1 and f_2 are the fractions of two Gaussian functions and σ_1 and σ_1 are their corresponding widths. To cross-check the agreement between the resolution found in the simulation and data for the Ξ_c^+ baryon, the $pK^-\pi^+$ invariant-mass spectrum in the simulation is fitted after the full selection is applied, which is shown in Figure 6.22. The resolution seen in data is consistent with its simulation value within 1–2 σ.

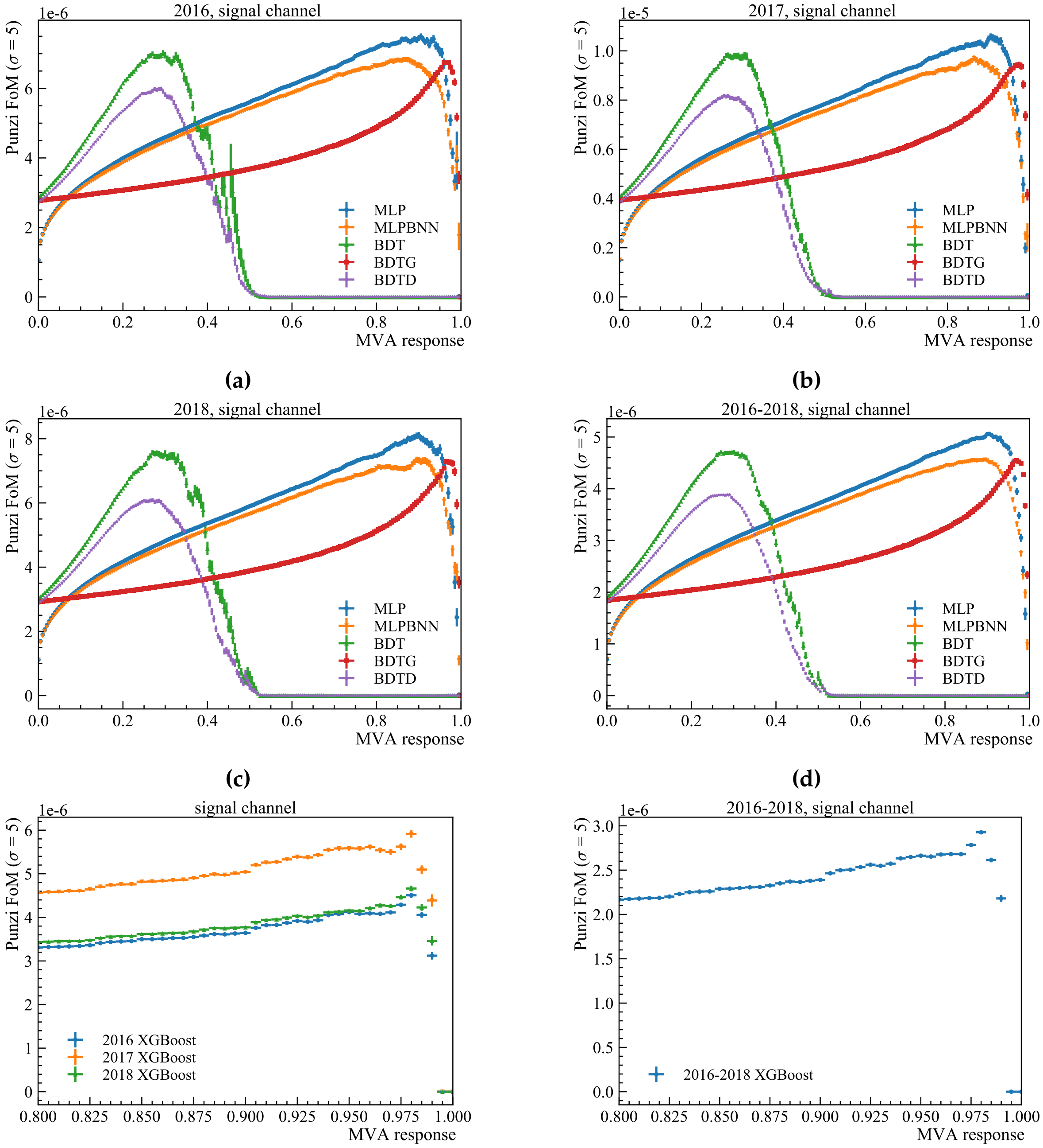

(a) **(b)**

(c) **(d)**

(e) **(f)**

Figure 6.16.: Punzi FoM for different MVA classifiers from the (a, b, c, d) TMVA package and for the (d, e) XGBoost method evaluated for (a, b, c, e) each year separately and for (d, f) all years combined for the default trigger.

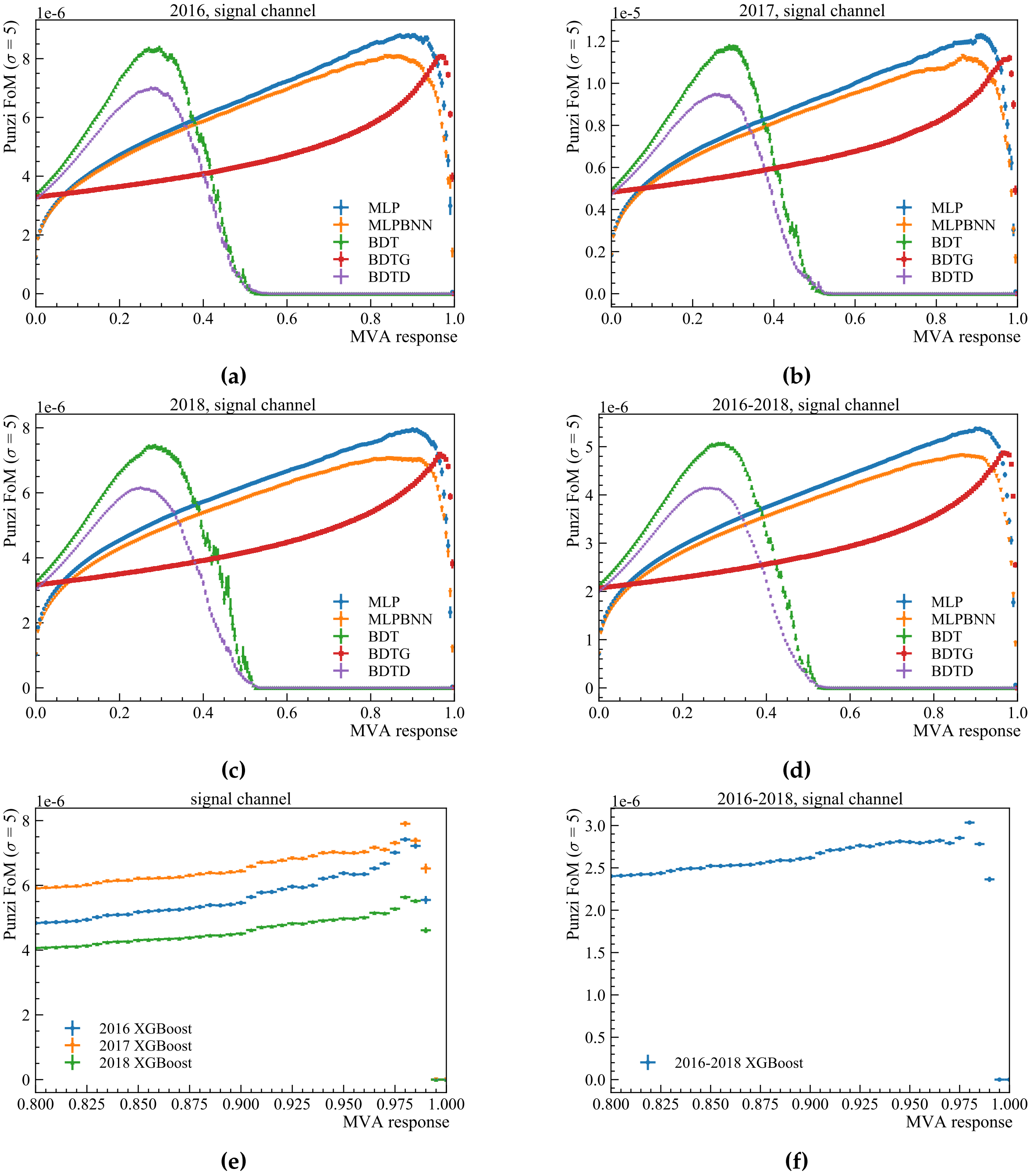

(a) **(b)** **(c)** **(d)** **(e)** **(f)**

Figure 6.17.: Punzi FoM for different MVA classifiers from the (a, b, c, d) TMVA package and for the (d, e) XGBoost method evaluated for (a, b, c, e) each year separately and for (d, f) all years combined for the extended trigger set.

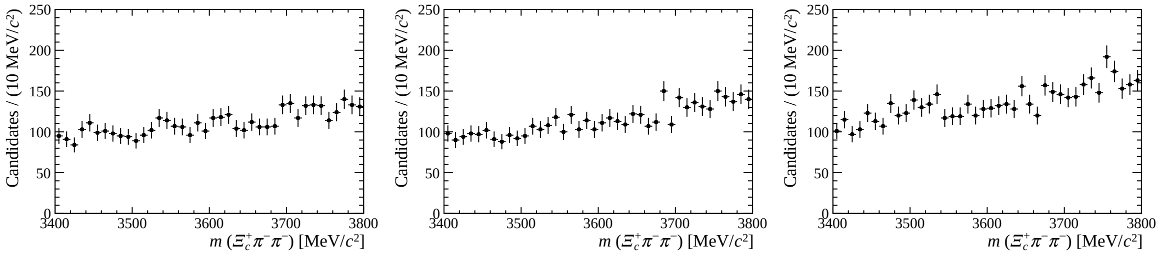

(a) **(b)** **(c)**

Figure 6.18.: Invariant-mass spectrum for the $\Xi_c^+\pi^-\pi^-$ final state for 20% of the WSM background sample for (a) 2016, (b) 2017 and (c) 2018 data in the default trigger set after all selection requirements (including the removal of multiple candidates) are applied.

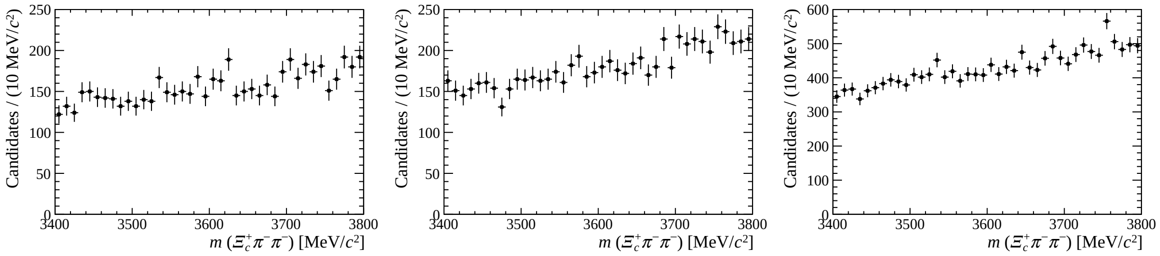

(a) **(b)** **(c)**

Figure 6.19.: Invariant-mass spectrum for the $\Xi_c^+\pi^-\pi^-$ final state for 20% of the WSM background sample for (a) 2016, (b) 2017 and (c) 2018 data in the extended trigger set after all selection requirements (including the removal of multiple candidates) are applied.

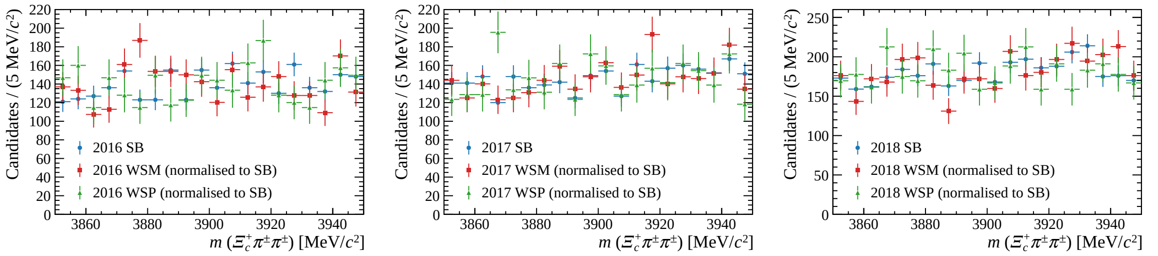

(a) **(b)** **(c)**

Figure 6.20.: Comparison of 20% of the SB (blue circles), WSM (red squares) and WSP (green triangles) invariant-mass distributions in the upper SB mass window for (a) 2016, (b) 2017 and (c) 2018 data for the default trigger set after all selection requirements (including the removal of multiple candidates) are applied. The WSM and WSP distributions are normalised to the one of the SB.

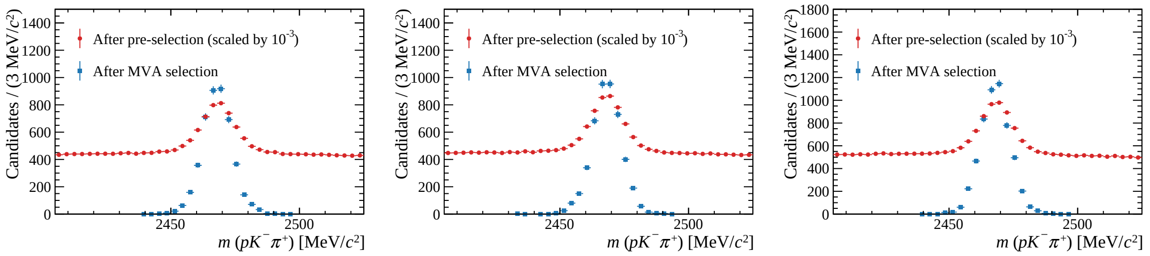

(a) (b) (c)

Figure 6.21.: Invariant-mass distribution of the Ξ_c^+ candidates in 20% of the WSM sample for (a) 2016, (b) 2017 and (c) 2018 data in the default trigger set before and after the optimal MVA requirement is applied. The mass-window requirement for the Ξ_c^+ baryon applied in the pre-selection is removed for this figure. The candidates before the MVA selection are scaled by a factor 10^{-3}.

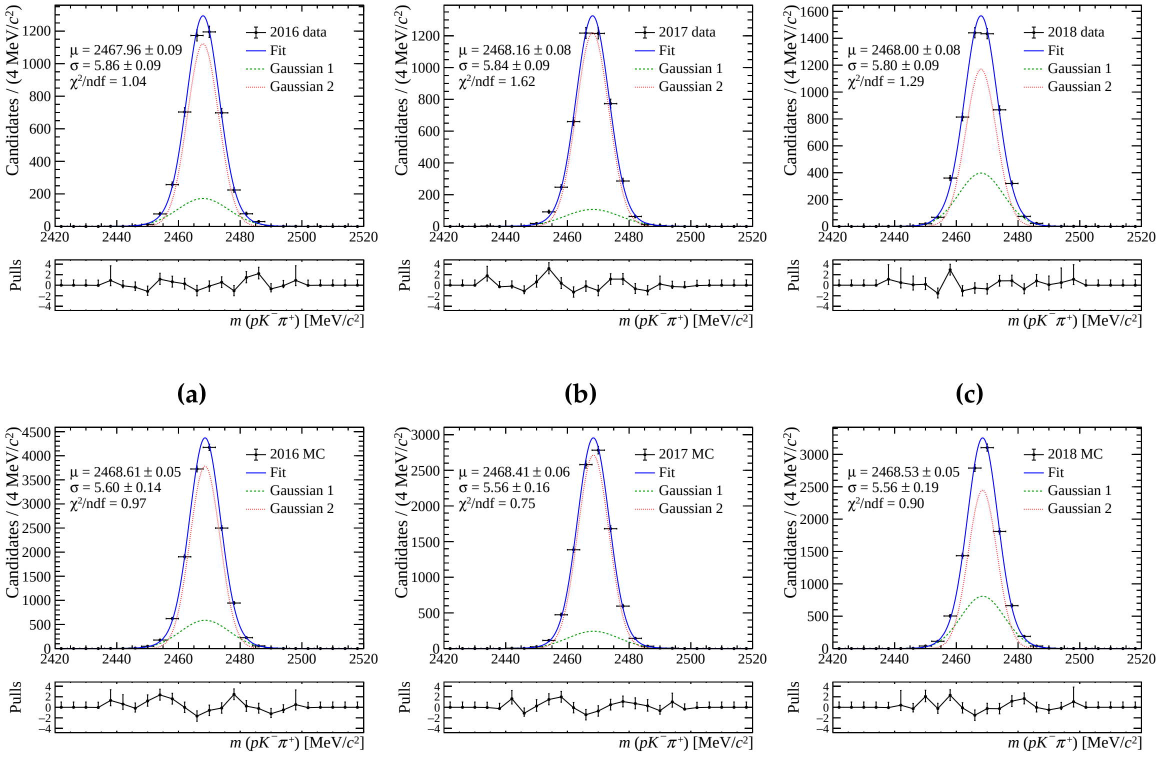

(a) (b) (c)

(d) (e) (f)

Figure 6.22.: Invariant-mass distribution of the Ξ_c^+ candidates in (a, b, c) 20% of the WSM sample and in the (d, e, f) simulation for (a, d) 2016, (b, e) 2017 and (c, f) 2018 data (black points) in the default trigger set fitted by the sum of two Gaussian functions after all selection requirements (including the removal of multiple candidates, but without the mass-window requirement for the Ξ_c^+ baryon applied in the pre-selection) are applied.

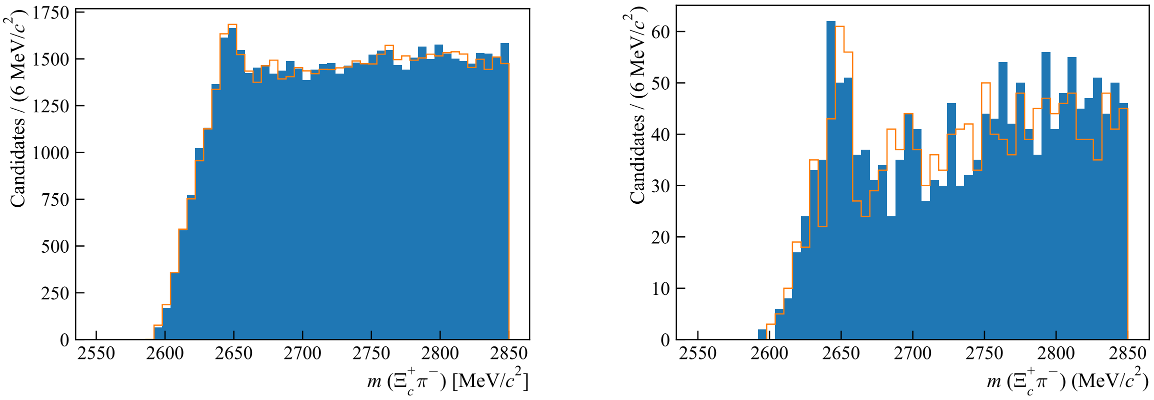

(a) **(b)**

Figure 6.23.: Invariant-mass distribution for the $\Xi_c^+\pi^-$ combinations in the 2017 WSM sample for the default trigger set (a) before and (b) after the MVA selection. Orange line and blue filled histograms correspond to combinations of the Ξ_c^+ baryon with one or the other companion negative pion.

The $\Xi_c^+\pi^-$ invariant-mass distribution in the WSM data sample before and after the MVA selection is also checked in order to inspect the expected resonant contribution of the $\Xi_c(2645)^0$ state. This check can also indicate how many $\Xi_c(2645)^0$ combined with random pions can be expected in the signal sample. Figure 6.23 shows the $\Xi_c^+\pi^-$ invariant-mass distribution in the 2017 WSM data sample. The structure corresponding to the $\Xi_c(2645)^0$ baryon is clearly visible around 2645 MeV/c^2. As a cross-check, the $\Xi_c^+\pi^+$ invariant-mass distribution in the WSP sample is examined as well, which is shown in Figure 6.24. As expected, the $\Xi_c(2645)^0$ resonance is not present in the $\Xi_c^+\pi^+$ invariant-mass spectrum of the WSP sample.

6.2.6.1. Punzi FoM as a function of different PID requirements

As was already described in Section 6.2.2, where the pre-selection requirements are discussed, only very loose PID requirements are applied offline since their performance is better than for a tighter PID selection. However, tighter PID requirements are also checked on top of the MVA selection to evaluate if the efficiency could be further improved. The Punzi FoM as a function of different ProbNN requirements is shown in Figure 6.25. The tighter PID requirements do not significantly improve the Punzi FoM, therefore they are not considered in a further selection.

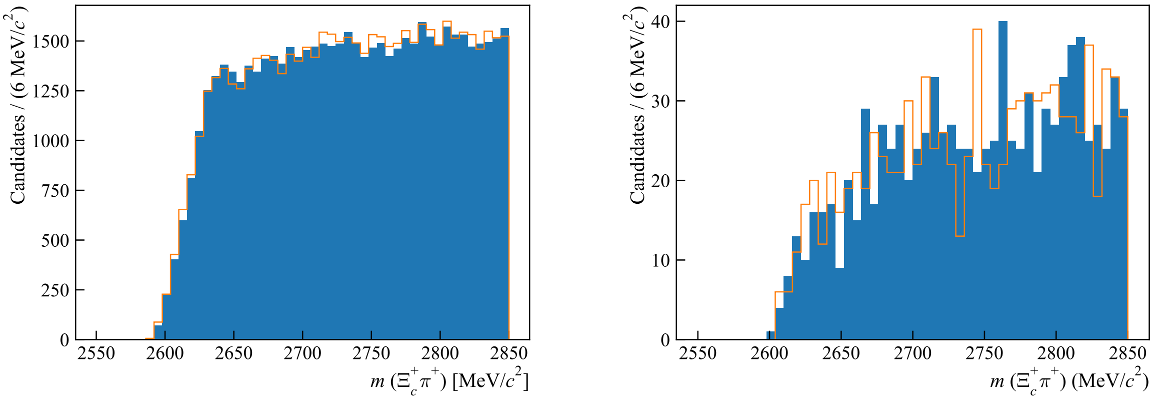

(a) **(b)**

Figure 6.24.: Invariant-mass distributions for the $\Xi_c^+\pi^-$ combinations in the 2017 WSP sample for the default trigger set (a) before and (b) after the MVA selection. Orange line and blue filled histograms correspond to combinations of the Ξ_c^+ baryon with one or the other companion positive pion.

6.2.6.2. Lifetime dependence

The Ξ_{cc}^{+} candidates in the simulation are generated with a lifetime of 80 fs as an approximation of about 2–4 times lower value than the measured lifetime of the doubly charged baryon Ξ_{cc}^{++}. However, the lifetime of the Ξ_{cc}^{+} baryon is *a priori* unknown and there is a significant spread in the theoretical predictions for its value, therefore the Punzi FoM at the optimal MVA threshold is evaluated for different lifetime hypotheses. The candidates with a lifetime t are weighted as

$$w(t) = \frac{\frac{1}{\tau}\exp(-\frac{t}{\tau})}{\frac{1}{\tau_0}\exp(-\frac{t}{\tau_0})}, \tag{6.5}$$

where τ_0 corresponds to the lifetime set in the simulation and τ is a considered lifetime hypothesis. The efficiencies for different lifetime hypotheses are calculated based on the weighted candidates as

$$\varepsilon = \frac{\sum_{i(pass)} w_i}{\sum_{j(all)} w_j}, \tag{6.6}$$

where the index i denotes the candidates that pass the selection and j all candidates before the selection. Figure 6.26 shows a dependence of the Punzi FoM on the Ξ_{cc}^{+} lifetime hypothesis at the optimal MVA threshold. As expected, the MVA efficiency is higher for longer lifetimes. However, the variation is not very large and even for

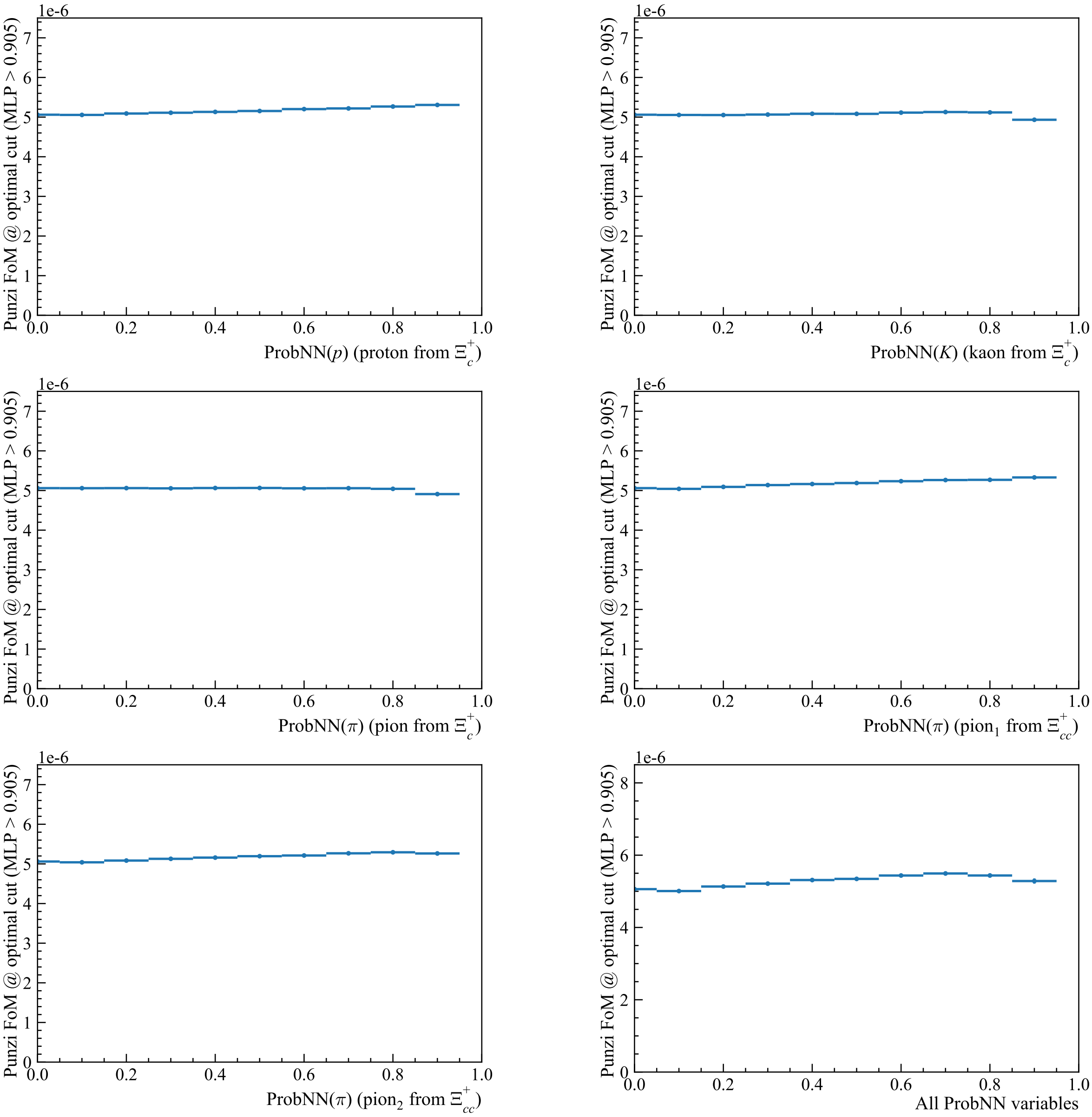

Figure 6.25.: Punzi FoM as a function of the ProbNN requirement applied to various final tracks after the MVA selection. The only ProbNN requirements applied in the selection is ProbNN(π) of the pions from the Ξ_{cc}^{+} baryon to be larger than 0.1.

the lower lifetimes the developed MVA selection is sufficiently efficient. The selection described in this chapter is fixed for the nominal Ξ_{cc}^{+} lifetime of 80 fs. However, for the determination of the UL on R, the efficiencies for different lifetimes of the Ξ_{cc}^{+} baryon are considered to evaluate the UL on R at different lifetime hypotheses, which is discussed in detail in Section 8.2.1.

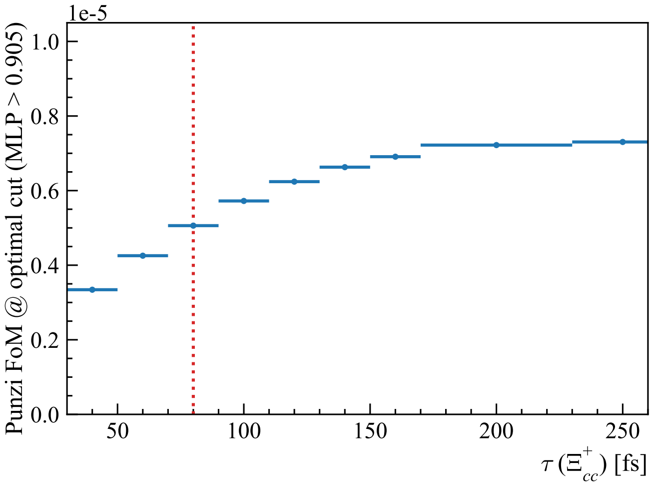

Figure 6.26.: Punzi FoM at the optimal MVA threshold (MLP $>$ 0.905) for different lifetime hypotheses. The red dotted vertical line represents the nominal Ξ_{cc}^{+} lifetime of 80 fs.

To check the dependence of the optimal working point on the Ξ_{cc}^{+} lifetime hypothesis, the Punzi FoM is calculated for different lifetime assumptions. Figure 6.27 shows the Punzi FoM as a function of the MLP threshold for six different lifetime hypotheses of the Ξ_{cc}^{+} baryon. The optimal MLP requirement is found to be 0.905 for all of the studied lifetime hypotheses larger than 80 fs. For the lifetime hypothesis of 60 fs, the optimal threshold is found to be 0.9, and it is 0.815 for the lifetime hypothesis of 40 fs. One can see that the optimal threshold of 0.905 is stable over a large range of the studied lifetimes, it is only slightly less optimal for its shorter values. However, the Punzi FoM for both 40 fs and 60 fs lifetime hypotheses is relatively high even at the chosen MLP threshold of 0.905.

6.2.6.3. Mass dependence

To evaluate the Punzi FoM as a function of the assumed Ξ_{cc}^{+} mass, the GBR algorithm is used, which was already described in Section 6.2.4 for the simulation correction of the p_{T}, η and nTracks distributions. Firstly, 50k events are generated for each of five different mass hypotheses: 3471, 3521, 3571, 3671 and 3771 MeV/c^2. The events are generated and saved only at the generator level without further event propagation and reconstruction in a detector to significantly speed-up the simulation production. Subsequently, using the transverse momentum spectra of the Ξ_{cc}^{+} decay products (Ξ_{c}^{+}, π^{+} and π^{-}) at the generator level, a fully simulated sample is used to train the

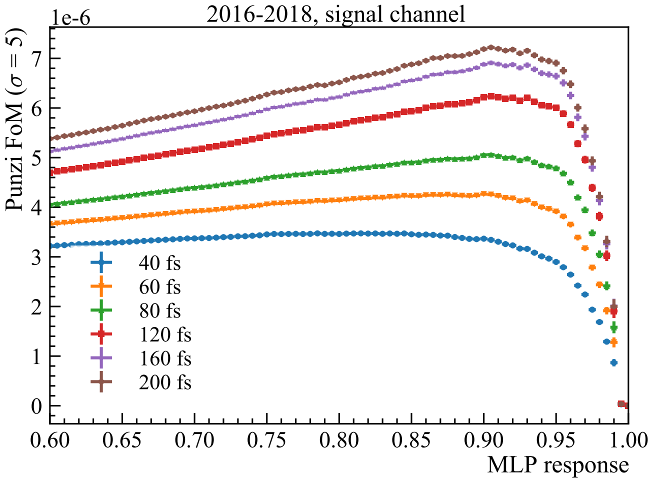

Figure 6.27.: Punzi FoM as a function of the MLP threshold for six different lifetime hypotheses.

GBR. The Punzi FoM is then calculated for each mass hypothesis, which is shown in Figure 6.28. Only a small and linear dependence on the mass is observed. The selection is fixed for the nominal Ξ_{cc}^{+} mass of 3621 MeV/c^2 and the efficiency ratio as a function of the assumed Ξ_{cc}^{+} mass is considered for the determination of the UL on R, described in Section 8.2.2.

Figure 6.29 shows the Punzi FoM as a function of the MLP threshold for six different mass hypotheses of the Ξ_{cc}^{+} baryon. The optimal MLP threshold is found to be 0.905 for all of the studied mass hypotheses, apart from the two smallest values (3471 MeV/c^2 and 3521 MeV/c^2), where the optimal threshold is found to be 0.9. The optimal threshold is therefore considered to be stable over a large range of masses.

6.2.6.4. WSP sample as a background proxy for MVA

One additional cross-check of the MVA performance is performed, where the WSP sample is used as a background proxy in the MVA training instead of the default WSM sample. The motivation behind the study is to check the performance of the WSP sample as the $\Xi_c(2645)^0 \to \Xi_c^+ \pi^-$ decay is present in the WSM and right-signed samples, but not in the WSP sample, as shown in Figures 6.23 and 6.24. The MVA classifiers are therefore trained using the 2016–2018 WSP samples in the same way as for the default training with the WSM samples.

After the MVA training, a requirement to retain 10% of the signal candidates is used for both the WSM and WSP trainings to directly compare the background suppression

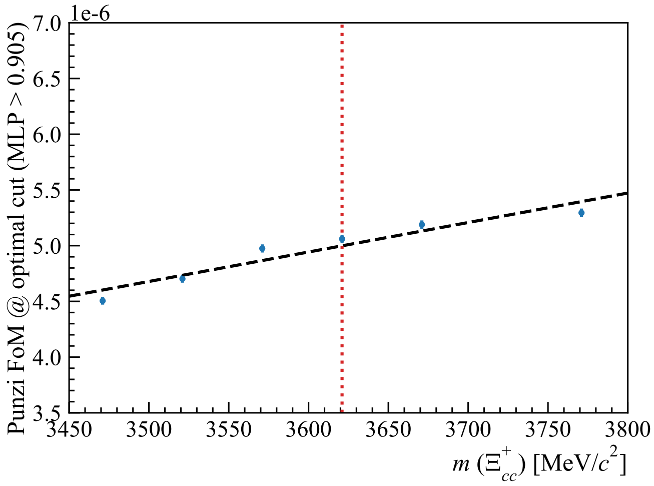

Figure 6.28.: Punzi FoM at the optimal MVA threshold (MLP > 0.905) for different Ξ_{cc}^{+} mass hypotheses. The red dotted vertical line represents the nominal Ξ_{cc}^{+} mass of 3621 MeV/c^2.

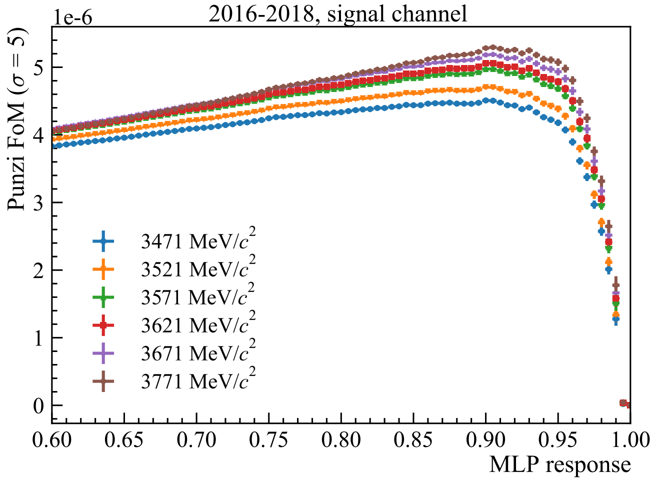

Figure 6.29.: Punzi FoM as a function of the MLP threshold for six different mass hypotheses.

for the same signal efficiency. The background efficiency of the WSM sample for the MVA training with the WSM sample used as a background proxy is found to be 0.022% , whereas the background efficiency of the WSP sample for the MVA training with the WSP sample used as a background proxy is 0.01%, which could indicate a better background suppression for the MVA training with the WSP sample. However, a better measure to compare the background rejection for the two trainings is to perform the evaluation of the background efficiencies using the side bands of the right-signed distribution. Table 6.19 shows the background efficiencies for the upper and lower side-band for both the WSP and WSM trainings with a requirement to retain 10% of the

Background sample used in the MVA	Lower SB efficiency (%)	Upper SB efficiency (%)
WSM	0.0232 ± 0.0004	0.0205 ± 0.0002
WSP	0.0389 ± 0.0005	0.0174 ± 0.0002

Table 6.19.: Background efficiencies for the upper and lower SB for a requirement to retain 10% of the signal candidates for the MVA training where different background samples are used as a background proxy.

signal candidates. Even though the signal peak is expected to be present somewhere between the lower and the upper side-band mass spectrum, taking into account a low suppression in the lower background region with the WSP training it can be concluded that the overall background suppression is better for the MVA training with the WSM sample, which also provides a more uniform background suppression in a wide mass region.

6.2.7. Removal of multiple candidates

There are two types of multiple Ξ_{cc}^{+} candidates that are removed after the MVA selection in order to avoid a fake peaking structure in the final invariant-mass spectrum.

The first type of removed multiple candidates are the track-clone candidates, which are the candidates for which at least one track is a clone of another track from the same candidate. A track is considered to be a clone track if it is a copy of another track, which happens when the pattern-recognition algorithms mark one real track as two different tracks. Since the studied signal mode contains five tracks in its final state, it is expected that some clone candidates are present in the selected sample, even though they are significantly suppressed already at the HLT2 level by the corresponding reconstruction algorithms. The track clone candidates are removed by requiring a minimal opening angle between any pair of tracks, as a distribution of the angle between two clone tracks is by definition very close to zero. For illustration, a distribution of the opening angle between the same charged proton and pion in the 2016 WSM and the truth-matched simulation data is shown in Figure 6.30. A peak around zero is clearly visible in the WSM sample, while not in the simulation sample as any possible track clone candidates are removed by the truth-matching requirements. Therefore a requirement

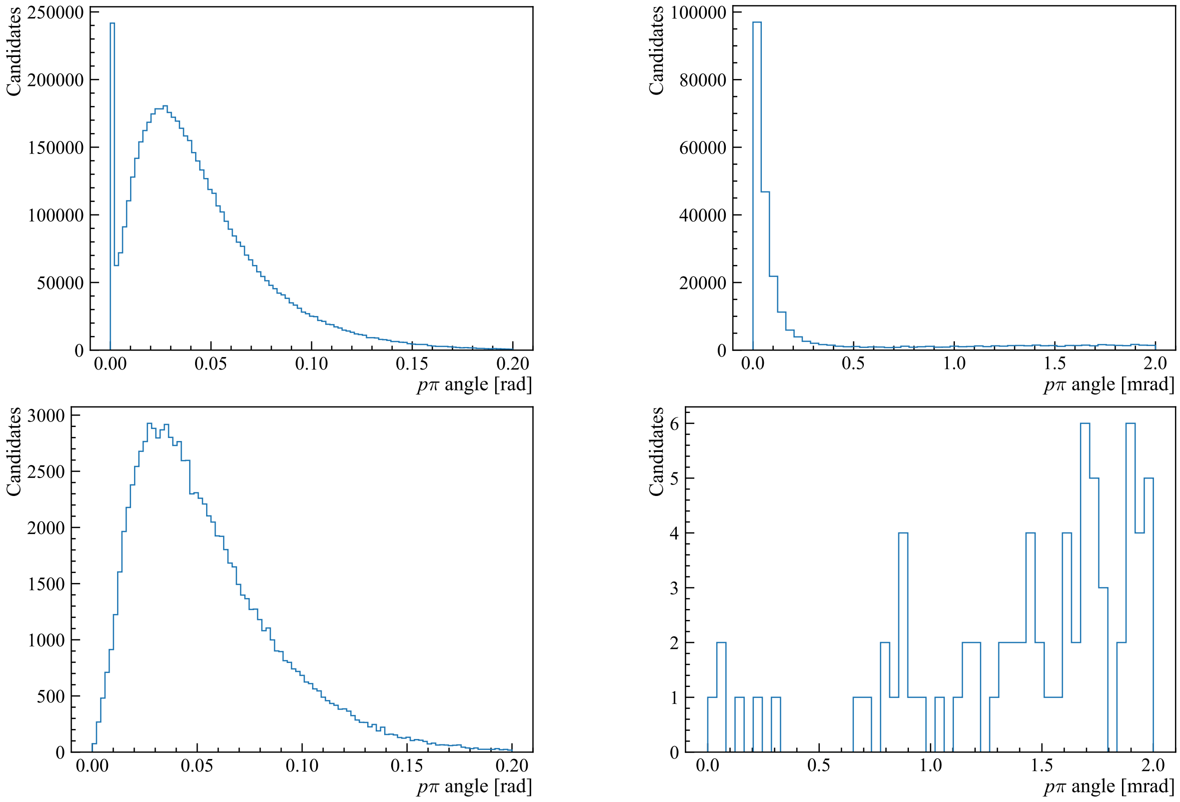

Figure 6.30.: Distribution of the opening angle between the same-charged proton and pion in the 2016 WSM data (top row) and the truth-matched 2016 simulation data (bottom row). The figures on the right side are the zoomed version (in units of mrad) of the distributions shown on the left side (in units of rad).

on the opening angle between any pair of tracks $\theta_{ij} > 0.5\,\text{mrad}$ is applied to all candidates passing the MVA selection, which removed all track clone candidates from the sample.

The second type of removed multiple candidates are the duplicate candidates, which have the same set of tracks, but they are assigned to a different final state due to a combination of the final decay products. For the studied $\Xi_{cc}^{+} \to (\Xi_{c}^{+} \to pK^{-}\pi^{+})\pi^{-}\pi^{+}$ decay, the π^{+} meson from the Ξ_{c}^{+} decay can be swapped with the π^{+} meson from the Ξ_{cc}^{+} decay. It is important to remove all duplicate candidates as they may artificially increase a signal significance since only one candidate can be a true signal candidate. The duplicate candidates are removed by checking the unique run and event number combinations and the Ξ_{cc}^{+} mass hypothesis as a verification that the candidates share all five tracks in the event. If they are the same, only one random candidate is kept in the final sample.

Dataset	Clones removed (%)	Duplicates removed (%)
WSM 2016 (inclusive line)	3.21	0.10
WSM 2017 (inclusive line)	3.41	0.32
WSM 2017 (exclusive line)	4.75	0.00
WSM 2018 (inclusive line)	3.24	0.57
WSM 2018 (exclusive line)	3.98	0.00
WSM 2018 (MVA inclusive line)	4.83	0.47
RS 2016 (inclusive line)	3.70	1.32
RS 2017 (inclusive line)	3.69	1.42
RS 2017 (exclusive line)	5.19	0.00
RS 2018 (inclusive line)	3.70	1.54
RS 2018 (exclusive line)	5.29	0.00
RS 2018 (MVA inclusive line)	5.56	3.28

Table 6.20.: Removed fractions of clone and duplicate candidates from the analysed WSM and right-signed (RS) data samples.

The removed fractions of the track clone and duplicate candidates after the MVA selection for the individual HLT2 trigger lines used in this analysis with the L0 requirement of TIS or TOS in the WSM and right-signed samples for each year are summarised in Table 6.20. The removed fractions in the right-signed sample were added only after unblinding.

6.3. Selection for the normalisation channel

The L0, HLT1 and HLT2 trigger requirements included in the default trigger set are precisely the same for the normalisation channel $\Xi_{cc}^{++} \to (\Xi_{c}^{+} \to pK^{-}\pi^{+})\pi^{+}$, since there is also the Ξ_{c}^{+} baryon in the decay chain. The pre-selection requirements are the same as for the signal-decay mode, with the exception that those for two companion pions are applied here only for one companion pion. All pre-selection requirements applied to the normalisation channel are summarised in Table 6.21. The same PID binning as described in Table 6.8 is used for this decay mode for the application of the PID weighting based on the PIDCalib package. The MVA variables used to train the MVA classifiers are again the same as for the signal mode, with the exception of

$2\,\mathrm{GeV}/c <$	p	$< 150\,\mathrm{GeV}/c$ for all tracks
$1.5 <$	η	< 5.0 for all tracks
$2.5\,\mathrm{GeV}/c <$	p_T	$< 25\,\mathrm{GeV}/c$ for Ξ_{cc}^{++}
$2.0 <$	η	< 4.5 for Ξ_{cc}^{++}
$2450\,\mathrm{MeV}/c^2 <$	$m(\Xi_c^+)$	$< 2488\,\mathrm{MeV}/c^2$
$\chi^2_\mathrm{vtx}/\mathrm{ndf}$ of Ξ_{cc}^{++}	$<$	25
χ^2_IP of Ξ_{cc}^{++}	$<$	25
p_T of Ξ_{cc}^{++}	$>$	$2500\,\mathrm{MeV}/c$
χ^2_DTF of Ξ_{cc}^{++}	$<$	50
p of pion from Ξ_{cc}^{++}	$>$	$2000\,\mathrm{MeV}/c$
p_T of pion from Ξ_{cc}^{++}	$>$	$200\,\mathrm{MeV}/c$
χ^2/ndf of pion track from Ξ_{cc}^{++}	$<$	3
ProbNN(ghost) of proton	$<$	0.9
ProbNN(ghost) of kaon	$<$	0.9
ProbNN(ghost) of pion	$<$	0.9
ProbNN of pion from Ξ_{cc}^{++}	$>$	0.1
$\mathrm{DLL}_{K\pi}$ for pion from Ξ_{cc}^{++}	$<$	5

Table 6.21.: Pre-selection requirements for the normalisation channel $\Xi_{cc}^{++} \to \Xi_c^+ \pi^+$.

the values for the second companion pion. The MVA variables for the normalisation channel which are used in the training are summarised in Table 6.22. The simulation samples for the normalisation channel are produced with the lifetime of the Ξ_{cc}^{++} baryon of 333 fs, therefore the lifetime is weighted according to Equation 6.5 to match the recently measured lifetime of the Ξ_{cc}^{++} baryon of 256 fs. The simulation samples are also weighted using the same weights as for the signal channel described in Section 6.2.4 to correct for the discrepancies between the data and simulation in the p_T, η and nTracks distributions.

The distributions of the variables for the signal and background samples, as well as the correlation matrices, overtraining checks, ROC curves and Punzi FoM plots, can be found in Appendix C. Table 6.23 summarises optimal working points based on the Punzi FoM with the corresponding signal and background efficiencies for different MVA classifiers. Based on the Punzi FoM, an MLP classifier with an optimal threshold of 0.97 is used in the final selection for the normalisation channel. The

Variable	Separation
p_{T} of pion from Ξ_{cc}^{++}	0.344
DIRA of Ξ_{cc}^{++}	0.329
$\log(\chi^2_{\mathrm{vtx}}/\mathrm{ndf}$ of $\Xi_{cc}^{++})$ with Ξ_c^+ mass and Ξ_{cc}^{++} PV constraints	0.281
(p_{T} of Ξ_c^+) / (sum of p_{T} of Ξ_{cc}^{++} decay products)	0.254
(χ^2_{IP} of Ξ_c^+) / (sum of χ^2_{IP} of Ξ_{cc}^{++} decay products)	0.229
$\log(\chi^2_{\mathrm{IP}}$ of $\Xi_{cc}^{++})$	0.194
max DOCA between any pair of Ξ_{cc}^{++} decay products	0.141
$\log(\chi^2_{\mathrm{FD}}$ of $\Xi_{cc}^{++})$	0.108
$\chi^2_{\mathrm{vtx}}/\mathrm{ndf}$ of Ξ_c^+	0.102
(p of proton) / (sum of p of Ξ_c^+ decay products)	0.094
max DOCA between any pair of Ξ_c^+ decay products	0.070
$\log(\chi^2_{\mathrm{FD}}$ of $\Xi_c^+)$	0.040
$\log(\chi^2_{\mathrm{IP}}$ of $\Xi_c^+)$	0.022
sum of p_{T} of Ξ_c^+ decay products	0.020
$\log(\chi^2_{\mathrm{vtx}}/\mathrm{ndf}$ of $\Xi_{cc}^{++})$	0.018

Table 6.22.: List of variables used in the MVA selection for the normalisation channel $\Xi_{cc}^{++} \to \Xi_c^+ \pi^+$ ordered by their separation power. The separation is one for shapes with no overlap, and it is zero for identical shapes.

scaling factors for the evaluation of the expected number of background events $B(t)$ used in Equation 6.3 for the normalisation channel are $f_{\mathrm{scale}} = 19.69$ for the use of only about 5% of the available WSM sample, and $f_{\mathrm{RS}} = 0.98$ calculated as a ratio of the right-signed and WSM events in the invariant-mass window from 3650 to 3750 MeV/c^2.

The MVA selection developed for the normalisation mode is applied to the full 2016–2018 data sample since this channel had already been unblinded for all studied years in the recently published measurement of the Ξ_{cc}^{++} mass [78]. As in the published analysis where the $\Xi_{cc}^{++} \to \Xi_c^+ \pi^+$ decay was first observed [103], the signal shape is modelled by a Double-Sided Crystal Ball (DSCB) function plus a Gaussian distribution that share the same mean value. The DSCB function is an extension of the Crystal Ball function [212] with a single central Gaussian core and power-law tails on both sides,

MVA method	Optimal threshold	FoM ($\times 10^{-5}$)	ε_{sig} (%)	ε_{bkg} (%)
MLP	0.97	2.59 $\pm$ 0.03	25.36 $\pm$ 0.13	0.039 $\pm$ 0.004
MLPBNN	0.965	2.20 $\pm$ 0.02	28.72 $\pm$ 0.13	0.071 $\pm$ 0.006
BDT	0.285	2.45 $\pm$ 0.03	23.46 $\pm$ 0.13	0.037 $\pm$ 0.004
BDTG	0.985	2.04 $\pm$ 0.02	26.42 $\pm$ 0.13	0.071 $\pm$ 0.006
BDTD	0.33	2.00 $\pm$ 0.03	20.53 $\pm$ 0.12	0.043 $\pm$ 0.005
XGBoost	0.98	1.62 $\pm$ 0.01	36.68 $\pm$ 0.14	0.221 $\pm$ 0.010

Table 6.23.: Optimal MVA working points for the $\Xi_{cc}^{++} \to \Xi_c^+ \pi^+$ decay based on the Punzi FoM evaluated for all studied years combined and the corresponding MVA signal and background efficiencies for the $\pm 3\sigma$ region around the Ξ_{cc}^{++} mass for different MVA classifiers for the default trigger set.

and is defined as

$$N \cdot \begin{cases} e^{-\frac{t^2}{2}} & \text{if } -\alpha_{\rm L} \leq t \leq \alpha_{\rm H} \\ e^{-\frac{\alpha_{\rm L}^2}{2}} [\frac{|\alpha_{\rm L}|}{n_{\rm L}} (\frac{n_{\rm L}}{|\alpha_{\rm L}|} - |\alpha_{\rm L}| - t)]^{-n_{\rm L}} & \text{if t} < -\alpha_{\rm L} \\ e^{-\frac{\alpha_{\rm H}^2}{2}} [\frac{|\alpha_{\rm H}|}{n_{\rm H}} (\frac{n_{\rm H}}{|\alpha_{\rm H}|} - |\alpha_{\rm H}| + t)]^{-n_{\rm H}} & \text{if t} > \alpha_{\rm H}, \end{cases} \tag{6.7}$$

where $t = (m(\Xi_c^+ \pi^+ \pi^-) - \mu_{\rm CB})/\sigma_{\rm CB}$, N is a normalization parameter, $\mu_{\rm CB}$ represents the peak of the Gaussian distribution, $\sigma_{\rm CB}$ is the width of the Gaussian part of the function, $\alpha_{\rm L}$ and $\alpha_{\rm H}$ parametrises the mass value where the distribution of the invariant mass becomes a power-law function on the low and the high mass side, respectively, and the $n_{\rm L}$ and $n_{\rm H}$ are the exponents of this function. An exponential function $e^{\lambda m}$ is used to model the background component of the invariant-mass distribution. The signal yield, mean and width parameters are kept free in the fit, as well as the background yield and λ parameter of the exponential function, all other parameters (the tails of the DSCB function, the fraction of the DSCB and Gaussian functions and the ratio of their widths) are fixed based on a fit to the simulation data, which is shown in Figure 6.31. The parameters extracted from the fit to simulation data can be found in Table 6.24. Figure 6.32 shows the fitted invariant-mass spectrum after all selection requirements are applied, including the removal of multiple candidates. The signal yield in the default trigger category shown in Figure 6.32 is 442 ± 56 candidates with a local significance of $11.8\,\sigma$, which is evaluated from the mass fits using Wilks' theorem [213] as a ratio of log-likelihoods for the signal-plus-background hypothesis and

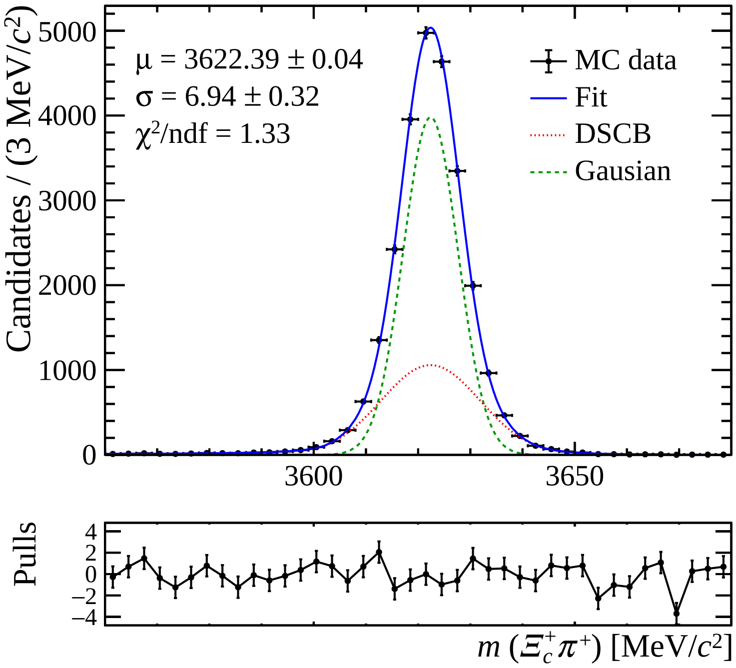

Figure 6.31.: Invariant-mass distribution of the Ξ_{cc}^{++} candidates in the combined 2017 and 2018 simulation samples for the default trigger set after the full selection is applied, fitted with the Gaussian plus DSCB function. The 2016 simulation sample is not used, as the Ξ_{cc}^{++} baryons are produced with a different mass than for the 2017 and 2018 simulation samples.

the background-only hypothesis. The values of the free parameters extracted from the fit are shown in Table 6.25. The resolution is measured to be 9.92 ± 1.44 which agrees with a value obtained from the simulation, 6.94 ± 0.32, within $2\,\sigma$.

To cross-check the optimal MLP working point chosen based on the Punzi FoM, the statistical significance of the peak is evaluated using Wilks' theorem for different MLP thresholds. The width of the peak is fixed to the value obtained from the fit with the optimal MLP threshold chosen based on the Punzi FoM to avoid fluctuations caused by the variation of the width in different fits. Figure 6.33a shows the evaluated local significance as a function of different MLP thresholds for the default trigger set using 2016–2018 data. The highest local significance of the Ξ_{cc}^{++} peak is evaluated for the MLP threshold of 0.965, which is close to the value obtained using the Punzi FoM. Figure 6.33b shows the relative statistical uncertainty on the signal yield as a function of the MLP response. One can notice more local minima caused by the signal and

Parameter	Value
μ [MeV/c^2]	3622.39 ± 0.04
σ [MeV/c^2]	6.94 ± 0.32
σ (Gaussian) [MeV/c^2]	5.23 ± 0.17
f (Gaussian)	0.67 ± 0.06
σ (DSCB)/σ (Gaussian)	1.81 ± 0.13
a_L	2.12 ± 0.10
n_L	1.01 ± 0.20
a_R	2.09 ± 0.14
n_R	4.26 ± 1.48

Table 6.24.: Fit parameters of the Gaussian plus DSCB function obtained from the fit to the $\Xi_{cc}^{++} \to \Xi_c^+ \pi^+$ invariant-mass distribution using the combined 2017 and 2018 simulation samples for the default trigger set after the full selection is applied. The 2016 simulation sample is not used, as the Ξ_{cc}^{++} baryons are produced with a different mass than for the 2017 and 2018 simulation samples.

Parameter	Value
μ [MeV/c^2]	3622.05 ± 0.94
σ [MeV/c^2]	9.92 ± 1.44
Signal yield	442 ± 56
λ [c^2/ MeV]	$(-6.81 \pm 3.21) \times 10^{-4}$

Table 6.25.: Fit parameters obtained from the fit to the $\Xi_{cc}^{++} \to \Xi_c^+ \pi^+$ invariant-mass distribution using the 2016-2018 data for the default trigger set.

background fluctuations in various MLP bins, however for the MLP threshold evaluated by the Punzi FoM, the relative uncertainty is close to one of the local minimum. The optimal MLP thresholds evaluated by different figures of merit are summarised in Table 6.26, where the signal yields and significances are also compared. Since there are no large differences between the evaluated significances and statistical uncertainties on the yield by using different figures of merit, the optimal MLP threshold evaluated by the Punzi FoM is used to avoid a potential bias caused by statistical fluctuations using figures of merit of maximum significance or minimal relative uncertainty on the signal yield.

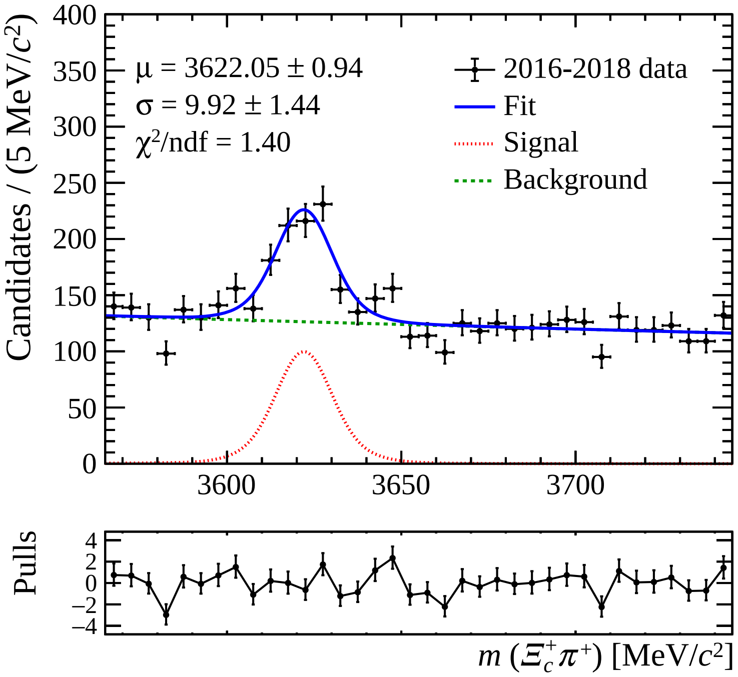

Figure 6.32.: Mass fit of the $\Xi_c^+\pi^+$ invariant-mass distribution after all selection requirements are applied for the combined 2016–2018 data samples in the default trigger set. The DSCB plus Gaussian fit (red dotted line) is used to model the signal component and the exponential function (green dashed line) is used for the background.

FoM	Optimal MLP threshold	Significance	Signal yield
Punzi FoM	0.970	11.8	442 ± 56
Maximum significance	0.965	12.0	457 ± 42
Minimum rel. yield unc.	0.965	12.0	457 ± 42

Table 6.26.: Comparison of a signal yield and a statistical significance for the normalisation channel in the default trigger set at the optimal MLP thresholds evaluated by various different figures of merit.

To quantitatively evaluate the choice of the L0 TIS category over the L0 TOS category for the default trigger set, a fraction of signal candidates in the L0 TIS and TOS categories with respect to the L0 TIS or TOS decision are measured in the default trigger set for the normalisation channel, as it is expected they are comparable to the fractions for the signal decay due to their similar decay kinematics. The fraction of the signal candidates in the L0 TOS category after the full selection in real data (simulation)

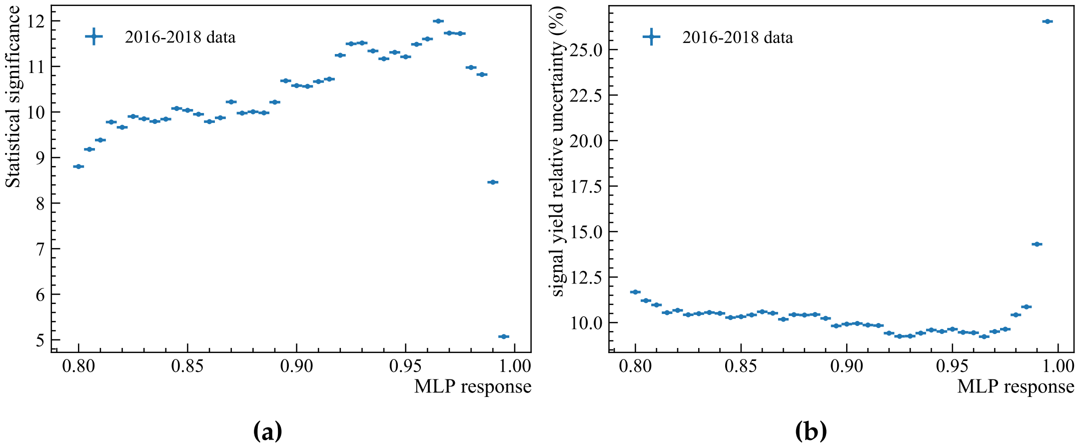

(a) **(b)**

Figure 6.33.: Statistical significance of the Ξ_{cc}^{++} peak (a) evaluated using Wilks' theorem and (b) a relative statistical uncertainty on the Ξ_{cc}^{++} signal yield, as a function of the MLP threshold for the 2016–2018 data in the default trigger set.

is 33.5 ± 9.25% (37.0%) and for the TIS category it is 81.1 ± 14.5% (79.3%), therefore it can be expected that choosing the L0 TIS category can provide a better statistical precision for the determination of the UL on R.

6.3.1. Extended trigger set for the normalisation channel

The extended trigger set for the normalisation decay mode is only used to check the signal yield in order to evaluate a potential gain of the extended trigger set for the signal channel. However, only the default trigger set selection is used for the normalisation channel in this analysis, namely for the determination of the UL on R described in Chapter 8. The optimal MLP threshold based on the Punzi FoM for the extended trigger set is 0.975. Figure 6.34 shows the fitted invariant-mass spectrum after all selection requirements are applied and multiple candidates are removed. The signal yield for the extended trigger set selection is 562 ± 58 candidates with a local significance of 14.2 evaluated using Wilks' theorem.

Figure 6.35a shows the evaluated local significance as a function of different MLP thresholds for the extended trigger set using 2016–2018 data samples. The highest local significance of the Ξ_{cc}^{++} peak is evaluated for the MLP threshold of 0.975, which agrees with the value obtained using the Punzi FoM. Figure 6.35b shows the relative statistical uncertainty on the signal yield as a function of the MLP response. As for the default trigger set, more local minima caused by the signal and background fluctuations in

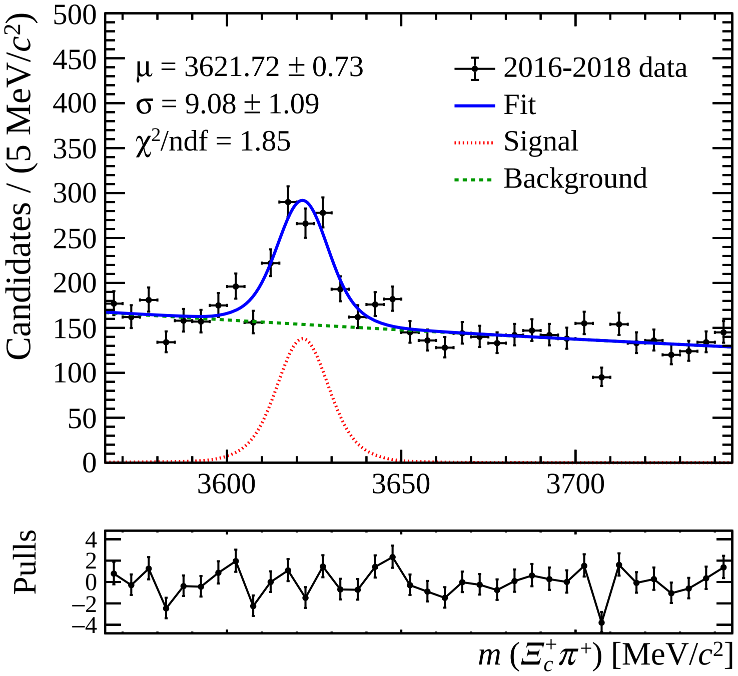

Figure 6.34.: Mass fit of the $\Xi_c^+\pi^+$ invariant-mass distribution after all selection requirements are applied for the combined 2016–2018 data samples in the extended trigger set. The DSCB plus Gaussian fit (red dotted line) is used to model the signal component and the exponential function (green dashed line) is used for the background.

different MLP bins are present, with one of them being at the MLP threshold of 0.975 evaluated by the Punzi FoM. The optimal MLP thresholds evaluated by different figures of merit are summarised in Table 6.27, where the signal yield and significance are compared. An increase of the signal yield in the extended trigger set is about 15% with respect to the default trigger set selection at the optimal MLP thresholds, but more importantly, the increase in the statistical significance is from 11.6 to 14.2.

6.3.2. Studies of a potential gain of a tighter PID selection

Two additional checks are performed to evaluate a potential gain of a tighter PID selection in addition to the already applied PID requirements in the trigger and preselection. Firstly, the ProbNN variables for proton, kaon and pion originating from the Ξ_c^+ baryon are added in the MVA training of the normalisation channel to check if there

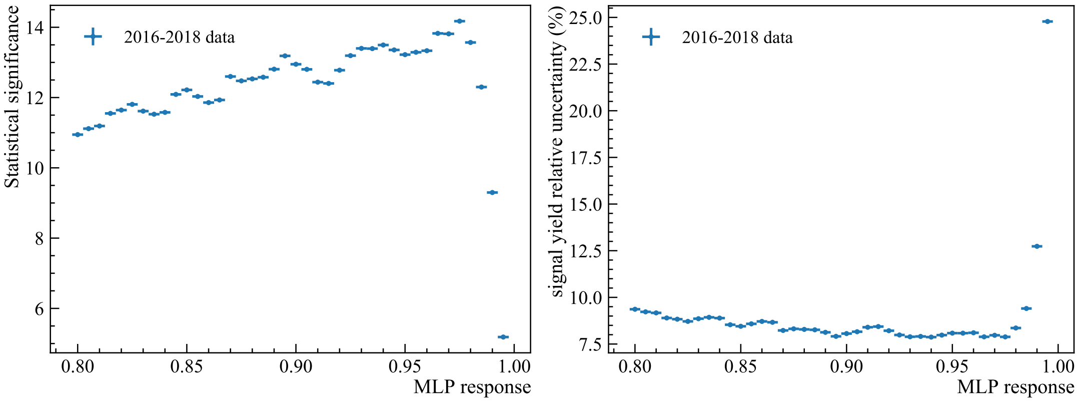

(a) **(b)**

Figure 6.35.: Statistical significance of the Ξ_{cc}^{++} peak (a) evaluated using Wilks' theorem and a relative statistical uncertainty on the Ξ_{cc}^{++} signal yield (b) as a function of the MLP threshold for the 2016–2018 data in the extended trigger set.

FoM	Optimal MLP threshold	Significance	Signal yield
Punzi FoM	0.975	14.2	562 ± 58
Maximum significance	0.975	14.2	562 ± 58
Minimum rel. yield unc.	0.940	13.5	993 ± 78

Table 6.27.: Comparison of signal yield and statistical significance for the normalisation channel in the extended trigger set at the optimal MLP thresholds evaluated by various different figures of merit.

is a significant gain in the signal yield which could indicate a potential improvement of the MVA selection by the use of additional PID variables in the training for the signal channel as well. At the optimal point evaluated by the Punzi FoM, the signal yield using the default trigger set selection for the MVA selection without the PID variables is 442 ± 56, whereas the signal yield for the MVA selection with the PID variables is increased to 508 ± 57 candidates. However, the background yield under the signal peak is also increased from 865 to 1412 candidates. Although the signal yield can be increased using the MVA training with the PID variables, there is no improvement in the overall signal purity, which is defined as $\mathrm{S}/\sqrt{\mathrm{S}+\mathrm{B}}$, where S is the number of the signal candidates and B is the number of the background candidates under the signal peak in the in $3\,\sigma$ mass region around the central mass value. This is probably caused by the fact that one of the variables used in the MVA training which approximates the momentum imbalance in the Ξ_{c}^{+} decay (Ξ_{c}^{+} proton momentum divided by the sum of the momenta of the Ξ_{c}^{+} decay products) is a measure of the particle misidentification,

PID cut	Signal yield	Background yield	Purity (%)	Significance
Default selection	399	833	32.39	11.8
ProbNN > 0.2	398	762	34.32	12.5
ProbNN > 0.3	387	722	34.90	12.4
ProbNN > 0.4	380	686	35.66	12.4
ProbNN > 0.5	361	651	35.66	12.3
ProbNN > 0.6	359	598	37.50	12.4
ProbNN > 0.7	337	544	38.23	12.2
ProbNN > 0.8	303	478	38.85	11.4
ProbNN > 0.9	239	363	39.71	10.7
$\mathrm{DLL}_{p\pi}$,$\mathrm{DLL}_{K\pi} > 6$	404	787	33.94	12.2
$\mathrm{DLL}_{p\pi}$,$\mathrm{DLL}_{K\pi} > 7$	378	748	33.53	11.9
$\mathrm{DLL}_{p\pi}$,$\mathrm{DLL}_{K\pi} > 8$	377	709	34.72	12.1
$\mathrm{DLL}_{p\pi}$,$\mathrm{DLL}_{K\pi} > 9$	361	678	34.73	12.0
$\mathrm{DLL}_{p\pi}$,$\mathrm{DLL}_{K\pi} > 10$	350	648	35.05	11.8

Table 6.28.: Signal and background yields in the $\pm 3\sigma$ invariant-mass window under the signal peak, a purity and a statistical significance extracted from the fit to the final invariant-mass spectrum after all selection requirements are applied for different additional PID requirements for proton and kaon from the Ξ_{c}^{+} baryon.

so part of the PID information is already used. Moreover, the PID requirements in the HLT2 trigger are already tight for the proton, kaon and pion originating from the Ξ_{c}^{+} baryon. Since the signal purity is not significantly improved, the PID variables are not used effectively in the MVA selection for the signal channel.

Additionally, the tighter PID requirements for a proton and a kaon from the Ξ_{c}^{+} baryon on top of the MVA selection are applied to check a potential gain in the signal purity of the normalisation channel. Table 6.28 shows the signal and background yields under the signal peak extracted from the fit to the final invariant-mass spectrum after all selection requirements are applied. One can see that there is a potential gain in purity by applying a tighter PID selection. However, as the increase in the evaluated significance is not very large, it was decided not to use the additional PID requirements, as the MVA selection would have to be re-trained since the rest of the PID requirements are applied in the pre-selection, which would significantly delay the analysis for only what appears as a marginal gain.

6.4. Agreement between the data and simulation

This section contains several studies to check the agreement between the variable distributions in the data and simulation.

6.4.1. Comparison for the Ξ_{cc}^{++} baryon

To check the simulation and data agreement for the variables used in this analysis, the s-weighted Ξ_{cc}^{++} candidates from the default trigger set are used and compared with their distributions in the simulation samples. The simulation samples use the PID and kinematic weights described in Sections 6.2.2 and 6.2.4. In order to increase the statistical precision for the comparison, more Ξ_{cc}^{++} candidates are selected for this study by using a looser MLP threshold of 0.925 based on the local minima of the evaluated relative statistical uncertainty on the signal yield shown in Figure 6.33b. The number of selected signal candidates for a given MLP threshold is 724 ± 67.

Firstly, the variables related to the VELO error parametrisation issue discussed in Section 4.1 are compared in order to check for any discrepancies between the 2016 and 2017–2018 data. Figure 6.36 shows distributions of the $\log(\chi^2_{\mathrm{IP}})$ variable for all final-state particles for both the s-weighted data and simulation samples separately for each year, whereas Figure 6.37 shows the same variables for all years combined, which benefits from the higher signal statistics. Figure 6.38 shows distributions of the $\log(\chi^2_{\mathrm{FD}})$ variable for the Ξ_c^+ baryon separately for each year. There are no significant differences between the studied years, but the low signal yield per year does not allow for any precise conclusions. However, the distributions for the s-weighted signal candidates for all years combined agrees well with their corresponding simulation distributions.

Figure 6.39 shows distributions of the variables used in the MVA training for both the s-weighted data and simulation samples. There are no large discrepancies observed between the data and simulation, and given the limited statistics for the s-weighted data, the distributions agree well within 1–2 σ of their statistical uncertainties. Since there are already corrections applied and systematic uncertainties assigned to account for the data and simulation differences, namely for the p_{T}, η, nTracks and PID variables where the discrepancies are the largest, there is no additional systematic uncertainty

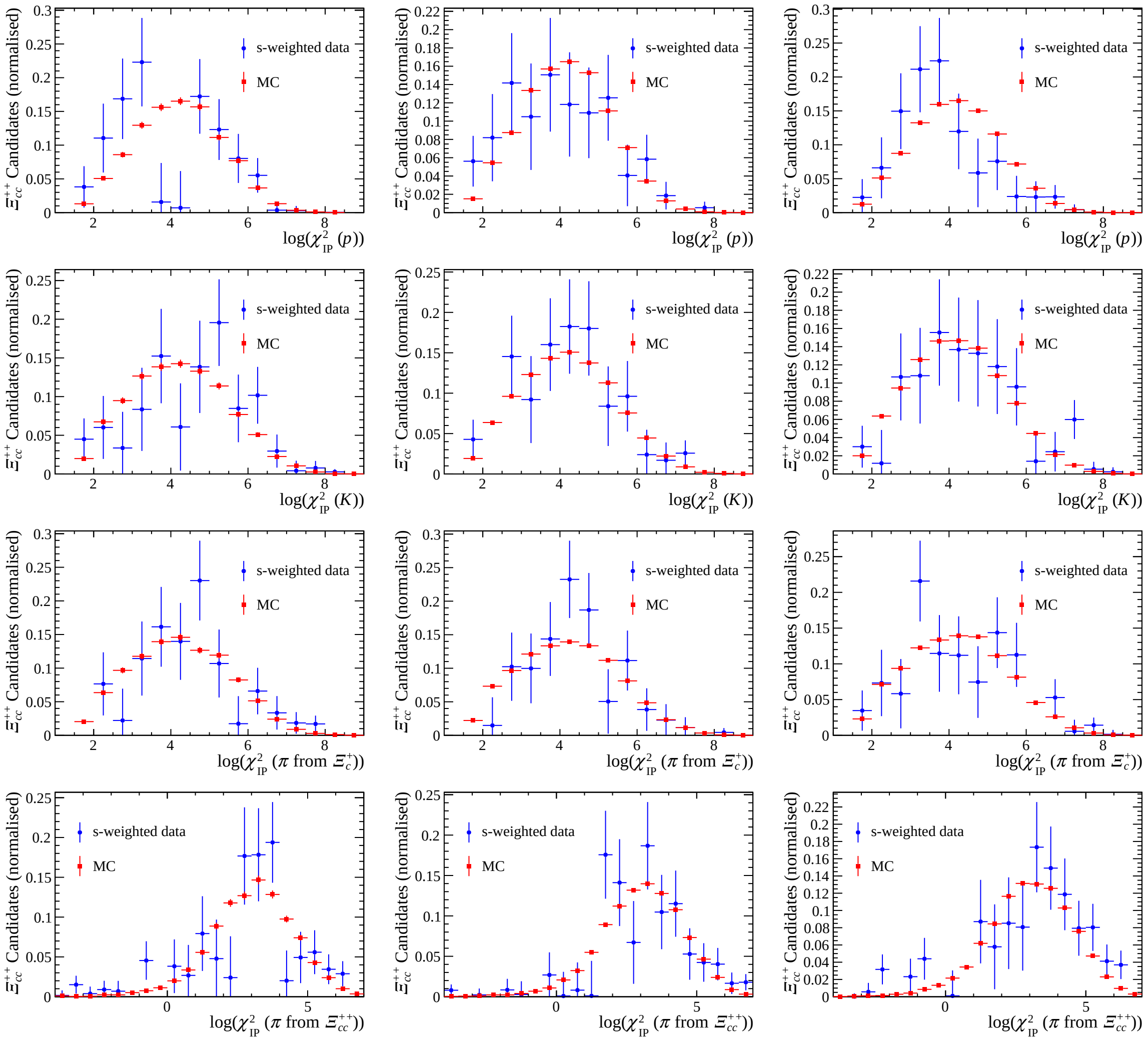

Figure 6.36.: Comparison of distributions for the $\log(\chi^2_{\rm IP})$ variable for all final state particles for the 2016 (first column), 2017 (middle column) and 2018 (last column) s-weighted (blue circles) and simulation (red squares) signal candidates after all selection requirements are applied.

considered, as it is expected to be covered by already assigned systematic uncertainties.

6.4.2. Comparison for the Ξ_c^{+} baryon

After the MVA selection, the sample of the Ξ_c^{+} candidates in the right-signed data of the normalisation channel is very clean. Therefore the distributions of the $\log(\chi^2_{\rm IP})$ and $\log(\chi^2_{\rm FD})$ variables in the data and simulation after the MVA selection are compared. Figures 6.40 and 6.41 show the distributions for all studied years separately. One can

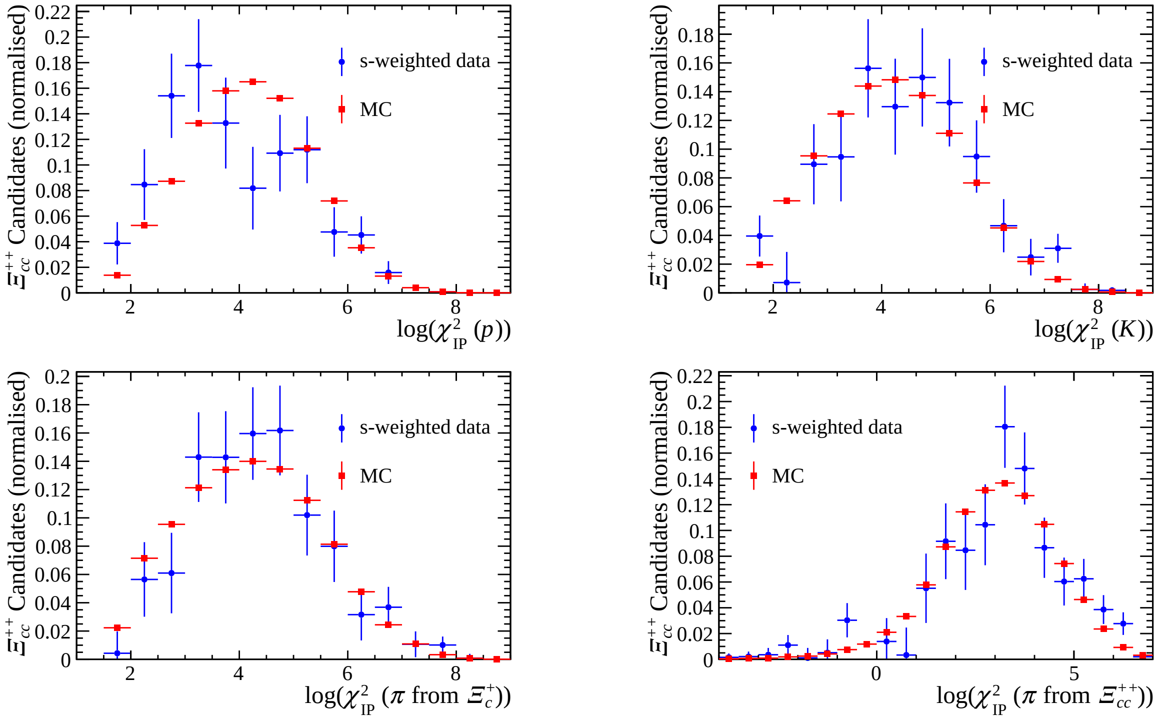

Figure 6.37.: Comparison of distributions for the $\log(\chi^2_{\rm IP})$ variable for all final state particles for the combined 2016–2018 s-weighted (blue circles) and simulation (red squares) signal candidates after all selection requirements are applied.

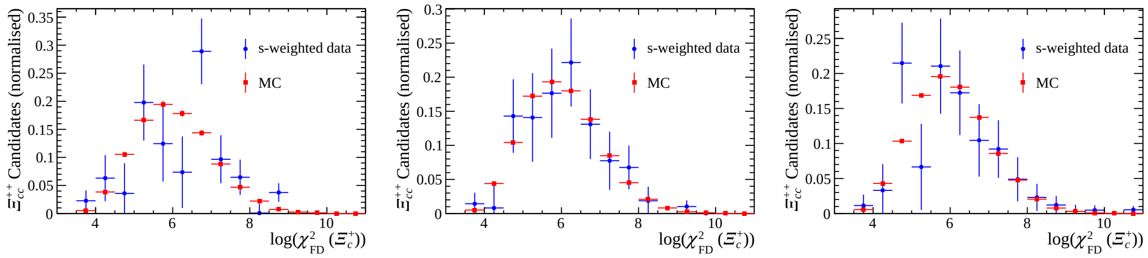

(a) **(b)** **(c)**

Figure 6.38.: Comparison of distributions for the $\log(\chi^2_{\rm FD})$ variable for the Ξ_c^+ baryon for the (a) 2016, (b) 2017 and (c) 2018 s-weighted (blue circles) and simulation (red squares) signal candidates after all selection requirements are applied.

see quite a significant disagreement between the data and simulation, especially in the $\log(\chi^2_{\rm IP}(\Xi_c^+))$ distributions of Figure 6.41, which is mainly caused by the fact that the simulation sample contains only the Ξ_c^+ baryons from the Ξ_{cc}^{++} decays, whereas there are also prompt and other secondary Ξ_c^+ candidates produced in the data sample that passed the final selection. However, no visible differences between the 2016 and 2017/2018 data samples are observed.

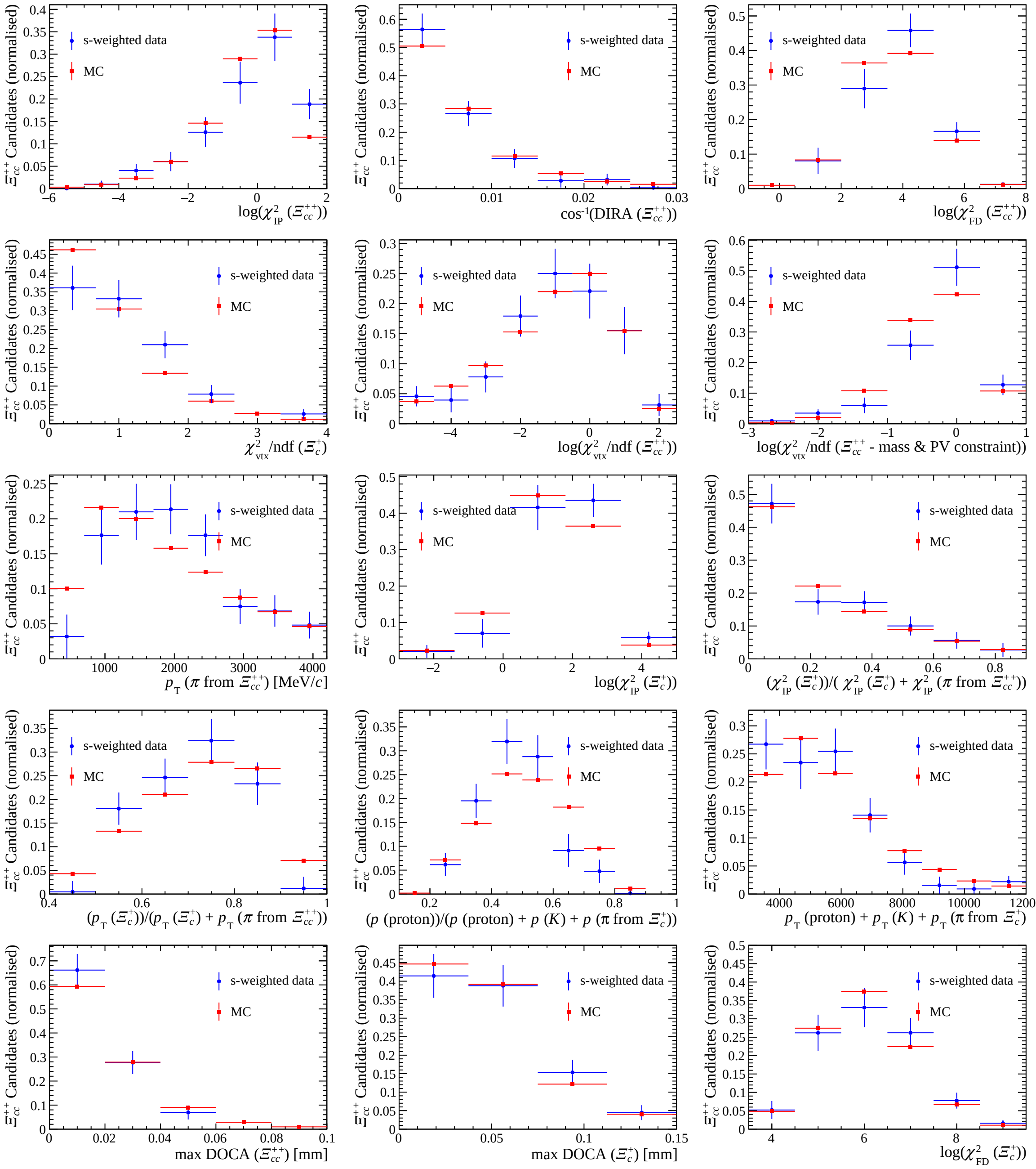

Figure 6.39.: Comparison of the variable distributions used in the MVA training for the s-weighted data (blue circles) from the $\Xi_{cc}^{++} \to \Xi_c^+ \pi^+$ decay and the corresponding simulation candidates (red squares) after all selection requirements are applied.

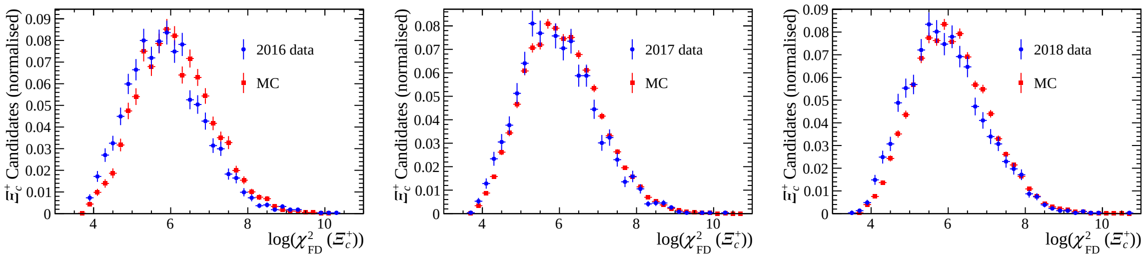

(a) **(b)** **(c)**

Figure 6.40.: Comparison of the Ξ_c^+ $\log(\chi^2_{\rm FD})$ distributions for the (a) 2016, (b) 2017 and (c) 2018 simulation (red squares) and right-signed (blue circles) data from the normalisation channel after all selection requirements are applied.

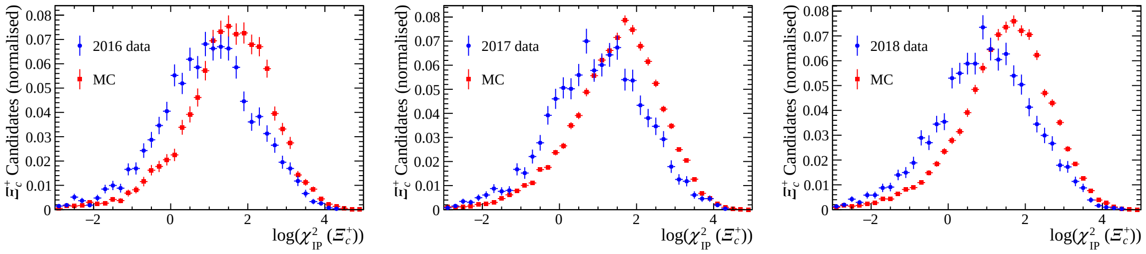

(a) **(b)** **(c)**

Figure 6.41.: Comparison of the Ξ_c^+ $\log(\chi^2_{\rm IP})$ distributions for the (a) 2016, (b) 2017 and (c) 2018 simulation (red squares) and right-signed (blue circles) data from the normalisation channel after all selection requirements are applied.

6.5. Summary

This chapter discussed the event and candidate selection for a search for the doubly charmed baryon Ξ_{cc}^{+} in the $\Xi_{cc}^{+} \to \Xi_{c}^{+}\pi^{-}\pi^{+}$ decays. This decay has never been searched for before, therefore the complete selection described in this chapter is uniquely designed to search for this particular decay channel. The selection is developed without the examination of the final invariant mass from 3.3 to 3.8 GeV to avoid any kind of bias, therefore the simulation candidates are used as a signal proxy to develop an efficient selection without a need to use the right-signed data in the blinded invariant-mass window.

The selection for the normalisation decay mode $\Xi_{cc}^{++} \to \Xi_{c}^{+}\pi^{+}$ is also developed and described in this chapter in order to design it in a similar way to the selection of the signal channel, so any potential systematic uncertainties introduced by the selection are minimised for the measurement of the UL on R.

To summarise, two main trigger sets are used to select the $\Xi_{cc}^{+} \to \Xi_{c}^{+}\pi^{-}\pi^{+}$ candidates - the default trigger set, which is used for both the signal and normalisation channel for the determination of the UL on R, and also for the first evaluation of the signal significance; and the extended trigger set with looser trigger requirements in order to enhance the probability of a signal observation. The extended trigger set is used only for the significance evaluation.

A number of thorough checks have been performed to ensure that the developed selection is robust, optimal, stable for different mass and lifetime hypotheses of the Ξ_{cc}^{+} baryon, and that no artificial peaking structures are introduced by the selection.

The selection described in this chapter is used for the measurements discussed in the following two chapters. Chapter 7 describes the observed unblinded mass spectrum and all related measurements and studies of the associated systematic uncertainties, together with the combination of the $\Xi_{cc}^{+} \to \Xi_{c}^{+}\pi^{-}\pi^{+}$ decay with the $\Xi_{cc}^{+} \to \Lambda_{c}^{+}K^{-}\pi^{+}$ decay mode. The determination of the UL on R, including the evaluation of the signal yield for the normalisation channel, the ratio of selection efficiencies, as well as the corresponding systematic uncertainties relevant for the study, are described in detail in Chapter 8.

Chapter 7.

Mass fit, significance, and combination with the $\Xi_{cc}^{+} \to \Lambda_c^+ K^- \pi^+$ decay

"Everyone, I have a very dramatic announcement. So anyone with a weak heart should leave now. Goodbye."
— Professor Farnsworth in Season 2 of *Futurama*

This chapter describes the studies related to the $\Xi_c^+ \pi^+ \pi^-$ invariant-mass distribution performed before and after unblinding. All procedures to measure the Ξ_{cc}^+ mass in case a significant signal would be observed were established before unblinding, together with the evaluation of the corresponding systematic uncertainties.

Firstly, the fit models to describe the signal and background distributions are presented in Section 7.1, followed by Section 7.2 where the methods to evaluate the local and global significances are described. Section 7.3 then presents the unblinded results for the $\Xi_c^+ \pi^+ \pi^-$ invariant-mass distribution, including the mass fit for both the default and extended trigger selections and the evaluation of the corresponding significances. Moreover, the combined mass fit with the $\Lambda_c^+ K^- \pi^+$ final state is described, as well as the evaluation of the combined local and global significances. The cross-checks performed before and after unblinding are discussed in Section 7.3.4. For completeness, the systematic uncertainties that would have been considered for the mass measurement performed in case a significant Ξ_{cc}^+ signal would have been observed are described in Section 7.4. Finally, the chapter is concluded and summarised in Section 7.5.

7.1. Fit to the mass spectra

To reduce the systematic uncertainty on the measured Ξ_{cc}^{+} mass, the difference in the measured mass between the Ξ_{cc}^{+} and Ξ_c^+ baryons is evaluated. The measured Ξ_{cc}^{+} mass is therefore defined as

$$m(\Xi_c^+ \pi^+ \pi^-) = m([\Xi_c^+ \pi^+ \pi^-]_{\Xi_{cc}^+}) - m([pK^- \pi^+]_{\Xi_c^+}) + m(\Xi_c^+), \tag{7.1}$$

where $m([\Xi_c^+ \pi^+ \pi^-]_{\Xi_{cc}^+})$ and $m([pK^- \pi^+]_{\Xi_c^+})$ represent the reconstructed invariant masses of the Ξ_{cc}^{+} and Ξ_c^+ baryons, respectively, and $m(\Xi_c^+)$ is the known mass of the Ξ_c^+ baryon of $2467.93 \pm 0.18\,\text{MeV}/c^2$ [188]. For a determination of the Ξ_{cc}^{+} and Ξ_c^+ invariant masses, the Decay Tree Fitter (DTF) is used [199], with a constraint on the Ξ_{cc}^{+} candidates to point to the PV. A momentum-scaling calibration to improve the mass resolution is also used in the refitting procedure. The $\Xi_c^+ \pi^+ \pi^-$ invariant-mass distribution is fitted with a signal and a combinatorial-background component. The studies to evaluate the signal component of the mass fit model are performed using the 2016–2018 simulation samples discussed in Section 6.1 with all selection requirements, which were described in Section 6.2, applied.

Figure 7.1 shows the signal mass fit, where the signal shape is modelled by the DSCB function [212] defined by Equation 6.7, plus a Gaussian distribution that shares the same mean value; thus is considered as a default mass model based on its fit quality. The DSCB function is considered as an alternative mass model for a systematic study which is discussed in Section 7.4.6. The number of signal candidates in the simulation extracted from the fit (taking into account kinematic, tracking and PID weights described in Chapter 6) is 26174 ± 156 for the default trigger set, and it is 35594 ± 189 for the extended trigger set, so the net increase of the signal yield for the extended trigger set with respect to the default trigger set is about 26%.

As described in Chapter 6, two different trigger selections are considered and for which the mass fit is prepared for the significance evaluation and for what would have been a mass measurement in case a significant signal would be observed. Figures 7.1a and 7.1b show the mass fit for the default and extended trigger sets, respectively. The mean and the width of the fitted mass peak are consistent for both trigger selections within their uncertainties. The fitted parameters for the default and extended trigger sets are summarised in Table 7.1. The mass resolution is given by equation

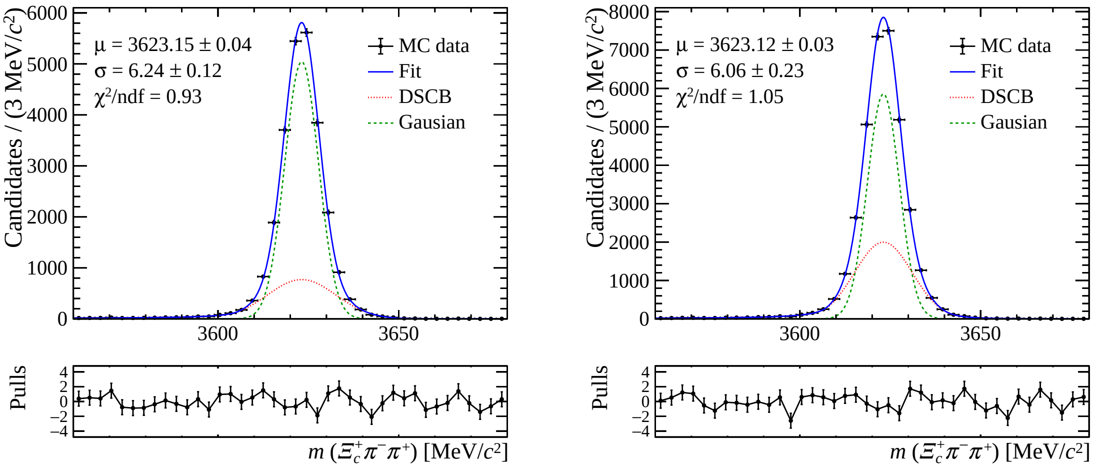

(a) **(b)**

Figure 7.1.: Invariant-mass distribution of the Ξ_{cc}^{+} candidates in the 2016–2018 simulation (black points) after all selection requirements are applied, fitted (blue solid line) with the Gaussian (green dashed line) plus DSCB (red dotted line) function for the (a) default and (b) extended trigger set.

$$\sigma = \sqrt{f \cdot \sigma_1^2 + (1-f)\cdot \sigma_2^2}, \tag{7.2}$$

where σ_1 and σ_2 are the widths of the Gaussian and the DSCB functions, respectively, and f is the fraction of the Gaussian component in the combined function. Since even a small change in a peak width can artificially influence the yield and therefore the evaluated significance, the resolution parameter is fixed in the final fit. The resolution is estimated to be $6.24 \pm 0.12\,\text{MeV}/c^2$ based on the fit to the simulation data for the default trigger set. However, the value of the mass resolution extracted from the simulation is corrected, in order to take into account a difference in resolution for data and simulation observed for the normalisation channel. The scale factor is based on the mass resolution for the normalisation channel, which is measured to be $6.94 \pm 0.32\,\text{MeV}/c^2$ for the simulation and $9.92 \pm 1.44\,\text{MeV}/c^2$ for the 2016–2018 data. As expected, the mass resolution in data is worse, even though it agrees with the simulation value within $2\,\sigma$. The resolution value for the signal channel in simulation is scaled by the same factor as observed in the normalisation channel, resulting in $8.92 \pm 1.37\,\text{MeV}/c^2$, and its central value of $8.92\,\text{MeV}/c^2$ is fixed in the final fit to the invariant-mass spectrum for the signal channel. All parameters of the fit, except from the signal yield and the mean, are fixed in the final mass fit to the Ξ_{cc}^{+} invariant-mass distribution after unblinding, based on the optimal fit performed on the simulation data. A systematic uncertainty arising from fixing the fit parameters is considered by using an alternative fit model, which is described in detail in Section 7.4.6.

An exponential function is chosen to model the combinatorial background based on the fit performed to the WSM invariant-mass distribution. The invariant-mass distributions for 20% of the WSM sample with the exponential fit after all selection requirements are applied for the default and extended trigger sets are shown in Figures 7.2a and 7.2b, respectively. The slope of the exponential function is kept free in the final fit. The exponential fit models the background distribution well, its χ^2/ndf is 0.79 for both trigger selections, therefore more complicated models with more parameters are not considered. The linear function is used as an alternative background model for the corresponding systematic study, which is described in Section 7.4.6.

Parameter	Value (default trigger)	Value (extended trigger)
μ [MeV/c^2]	3623.15 ± 0.04	3623.12 ± 0.03
σ [MeV/c^2]	6.24 ± 0.12	6.06 ± 0.23
σ (Gaussian)	4.67 ± 0.07	4.42 ± 0.14
f (Gaussian)	0.75 ± 0.02	0.56 ± 0.03
a_L	1.85 ± 0.12	1.94 ± 0.08
n_L	0.96 ± 0.23	1.19 ± 0.13
a_R	2.96 ± 0.18	2.21 ± 0.11
n_R	0.57 ± 0.40	3.29 ± 0.77

Table 7.1.: Fit parameters of the Gaussian plus DSCB function obtained from the fit to the $\Xi_c^+ \pi^- \pi^+$ invariant-mass distribution using the 2016–2018 simulation for the default and extended trigger sets after all selection requirements are applied. The mass of the Ξ_{cc}^{+} baryon in the simulation is set to 3621.4 MeV/c^2.

7.1.1. Partially reconstructed signal

In a recently published measurement of the Ξ_{cc}^{++} mass described in reference [78], significant contributions of the partially reconstructed $\Xi_{cc}^{++} \to (\Xi_c^{\prime +} \to \Xi_c^+ \gamma)\pi^+$ and $\Xi_{cc}^{++} \to \Xi_c^+(\rho^+ \to \pi^+ \pi^0)$ decays were observed. A measurement of the branching fraction of the $\Xi_{cc}^{++} \to (\Xi_c^{\prime +} \to \Xi_c^+ \gamma)\pi^+$ decay relative to that of the $\Xi_{cc}^{++} \to \Xi_c^+ \pi^+$ decay

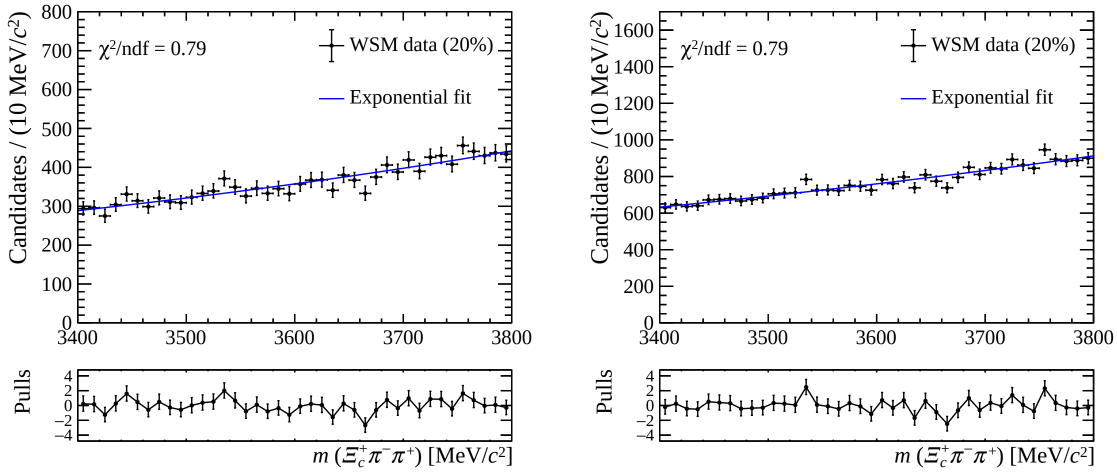

(a) **(b)**

Figure 7.2.: Invariant-mass distribution of the 2016–2018 WSM data (black points) with the exponential fit (blue solid line) after all selection requirements are applied for the (a) default and (b) extended trigger set.

was recently published in a dedicated analysis [214]. To examine possible similar contributions for the studied decay mode $\Xi_{cc}^{+}\to\Xi_c^+\pi^-\pi^+$, the simulation samples are locally generated for the following decay channels:

- $\Xi_{cc}^{+}\to(\Xi_c^{\prime +}\to\Xi_c^+\gamma)\pi^-\pi^+$,
- $\Xi_{cc}^{+}\to\Xi_c^+(\omega\to\pi^-\pi^+\pi^0)$,
- $\Xi_{cc}^{+}\to\Xi_c^+(\eta\to\pi^-\pi^+\pi^0)$,
- $\Xi_{cc}^{+}\to\Xi_c^+(\eta\to\pi^-\pi^+\gamma)$,
- $\Xi_{cc}^{+}\to\Xi_c^+\pi^-(\rho^+\to\pi^+\pi^0)$,
- $\Xi_{cc}^{+}\to\Xi_c^+(\eta^\prime\to\pi^-\pi^+\gamma)$,
- $\Xi_{cc}^{++}\to\Xi_c^+\pi^-\pi^+\pi^+$.

The masses of the Ξ_{cc}^{+} and Ξ_{cc}^{++} baryons in the simulation samples are set to 3621.4 MeV/c^2. For the purpose of this study, only 100k simulation events are produced at the generator level for each of the mentioned partially reconstructed decays, (apart from the $\Xi_{cc}^{+}\to\Xi_c^+\pi^-(\rho^+\to\pi^+\pi^0)$ decay, for which it is 60k events), in order to save the CPU resources by not requesting the full simulation sample as before unblinding it was not clear whether those components would be visible or not. In case a significant signal would be observed with some visible partially reconstructed decays, the full simulation samples would be requested in order to model them properly.

Since the generator-level simulation samples do not contain the information from the reconstruction, the generated momenta of the charged final-state particles are smeared using a smearing factor obtained from the full simulation samples used in this analysis by comparing their generated and reconstructed momenta. The smeared momenta of the charged final state particles are used to calculate the $\Xi_c^{+} \pi^{+} \pi^{-}$ invariant mass to approximate the reconstructed line shapes of these partially reconstructed decays and their potential contribution to the fitted mass spectra, as shown in Figure 7.3.

As the presence of the partially reconstructed decays in the studied invariant-mass window can impact the signal significance, a study based on pseudoexperiments is performed to evaluate its effect before unblinding. The number of background events used in the generated pseudoexperiments is estimated from the WSM data in the invariant-mass window from 3400 to 3800 MeV/c^2, scaled up to take into account that only 20% of the WSM data is used and to consider a different number of events in the WSM and right-signed data, as discussed for the Punzi FoM in Section 6.2.6. Only a marginal signal yield of 225 candidates with an average local significance of about 2.5 σ is injected, to estimate the impact around 3 σ of the decision threshold and to test the partially reconstructed decays that could be mistaken for a combinatorial background. The number of candidates considered for different partially reconstructed decays can be found in Table 7.2. As the relative branching fractions of these decays with respect to the signal mode are unknown, the estimates of the yields are based on similar components seen for the $\Xi_{cc}^{++} \to \Xi_c^{+} \pi^{+}$ decay [78,214]. The probability density functions for these components are obtained from the line shapes shown in Figure 7.3 by kernel density estimation using ROOT [174] class *RooKeysPdf*.

The study is perfomed with 1000 pseudoexperiments, each one generating a dataset for two models: the signal plus combinatorial background model, and the signal plus combinatorial model with partially reconstructed decays. Both datasets are fitted with the nominal fit model and the significance difference between the two datasets is evaluated for each pseudoexperiment using Wilks' theorem [213] at the nominal Ξ_{cc}^{+} mass of 3621.4 MeV/c^2. Figure 7.4 shows the difference between the significance obtained from the nominal fit to the spectra without the partially reconstructed components and the significance from the nominal fit to the spectra with these components considered. The significance bias based on the Gaussian fit is 0.58. The pseudoexperiments are also

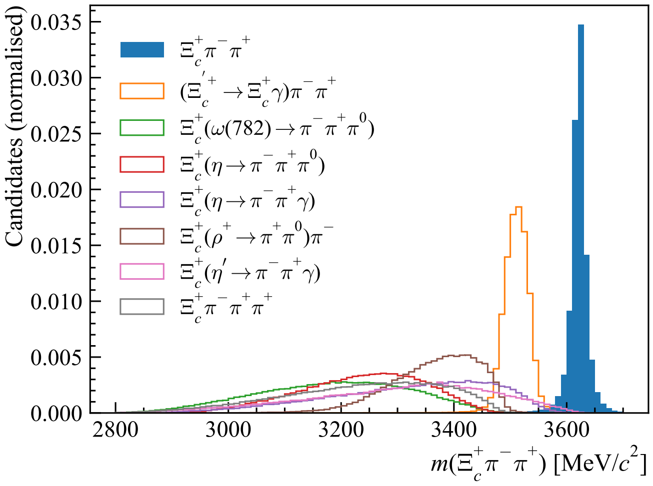

Figure 7.3.: Invariant mass of the $\Xi_{cc}^{+(+)}$ baryons, decaying into the final states given in the legend, that could potentially contribute to the invariant-mass distribution of the $\Xi_c^+\pi^-\pi^+$ final state due to a partial reconstruction of their decay. The invariant mass is calculated from the smeared generator-level momenta of the charged final state particles.

Decay	Estimated yield
$\Xi_{cc}^{+}\to(\Xi_c^{\prime +}\to\Xi_c^+\gamma)\pi^-\pi^+$	360
$\Xi_{cc}^{+}\to\Xi_c^+(\omega\to\pi^-\pi^+\pi^0)$	135
$\Xi_{cc}^{+}\to\Xi_c^+(\eta\to\pi^-\pi^+\pi^0)$	135
$\Xi_{cc}^{+}\to\Xi_c^+(\eta\to\pi^-\pi^+\gamma)$	25
$\Xi_{cc}^{+}\to\Xi_c^+\pi^-(\rho^+\to\pi^+\pi^0)$	135
$\Xi_{cc}^{+}\to\Xi_c^+(\eta'\to\pi^-\pi^+\gamma)$	25
$\Xi_{cc}^{++}\to\Xi_c^+\pi^-\pi^+\pi^+$	225

Table 7.2.: Number of candidates for the partially reconstructed decays estimated from the structures seen in the normalisation decay $\Xi_{cc}^{++}\to\Xi_c^+\pi^+$ [78,214] used for the study with pseudoexperiments.

generated for double and half of the yields for the partially reconstructed components summarised in Table 7.2. The presence of an unknown partially reconstructed background in all cases decreases the evaluated significance, so it can be concluded that the evaluated significance is not artificially inflated by not including these components in the final mass model even if they would be present in the selected data set.

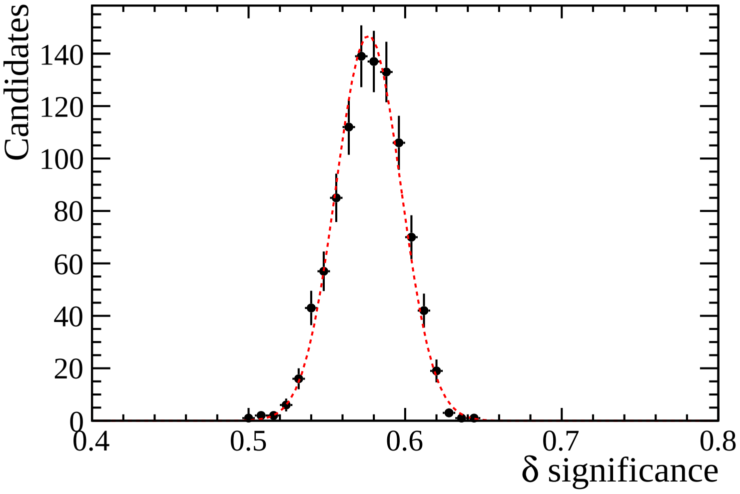

Figure 7.4.: Difference between the significance obtained from the nominal fit to the spectra without the partially reconstructed components and the significance from the nominal fit to the spectra with these components considered (black points), fitted by the Gaussian function (red dashed line) with a mean of 0.58. The positive shift means that the significance is decreased if the presence of the partially reconstructed background is not considered.

7.2. Method to evaluate a signal significance

As mentioned in Section 5.2, the decision for the final strategy of this analysis is carried out only after unblinding, and it depends on the evaluated local and global significances, as shown in Figure 5.2. Procedures for the evaluation of both significances are described in this section, whereas the corresponding unblinded results are discussed in the dedicated Section 7.3.

A signal significance is based on the evaluated p-value, which is a probability of a given dataset being more compatible with the signal-plus-background hypothesis, assuming the background-only hypothesis is true. There is a difference between a local significance, which is evaluated for a signal at one particular mass, and a global significance given for some particular mass range taking into account the look-elsewhere effect (LEE), which evaluates the probability under the background-only hypothesis to observe a particular signal anywhere in the considered mass range. As the relation between the number of equivalent one-sided Gaussian sigma and the p-value is non-linear, the LEE effect is an important correction for low local significance where the difference in p-values between $2\,\sigma$ and $3\,\sigma$ is at the level of 20, whereas for a high significance above $6\,\sigma$, the LEE correction is negligible. Therefore if there would be a peak with the local significance $> 6\,\sigma$ observed after unblinding, only the local significance would be quoted, the observation would be reported and the mass and R evaluation would be performed. If there would be a peak with the local significance between $3\,\sigma$ to $6\,\sigma$, the LEE correction would be determined. If the global significance would be above $5\,\sigma$, the observation would be reported and the mass and R evaluation would be performed, otherwise the local and global significances would be evaluated with the extended trigger set selection applied. Full details of the prepared post-unblinding decisions can be found in Figure 5.2 and in Chapter 5. Lastly, the case that actually happened after unblinding was that the local significance for the default trigger set was less than $3\,\sigma$, therefore the local significance was evaluated also for the extended trigger set, which was also found to be less than $3\,\sigma$, as described in Section 7.3. Therefore the combined fit with the $\Lambda_c^+ K^- \pi^+$ final state was performed and the corresponding significances were evaluated for a combined spectrum based on the same rules as described above for one spectrum.

The systematic uncertainty on the measured yield, which is described in the following Chapter 8 in Section 8.4.4, was taken into account for the significance evaluation for the combination with the $\Lambda_c^+ K^- \pi^+$ final state, since the corresponding significance was between 3 and $4\,\sigma$. The pre-unblinding strategy for this analysis outlined also a case if a significance would be 5–$6\,\sigma$, in which case this systematic uncertainty would be also considered, otherwise only a statistical significance would be quoted as the systematic correction would not have any impact on the decision based on the measured significance.

7.2.1. Local significance

To calculate a local p-value as a function of the Ξ_{cc}^{+} mass, the test statistic $q_{\pm}$, similar to that described in reference [215], is firstly evaluated as

$$q_{\pm} = \begin{cases} -2\ln\left(\frac{L(0,\hat{\theta})}{L(\hat{\mu},\hat{\theta})}\right), & \hat{\mu} \geq 0 \\ 2\ln\left(\frac{L(0,\hat{\theta})}{L(\hat{\mu},\hat{\theta})}\right), & \hat{\mu} < 0, \end{cases} \tag{7.3}$$

where $L(\mu,\theta)$ is the profile-likelihood function, the variable $\hat{\mu}$ is the signal yield and $\hat{\theta}$ represents the nuisance parameters that maximise the likelihood. The log-likelihoods are evaluated from the mass fits to the Ξ_{cc}^{+} invariant-mass spectrum, where the signal yield is fixed to zero for the numerator and left floating for the denominator, for which the negative values are also allowed. The test statistic in Equation 7.3 is based on the test statistic q_0 defined in reference [215], but contrary to q_0 the test statistic $q_\pm$ is assigned the value $-q_0$ instead of zero when the fit yields a negative number of signal candidates, in order to obtain a smooth p-value curve for downward fluctuations. The statistical distribution of the $q_\pm$ asymptotically follows a chi-square (χ^2) distribution under the background-only hypothesis, as shown in reference [215] for q_0. The p-values are therefore calculated from the observed test statistic $q_\pm$ using the asymptotic formula corresponding to a χ^2 distribution for one degree of freedom, $0.5 \cdot \chi_1^2(q_\pm)$, which follows Wilks' theorem [213].

The minimum p-value in the evaluated invariant-mass spectrum is then transformed into the number of equivalent one-sided Gaussian significance (σ) such that

$$\text{significance} = \sqrt{2} \times \text{erfc}^{-1}(p\text{-value} \times 2), \tag{7.4}$$

where erfc^{-1} is the inverse complementary error function.

To cross-check that the test statistic used for the evaluation of the local p-values follows the expected χ^2 distribution with one degree of freedom, two different studies are performed. Firstly, 50k background-only pseudoexperiments are generated, where the number of events for each sample is determined from a Poisson distribution based on the expected number of background candidates extracted from the WSM sample and the corresponding background shape. The test statistic $q_\pm$ is subsequently calculated from the mass fits as shown in Equation 7.3. Figure 7.5a shows the distribution of the test statistic calculated from the fits for the nominal Ξ_{cc}^{+} mass fitted by the χ^2 function with one degree of freedom.

Alternatively, a less computationally expensive method can be used with many more generated pseudoexperiments, for which the number of signal and background candidates observed in a signal window are considered rather than generating the full mass spectra with the background-only and signal-plus-background fits. One can simply calculate the test statistic by sampling the number of observed signal candidates n and the number of expected background candidates b in the signal region from the Poisson distribution, sometimes called a counting experiment. Using the Poisson distributions for the background-only and the signal-plus-background hypotheses in Equation 7.3, the test statistic $q_{\pm}$ can be calculated as

$$q_{\pm} = \begin{cases} 2\cdot\left(n\ln(\frac{n}{b})+b-n\right), & n\geq b, n\neq 0\\ -2\cdot\left(n\ln(\frac{n}{b})+b-n\right), & n<b, n\neq 0\\ -2b, & n=0. \end{cases} \tag{7.5}$$

The numbers of the observed signal candidates n and the expected background candidates b in the signal region $\pm 2\sigma$ around the studied mass are sampled from a Poisson distribution by generating 10 million pseudoexperiments. Figure 7.5b shows the distribution of the test statistic calculated from the counting experiment for the nominal Ξ_{cc}^{+} mass fitted by the χ^2 function with one degree of freedom.

Both results are compatible and give very similar p-values. For example, for one generated observed spectrum with the test statistic of 0.22, the p-value extracted from the pseudoexperiments for the Poisson statistics is 0.3191, it is 0.3186 based on the fitted pseudoexperiments, and it is 0.3195 using the asymptotic formula.

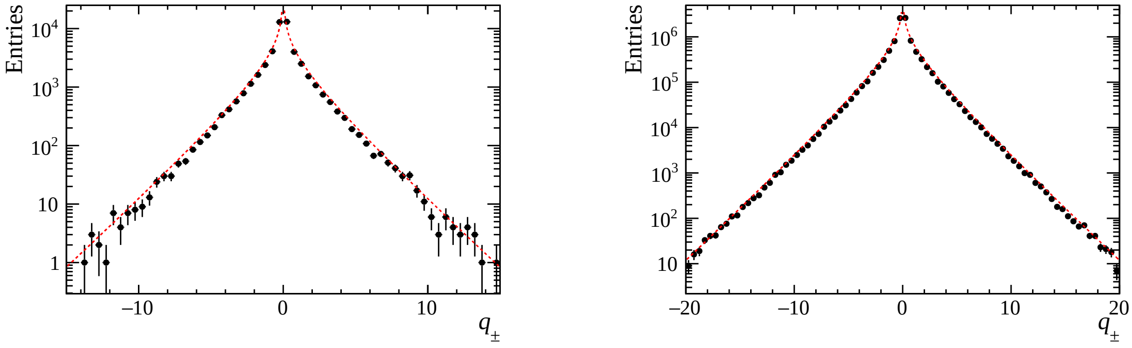

(a)

(b)

Figure 7.5.: Distributions of the test statistic for the nominal Ξ_{cc}^{+} mass fitted by the χ^2 function with one degree of freedom, where the test statistic is calculated (a) from the fits and (b) from Poisson statistics.

7.2.2. Global significance

For a global significance, the LEE is taken into account in the $\Xi_c^{+}\pi^{-}\pi^{+}$ invariant-mass window from 3.5 to 3.7 GeV/c^2, which covers most of the theoretical predictions for the mass of the Ξ_{cc}^{+} baryon, the mass of the observed isospin partner Ξ_{cc}^{++}, and also the mass of the Ξ_{cc}^{+} state reported by the SELEX experiment. Firstly, the following procedure is used to estimate the optimal method for the estimation of the global p-value, accounting for the LEE:

- performing 10k pseudoexperiments by generating a full mass spectrum from 3.5 to 3.7 GeV/c^2 under the background-only hypothesis;
- for each pseudoexperiment, evaluating the p-value as a function of the Ξ_{cc}^{+} mass, using a 2 MeV/c^2 step and the mean value of the signal component fixed to the centre of the bin, and finding the smallest p-value in the spectrum;
- evaluating what fraction of pseudoexperiments have their minimal p-value smaller than the one observed in the data.

In case the evaluated global significance by the described procedure would be less than 3 σ, steps described above would be repeated for 10k more pseudoexperiments in order to evaluate the global significance more precisely.

However, the procedure described above is CPU intensive for larger significance values as more pseudoexperiments need to be generated in order to reach a desired precision. Therefore in case the observed significance would be $> 3\,\sigma$, the global p-value would be estimated using the asymptotic formula [216]

$$P_{\text{global}} = P(\chi_s^2 > c) + \langle N(c_0) \rangle \left(\frac{c}{c_0} \right)^{(s-1)/2} e^{-(c-c_0)/2}, \tag{7.6}$$

where c is the observed extended likelihood ratio $2\Delta \ln \mathcal{L}$, s is the number of degrees of freedom of the χ_s^2 distribution, which is 1 for one mass spectrum, and c_0 is a reference level across which the number of *upcrossings* $\langle N(c_0) \rangle$ is calculated. The number of *upcrossings* $\langle N(c_0) \rangle$ is the number of times that the likelihood ratio curve goes from below to above a certain threshold c_0.[1] The threshold c_0 should be chosen to be close to zero, but above the numerical noise, and it is recommended to be 0.5 for $s = 1$ in reference [216]. However, a correctly chosen value of c_0 should not have a significant impact on the result once it is evaluated with many pseudoexperiments. The $\langle N(c_0) \rangle$ is evaluated with at least 1000 pseudoexperiments with zero signal yield in the mass region from 3.5 to 3.7 GeV/c^2. The observed $\langle N(c_0) \rangle$ is then converted into the global p-value. Since the global significance is evaluated for a combined spectrum with the $\Lambda_c^+ K^- \pi^+$ final state, the asymptotic formula is extended to fitting

---

[1] To better illustrate what the number of upcrossings represents, one can have a sneak peek at Figure 7.17 on page page 178 where the results for the combination with the $\Lambda_c^+ K^- \pi^+$ final state are presented.

two spectra simultaneously, as discussed in [216], for which the number of degrees of freedom $s = 2$ and the threshold $c_0 = 1$. For the local significance around $3\,\sigma$, both pseudoexperiments and the asymptotic formula are evaluated in order to cross-check the result.

7.3. Unblinded results

This section describes the mass fit and the significance evaluation of the unblinded $\Xi_c^{+} \pi^{-} \pi^{+}$ invariant-mass spectrum for the 2016–2018 data. Based on the evaluated local significance of the $\Xi_{cc}^{+} \to \Xi_c^{+} \pi^{-} \pi^{+}$ final state for the default and extended trigger sets described below, a combination with the $\Xi_{cc}^{+} \to \Lambda_c^{+} K^{-} \pi^{+}$ final state is also performed, and the results for the simultaneous fit and the combined local and global significances are discussed. All p-value scans are performed with $1\,\mathrm{MeV}/c^2$ step with the mass fixed at the centre of the bin. The invariant-mass spectra are fitted in the range from 3385 to $3815\,\mathrm{MeV}/c^2$ to avoid edge effects on the p-value plots. The values of the local significances are evaluated from the corresponding p-values using Equation 7.4.

Figure 7.6 shows the unblinded $\Xi_{cc}^{+} \to \Xi_c^{+} \pi^{-} \pi^{+}$ invariant-mass spectrum and the WSM distribution normalised to the right-signed data for the default and extended trigger sets. The WSM sample for the extended trigger set contains only 20% of the data sample randomly selected, since the full data sample is not needed for any of the studies performed in this analysis. A comparison of the right-signed and WSM data with the WSP distribution can be found in Figure 7.7.

7.3.1. Default and extended trigger sets

Figure 7.8 shows the p-value scans of the unblinded $\Xi_c^{+} \pi^{+} \pi^{-}$ invariant-mass spectrum for the default and extended trigger sets using 2016–2018 data. The minimum p-value of 0.0108 at the mass of $3617\,\mathrm{MeV}/c^2$, corresponding to $2.3\,\sigma$ local significance, is found for the default trigger set. Since the evaluated significance for the default trigger set is below $3\,\sigma$, the p-value scan is also performed for the extended trigger set. The minimum p-value for the extended trigger set is 0.0024 corresponding to a local significance of $2.8\,\sigma$ at the mass of $3452\,\mathrm{MeV}/c^2$, with the second minimum at the same mass as for the default trigger set at $3617\,\mathrm{MeV}/c^2$, corresponding to a p-value of 0.0101 and a local significance of $2.3\,\sigma$. There is a visible double-peak

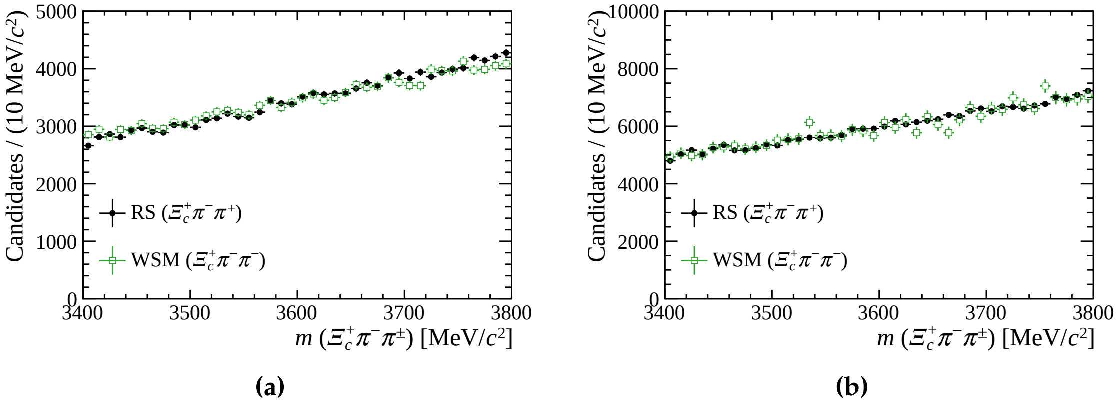

Figure 7.6.: Unblinded 2016–2018 $\Xi_c^+\pi^-\pi^+$ invariant-mass spectrum (black points) and the 2016–2018 WSM data (green squares) normalised to the $\Xi_c^+\pi^-\pi^+$ distribution for the (a) default and (b) extended trigger set. The WSM sample for the extended trigger set contains only 20% of the full data sample randomly selected.

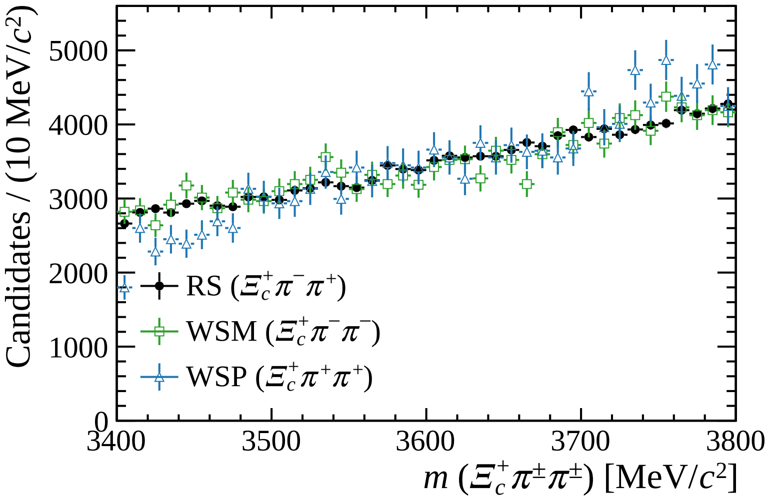

Figure 7.7.: Unblinded 2016–2018 $\Xi_c^+\pi^-\pi^+$ invariant mass spectrum (black points) and 20% of the 2016–2018 WSM (green squares) and WSP data (blue triangles) normalised to the $\Xi_c^+\pi^-\pi^+$ distribution for the default trigger set.

structure around 3450 MeV/c^2 that could be just a statistical fluctuation, but if it would be caused by the presence of the signal it could be a partially reconstructed decay, most likely the $\Xi_{cc}^{+} \to \Xi_c^+\pi^-\rho^+$ decay with the ρ^+ meson decaying into the $\pi^+\pi^0$ final state, as discussed in detail in Section 7.1.1. However, this decay, and also other partially reconstructed decays, are not considered for further study before the first observation of the Ξ_{cc}^{+} baryon in a fully-reconstructed final state, since the missing (or even reconstructed) π^0 meson or photon would significantly worsen a mass resolution.

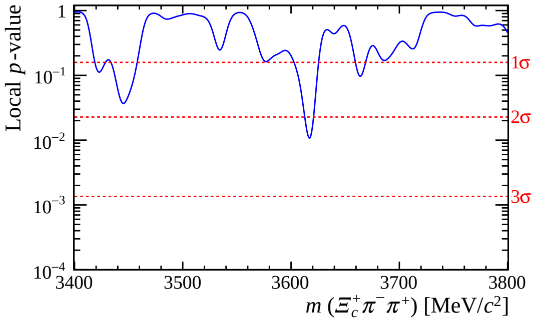

(a) **(b)**

Figure 7.8.: Local p-values as a function of the Ξ_{cc}^{+} invariant mass for the (a) default and (b) extended trigger set.

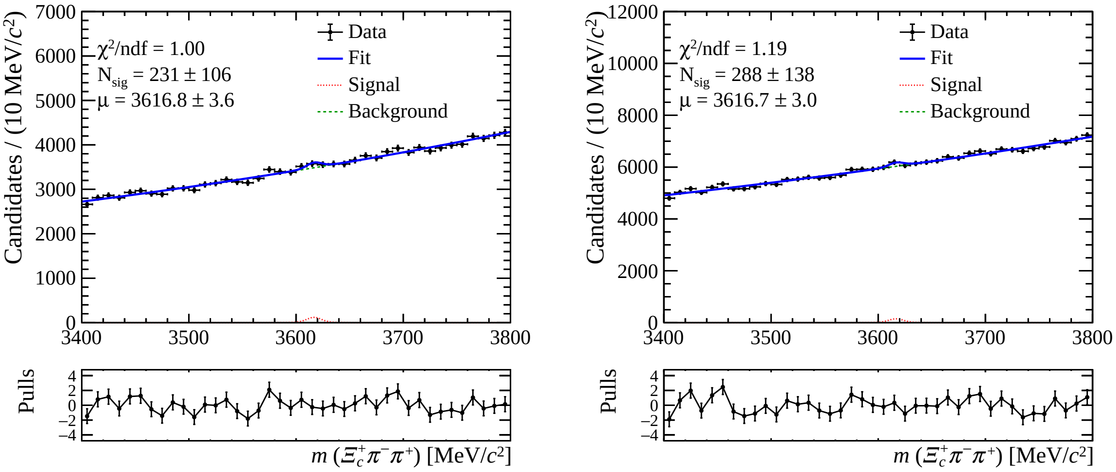

(a) **(b)**

Figure 7.9.: Mass fit to the unblinded 2016–2018 $\Xi_c^+\pi^-\pi^+$ invariant-mass spectrum for the (a) default and (b) extended trigger set.

The mass fit to the unblinded $\Xi_c^+\pi^+\pi^-$ invariant-mass spectrum for the default and extended trigger sets using 2016–2018 data is shown in Figure 7.9. The mass parameter is floated in the fit but its initial value is set to where the minimum p-value is found. All other parameters for the signal model are fixed to the values obtained from the simulation as shown in Table 7.1, whereas the parameter of the exponential fit is kept free in the final fit. A good quality of the final fit is obtained. The fitted mass is $3616.8 \pm 3.6\,\text{MeV}/c^2$ and $3616.7 \pm 3.0\,\text{MeV}/c^2$ and the number of fitted signal candidates is 231 ± 106 and 288 ± 138 the for the default and extended trigger sets, respectively.

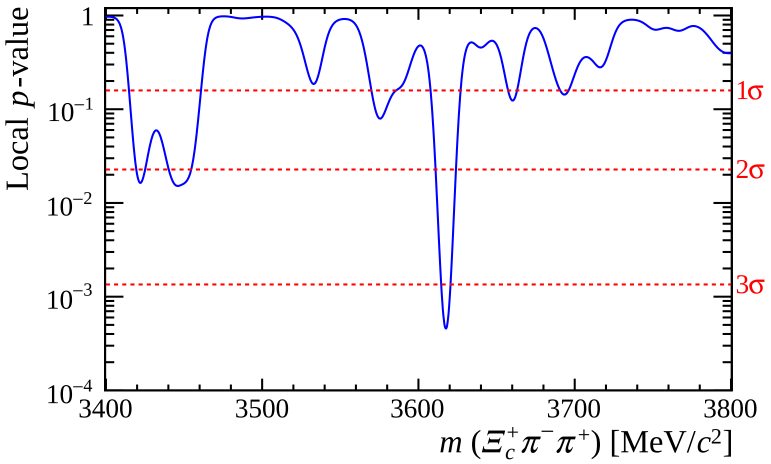

Figure 7.10.: Local p-values as a function of the Ξ_{cc}^{+} invariant mass using the HLT selection of the default trigger set and the L0 requirements of the extended trigger set (L0 TIS or TOS).

Figure 7.10 shows the p-value scan using the HLT selection of the default trigger set and the L0 requirements of the extended trigger set (L0 TIS or TOS). For this scenario, the minimum p-value is 0.00047, corresponding to a significance of $3.3\,\sigma$ at the mass of $3617\,\mathrm{MeV}/c^2$. Figure 7.11 shows the mass fit to the $\Xi_c^+\pi^-\pi^+$ invariant-mass spectrum with this configuration, for which 371 ± 121 candidates is found. This configuration is not used in any of the subsequent analysis decisions as it was not chosen to be used in the decision tree before unblinding, but it provides an additional cross-check that the structure seen around $3620\,\mathrm{MeV}/c^2$ is stable using a different trigger selection.

Since the local significance is below $3\,\sigma$ for both the default and extended trigger sets, the combination with the $\Lambda_c^+ K^- \pi^+$ final state is performed, which is described in detail in Section 7.3.3.

7.3.2. Resonant decay $\Xi_{cc}^{+} \to \Xi_c(2645)^0 \pi^+$

As described in Section 5.2.2, an additional planned cross-check after unblinding was to restrict the $\Xi_c^+\pi^-$ invariant-mass region from 2635 to $2660\,\mathrm{MeV}/c^2$ in order to evaluate the significance of the possible resonant decay $\Xi_{cc}^{+} \to (\Xi_c(2645)^0 \to \Xi_c^+\pi^-)\pi^+$. Figure 7.12 shows the $\Xi_c^+\pi^-$ invariant-mass spectrum for the 2016-2018 right-signed data in the default trigger set, where the $\Xi_c(2645)^0$ resonance is clearly visible. The $\Xi_c^+\pi^-\pi^+$ invariant-mass spectrum after the $\Xi_c^+\pi^-$ invariant-mass constraint is applied is shown in Figures 7.13a and 7.13b for the default and extended trigger sets,

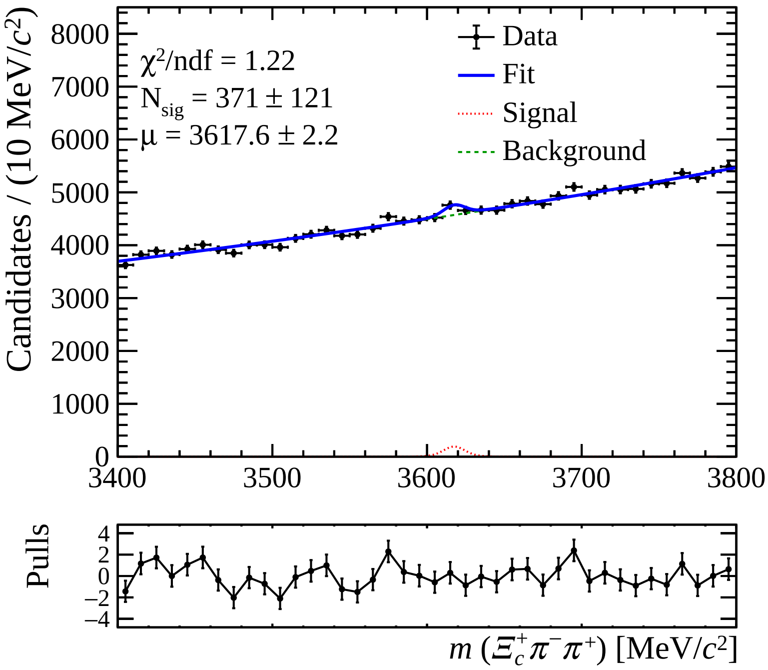

Figure 7.11.: Mass fit to the unblinded 2016–2018 $\Xi_c^+ \pi^- \pi^+$ invariant-mass spectrum using the HLT selection of the default trigger set and the L0 requirements of the extended trigger set (L0 TIS or TOS).

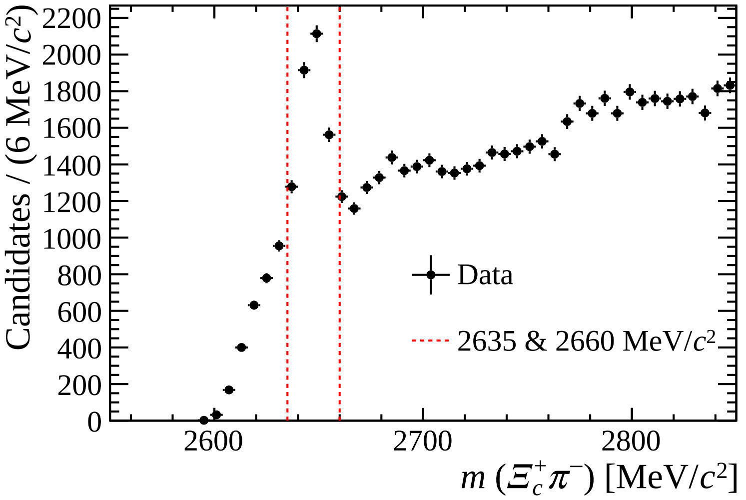

Figure 7.12.: Invariant-mass spectrum of the $\Xi_c^+ \pi^-$ final state for the 2016-2018 data in the default trigger set. The visible peak corresponds to the $\Xi_c(2645)^0$ resonance.

respectively. Only the background fluctuations are visible in the studied mass spectra, without any sign of a significant signal peak.

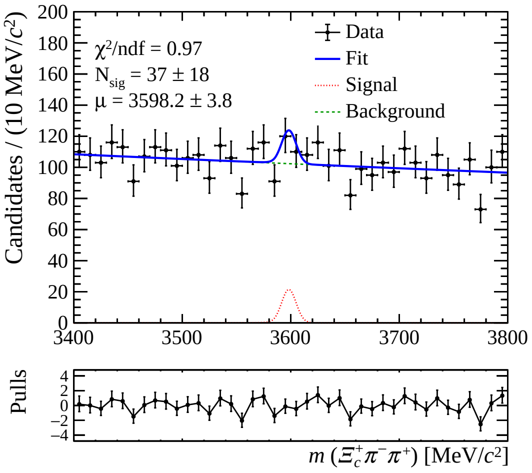

(a) **(b)**

Figure 7.13.: Mass fit to the unblinded 2016–2018 $\Xi_c^+\pi^-\pi^+$ invariant-mass spectrum for the (a) default and (b) extended trigger set after the $\Xi_c^+\pi^-$ invariant-mass constraint is applied.

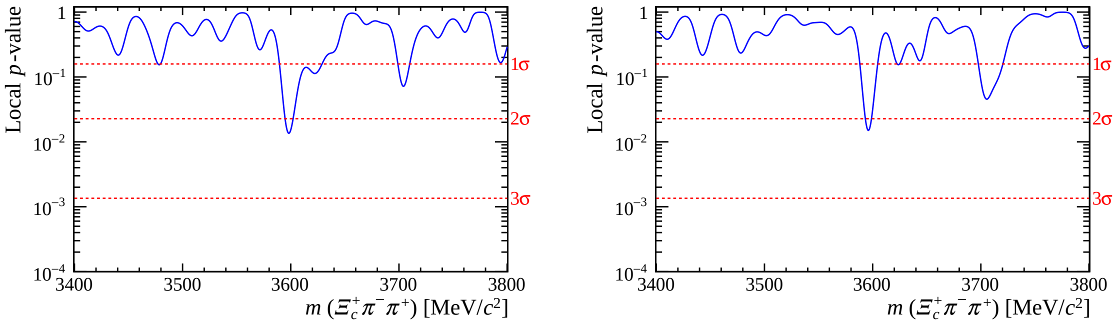

(a) **(b)**

Figure 7.14.: Local p-values as a function of the Ξ_{cc}^{+} invariant mass for the (a) default and (b) extended trigger set after the $\Xi_c^+\pi^-$ invariant-mass constraint.

Figure 7.14 shows the p-value plots for the default and extended trigger sets after the $\Xi_c^+\pi^-$ invariant-mass is constrained. The minimum p-value for the mass spectrum from the default trigger set is evaluated to be 0.01358, corresponding to a significance of $2.2\,\sigma$ at the mass of 3598 MeV/c^2. For the extended trigger set, the p-value is 0.01501, corresponding to a significance of $2.2\,\sigma$ at the mass of 3596 MeV/c^2. Since the evaluated significance is under $3\,\sigma$ in both cases, there is no evidence for this resonant decay in the studied dataset either.

7.3.3. Combination with the $\Xi_{cc}^{+} \to \Lambda_c^+ K^- \pi^+$ decay

Since the local significance for the $\Xi_c^+ \pi^- \pi^+$ final state is below $3\,\sigma$ for both trigger selections, a combination of the $\Xi_c^+ \pi^- \pi^+$ final state using the extended trigger set with the $\Lambda_c^+ K^- \pi^+$ final state is also performed.

A selection for the $\Xi_{cc}^{+} \to \Lambda_c^+ K^- \pi^+$ decay used for the combination is Selection B described in reference [101], using the full Run 1 and Run 2 data sample. Figure 7.15 shows the simultaneous unbinned extended maximum-likelihood fit to both decays, with a common mass, independent signal and background yields, and the signal shape parameters fixed to the corresponding values obtained from the simulation. The best-fit mass value is $3623.0 \pm 1.4\,\text{MeV}/c^2$, the number of signal candidates for the $\Xi_{cc}^{+} \to \Xi_c^+ \pi^- \pi^+$ decay is 145 ± 139, and for the $\Xi_{cc}^{+} \to \Lambda_c^+ K^- \pi^+$ decay it is 224 ± 53. The uncertainty on the mass is only statistical.

7.3.3.1. Local significance

Figure 7.16a shows the local p-values as a function of the Ξ_{cc}^{+} mass for the individual decay channels, which are subsequently used for the combination. Since the compatibility with the background-only hypothesis is not unambiguously defined for a fit to two spectra, three different methods are cross-checked to evaluate the combined

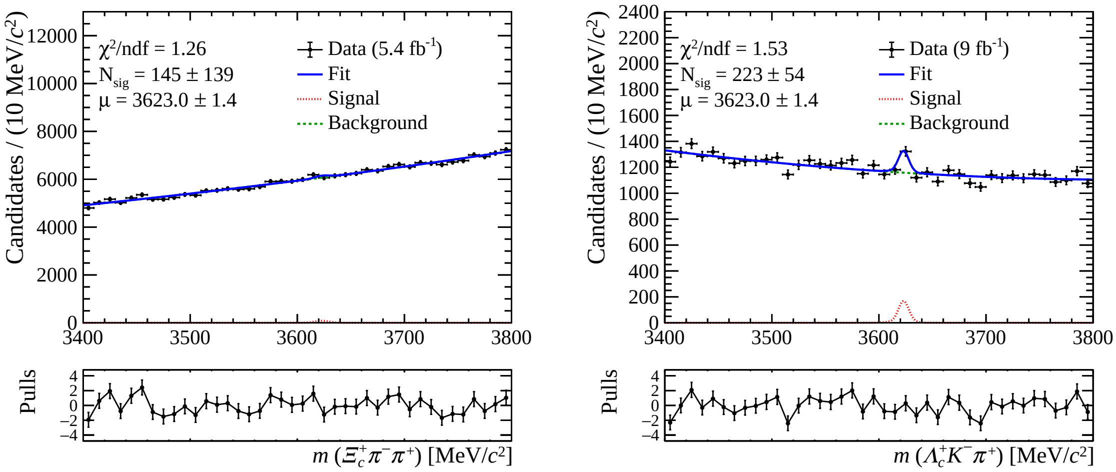

(a) (b)

Figure 7.15.: Simultaneous fit to the (a) $\Xi_c^+ \pi^- \pi^+$ and (b) $\Lambda_c^+ K^- \pi^+$ invariant-mass spectrum.

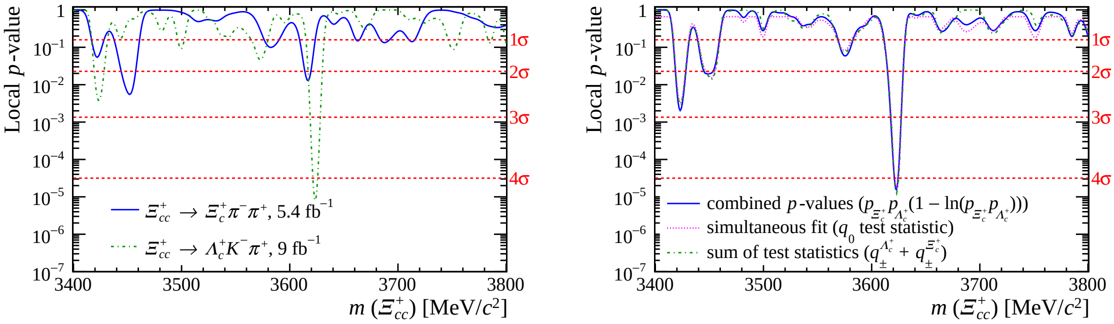

(a) **(b)**

Figure 7.16.: Local p-values as a function of the Ξ_{cc}^{+} mass for the (a) individual $\Xi_c^+ \pi^- \pi^+$ and $\Lambda_c^+ K^- \pi^+$ final states and the (b) combination of these final states using different methods for the combination of the p-values described in the text.

p-value to make sure that the p-value is calculated correctly. Figure 7.16b shows the combined p-value plot, where the three curves represent the following different methods to evaluate the p-value for the combination of two decay channels:

1. A combination of the individual p-values, computed from the $q_{\pm}$ test statistic using the asymptotic formula, with the combination formula [217]

$$p\text{-value} = p_{\Xi_c^+} \cdot p_{\Lambda_c^+} \cdot \left(1 - \ln(p_{\Xi_c^+} \cdot p_{\Lambda_c^+})\right), \tag{7.7}$$

   where $p_{\Xi_c^+}$ and $p_{\Lambda_c^+}$ are the individual p-values for the $\Xi_c^+ \pi^- \pi^+$ and $\Lambda_c^+ K^- \pi^+$ final states, respectively. The minimum p-value for this method is evaluated to be 0.000016, corresponding to a significance of 4.2 σ at the mass of 3623 MeV/c^2.

2. A simultaneous fit with a requirement of positive yields in both channels, using the q_0 as the test statistic, for which the minimum p-value of 0.000017 is found, corresponding to a significance of 4.2 σ at the mass of 3623 MeV/c^2.

3. A sum of the test statistics $q_{\pm}$ from the individual channels, for which the minimum p-value is 0.000012, corresponding to the significance of 4.2 σ at the mass of 3623 MeV/c^2.

The combined p-values are not well defined for regions where a local significance is low, and there are inconsistencies especially for regions where a negative fluctuation is observed in one spectrum and a positive fluctuation in the other spectrum. However, for regions with higher significances that are relevant when rejecting a background-only hypothesis, a good agreement between all of the described methods is observed, and they result in the identical local significances at the same Ξ_{cc}^{+} mass, which provides a good cross-check for the evaluated combined local p-value. The p-values for the first method are calculated using the asymptotic formula $0.5 \cdot \chi_1^2(q_\pm)$, where a subscript of χ^2 represents the number of degree of freedom for a corresponding χ^2 distribution. The p-values for the second and the third method are calculated in the two following steps. The p-values above 0.00022 (below $3.5\,\sigma$) are calculated from their corresponding test-statistic distributions based on 50k generated background-only pseudoexperiments, as the number of pseudoexperiments that have the test statistic larger than the observed one. Subsequently, the p-values below 0.00022 (above $3.5\,\sigma$) are calculated using the asymptotic formula for low p-values for the corresponding methods, namely $0.25 \cdot (2 \cdot \chi_1^2(q_0) + \chi_2^2(q_0))$ for the second method and $0.25 \cdot \chi_2^2(q_\pm)$ for the third method, since it is not CPU efficient to generate enough pseudoexperiments to be able to evaluate the low p-values with a sufficient precision.

7.3.3.2. Global significance

Since the evaluated combined local significance is between 3-5 σ, the global p-value is also evaluated for the three methods used for the combination described in the previous paragraph. The global p-value is computed by generating 40k pseudoexperiments and calculating how many pseudoexperiments have the maximum test statistic found in the invariant-mass window from 3500 to 3700 MeV/c^2 larger than the observed test statistic. The combined global significance is evaluated to be $3.1\,\sigma$ and is consistent between the different methods.

Additionally, the global p-value is also evaluated using the asymptotic formula shown in Equation 7.6, where the reference level c_0 for the number of upcrossings $N(c_0)$ is chosen to be 1 as there are two degrees of freedom for the combination of two spectra. The $\langle N(c_0) \rangle$ is evaluated by generating 2000 pseudoexperiments for the background-only hypothesis and calculating the average number of upcrossings in the mass region from 3500 to 3700 MeV/c^2 among the pseudoexperiments. The asymptotic formula is used for the second and third combination method, since the first method uses the p-values directly and therefore it is not possible to apply the asymptotic formula for this case. As an example, Figure 7.17 shows the evaluated test statistic in the invariant-mass range from 3500 to 3700 MeV/c^2, for which the number of upcrossing is 4. The $\langle N(c_0) \rangle$ is evaluated for the second method to be 3.5, whereas

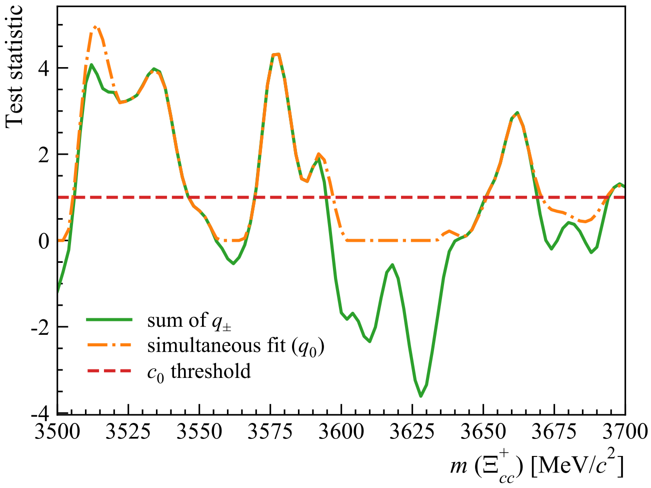

Figure 7.17.: Test statistic in the invariant-mass window from 3500 to 3700 MeV/c^2 calculated for one of the generated background-only pseudoexperiments for the evaluation of the global p-value using the asymptotic formula, with the highlighted c_0 reference level equal to 1.

for the third method it is 4.0. Both methods give a consistent result for the evaluated global significance using the asymptotic formula.

Table 7.3 summarises the evaluated combined local and global significances for all presented methods. The resulting global p-values evaluated by the asymptotic formula are larger, but that it is an expected feature of the asymptotic formula since it only gives an upper limit on the global p-value. Since a sufficient number of pseudoexperiments to evaluate the global p-value is generated, it is considered to be the baseline method for the evaluation of the global p-value and therefore used for the subsequent evaluation of the global p-value including the systematic uncertainties described in the next section.

7.3.3.3. Global significance with systematic uncertainties

The p-values, including the systematic uncertainties, are evaluated using only one of the combination methods, namely the sum of the test statistic from the individual decay channels, since it was shown that all of the used methods give consistent results for the local and global p-values. The systematic uncertainties which are considered for the evaluation of the combined p-value are the following:

Test statistic	local p-value	global p-value (40k pseudoexp.)	global p-value (asympt.)	local p-value (with system.)	global p-value (with system.)
combined p-values	0.000016 ($4.17\,\sigma$)	0.0009 ($3.11\,\sigma$)	-	-	-
simultaneous fit	0.000017 ($4.15\,\sigma$)	0.0009 ($3.11\,\sigma$)	0.0015 ($2.97\,\sigma$)	-	-
sum of test statistic	0.000012 ($4.22\,\sigma$)	0.0009 ($3.12\,\sigma$)	0.0013 ($3.01\,\sigma$)	0.00004 ($3.98\,\sigma$)	0.0022 ($2.85\,\sigma$)

Table 7.3.: Combined local and global p-values and their corresponding significances for different methods to evaluate the test statistic for the combination of the $\Xi_c^+ \pi^- \pi^+$ and $\Lambda_c^+ K^- \pi^+$ final states.

- A mass shift due to the possible relative shift between the two mass spectra calculated as a squared sum of the systematic uncertainties on the mass that are not correlated between the two spectra. These are the systematic uncertainties on the mass of the Λ_c^+ and Ξ_c^+ baryons and the uncertainty due to the Ξ_{cc}^+ mass model, resulting in $0.52\,\mathrm{MeV}/c^2$;

- An uncertainty due to the difference in the mass resolution in the simulation and data considered to be $1.37\,\mathrm{MeV}/c^2$ for the $\Xi_c^+ \pi^+ \pi^-$ final state and $0.70\,\mathrm{MeV}/c^2$ for the $\Lambda_c^+ K^- \pi^+$ final state. For the $\Xi_{cc}^+ \to \Xi_c^+ \pi^- \pi^+$ decay, it is calculated as an uncertainty on the scaled mass resolution using the difference between the mass resolution in data and simulation for the normalisation channel described in Section 7.1. For the $\Xi_{cc}^+ \to \Lambda_c^+ K^- \pi^+$ decay, a scaling of the resolution is not performed since the observed mass resolution of the normalisation channel between the data and simulation agreed within $1.8\,\sigma$, therefore this systematic uncertainty is calculated as a squared sum of the uncertainties of the mass resolution in data and simulation for the $\Xi_{cc}^{++} \to \Lambda_c^+ K^- \pi^+ \pi^+$ decay, which is used as the normalisation channel in the corresponding $\Xi_{cc}^+ \to \Lambda_c^+ K^- \pi^+$ search described in reference [101];

- An uncertainty on the measured signal yield due to the mass-fit model evaluated by generating 10k pseudoexperiments and calculating a difference between the generated yield using the alternative mass model and the fitted yield using the nominal mass model. This results in 3.1% uncertainty (corresponding to 8.7

candidates) for the $\Xi_{cc}^{+} \to \Xi_c^+ \pi^- \pi^+$ decay and 3.3% uncertainty (corresponding to 7.4 candidates) for the $\Xi_{cc}^{++} \to \Lambda_c^+ K^- \pi^+ \pi^+$ decay, as shown in Figure 7.18.

The mass spectra are shifted with respect to each other by $\pm 0.52\,\text{MeV}/c^2$ with a fixed mass resolution varied by $\pm 1.37\,\text{MeV}/c^2$ for the $\Xi_c^+ \pi^+ \pi^-$ decay and $\pm 0.70\,\text{MeV}/c^2$ for the $\Lambda_c^+ K^- \pi^+$ decay and the smallest value for the test statistic is chosen out of these variations. The negative log likelihood (NLL) curve for the smallest test statistic is subsequently used to consider the uncertainty due to the fit model, for which the statistical uncertainty on the signal yield σ_{stat} of the NLL distribution is increased to $\sigma = \sqrt{\sigma_{stat}^2 + \sigma_{syst}^2}$, which is shown in Figure 7.19. There is almost no difference between the curves since the applied correction due to the mass fit model is almost negligible, therefore only a marginal decrease in the test statistic is observed.

Table 7.4 summarises the evaluated test statistics and the global significances after the individual components of the considered systematic uncertainty are applied. As expected, the largest impact is due to the uncertainty on the unknown mass resolution. A combination of all three components of the systematic uncertainty yields the combined local significance, including the systematic uncertainties, of $4\,\sigma$ and the global significance of $2.9\,\sigma$. This value for the global significance is considered to make the final conclusion on the combination that there is no significant evidence for the Ξ_{cc}^{+} baryon in the combination of the two decay channels.

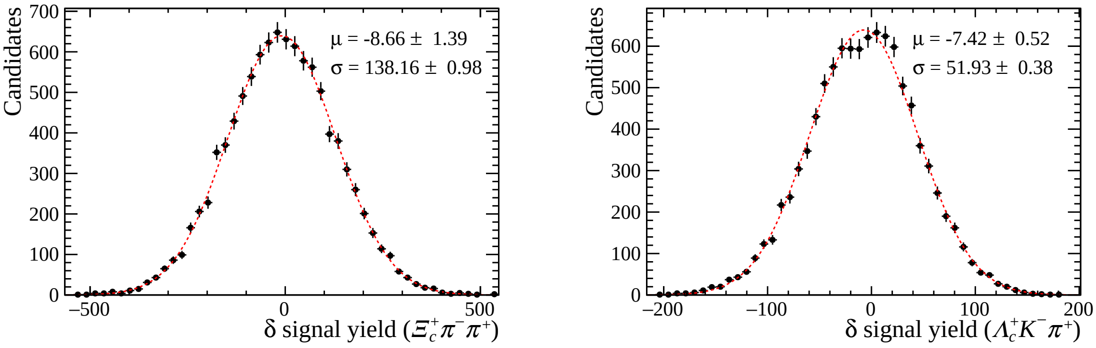

(a) (b)

Figure 7.18.: Difference between the generated (double Gaussian model) and the fitted (DSCB plus Gaussian model) signal yield for 10k pseudoexperiments for the (a) $\Xi_c^+ \pi^- \pi^+$ and (b) $\Lambda_c^+ K^- \pi^+$ final state.

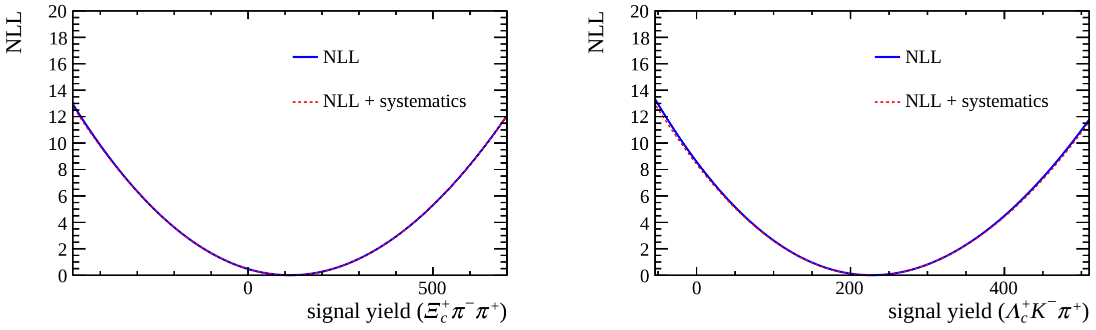

(a) **(b)**

Figure 7.19.: Curve of the NLL for the smallest observed test statistic after the systematic uncertainties for the mass shift and mass resolution are considered for the (a) $\Xi_c^+\pi^-\pi^+$ and (b) $\Lambda_c^+K^-\pi^+$ final state before (blue solid line) and after (red dashed line) the systematic uncertainty for the mass model is added.

Systematic uncertainty	test statistic	global significance
No uncertainty	19.84	$3.12\,\sigma$
Mass shift	19.56	$3.10\,\sigma$
Resolution difference	18.48	$2.95\,\sigma$
Fit model	19.46	$3.08\,\sigma$
Combined uncertainty	17.75	$2.85\,\sigma$

Table 7.4.: Combined test statistics and global significances after different components of the systematic uncertainty are considered individually, and combined together.

7.3.4. Cross-checks before unblinding

This section describes the cross-checks performed for the signal yield consistency as the last step before unblinding, already introduced in Section 5.2.2. The mass consistency check is not performed since no significant signal of the Ξ_{cc}^{+} baryon is observed.

Table 7.5 shows the results of the pre-unblinding checks performed in order to evaluate the yield consistency in the different data categories. The compatibility of two signal yields y_1 and y_2 is computed as the number of standard deviations σ from 0 for the relative difference

$$\frac{y_1 - y_2}{\text{average}(y_2, y_2)} \tag{7.8}$$

Data category	Compatibility
Ξ_{cc}^{+} vs. Ξ_{cc}^{-}	0.012σ
Default vs. extended trigger set	0.66σ
L0 TOS vs. L0 TIS (and not TOS)	0.42σ
Magnet up vs. magnet down	0.079σ
2016 vs. 2017	0.62σ
2016 vs. 2018	0.74σ
2017 vs. 2018	1.3σ

Table 7.5.: Results of the pre-unblinding checks for the signal yield consistency in different data categories.

with the associated uncertainty σ computed using the error propagation. The signal yields in the 2017 and 2018 datasets are compatible within $2\,\sigma$, other categories are compatible within $1\,\sigma$, therefore no further pre-unblinding checks are considered. The correlation between the data samples is taken into account for the default-extended trigger compatibility test, other datasets are treated as independent categories. A correction factor due to the different number of events in the different categories is also considered for the computation of the compatibility between the categories. The procedure to perform the pre-unblinding checks is firstly carefully checked on the WSM data in order to make sure it is properly set up without any unintentional unblinding.

The procedure to perform the considered pre-unblinding checks is as follows. Firstly, the p-value scan is performed in the invariant-mass range from 3400 to $3800\,\mathrm{MeV}/c^2$ using the full data sample in order to find the global minimum, as the mass fit is sensitive to the initial mass value and so it could therefore converge only at a local minimum. The mass, for which the minimal p-value is found, is saved. Subsequently, the mass fits for the subsets of data are performed at the mass fixed to the optimal mass based on the p-value scan. The compatibility between the yields is computed and saved to an output file, all other output files (p-value scan, mass and fit information) are deleted before the check is finalised. Table 7.6, which shows the unblinded values for the signal yields in the different data categories, was completed only after unblinding.

Data category	Signal yield
Ξ_{cc}^{+}	111 ± 69
Ξ_{cc}^{-}	112 ± 69
Default trigger set	223 ± 97
Extended trigger set	297 ± 128
L0 TOS	168 ± 85
L0 TIS (and not TOS)	149 ± 95
Magnet up	106 ± 68
Magnet down	116 ± 70
2016	76 ± 54
2017	129 ± 56
2018	18 ± 59

Table 7.6.: Signal yields with their statistical uncertainties for various data categories added after unblinding.

7.4. Systematic uncertainties for the mass measurement

The following sections describe possible sources of systematic effects on the mass measurement, which would have been performed in case a significant Ξ_{cc}^{+} signal would be observed. All of the methods presented to evaluate the systematic uncertainties are studies prior to unblinding, in order to avoid any bias on the mass measurement after unblinding in case it would have been performed.

7.4.1. Momentum scaling calibration

The momentum scaling calibration is used in this analysis in order to correct for an imperfect alignment of the tracking system and to account for the uncertainty on the magnetic field, which improves the precision on the measured mass. In Run 2, the calibration of the momentum is done using large samples of the $J/\psi \to \mu^+\mu^-$ and $B^+ \to J/\psi K^+$ decays separately for the two magnet polarities and track charges. The momenta of the tracks are scaled by a value $1 - \alpha$, where α is the momentum correction factor. The overall correction factor is at the level of 0.03% and the overall mass correction depends on the Q value of a particular decay as $\Delta\mu \approx Q \cdot \alpha$, where the Q is the energy released for that decay. The Q value of the studied decay channel

$\Xi_{cc}^{+} \to \Xi_c^{+} \pi^{-} \pi^{+}$ is approximately 874 MeV, where the mass of the Ξ_{cc}^{+} baryon is considered to be the same as the measured mass of the Ξ_{cc}^{++} baryon, therefore the expected mass correction is 0.26 MeV/c^2.

To calculate the corresponding systematic uncertainty related to the momentum scaling correction, the momenta of the companion pions are varied by 0.03%. The Ξ_{cc}^{+} invariant-mass distribution is recalculated and compared with the reconstructed mass. The average shift between the reconstructed and recalculated mass is 0.31 MeV/c^2, which is taken as the systematic uncertainty due to the momentum scaling calibration. This value can be subsequently corrected by the Q value observed in data after unblinding by a factor $Q_{\mathrm{data}}/Q_{\mathrm{MC}}$.

7.4.2. Bias due to the Ξ_c^{+} and Ξ_{cc}^{++} selections

A systematic uncertainty on the Ξ_{cc}^{+} mass introduced by the Ξ_c^{+} selection is reduced by measuring the difference in mass between the Ξ_{cc}^{+} and Ξ_c^{+} baryons, as shown in Equation 7.1. However, in general, a lifetime-biasing selection is correlated with a mass bias and since the selection used in this analysis contains some lifetime-biasing requirements, the impact of the overall selection on the measured Ξ_{cc}^{+} mass is evaluated.

The impact of the selection is evaluated by comparing the fitted mass in the simulation before and after full selection is applied. As the Ξ_{cc}^{+} lifetime is *a priori* unknown, the difference is evaluated also for half and double the value of the nominal Ξ_{cc}^{+} lifetime hypothesis of 80 fs. Table 7.7 shows the fitted mass values obtained from the fits before and after full selection is applied in the simulation. The selection causes a bias on the measured Ξ_{cc}^{+} mass by 1.18 MeV/c^2 at the nominal lifetime of the Ξ_{cc}^{+} baryon. Therefore a correction for the selection bias in the final mass measurement is considered, with half of that correction taken as a systematic uncertainty, resulting in 0.59 MeV/c^2.

Additional uncertainty arises from the unknown lifetime of the Ξ_{cc}^{+} baryon. The bias for the half and double the lifetime of the Ξ_{cc}^{+} baryon varies by $+0.73$ MeV/c^2 and -0.78 MeV/c^2 with respect to its nominal lifetime. The largest difference of 0.78 MeV/c^2 is taken as a systematic uncertainty and it is subsequently added in quadrature to the uncertainty of 0.59 MeV/c^2 mentioned above. The combined final systematic uncertainty due to the selection is therefore 0.98 MeV/c^2.

Applied selection	μ [MeV/c^2] for 40 fs	μ [MeV/c^2] for 80 fs	μ [MeV/c^2] for 160 fs
Reconstruction only	3621.94 ± 0.03	3621.95 ± 0.03	3621.96 ± 0.04
Full selection	3623.86 ± 0.04	3623.13 ± 0.03	3622.35 ± 0.04

Table 7.7.: Fitted Ξ_{cc}^{+} mass before and after full selection is applied in the simulation, evaluated at different Ξ_{cc}^{+} lifetime hypotheses.

7.4.3. Final-state radiation

As discussed in reference [206], the Crystal Ball function models the effect of the radiative tail caused by the final-state radiation (FSR) far from the peak well, however close to the signal peak its shape is still Gaussian, resulting in a bias on the fitted mass compared to the input value.

To evaluate this bias, which depends on the mass resolution, the generated momenta of the tracks for all final state particles are smeared in the simulation for different values of the Ξ_{cc}^{+} mass resolution up to about 11 MeV/c^2 to cover the expected mass resolution in data. The smearing of the final-tracks momenta is done in order to simulate the resolution effect for radiated soft pions which are not reconstructed. After the smearing, the Ξ_{cc}^{+} invariant mass is recalculated and fitted using the nominal fit model and compared with the result of the fit to the reconstructed invariant-mass spectra without any momentum smearing. Figure 7.20 shows the bias as a function of the mass resolution σ fitted by a linear function, from which one can estimate that for the expected resolution of 8.92 MeV/c^2, the bias due to the FSR is 0.12 MeV/c^2. This systematic uncertainty would have been re-evaluated after unblinding by the resolution observed in data in case a significant Ξ_{cc}^{+} signal would have been observed.

7.4.4. Uncertainty on the Ξ_c^+ mass

The reported Ξ_{cc}^{+} mass includes the PDG value of the Ξ_c^+ mass, as shown in Equation 7.1. The uncertainty of the PDG value for the Ξ_c^+ mass is 0.18 MeV/c^2 [188], which is included in the final uncertainty for the Ξ_{cc}^{+} mass measurement.

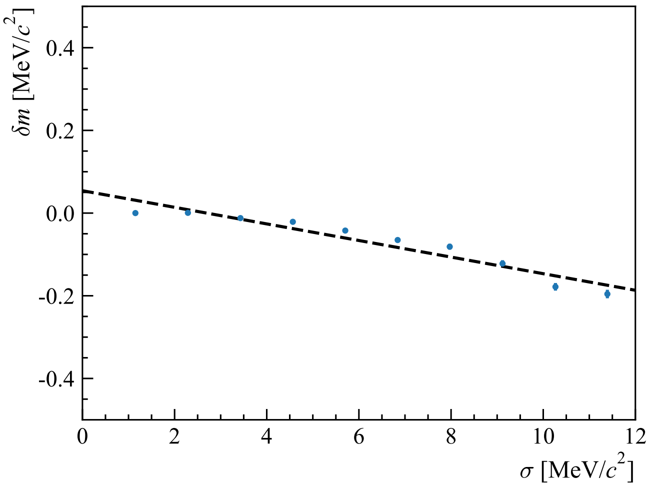

Figure 7.20.: Difference in the fitted Ξ_{cc}^{+} mass extracted from the mass fit to invariant-mass spectra calculated from the smeared generated momenta of the tracks for all final state particles with respect to the invariant mass with no smearing, as a function of the resolution σ extracted from the mass fit.

7.4.5. Uncertainty due to the simulation correction

As discussed in Section 6.2.4, the p_{T}, η and nTracks distributions for the Ξ_{cc}^{+} baryon in the simulation are corrected using the 2016–2018 simulation and s-weighted data for the $\Xi_{cc}^{++} \to \Lambda_c^+ K^- \pi^+ \pi^+$ and $\Xi_{cc}^{++} \to \Xi_c^+ \pi^+$ decays by the multidimensional weighting procedure with the GBR tool. To evaluate the uncertainty due to the weighting procedure, one-dimensional weights in bins of the individual variables is evaluated using the same simulation and s-weighted data for the $\Xi_{cc}^{++} \to \Lambda_c^+ K^- \pi^+ \pi^+$ and $\Xi_{cc}^{++} \to \Xi_c^+ \pi^+$ decays. The final invariant-mass distribution is fitted with the nominal fit using the product of calculated three one-dimensional weightings of the individual variables. The difference in the fitted mass with respect to the GBR weighting is taken as a systematic uncertainty, resulting in an uncertainty of 0.06 MeV/c^2.

7.4.6. Fit-model uncertainty

In order to evaluate the systematic uncertainty introduced by a choice of a specific fit model, alternative fit models are considered. A DSCB function is used as an alternative model for a signal component and a linear function is chosen as an alternative for a background shape. Using the alternative signal fit model, 1000 pseudoexperiments are generated and fitted with the alternative and nominal signal fit models, and separately repeated for the background alternative and nominal models as well. The pseudoexperiments are generated in the mass range from 3400 to 3800 MeV/c^2. The number of expected background events used for pseudoexperiments is extracted from the fit to the WSM distribution shown in Figure 7.2a, with the scale factors to correct for the different number of events in the WSM and right-signed data and to take into account that only 20% of the WSM data is used. The number of generated signal events is chosen to approximately pass a 5 σ local significance threshold.

Figure 7.21 shows the difference between the mean parameters extracted from the fit by the DSCB and DSCB-plus-Gaussian functions, with exponential functions for the background component in both cases, for all generated pseudoexperiments. The distribution is fitted with a Gaussian function, with a mean of -0.04 MeV/c^2 and a width of 0.41 MeV/c^2. The shift plus the width is taken as a systematic uncertainty, which results in 0.45 MeV/c^2. For the background component, no significant impact on the measured Ξ_{cc}^{+} mass is found, since the shift in the corresponding mean plus the width of the fitted Gaussian to the mass difference between the alternative and nominal background models is only 0.02 MeV/c^2.

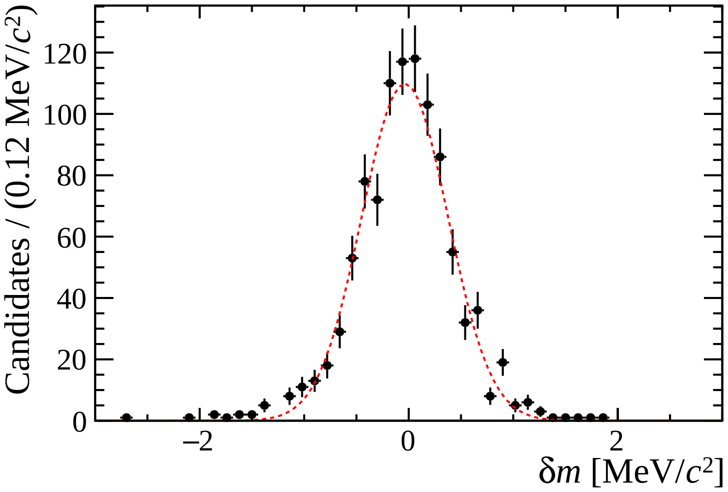

Figure 7.21.: Difference between the mean parameter extracted from the DSCB and DSCB-plus-Gaussian fits to 1000 pseudoexperiments (black points) generated using DSCB model, and fitted by a Gaussian function (red dashed line).

7.4.7. Potential bias due to partially reconstructed decays

As already discussed in Section 7.1.1, there are several possible contributions of partially reconstructed decays in the final invariant-mass spectrum. As the presence of partially reconstructed decays in the studied invariant-mass window can impact the evaluated mass, a study based on pseudoexperiments is considered to evaluate a potential bias. However, the size of the bias highly depends on the size of the signal yield and the yields of the individual partially reconstructed decays, therefore the corresponding systematic uncertainty would have been evaluated after unblinding based on the observed result in case a significant Ξ_{cc}^{+} signal would have been observed. As the procedure is identical to the study described in Section 7.1.1, the strategy and technique were in place prior to unblinding.

7.4.8. Summary of the systematic uncertainties for the mass measurement

Table 7.8 summarises the systematic uncertainties considered for the mass measurement discussed in the previous sections. As all of the evaluated uncertainties are considered to be independent, they are taken in quadrature to get the combined systematic uncertainty on the mass measurement, which results in 1.14 MeV/c^2. In addition to the uncertainties shown in Table 7.8, a systematic uncertainty due to possible partially reconstructed decays would have been evaluated after unblinding in case of a signal observation, as discussed in Section 7.4.7. All of the discussed uncertainties are evaluated for the Ξ_{cc}^{+} mass of 3621.4 MeV/c^2 and the expected mass resolution of 8.92 ± 1.37 MeV/c^2 discussed in Section 7.1. As some of the systematic uncertainties depend on these values to be precisely determined, they would have been re-evaluated after unblinding based on the observed Ξ_{cc}^{+} mass, the mass resolution of the Ξ_{cc}^{+} peak, and the corresponding Q value of the $\Xi_{cc}^{+} \to \Xi_c^+ \pi^- \pi^+$ decay.

Since no significant signal of the Ξ_{cc}^{+} baryon has been observed after unblinding, the mass measurement was not performed and the studies discussed in the previous sections dedicated to the systematic uncertianties related to the mass measurement were not used after unblinding. However, the procedures to evaluate all of the uncertainties considered for the mass measurement were in place before unblinding, as described earlier, therefore they are summarised in this thesis for completeness.

Source	Value [MeV/c^2]
Momentum scale calibration	0.31
Selection bias	0.98
FSR	0.12
Uncertainty on the Ξ_c^+ mass	0.18
Simulation correction	0.06
Mass fit model	0.45
Combined	1.14

Table 7.8.: Systematic uncertainties considered for the Ξ_{cc}^{+} mass measurement.

7.5. Summary

This chapter presented the studies and results related to the $\Xi_c^+\pi^+\pi^-$ invariant-mass distribution. After description of the fit models to describe the signal and background components and the methods to evaluate a signal significance, the corresponding unblinded results were presented.

To summarise, no significant signal was observed for the studied decay $\Xi_{cc}^{+}\to\Xi_c^+\pi^-\pi^+$. A minimum p-value of 0.0108 (0.0024) at the mass of 3617 (3452) MeV/c^2 corresponding to 2.3 σ (2.8 σ) local significance was found for the default (extended) trigger set. Since the local significance for the $\Xi_c^+\pi^-\pi^+$ final state was below 3 σ, a combined fit with the $\Xi_{cc}^{+}\to\Lambda_c^+K^-\pi^+$ final state was performed. The evaluated significances for the combined spectrum with (without) systematic uncertainties included are 4.0 σ (4.2 σ) for the local and 2.9 σ (3.1 σ) for the global significance. The fitted mass for the simultaneous fit to the two spectra at the minimum p-value was $3623.0 \pm 1.4\,(\text{stat})$ MeV/c^2, where the uncertainty is only statistical. Since the combined global significance including the systematic uncertainties was below 3 σ, no significant evidence for the Ξ_{cc}^{+} baryon was found in the combination of the two decay channels either. Therefore the mass measurement of the Ξ_{cc}^{+} baryon was not performed, however the best-fit mass value for the combined spectrum is consistent with the mass of its isospin partner Ξ_{cc}^{++}.

Given the intriguing but inconclusive results presented in this chapter, future searches for the Ξ_{cc}^{+} baryon in other decay modes using the data already collected by the LHCb detector are important to clarify the picture. As it was already mentioned in

Section 1.3.1.4, the $\Xi_{cc}^{+} \to (\Xi_c^{0} \to pK^{-}K^{-}\pi^{+})\pi^{+}$ decay is a potentially good candidate to search for the Ξ_{cc}^{+} baryon based on theoretical predictions [94, 218]. Moreover, the $\Xi_{cc}^{+} \to (D^{+} \to K^{-}\pi^{+}\pi^{+})pK^{-}$ decay is also an interesting candidate from the experimental point of view, since a high signal purity can be achieved for the D^{+} meson at LHCb due to its longer lifetime of 1040 fs [188] compared to the lifetime of charmed baryons. However, there are no direct theoretical predictions for this decay as most of the theory predictions for the branching fractions are calculated for two-body decays, as described in Section 1.3.1.4. In addition to the searches for the Ξ_{cc}^{+} baryon in other decay modes, a significantly larger data sample will be recorded in the upcoming years by the upgraded LHCb detector [185], as described in the summary of Chapter 2, which will provide more insight into doubly charmed baryons.

Since no evidence for the Ξ_{cc}^{+} baryon was found in the $\Xi_c^{+}\pi^{-}\pi^{+}$ final state, the upper limit on the ratio of production cross-sections times the ratio of branching fractions between this decay and the normalisation decay $\Xi_{cc}^{++} \to \Xi_c^{+}\pi^{+}$ is determined, which is discussed in the next chapter.

Chapter 8.

Upper limits for the $\Xi_{cc}^{+} \to \Xi_{c}^{+} \pi^{-} \pi^{+}$ decay

"The trick is to acknowledge each other's limitations, and build from there."
— Carol Dweck in her book *Mindset*

In case a significant signal of the Ξ_{cc}^{+} baryon would be observed, the ratio of production cross-sections times the ratio of branching fractions between the signal and normalisation channel defined as

$$R = \frac{\sigma(\Xi_{cc}^{+}) \times \mathcal{B}(\Xi_{cc}^{+} \to \Xi_{c}^{+} \pi^{-} \pi^{+})}{\sigma(\Xi_{cc}^{++}) \times \mathcal{B}(\Xi_{cc}^{++} \to \Xi_{c}^{+} \pi^{+})} \tag{8.1}$$

would have been determined, as described in detail in Section 5.2. However, no significant Ξ_{cc}^{+} signal has been observed, as discussed in the previous chapter. This chapter therefore describes a determination of the upper limits on R as a function of the Ξ_{cc}^{+} mass and for different Ξ_{cc}^{+} lifetime hypotheses.

Firstly, the ratio of efficiencies between the signal and normalisation channel is discussed in Section 8.1, followed by Section 8.2 with a description of various corrections to the evaluated efficiency ratio. Section 8.3 then discusses a determination of the signal yield. The systematic uncertainties considered for the UL measurement, that were defined before unblinding and would have been also considered for a determination of R, are described in Section 8.4. A method to evaluate the upper limits on R and the corresponding results are discussed in Section 8.5. The chapter is summarised in Section 8.6.

8.1. Ratio of efficiencies

Equation 8.1 can be rewritten so it contains the number of observed signal candidates N_{sig} for the signal channel, N_{norm} for the normalisation channel and corresponding efficiencies ε_{sig} and $\varepsilon_{\text{norm}}$, as

$$R = \frac{\mathcal{L}_{\text{norm}}}{\mathcal{L}_{\text{sig}}} \frac{\varepsilon_{\text{norm}}}{\varepsilon_{\text{sig}}} \frac{N_{\text{sig}}}{N_{\text{norm}}} \equiv \alpha N_{\text{sig}}, \tag{8.2}$$

where $\mathcal{L}_{\text{norm}}$ and $\mathcal{L}_{\text{sig}}$ are luminosities of the data samples used for the signal mode and normalisation modes, respectively, and α denotes the single-event sensitivity, which is discussed in detail in Section 8.5. Since the data used for the signal and normalisation modes are collected in the same data streams, the ratio of luminosities cancels out. There are two main components in Equation 8.2 that need to be evaluated before the UL can be determined: the ratio of efficiencies, $\varepsilon_{\text{norm}}/\varepsilon_{\text{sig}}$, which can be broken down into several components of the individual efficiencies (acceptance, reconstruction, trigger, pre-selection, PID and MVA); and the number of signal candidates, N_{sig} and N_{norm}, for both the signal and normalisation channels.

The efficiencies are determined for the Ξ_{cc}^{++} lifetime of 256 fs and for the Ξ_{cc}^{+} lifetime of 80 fs. Since the lifetime and mass of the Ξ_{cc}^{+} baryon are *a priori* unknown, the variations of the final efficiency ratio with the lifetime and mass of the Ξ_{cc}^{+} baryon are also determined. The final efficiency ratio is then computed as a product of the partial efficiency ratios

$$\frac{\varepsilon_{\text{norm}}}{\varepsilon_{\text{sig}}} = \frac{\varepsilon_{\text{norm}}^{\text{Acc}}}{\varepsilon_{\text{sig}}^{\text{Acc}}} \cdot \frac{\varepsilon_{\text{norm}}^{\text{Reco}\,|\,\text{Acc}}}{\varepsilon_{\text{sig}}^{\text{Reco}\,|\,\text{Acc}}} \cdot \frac{\varepsilon_{\text{norm}}^{\text{HLT}\,|\,\text{Reco}}}{\varepsilon_{\text{sig}}^{\text{HLT}\,|\,\text{Reco}}} \cdot \frac{\varepsilon_{\text{norm}}^{\text{Pre-sel}\,|\,\text{HLT}}}{\varepsilon_{\text{sig}}^{\text{Pre-sel}\,|\,\text{HLT}}} \cdot \frac{\varepsilon_{\text{norm}}^{\text{PID}\,|\,\text{Pre-sel}}}{\varepsilon_{\text{sig}}^{\text{PID}\,|\,\text{Pre-sel}}} \cdot \frac{\varepsilon_{\text{norm}}^{\text{MVA}\,|\,\text{PID}}}{\varepsilon_{\text{sig}}^{\text{MVA}\,|\,\text{PID}}} \cdot \frac{\varepsilon_{\text{sig}}^{\text{MC-match}}}{\varepsilon_{\text{norm}}^{\text{MC-match}}}, \tag{8.3}$$

where the individual efficiency components are discussed in detail in the following sections.

8.1.1. Acceptance and generator-level efficiency

The acceptance efficiency ε^{Acc} is a measure of the $\Xi_{cc}^{+(+)}$ candidates to pass the minimal acceptance requirements with respect to all generated candidates. The $\Xi_{cc}^{+(+)}$ decay products are required to be in the acceptance of the LHCb detector, which is defined as $2.0 < \eta < 5.0$, and also passing the minimal kinematic requirements applied at the generator level for the simulation samples, namely the Ξ_{cc}^{+} candidates with a p_{T} larger than 2.5 GeV/c and all Ξ_{cc}^{+} decay products with $p_{\mathrm{T}} > 200$ MeV/c for the signal mode, and the Ξ_{cc}^{++} candidates with a p_{T} larger than 2.0 GeV for the normalisation mode. The acceptance efficiency is evaluated from the generator-level requirements applied in the simulation samples, as a ratio of candidates passing the requirements summarised above with respect to all generated candidates.

8.1.2. Reconstruction efficiency

As described in Section 6.1, the truth-matching requirements are applied to the simulation samples in order to have a pure signal sample. The reconstruction efficiency $\varepsilon^{\mathrm{Reco}\,|\,\mathrm{Acc}}$ is therefore determined for the signal based on the truth-matching requirements shown in Table 6.2 and with the additional requirement for the Ξ_{cc}^{+} candidates to be in a signal category corresponding to either the candidates with or without any intermediate resonances, so the candidates classified as a low-mass background are removed. For the normalisation channel, the same background category criteria are applied in addition to the truth-matching requirements summarised in Table 6.3.

The simulation correction based on the GBR weighting using the p_{T}, nTracks and η variables, as described in Section 6.2.4, is also included in the reconstruction efficiency, by using weighted events in the efficiency calculation. Moreover, the tracking efficiency correction to account for a possible mismodelling of tracking efficiency in the simulation is determined for each track using the correction tables from the TrackCalib tool. These corrections are also included in the reconstruction efficiency. Figure 8.1 shows the tracking efficiency tables for 2016, 2017 and 2018 data produced by the tracking group using a tag-and-probe method. To get the final correction for the candidate, a correction for each track is multiplied for all tracks in the final state. As the low momentum tracks are not covered by the tracking efficiency tables, which gives the correction to tracks only with a momentum above 5 GeV, a correction factor based on the nearest bin is assigned to the track, with a conservative 5% uncertainty on that track applied. The corresponding systematic uncertainties associated with the simulation correction using GBR weighting and TrackCalib package are discussed in Sections 8.4.5 and 8.4.1, respectively.

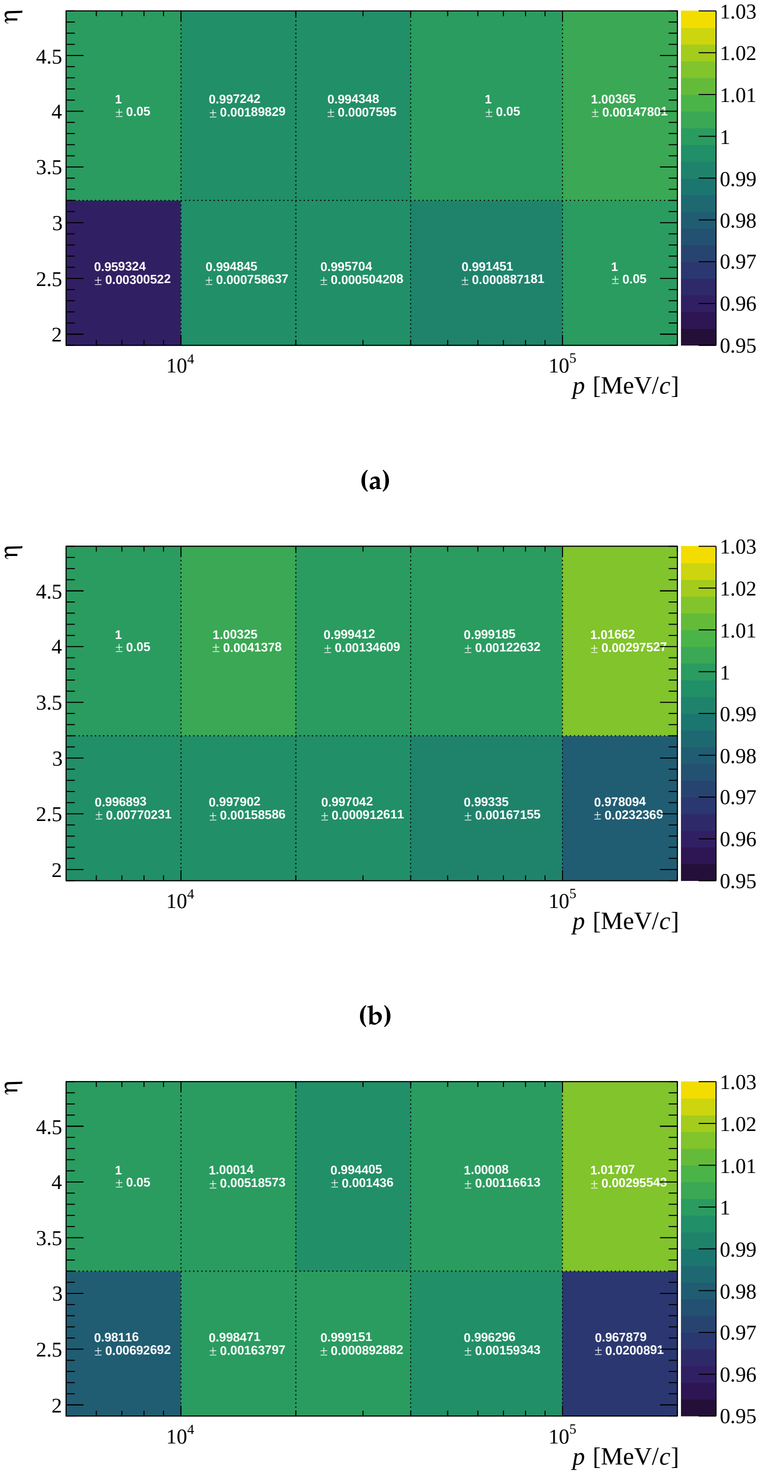

(a)

(b)

(c)

Figure 8.1.: Tracking efficiency tables in the bins of a p and η for (a) 2016, (b) 2017 and (c) 2018 data produced by the tracking group using the tag-and-probe method.

8.1.3. Software trigger efficiency

The efficiency of the HLT selection $\varepsilon^{\mathrm{HLT}\,|\,\mathrm{Reco}}$ is also determined from the simulation samples. The HLT1 and HLT2 efficiencies are not evaluated separately since the HLT1 requirements are already included in the HLT2 inclusive trigger line. The same HLT requirements are applied to both the signal and normalisation modes, which allows to have a precise control over the trigger selection and the corresponding efficiency ratio. The efficiency of the PID selection is evaluated separately using the event weights obtained from the PIDCalib package, therefore the HLT trigger efficiency includes all requirements of the used HLT1 and HLT2 trigger lines, apart from the PID requirements.

Although the HLT2 selection did not change over the studied years, there were some changes in the HLT1 and L0 trigger thresholds, mainly looser L0 thresholds in 2017 due to decreased number of colliding bunches [141], which is reflected in different HLT efficiencies between the studied years. Finally, the ratio of efficiencies is corrected to take into account the observed non-negligible differences between the fractions of candidates in different HLT1 categories in the simulation and data, which is discussed in the dedicated Section 8.2.3.

8.1.4. Pre-selection efficiency

The pre-selection efficiency $\varepsilon^{\mathrm{Pre\text{-}sel}\,|\,\mathrm{HLT}}$ is evaluated based on the candidates passing all pre-selection requirements summarised in Table 6.7 for the signal mode and in Table 6.21 for the normalisation mode, excluding the PID requirements which are discussed below and accounted for separately in the PID efficiency. In addition to the pre-selection requirements, a requirement on the opening angle between any pair of tracks $\theta_{ij} > 0.5\,\mathrm{mrad}$ to remove the clone candidates and veto mis-ID requirements discussed in Section 6.2.3 are also included in the pre-selection efficiency.

8.1.5. PID efficiency

The PIDCalib package [189,201,202] is used to determine the PID efficiency $\varepsilon^{\mathrm{PID}\,|\,\mathrm{Pre\text{-}sel}}$, as described in Section 6.2. The PID requirements used in HLT2 and in the pre-selection for each track are determined in bins of p and η, using a binning scheme summarised in Table 6.8. The total PID efficiency is a product of the PID efficiencies of all final state tracks.

8.1.6. MVA efficiency

The separate MVA selections, as described in Section 6.2, are developed for the signal and normalisation modes, however they are kept as similar as possible in order to minimise systematic effects on the evaluated ratio of efficiencies. The MVA efficiency $\varepsilon^{\mathrm{MVA}\,|\,\mathrm{PID}}$ is evaluated for both the signal and normalisation mode at their optimal working points based on the Punzi FoM.

8.1.7. Hardware-trigger efficiency

The default trigger set requirements, which are used for the determination of the UL on R, include the L0 TIS requirement on the $\Xi_{cc}^{+(+)}$ baryon with respect to a collection of all L0 lines (hadron, electron, photon, muon, and di-muon). It is not possible to use the simulation samples for a precise evaluation of the L0 efficiencies as the simulation does not reproduce the L0 trigger decisions well, which is mainly caused by the underestimation of the track multiplicity in the simulation, which is an important quantity used in most of the L0 trigger lines. Since the production spectra of the Ξ_{cc}^{++} and Ξ_{cc}^{+} baryons as isospin partners are expected to be the same, the ratio of L0 TIS efficiencies between the signal and normalisation modes is assumed to be one. A correction is considered to take into account differences in kinematics that come from the selection for the two modes impacting the L0 efficiency ratio, which is discussed in Section 8.2.5, with a corresponding systematic uncertainty described in Section 8.4.3.

8.1.8. Simulation-matching efficiency

As described in Section 8.1.2, the truth matching is used to evaluate the reconstruction efficiency. The reconstructed candidates pass the truth-matching selection if more than 70% of their hits match the hits created by the corresponding simulated particle. Since 70% is an arbitrary threshold used in the LHCb reconstruction, a correction needs to be applied to avoid underestimating the final efficiency. This correction is decay-dependent, therefore it is important to evaluate it even for the determination of the ratio of efficiencies. The correction is evaluated using the simulation samples after all other selection requirements are applied. A mass fit is performed to the invariant-mass distribution of the candidates that did not pass the truth-matching requirements, where the signal yield of the fit estimates the number of incorrectly matched signal candidates in the invariant-mass window from 3600 to 3644 MeV/c^2, denoted as U. Figure 8.2 shows fits to the candidates that did not pass the truth matching for the signal and normalisation candidates in the 2018 data sample for the default trigger set. The simulation matching (MC-match) correction $\rho^{\text{MC-match}}$, which relates to the $\varepsilon^{\text{MC-match}}$ used in Equation 8.3 as $\rho^{\text{MC-match}} = 1/\varepsilon^{\text{MC-match}}$, is then evaluated as $(U + N)/N$, where N is the number of correctly truth matched candidates after all selection requirements are applied. Table 8.1 shows $\rho^{\text{MC-match}}$ evaluated for both signal and normalisation modes for all studied years.

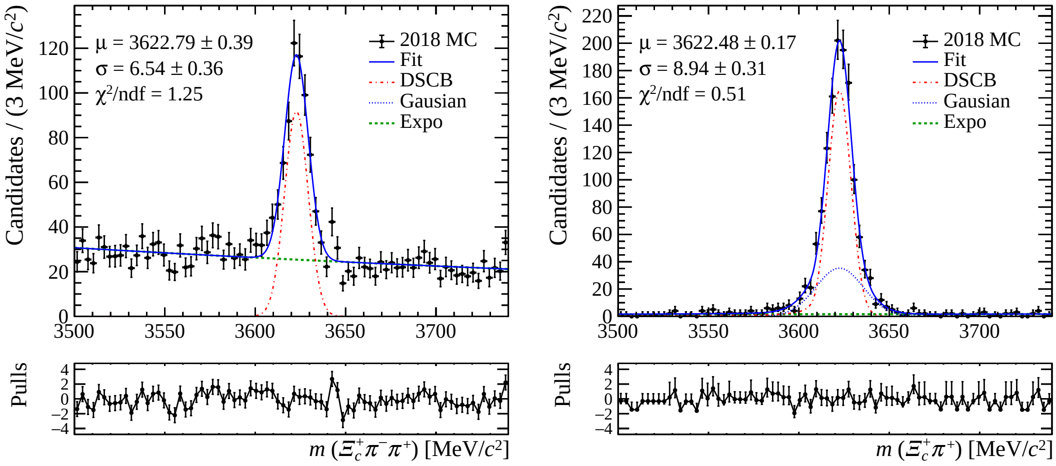

(a) **(b)**

Figure 8.2.: Invariant-mass fit (DSCB plus Gaussian for the signal and exponential for the background components) to the 2018 simulation candidates that did not pass the truth matching for the (a) signal and (b) normalisation decay channel in the default trigger set.

8.1.9. Summary of the evaluated efficiencies

Tables 8.2 and 8.3 summarise the total efficiencies for the signal and normalisation decays, respectively, at their nominal lifetime hypotheses for each year separately and for all years combined according to their luminosity contribution, namely 1.66, 1.63

Decay channel	$\rho^{\text{MC-match}}$ (%)			
	2016	2017	2018	combined
$\Xi_{cc}^{+} \to \Xi_{c}^{+} \pi^{-} \pi^{+}$	105.53 ± 0.20	105.20 ± 0.13	104.65 ± 0.10	105.08 ± 0.08
$\Xi_{cc}^{++} \to \Xi_{c}^{+} \pi^{+}$	107.36 ± 0.37	104.79 ± 0.03	106.14 ± 0.05	106.09 ± 0.11

Table 8.1.: Simulation matching correction $\rho^{\text{MC-match}}$ for the $\Xi_{cc}^{+} \to \Xi_{c}^{+} \pi^{-} \pi^{+}$ decay at its nominal lifetime of 80 fs and the $\Xi_{cc}^{++} \to \Xi_{c}^{+} \pi^{+}$ decay at its nominal lifetime of 256 fs.

and 2.08 fb^{-1} for the 2016, 2017 and 2018 data, respectively. Table 8.4 shows the ratio of the individual and overall efficiencies. One can see that the combined efficiency for the normalisation channel is about 3.4 times larger than for the signal channel. This is mainly caused by the longer lifetime of the Ξ_{cc}^{++} baryon with respect to that of the Ξ_{cc}^{+} baryon. Moreover, a higher acceptance and reconstruction efficiency of the $\Xi_{c}^{+} \pi^{+}$ final state with respect to the $\Xi_{c}^{+} \pi^{-} \pi^{+}$ final state is expected due to one less track in its final state.

All simulation events are used for the calculation of the efficiencies, however an independent check is done to evaluate the efficiencies separately for the MVA training and testing samples. Table 8.5 shows the overall ratio of efficiencies using all simulation events compared to the training and testing subsets. All results are compatible within their statistical uncertainties.

Category	Efficiency for the $\Xi_{cc}^{+} \to \Xi_{c}^{+} \pi^{-} \pi^{+}$ decay			
	2016	2017	2018	combined
ε^{Acc}	7.439 ± 0.009	7.257 ± 0.009	7.269 ± 0.009	7.318 ± 0.005
$\varepsilon^{\text{Reco}\,\vert\,\text{Acc}}$	14.868 ± 0.025	15.583 ± 0.016	15.214 ± 0.013	15.219 ± 0.010
$\varepsilon^{\text{HLT}\,\vert\,\text{Reco}}$	3.508 ± 0.026	5.487 ± 0.021	4.459 ± 0.016	4.477 ± 0.012
$\varepsilon^{\text{Presel}\,\vert\,\text{HLT}}$	85.39 ± 0.26	85.53 ± 0.14	85.76 ± 0.13	85.58 ± 0.10
$\varepsilon^{\text{PID}\,\vert\,\text{Presel}}$	74.5 ± 0.4	75.74 ± 0.22	75.07 ± 0.21	75.10 ± 0.17
$\varepsilon^{\text{MVA}\,\vert\,\text{PID}}$	20.02 ± 0.31	18.04 ± 0.15	18.88 ± 0.15	18.98 ± 0.12
$\varepsilon^{\text{MC-match}}$	94.76 ± 0.18	95.06 ± 0.11	95.56 ± 0.09	95.16 ± 0.07
Overall ($\times 10^{3}$)	5.22 ± 0.09	7.63 ± 0.07	6.27 ± 0.05	6.36 ± 0.04

Table 8.2.: Efficiencies (in %) for the signal channel $\Xi_{cc}^{+} \to \Xi_{c}^{+} \pi^{-} \pi^{+}$ at its nominal lifetime of 80 fs and its nominal mass of 3621 MeV/c^{2} evaluated from the simulation. The uncertainties are statistical only.

Category	Efficiency for the $\Xi_{cc}^{++}\to\Xi_{c}^{+}\pi^{+}$ decay			
	2016	2017	2018	combined
ε^{Acc}	13.653 ± 0.016	13.602 ± 0.016	13.609 ± 0.016	13.620 ± 0.009
$\varepsilon^{\text{Reco}\,\vert\,\text{Acc}}$	16.771 ± 0.028	16.285 ± 0.016	15.961 ± 0.016	16.310 ± 0.012
$\varepsilon^{\text{HLT}\,\vert\,\text{Reco}}$	3.866 ± 0.029	6.809 ± 0.024	5.479 ± 0.022	5.384 ± 0.014
$\varepsilon^{\text{Presel}\,\vert\,\text{HLT}}$	86.87 ± 0.25	86.97 ± 0.12	86.92 ± 0.14	86.92 ± 0.10
$\varepsilon^{\text{PID}\,\vert\,\text{Presel}}$	74.3 ± 0.4	75.59 ± 0.20	75.89 ± 0.23	75.29 ± 0.17
$\varepsilon^{\text{MVA}\,\vert\,\text{PID}}$	26.32 ± 0.33	26.02 ± 0.16	26.34 ± 0.18	26.24 ± 0.13
$\varepsilon^{\text{MC-match}}$	93.15 ± 0.32	95.430 ± 0.030	94.22 ± 0.04	94.26 ± 0.10
Overall ($\times\,10^{3}$)	16.13 ± 0.23	27.04 ± 0.19	21.95 ± 0.17	21.69 ± 0.11

Table 8.3.: Efficiencies (in %) for the normalisation channel $\Xi_{cc}^{++}\to\Xi_{c}^{+}\pi^{+}$ at its nominal lifetime of 256 fs and its nominal mass of 3621 MeV/c^2 evaluated from the simulation. The uncertainties are statistical only.

Category	Ratio of efficiencies $\varepsilon_{\text{norm}}/\varepsilon_{\text{sig}}$			
	2016	2017	2018	combined
ε^{Acc}	1.8353 ± 0.0031	1.8743 ± 0.0032	1.8722 ± 0.0032	1.8613 ± 0.0018
$\varepsilon^{\text{Reco}\,\vert\,\text{Acc}}$	1.1280 ± 0.0026	1.0451 ± 0.0015	1.0491 ± 0.0014	1.0717 ± 0.0010
$\varepsilon^{\text{HLT}\,\vert\,\text{Reco}}$	1.102 ± 0.012	1.241 ± 0.007	1.229 ± 0.007	1.203 ± 0.005
$\varepsilon^{\text{Presel}\,\vert\,\text{HLT}}$	1.017 ± 0.004	1.0168 ± 0.0022	1.0136 ± 0.0022	1.0157 ± 0.0017
$\varepsilon^{\text{PID}\,\vert\,\text{Presel}}$	0.997 ± 0.008	0.998 ± 0.004	1.011 ± 0.004	1.0026 ± 0.0033
$\varepsilon^{\text{MVA}\,\vert\,\text{PID}}$	1.315 ± 0.026	1.442 ± 0.015	1.395 ± 0.014	1.382 ± 0.011
$\varepsilon^{\text{MC-match}}$	0.983 ± 0.004	1.0039 ± 0.0012	0.9860 ± 0.0010	0.9905 ± 0.0013
Overall	3.09 ± 0.07	3.54 ± 0.04	3.50 ± 0.04	3.412 ± 0.028

Table 8.4.: Ratio of efficiencies for the normalisation and signal decays evaluated from the simulation. The uncertainties are statistical only.

Simulation set	Ratio of efficiencies $\varepsilon_{\text{norm}}/\varepsilon_{\text{sig}}$			
	2016	2017	2018	combined
All simulation events	3.09 ± 0.07	3.54 ± 0.04	3.50 ± 0.04	3.412 ± 0.028
MVA training sample (2/3)	3.15 ± 0.08	3.57 ± 0.05	3.50 ± 0.05	3.435 ± 0.034
MVA testing sample (1/3)	2.99 ± 0.12	3.49 ± 0.07	3.50 ± 0.07	3.37 ± 0.05

Table 8.5.: Ratio of overall efficiencies for the normalisation and signal decays evaluated from the simulation using all available samples compared to the MVA training and testing subsets. The uncertainties are statistical only.

8.2. Efficiency corrections

Since the lifetime and mass of the Ξ_{cc}^{+} baryon are *a priori* unknown, the variations of the final efficiency ratio with the lifetime and mass of the Ξ_{cc}^{+} baryon are discussed in the following Sections 8.2.1 and 8.2.2, respectively.

The corrections to the overall efficiency ratio, which was summarised in Section 8.1.9, are discussed below. There are three different corrections applied to the overall efficiency ratio, namely a correction to account for the difference in the fractions of events that are selected by different software trigger categories between simulation and data discussed in Section 8.2.3, a correction due to possible resonant contributions of the $\Xi_{cc}^{+} \to \Xi_{c}^{+} (\rho^{0} \to \pi^{-} \pi^{+})$ decay described in Section 8.2.4, and a hardware-trigger correction discussed in Section 8.2.5.

8.2.1. Variation with the Ξ_{cc}^{+} lifetime

The ratio of overall efficiencies is evaluated for several lifetime hypothesis of the Ξ_{cc}^{+} baryon, which are shown in Table 8.6 and Figure 8.3. The determination of the UL on R is evaluated at four different lifetime hypotheses: 40, 80, 120 and 160 fs. The efficiencies are therefore evaluated for these lifetime hypotheses and they are considered for the final determination of the UL on R discussed in Section 8.5.

Ξ_{cc}^{+} lifetime hypothesis [fs]	Ratio of efficiencies $\varepsilon_{\text{norm}}/\varepsilon_{\text{sig}}$ 2016	2017	2018	combined
40	4.52 ± 0.12	5.31 ± 0.07	5.16 ± 0.07	5.05 ± 0.05
60	3.63 ± 0.08	4.20 ± 0.05	4.11 ± 0.05	4.021 ± 0.034
80	3.09 ± 0.07	3.54 ± 0.04	3.50 ± 0.04	3.412 ± 0.028
100	2.76 ± 0.06	3.14 ± 0.04	3.12 ± 0.04	3.038 ± 0.025
120	2.55 ± 0.06	2.89 ± 0.04	2.88 ± 0.04	2.799 ± 0.025
140	2.42 ± 0.06	2.72 ± 0.04	2.72 ± 0.04	2.646 ± 0.025
160	2.33 ± 0.06	2.61 ± 0.04	2.62 ± 0.04	2.546 ± 0.026
200	2.25 ± 0.07	2.50 ± 0.04	2.53 ± 0.04	2.448 ± 0.028
250	2.25 ± 0.07	2.46 ± 0.05	2.51 ± 0.05	2.429 ± 0.032
300	2.30 ± 0.08	2.50 ± 0.06	2.56 ± 0.05	2.47 ± 0.04

Table 8.6.: Ratio of overall efficiencies for the normalisation and signal channels for different lifetime hypotheses of the Ξ_{cc}^{+} baryon. The uncertainties are statistical only.

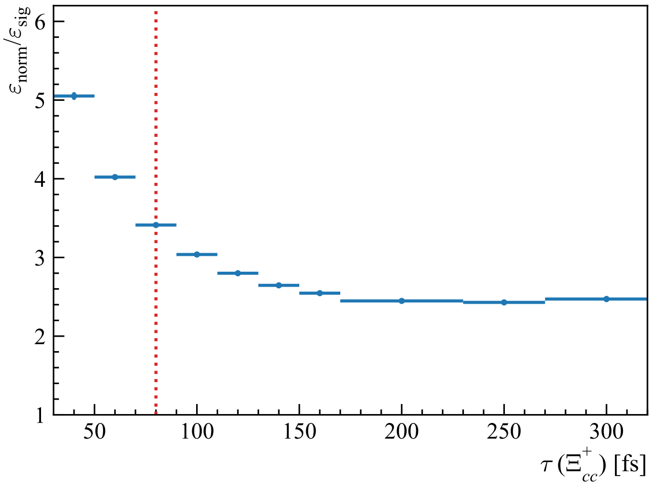

Figure 8.3.: Ratio of overall efficiencies for the normalisation and signal channels for different lifetime hypotheses of the Ξ_{cc}^{+} baryon. The red dotted vertical line represents the nominal Ξ_{cc}^{+} lifetime of 80 fs.

8.2.2. Variation with the Ξ_{cc}^{+} mass

To evaluate the variation of the ratio of efficiencies for the normalisation and signal channels with the assumed Ξ_{cc}^{+} mass, the Ξ_{cc}^{+} mass is weighted using the GBR tool. Section 6.2.6.3 describes the weighting procedure for different masses using GBR in more details. Table 8.7 summarises the ratio of overall efficiencies for five mass hypotheses in addition to the nominal mass of 3621.4 MeV/c^2, with the values of the combined overall ratio for different Ξ_{cc}^{+} assumed masses shown in Figure 8.4. The determination of the UL is performed as a function of the assumed Ξ_{cc}^{+} mass, taking into account a linear variation of the efficiency with the Ξ_{cc}^{+} mass shown in Figure 8.4.

Ξ_{cc}^{+} mass hypothesis [MeV/c^2]	Ratio of efficiencies $\varepsilon_{\rm norm}/\varepsilon_{\rm sig}$			
	2016	2017	2018	combined
3471	3.40 ± 0.08	3.96 ± 0.05	3.94 ± 0.05	3.807 ± 0.032
3521	3.27 ± 0.07	3.79 ± 0.04	3.76 ± 0.04	3.645 ± 0.030
3571	3.09 ± 0.07	3.60 ± 0.04	3.54 ± 0.04	3.447 ± 0.028
3621	3.09 ± 0.07	3.54 ± 0.04	3.50 ± 0.04	3.412 ± 0.028
3671	2.97 ± 0.07	3.47 ± 0.04	3.40 ± 0.04	3.317 ± 0.027
3771	2.89 ± 0.07	3.42 ± 0.04	3.34 ± 0.04	3.252 ± 0.027

Table 8.7.: Ratio of overall efficiencies for the normalisation and signal channels for different mass hypotheses of the Ξ_{cc}^{+} baryon. The uncertainties are statistical only.

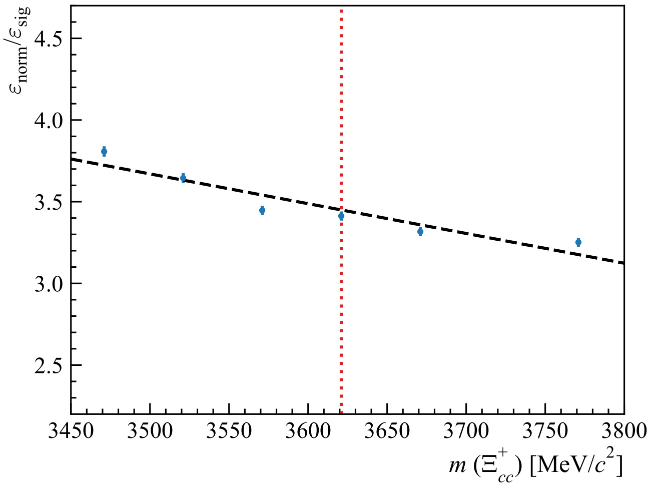

Figure 8.4.: Ratio of overall efficiencies for the normalisation and signal channels for different mass hypotheses of the Ξ_{cc}^{+} baryon. The red dotted vertical line represents the nominal Ξ_{cc}^{+} mass of 3621 MeV/c^2.

8.2.3. Correction for different fraction of events in HLT1 categories

The fraction of events in the HLT1 track and two-track categories and in their overlap for the WSM, upper SB and simulation data after all selection requirements are applied shown in Table 6.5 suggested that there are some non-negligible discrepancies between the fractions observed in the simulation and data. Therefore the simulation samples for both the signal and normalisation channels are weighted to have the same relative fractions of candidates as observed in the corresponding upper SB data of the signal channel separately for each of the studied years. Table 8.8 shows the overall efficiency ratio after the simulation samples for both the signal and normalisation channesl are corrected to have the same relative fraction of the HLT1 categories as observed in the SB sample for the signal channel and the right-signed sample for the normalisation channel for each studied year separately. The overall efficiency ratio for 2016 is more consistent with the ratios for 2017 and 2018 after the correction is applied.

Weighting stage	Ratio of efficiencies $\varepsilon_{\text{norm}}/\varepsilon_{\text{sig}}$			
	2016	2017	2018	combined
Before HLT1 weighting	3.09 ± 0.07	3.54 ± 0.04	3.50 ± 0.04	3.412 ± 0.028
After HLT1 weighting	3.32 ± 0.11	3.55 ± 0.07	3.62 ± 0.07	3.52 ± 0.05

Table 8.8.: Ratio of overall efficiencies before and after the application of the HLT1 weights to correct the simulation samples. The uncertainties are statistical only.

8.2.4. Correction for possible resonant contributions

As already mentioned in Section 5.1 where the signal decay is introduced, it is possible that the resonant decay $\Xi_{cc}^{+} \to \Xi_{c}^{+} (\rho^{0} \to \pi^{-} \pi^{+})$ can represent a significant contribution in the final state. Therefore its possible contribution is considered and a correction is applied. The $\pi^{-}\pi^{+}$ invariant-mass spectrum in the simulation is weighted to match the ρ^{0} line shape, as an extreme case in which 100% of the companion pions would come from the ρ^{0} resonance. The efficiency ratio is subsequently recalculated, also taking into account different generator-level efficiencies for the decay through the ρ^{0} resonance estimated from 100k locally generated events. Figure 8.5 shows the $\pi^{+}\pi^{-}$ invariant-mass distribution for the 2017 simulation sample with and without the ρ^0 weights applied. A correction for this possible contribution is estimated by averaging over the nominal efficiency ratio with 0% of the resonance contribution, and the efficiency ratio after the ρ^0 weighting, where there is 100% of the resonance contribution. The associated systematic uncertainty for this correction is considered and discussed in Section 8.4.7.

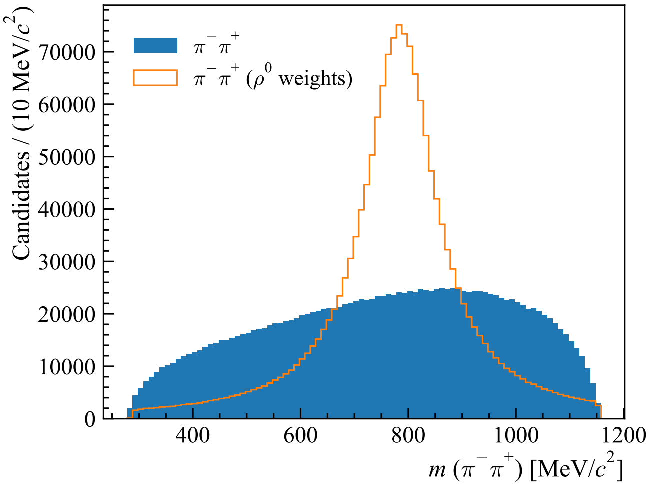

Figure 8.5.: Invariant-mass distribution of the Ξ_{cc}^{+} companion pions $\pi^+\pi^-$ for the 2017 simulation sample for a non-resonance decay of the pions (blue histogram) and their decay through the ρ^0 resonance (orange line) based on the weighting to match the ρ^0 line shape.

8.2.5. Hardware-trigger correction

As described in Section 8.1.7, the L0 TIS efficiency ratio between the signal and normalisation modes is considered to be one since the Ξ_{cc}^{+} and Ξ_{cc}^{++} baryons are expected to have the same production and p_{T} spectra as they are isospin partners. However, a correction is considered to take into account any differences in kinematics that come from the selection for the two modes. This is done by comparing the L0 TIS efficiency ratios before and after full selection is applied. The candidates before the selection represent only the reconstructed candidates with aligned generator-level requirements. Table 8.9 shows the ratio of the L0 TIS efficiencies before and after the selection for the nominal, half the nominal, and double the nominal Ξ_{cc}^{+} lifetime hypothesis. The shift in the efficiency from the selection at the nominal lifetime is 1.019 and is taken as a correction for the L0 efficiency due to the selection. The associated systematic uncertainty, taking into account also the Ξ_{cc}^{+} lifetime variation, is discussed in Section 8.4.3.

Only the 2017 and 2018 simulation samples are considered for this study, because the simulation samples for both the signal and normalisation modes are produced with the same simulation version. The ratio of L0 efficiencies using simulation samples for 2016 after the reconstruction stage is 0.8508 ± 0.0029 and it deviates from one rather significantly, which is considered to be an artefact of different simulation versions with the inconsistent L0 thresholds, as discussed in Section 6.1.2. Since the L0 TIS efficiency ratio is not expected to be different between the years, it is concluded that it is sufficient to use only the 2017 and 2018 simulation samples in order to avoid requesting new 2016 simulation samples with the same simulation versions.

Selection stage	Ratio of efficiencies $\varepsilon_{\text{norm}}/\varepsilon_{\text{sig}}$ at the Ξ_{cc}^{+} lifetime of		
	40 fs	80 fs	160 fs
Before selection	1.0165 ± 0.0017	1.0152 ± 0.0015	1.0144 ± 0.0024
After selection	1.053 ± 0.006	1.034 ± 0.005	1.021 ± 0.006

Table 8.9.: Ratio of L0 TIS efficiencies for the normalisation and signal channels before and after the selection is applied, evaluated for different Ξ_{cc}^{+} lifetime hypotheses. The uncertainties are statistical only.

8.2.6. Summary of the efficiency corrections

Table 8.10 summarises the ratio of efficiencies between the normalisation and signal decay modes before corrections and after subsequent application of the individual efficiency corrections described in Sections 8.2.3, 8.2.4, and 8.2.5 .

Efficiency correction	Ratio of efficiencies $\varepsilon_{\text{norm}}/\varepsilon_{\text{sig}}$
Before correction	3.41 ± 0.03
HLT1 correction	3.52 ± 0.05
ρ^{0}-resonance correction	3.56 ± 0.04
Hardware-trigger correction	3.63 ± 0.04

Table 8.10.: Ratio of efficiencies for all studied years combined after the individual efficiency corrections are subsequently applied. The uncertainties are statistical only.

8.3. Signal-yield determination

To measure the UL on R, the signal yield N_{norm} for the normalisation decay $\Xi_{cc}^{++} \rightarrow \Xi_{c}^{+} \pi^{+}$ needs to be evaluated, as shown in Equation 8.2. An unbinned extended maximum-likelihood fit is performed to the $\Xi_{c}^{+} \pi^{+}$ invariant-mass spectrum in order to extract the corresponding signal yield. Figure 8.6 shows the mass fit to the $\Xi_{c}^{+} \pi^{+}$ invariant-mass spectrum in the 2016–2018 data using the default trigger set, from which the signal yield is determined to be 442 ± 56.

In case the Ξ_{cc}^{+} baryon would have been observed in the studied final state $\Xi_{c}^{+} \pi^{-} \pi^{+}$ after unblinding, its signal yield would have been determined as well in order to evaluate N_{sig} needed for the calculation of R. The procedure to evaluate N_{sig} would have been the same as for the normalisation channel, using the invariant-mass fit for the signal channel introduced in Section 7.1. However, since no significant signal has been observed, the UL on R, which is basically the UL on N_{sig}, is determined. It is discussed in detail in Section 8.5.

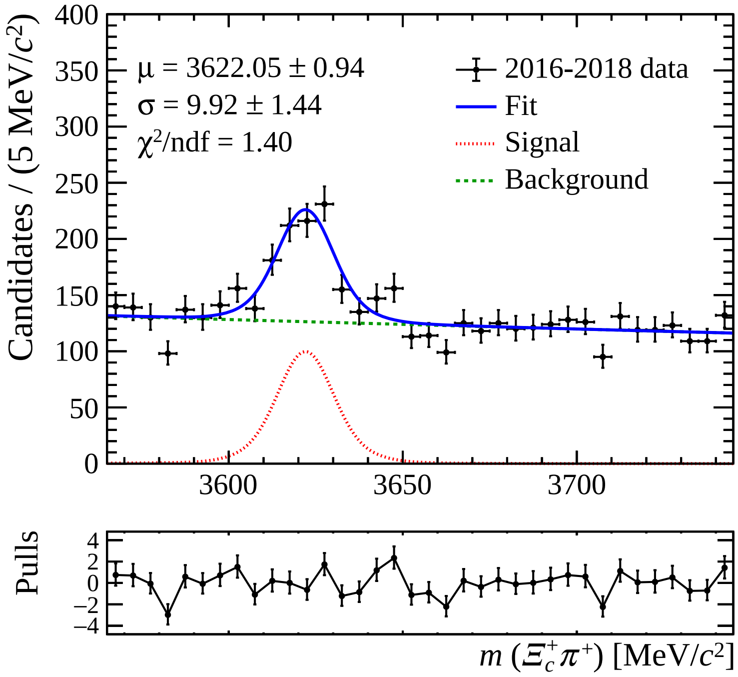

Figure 8.6.: Mass fit (DSCB plus Gaussian for the signal and exponential for the background components) to the $\Xi_{c}^{+} \pi^{+}$ invariant-mass distribution after all requirements are applied for all years (2016–2018) combined for the default trigger set.

8.3.1. Sensitivity study

As was discussed in Section 1.3.1.1, it is expected that both the Ξ_{cc}^{+} and Ξ_{cc}^{++} baryons have the same production cross-section [38]. Using the result of the efficiency ratio described in Section 8.1.9, the signal yield for the normalisation channel discussed in Section 8.3, and the expected background yield and shape for the signal decay $\Xi_{cc}^{+} \to \Xi_{c}^{+} \pi^{-} \pi^{+}$ described in Section 7.1, the expected yield and significance for the signal decay can be estimated before unblinding for various ratios of BF hypotheses, assuming $\sigma(\Xi_{cc}^{+}) = \sigma(\Xi_{cc}^{++})$.

Five different ratios of BF hypotheses are studied, namely the ratio of $\mathcal{B}\,(\Xi_{cc}^{+} \to \Xi_{c}^{+} \pi^{-} \pi^{+})$ to $\mathcal{B}\,(\Xi_{cc}^{++} \to \Xi_{c}^{+} \pi^{+})$ varying from 1 to 5, for which 200 pseudoexperiments are produced. The mean values for the expected signal yield and its significance are extracted for each pseudoexperiment. Figure 8.7 shows the fraction of pseudoexperiments that passed $3\,\sigma$, $5\,\sigma$ or $6\,\sigma$ thresholds of the statistical significance. One can see that there is no significant signal expected for the signal channel under the assumption that the BFs for both decay modes are the same. However, if the BF for the signal decay is more than 2.5 times larger than that of the normalisation mode, there can be evidence for the searched decay mode in the studied dataset, since at least 50% of the pseudoexperiments have an evaluated local significance larger than $3\,\sigma$. If the ratio of the corresponding BFs is larger than 4, more than 50% of the pseudoexperiments have an evaluated local significance larger than $5\,\sigma$, and if the ratio of the BFs is larger than 4.5, 50% of the pseudoexperiments pass the observation threshold of the local significance of $6\,\sigma$, as defined by the decision tree discussed in Section 5.2.

8.4. Systematic uncertainties for the upper limits

The following sections describe the evaluation of the systematic uncertainties considered for the determination of the UL on R. All of the presented methods were developed prior to unblinding.

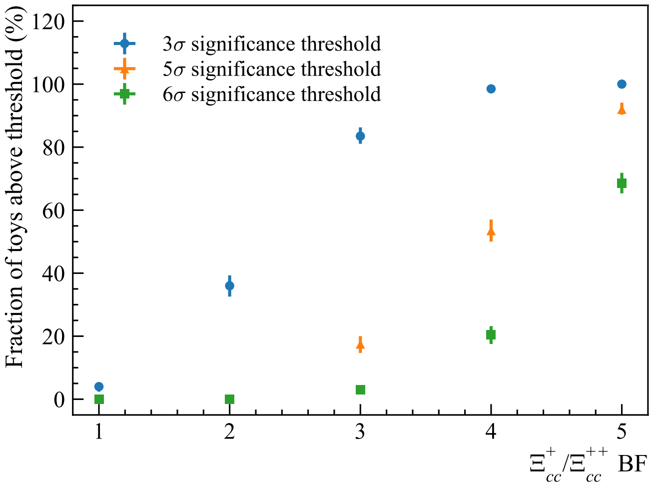

Figure 8.7.: Fraction of pseudoexperiments above $3\,\sigma$ (blue circles), $5\,\sigma$ (orange triangles) and $6\,\sigma$ (green squares) thresholds for different $\Xi_{cc}^{+} \to \Xi_{c}^{+} \pi^{-} \pi^{+}$ to $\Xi_{cc}^{++} \to \Xi_{c}^{+} \pi^{+}$ BF hypotheses, extracted from 200 pseudoexperiments for each BF hypothesis. The uncertainties are computed using the Wilson interval for 68% confidence level implemented in the ROOT TEfficiency class.

8.4.1. Tracking-efficiency uncertainty

The tracking-efficiency correction to account for a possible mismodelling of tracking efficiency in the simulation is evaluated using the TrackCalib tool, which is discussed in Section 8.1.2. There are three sources of a systematic uncertainty associated with the tracking efficiency. The first source is the statistical uncertainty of the tracking correction tables used for the tracking efficiency evaluation. The associated systematic uncertainty is evaluated using 1000 pseudoexperiments which produce new tracking-efficiency tables with a correction factor in each bin generated from a Gaussian distribution with its mean equal to the correction factor in the nominal table and the width equal to its statistical uncertainty. As the low momentum and η bins are not covered by the tracking efficiency tables, a correction factor based on the nearest bin is assigned to the corresponding bins, and a 5% uncertainty in that bin is considered. Figure 8.8 shows a distribution of the ratio of efficiencies for 1000 pseudoexperiments, fitted by a Gaussian function. The width of the Gaussian divided by the central value of the nominal efficiency is equal to 0.37%, which is assigned as a systematic uncertainty.

The remaining two sources of the systematic uncertainty considered for the tracking efficiency are associated with the individual tracks in the final state. These uncertainties cancel out in the efficiency ratio, however, there is one more pion track for the signal channel that is not present in the normalisation mode, which has to be taken into account. A 2.5% uncertainty on the pion-reconstruction efficiency due to modelling of hadronic interactions with the detector material [165] and uncertainty on the tracking efficiency from the method itself, which is 0.8% for a track at 13 TeV according to the recommendation of the tracking group, are assigned for a pion track which does not cancel out in the efficiency ratio. All of the mentioned uncertainties associated with the tracking efficiency are summed up in quadrature to get the final tracking-efficiency uncertainty, which results in 2.65%.

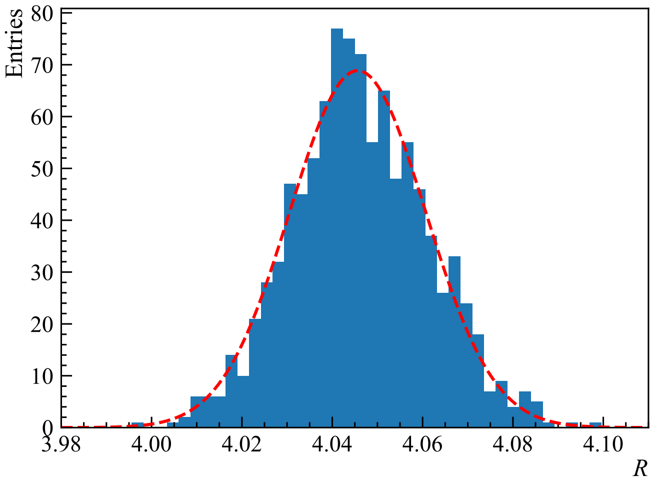

Figure 8.8.: Distribution of the efficiency ratio for 1000 pseudoexperiments for which a tracking-efficiency correction in each bin of p and η is sampled from the Gaussian distribution with the mean equal to the correction factor in the nominal table and width equal to its statistical uncertainty, fitted by a Gaussian function.

8.4.2. PID-efficiency uncertainty

The systematic uncertainty for the method of correcting the PID efficiency is evaluated by varying the binning scheme of the kinematic variables used to correct the simulation samples with the PIDCalib package. The binning scheme is varied by changing the size of the corresponding bins, namely the bins are halved, doubled and tripled, consistently for both the signal and normalisation modes. The largest difference of the overall efficiency ratios between the different binning schemes is 0.25%, which is accounted as a PID systematic uncertainty. The systematic uncertainty associated with the finite size of the calibration samples used for the PID correction is evaluated similarly as for the tracking corrections described in Section 8.4.1, but it is found to be negligible with respect to the evaluated PID systematic uncertainty of 0.25%.

8.4.3. Hardware-trigger uncertainty

A systematic uncertainty related to the correction for the L0 efficiency due to the selection, discussed in Section 8.2.5, is considered. The variation with the lifetime shown in Table 8.9 is 1.84%, which in quadrature with a half of the applied correction of 0.95% is taken as a systematic uncertainty due the L0 efficiency uncertainty, resulting in 2.07%.

8.4.4. Yield-measurement uncertainty

A variation of the default signal and background shapes using alternative fit models was described in Section 7.4.6 to evaluate a systematic uncertainty on the measured mass. The same method is also considered for a variation of the extracted signal yield to assign a systematic uncertainty due to the chosen fit model. This uncertainty is taken into account also for the evaluation of the global significance for the combination with the $\Lambda_c^{+} K^{-} \pi^{+}$ final state discussed in Section 7.3.3.3.

For the normalisation mode, the signal and background yields observed in the data are used to generate pseudoexperiments and evaluate a bias on the measured yield depending on the chosen model. A double-Gaussian function is used as an alternative model for a signal component and the first-order Chebychev polynomial function is used as an alternative model for a background shape. Using the alternative fit model for the signal and background, 10k pseudoexperiments are produced and fitted with the nominal fit model. Figure 8.9 shows the difference between the generated and fitted signal yields. The distribution is fitted with the Gaussian function, and its mean of 9.7 candidates is taken as a systematic uncertainty. For the background component, no significant impact is found on the signal yield shift. The normalisation channel signal yield N_{norm} with its combined statistical and systematic uncertainty added in quadrature is therefore 442 ± 57.

Since the measurement of R is not performed, the uncertainty on the signal yield from the chosen mass fit model does not have any impact on the determination of the UL on R as the mass model is not used for its evaluation. However, the background fit is used to evaluate the number of expected background candidates, therefore a systematic uncertainty due to the background model is evaluated using the numbers from the observed invariant-mass spectrum after unblinding. The method and the

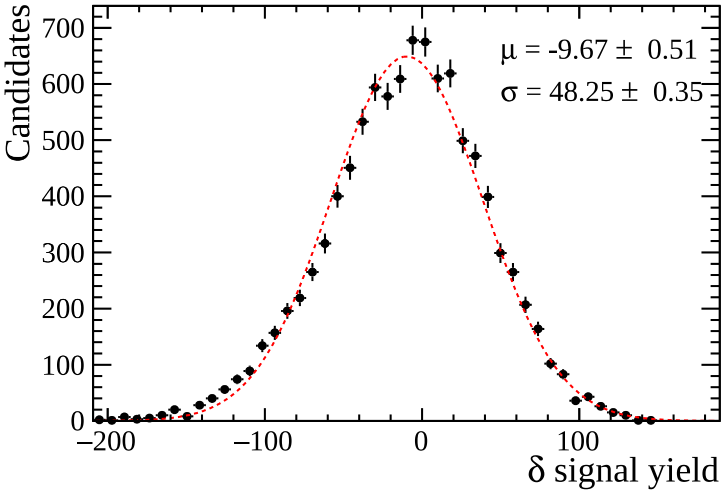

Figure 8.9.: Difference between the generated (double Gaussian model) and fitted (DSCB plus Gaussian model) signal yield for 10k pseudoexperiments for the normalisation channel $\Xi_{cc}^{++} \to \Xi_{c}^{+} \pi^{+}$ fitted by a Gaussian function.

alternative model are the same as already described above for the normalisation channel. However, the impact of the alternative background model is evaluated with respect to the extracted background yield of the signal channel since that is the quantity used in the calculation of the UL. Three different mass windows are considered in order to evaluate the impact on the measured background yield in different mass regions: lower edge mass region of $(3400 + 6\,\sigma)\,\mathrm{MeV}/c^2$, middle mass region of $(3600 \pm 3\,\sigma)\,\mathrm{MeV}/c^2$, and the upper edge mass region of $(3800 - 6\,\sigma)\,\mathrm{MeV}/c^2$, where σ is the Ξ_{cc}^{+} mass resolution of $8.92\,\mathrm{MeV}/c^2$ evaluated from the simulation. The largest variation of the fitted background yield with respect to the generated background yield for 10k pseudoexperiments is 1.27%, which is taken as the systematic uncertainty on the measurement of the background yield considered for the UL determination.

Moreover, the partially reconstructed decays in Section 7.1.1 not taken into account in the signal modelling can also impact the measured yield. The same pseudoexperiment study as discussed in Section 7.1.1 used to evaluate the impact of the partially reconstructed background on the evaluated significance is performed for the measured signal yield. Figure 8.10 shows a difference between the yield obtained from the nominal fit to the spectra without the partially reconstructed components and the yield from the nominal fit to the spectra with these components considered. Based on the Gaussian fit of the yield difference, the signal yield is decreased by 52 candidates, which is 23.1% from the average number of the injected signal candidates. Since the signal yield is always decreased if the presence of the partially reconstructed background is not taken into the account, it is not considered as a systematic uncertainty for the evaluation of the UL on R as any partially reconstructed background would only increase the UL.

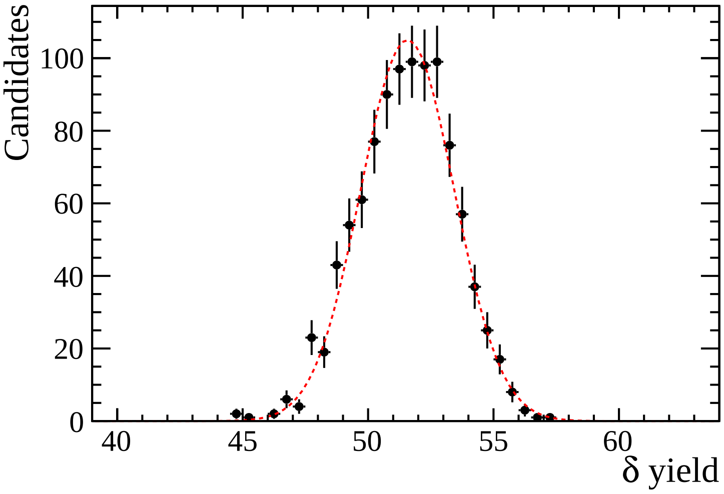

Figure 8.10.: Difference between the signal yield obtained from the nominal fit to the spectra without the partially reconstructed components and the signal yield from the nominal fit to the spectra with these components considered (black points), with the Gaussian fit (red dashed line) with a mean of 52. The signal yield is decreased by 23.1% if the presence of the partially reconstructed decays is not taken into the account.

8.4.5. Uncertainty due to the simulation correction

The uncertainty due to the multidimensional weighing of the p_{T}, η and nTracks distributions in the simulation is evaluated by calculating one dimensional weights in bins of the individual variables and re-evaluating the efficiency ratio. The variation of the ratio of overall efficiencies with respect to its nominal value is 1.70%, which is taken as the systematic uncertainty.

8.4.6. Uncertainty on the Ξ_{cc}^{++} lifetime

The lifetime of the Ξ_{cc}^{++} baryon was measured by the LHCb collaboration to be $0.256^{+0.024}_{-0.022}\,(\text{stat}) \pm 0.014\,(\text{syst})$ ps [102]. Since the lifetime affects the efficiency, the uncertainty on the Ξ_{cc}^{++} lifetime has to be accounted for as a systematic uncertainty for the determination of the UL on R, as the $\Xi_{cc}^{++} \to \Xi_{c}^{+} \pi^{+}$ decay is used as the normalisation channel. The associated systematic uncertainty is evaluated by changing the lifetime of the Ξ_{cc}^{++} baryon by $\pm 1\,\sigma$ around its nominal lifetime of 256 fs, where σ is the combined measured uncertainty on the Ξ_{cc}^{++} lifetime. Table 8.11 shows the variation of the ratio of efficiencies for different Ξ_{cc}^{++} lifetime hypothesis. The largest difference between the nominal ratio of efficiencies and ratio of efficiencies for the changed lifetimes is 6.75%, which is taken as a systematic uncertainty.

Ξ_{cc}^{++} lifetime	Ratio of efficiencies $\varepsilon_{\text{norm}}/\varepsilon_{\text{sig}}$			
hypothesis [fs]	2016	2017	2018	combined
230	2.89 ± 0.06	3.30 ± 0.04	3.26 ± 0.04	3.182 ± 0.026
256	3.09 ± 0.07	3.54 ± 0.04	3.50 ± 0.04	3.412 ± 0.028
284	3.28 ± 0.07	3.77 ± 0.04	3.71 ± 0.04	3.622 ± 0.030

Table 8.11.: Ratio of overall efficiencies for the normalisation and signal channels for the variation of the Ξ_{cc}^{++} lifetime by $\pm 1\,\sigma$ around its nominal lifetime of 256 fs.

8.4.7. Uncertainty due to possible resonant contributions

A systematic uncertainty due to a possible $\Xi_{cc}^{+} \to \Xi_{c}^{+} (\rho^{0} \to \pi^{-} \pi^{+})$ resonant contribution is based on the study described in Section 8.2.4, where a correction for this possible contribution is estimated by averaging over the efficiency ratio with 0% of the resonance contribution, and the efficiency ratio after the ρ^{0} weighting with 100% of the resonance contribution. A systematic uncertainty of 1.1% is assigned as the difference between both of these extreme cases.

8.4.8. Summary of the systematic uncertainties for the UL determination

Table 8.12 summarises the systematic uncertainties discussed in the previous sections, which are considered for the evaluation of the efficiency ratio used for the determination of the UL on R. As all of the evaluated uncertainties are uncorrelated, they are taken in quadrature to evaluate the final systematic uncertainty on the efficiency ratio, which gives 7.81%. In addition, the systematic uncertainty on the measured signal yield of the normalisation channel discussed in Section 8.4.4 is evaluated to be 2.19%, and the systematic uncertainty associated with the measured background yield for the signal decay mode is 1.27%. As a reminder, the signal yield of the normalisation channel discussed in Section 6.3 was measured to be 442 ± 56, where the uncertainty is only statistical. The associated statistical uncertainty of 12.67% is therefore a dominant uncertainty in the upper-limit determination with respect to the evaluated systematic uncertainties described above.

Category	Uncertainty on the $\varepsilon_{\text{norm}}/\varepsilon_{\text{sig}}$ (%)
Tracking	2.65
PID	0.25
Hardware trigger	2.07
Simulation correction	1.70
Ξ_{cc}^{++} lifetime	6.75
$\Xi_{cc}^{+} \to \Xi_{c}^{+} \rho^{0}$ contribution	1.11
Combined	7.81

Table 8.12.: Systematic uncertainties on the ratio of efficiencies for the determination of the UL on R.

8.5. Determination of the upper limits

Based on the evaluated ratio of efficiencies $\varepsilon_{\text{norm}}/\varepsilon_{\text{sig}}$ and the signal yield of the normalisation channel N_{norm} described in Sections 8.1 and 8.3, respectively, a single-event sensitivity α from Equation 8.2 is calculated. Table 8.13 shows the single-event sensitivity for different lifetime hypotheses including all corrections to the efficiency ratio described in Section 8.2 and the combined systematic uncertainties summarised in Section 8.4.8. Since no significant signal has been observed for the $\Xi_{cc}^{+} \to \Xi_{c}^{+}\pi^{-}\pi^{+}$ decay, an UL on its signal yield N_{sig} is determined based on the unblinded invariant-mass spectrum shown in Chapter 7. The method to evaluate the UL and the corresponding results are discussed in the following two sections.

Lifetime [fs]	α
40	0.0122 ± 0.0018
80	0.0082 ± 0.0012
120	0.0067 ± 0.0010
160	0.0061 ± 0.0009

Table 8.13.: Single-event sensitivity for different Ξ_{cc}^{+} lifetime hypotheses including all statistical and systematic uncertainties, and the corrected efficiency ratio.

8.5.1. Method to determine the upper limits

The efficiency ratio described in Section 8.1 is a crucial input to the UL determination and it is considered in the same way for the UL evaluation as it would have been for the determination of R in case a significant signal would have been observed. Since the Ξ_{cc}^{+} baryon has never been unambiguously observed, its mass and lifetime are unknown, therefore the ULs on R are evaluated in the mass region from 3400 to 3800 MeV/c^2 and for four different lifetime hypotheses: 40, 80, 120 and 160 fs.

The UL on R shown in Equation 8.2 is determined using the CLs method [219], which uses the ratio of the confidences in the signal-plus-background to background-only hypotheses to set a limit on some observable in the experiment. In this analysis, the observable, or the so-called a test statistic, is the number of observed signal candidates n_{obs}, which is the number of candidates observed in a certain invariant-mass window. For each hypothetical value of R, the expected number of signal candidates is $\hat{n}_{\text{s}} = R/\alpha$. The single-event sensitivity α is sampled from a Gaussian distribution centred at the value of α with a standard deviation equal to the total uncertainty on α. There are two common ways to evaluate the test statistic using pseudoexperiments:

either the full invariant-mass spectrum is generated and a mass fit is used to extract the corresponding signal yields, or the number of signal (n_{s}) and background (n_{b}) candidates in the signal region are sampled from Poisson distributions. Since the pseudoexperiments need to be performed for different lifetime and mass hypotheses and also for the different hypothetical values of R, generating and fitting the full mass spectrum is considerably more CPU intensive than evaluating the test statistic as a counting experiment. The test statistic is therefore sampled from the Poisson distribution, in which case the CLs can be computed as shown in reference [219] as

$$\mathrm{CLs} = \frac{P(n \leq n_{\mathrm{obs}})}{P(n_{\mathrm{b}} \leq n_{\mathrm{obs}})}, \tag{8.4}$$

where n and n_{b} are the number of events from the Poisson distributions produced by pseudoexperiments for the signal-plus-background and background-only models, respectively, and n_{obs} is the number of observed candidates in the invariant-mass window, which is determined to be $\pm 2\sigma$ around the considered mass hypothesis. The value for $\hat{n_{\mathrm{b}}}$ to sample the Poisson distribution is determined from the extracted background yield from the mass fit to the final invariant-mass spectrum. The CLs curve is then derived from running 3×10^{5} pseudoexperiments for each hypothetical value of R and the assumed Ξ_{cc}^{+} mass, using $2\,\mathrm{MeV}/c^{2}$ steps in the $\Xi_{c}^{+}\pi^{-}\pi^{+}$ invariant-mass window from 3400 to $3800\,\mathrm{MeV}/c^{2}$, repeated for four lifetime hypotheses. The derived CLs curve as a function of R is determined for each mass and lifetime hypothesis and the UL on R at 90% and 95% confidence level (CL) is set as a value for which the CLs is equal to 0.1 and 0.05, respectively.

8.5.2. Results for the upper-limit determination

The overall efficiency ratio without any corrections applied is evaluated to be 3.412 ± 0.028, as shown in Table 8.4. To use the efficiency ratio for the determination of the UL on R, all corrections to the evaluated efficiency ratio need to be applied subsequently to determine the final corrected efficiency ratio. Firstly, the efficiency correction due to the different fraction of events in the HLT1 categories described in Section 8.2.3 is applied, followed by the correction due to possible resonant contributions described in Section 8.2.4, and finally the L0 correction due to the shift of the efficiency ratio before and after the selection described in Section 8.2.5. The resulting corrected efficiency ratio is determined to be 3.63 ± 0.04. The overall systematic uncertainty on the efficiency ratio is 7.81%, as summarised in Table 8.12 before unblinding. The corrected efficiency ratio with its combined statistical and systematic uncertainty is therefore 3.63 ± 0.29.

The normalisation channel signal yield N_{norm} with its combined statistical and systematic uncertainty is evaluated to be 442 ± 57, resulting in the single-event sensitivity α with the combined uncertainty equal to 0.0082 ± 0.0012 for the nominal Ξ_{cc}^{+} lifetime hypothesis of 80 fs. The variation of α with the lifetime using the corrected efficiency ratio and with the combined uncertainty is summarised in Table 8.13.

To consider the variation of the corrected efficiency ratio with the assumed Ξ_{cc}^{+} mass, a linear approximation is used, as described in Section 8.2.2. Figure 8.11 shows the corrected efficiency ratio for six different mass hypotheses fitted by a linear function, for which the slope a_1 is determined to be $(-2.1 \pm 0.16) \times 10^{-3} c^2/\,\text{MeV}$. The efficiency ratio $\varepsilon_{\text{r}}(m)$ at the mass m given in MeV/c^2 is then evaluated using a linear approximation

$$\varepsilon_{\text{r}}(m) = \varepsilon_{\text{r}}(3621) + (m - 3621) \times a_1, \tag{8.5}$$

where $\varepsilon_{\text{r}}(3621)$ is the efficiency ratio evaluated for the nominal Ξ_{cc}^{+} mass of $3621.4\,\text{MeV}/c^2$ and the nominal Ξ_{cc}^{+} lifetime of 80 fs. Only the statistical uncertainties on the $\varepsilon_{\text{r}}(3621)$ and a_1 parameter are propagated in Equation 8.5 to evaluate the statistical uncertainty on $\varepsilon_{\text{r}}(m)$. The systematic uncertainty is then calculated as 7.81% of the evaluated efficiency ratio $\varepsilon_{\text{r}}(m)$ and added with the statistical component in quadrature to calculate the final uncertainty on $\varepsilon_{\text{r}}(m)$. Finally, to take into account the lifetime scaling on top of the mass variation, the efficiency ratio $\varepsilon_{\text{r}}(m)$ is scaled by the factors summarised in Table 8.14 calculated as the ratio between the efficiency ratio at the particular Ξ_{cc}^{+} lifetime and the nominal Ξ_{cc}^{+} lifetime of 80 fs.

Lifetime [fs]	scaling factor
40	1.48 ± 0.02
120	0.82 ± 0.01
160	0.74 ± 0.01

Table 8.14.: Scaling factors to evaluate the Ξ_{cc}^{+} lifetime variation on top of its mass variation, calculated as the ratio between the efficiency ratio at the particular Ξ_{cc}^{+} lifetime and the nominal Ξ_{cc}^{+} lifetime of 80 fs. The uncertainties are statistical only.

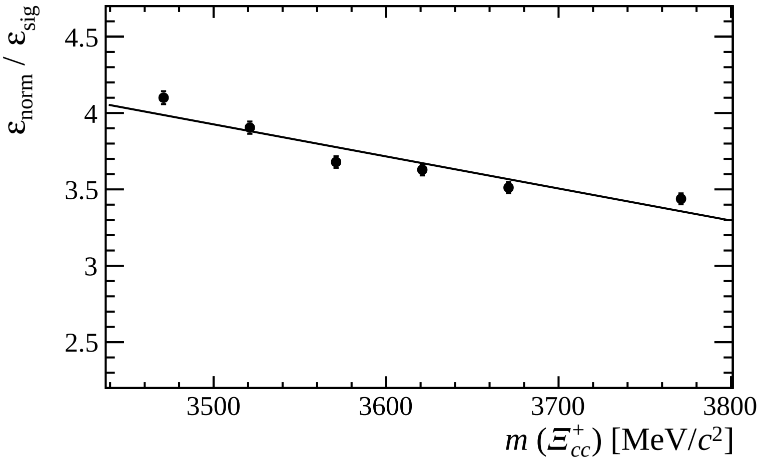

Figure 8.11.: Overall corrected ratio of efficiencies for the normalisation and signal channels for different Ξ_{cc}^{+} mass hypotheses. The uncertainties are statistical only.

To calculate the UL, the single-event sensitivity α is sampled from a Gaussian distribution centred at the value of α with a standard deviation equal to the total uncertainty on α, as described in Section 8.5.1. An additional uncertainty of 1.27% on the background yield is evaluated after unblinding by using the numbers from the observed invariant-mass spectrum, which is described in detail in Section 8.4.4. The number of background candidates is therefore firstly sampled from a Gaussian centred at the number of observed background events determined from the background only fit to the final mass spectra in $\pm 2\,\sigma$ mass window around the evaluated mass, with a standard deviation corresponding to 1.27% of the observed background yield, which is subsequently used as a central value of the Poission distribution to determine $n_{\rm b}$. Figure 8.12 shows the background only fit to the $\Xi_{c}^{+}\pi^{-}\pi^{+}$ invariant-mass spectrum performed in the mass range from 3380 to 3820 MeV/c^2 in order to have a wide enough window for the masses on the edges of the plot.

There is also a non-negligible impact of the unknown Ξ_{cc}^{+} mass resolution, which is taken into account by evaluating $n_{\rm obs}$ and $n_{\rm b}$ in larger and smaller mass windows by varying the mass resolution by ± 1.37 MeV/c^2, which is determined as the uncertainty on the fixed resolution calculated from the difference between the mass resolution in data and simulation for the normalisation channel described in Section 7.1. The values of the UL are subsequently compared for the larger and smaller mass windows with the default mass window. The larger mass window gives a larger UL on average by about 12.5%, therefore the larger mass window is used for the final evaluation of the UL on R.

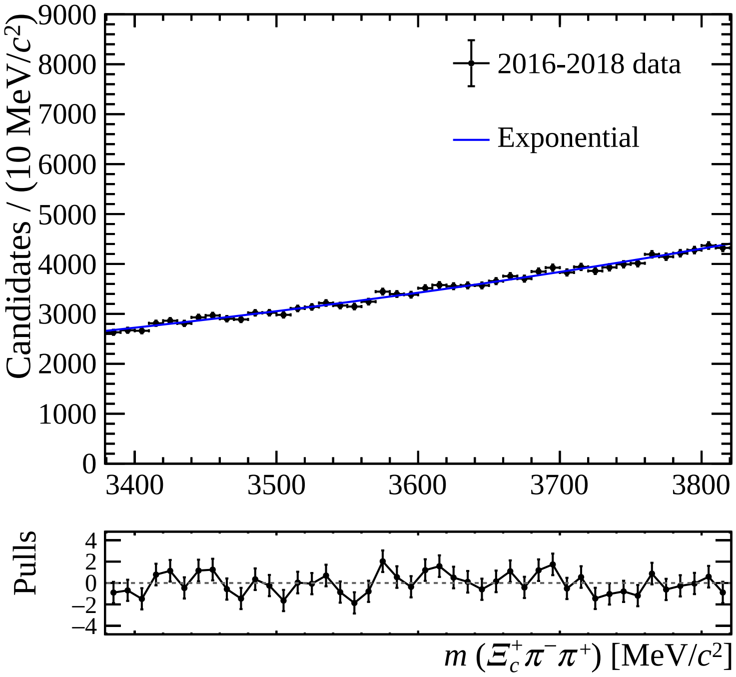

Figure 8.12.: Background-only fit to the unblinded $\Xi_c^+\pi^-\pi^+$ invariant-mass distribution to evaluate the number of background candidates for the UL calculation.

The number of generated pseudoexperiments for each possible combination of R and mass is 300k. The UL on R at 90% and 95% CL is determined from the derived CLs curve as the value of R for which the CLs is equal to 0.1 and 0.05, respectively. An example of the CLs curve for the Ξ_{cc}^{+} for mass of 3623 MeV/c^2, for which the minimum p-value is found based on the combined mass fit with the $\Xi_{cc}^{+}\to\Lambda_c^+K^-\pi^+$ decay described in Section 7.3.3, is shown in Figure 8.13 with the highlighted 90% and 95% CL, which are $R < 4.0$ at 90% CL and $R < 4.7$ at 95% CL. Figures 8.14 and 8.15 show the plots for the UL on R as a function of the assumed Ξ_{cc}^{+} mass for four different Ξ_{cc}^{+} lifetime hypotheses at 90% and 95% CL, respectively.

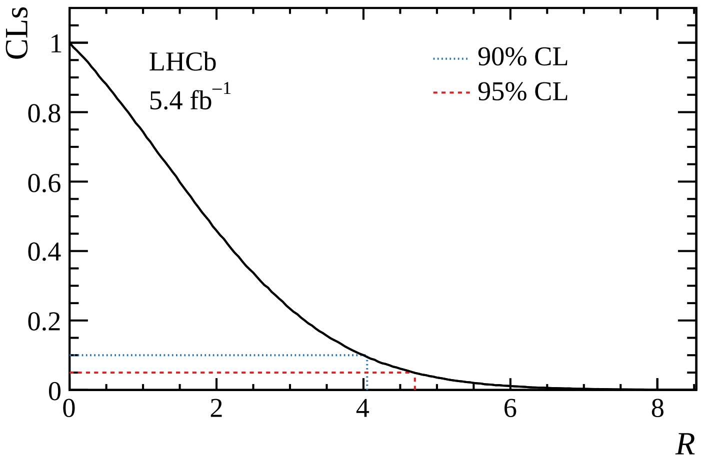

Figure 8.13.: Calculated CLs values (black solid line) versus hypothetical values of R for the Ξ_{cc}^{+} mass of 3623 MeV/c^2 and the lifetime of 80 fs. The blue dotted (red dashed) line represents 90% (95%) CL.

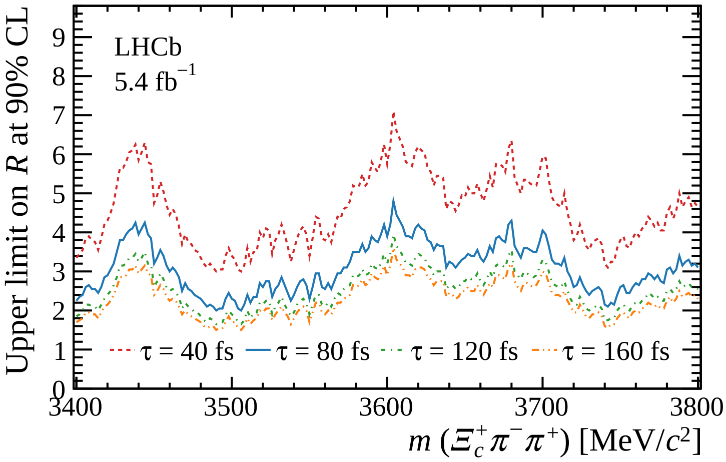

Figure 8.14.: Upper limits on R as a function of the assumed Ξ_{cc}^{+} mass for four different lifetime hypotheses (τ) at 90% CL.

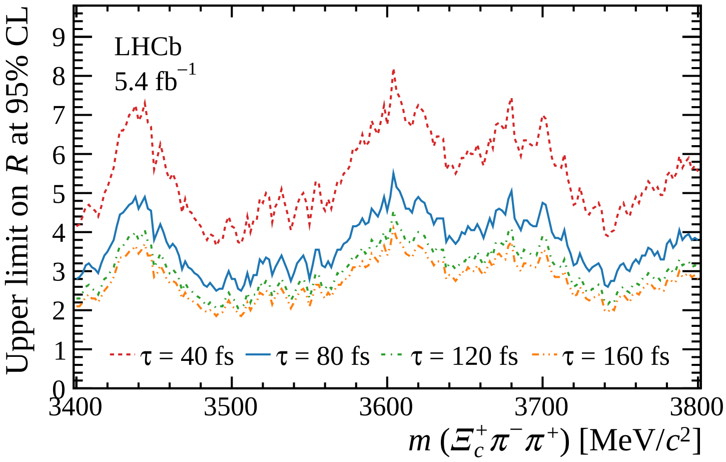

Figure 8.15.: Upper limits on R as a function of the assumed Ξ_{cc}^{+} mass for four different lifetime hypotheses (τ) at 95% CL.

8.6. Summary

This chapter discussed the determination of the upper limits on the relative production cross-section times branching fraction of the $\Xi_{cc}^{+} \to \Xi_{c}^{+}\pi^{-}\pi^{+}$ decay compared to the normalisation channel $\Xi_{cc}^{++} \to \Xi_{c}^{+}\pi^{+}$.

The upper limits are determined using the CLs method and they are evaluated as a function of the assumed Ξ_{cc}^{+} mass in the mass region from 3400 to 3800 MeV/c^2 for four different Ξ_{cc}^{+} lifetime hypotheses at 90% and 95% CL. For the nominal lifetime hypothesis of the Ξ_{cc}^{+} baryon of 80 fs, the UL on R varies between 2 and 5 at the 95% CL in the evaluated mass range. For the mass with the minimum p-value in the combined fit with the $\Lambda_c^{+}K^{-}\pi^{+}$ final state evaluated to be 3623 MeV/c^2 and at the nominal Ξ_{cc}^{+} lifetime of 80 fs, the UL is

$$R < 4.0\ (4.7)\ \text{at}\ 90\%\ (95\%)\ \text{CL}.$$

Chapter 9.

Conclusions

"In the best goodbyes, there's always the feeling that there's something more to say."
— Lori Gottlieb in her book *Maybe You Should Talk to Someone*

The previous chapters of this thesis described my main research activities, as well as the theoretical background to the performed studies. Firstly, the theoretical overview and the status of the field were discussed in Chapter 1, followed by a description of the LHCb experiment in Chapter 2, since the data that were used in the performed studies were collected by the LHCb detector.

Subsequently, three different studies were presented, namely the trigger development for charmed baryons, a study of the VELO hit resolution, and the main analysis devoted to the search for the doubly charmed baryon Ξ_{cc}^{+}, which are together summarised in this chapter in Section 9.1. This thesis then concludes in Section 9.2 with a discussion of future prospects for the presented studies.

9.1. Summary

The first study presented in this thesis was the development of the MVA-based inclusive Turbo++ trigger line for the Ξ_c^0 baryon, which was implemented for the 2018 data taking. The goal of the study was to develop an efficient MVA-based selection for the $\Xi_c^0 \to pK^-K^-\pi^+$ decay, independent of the origin of the Ξ_c^0 baryon. It is estimated that the efficiency of the newly developed MVA-based Turbo++ line is improved with respect to the existing cut-based trigger line, especially for the $\Xi_{cc}^{+} \to \Xi_{c}^{0}\pi^{+}$ decay, which is particularly important for future searches and studies of the doubly charmed baryon Ξ_{cc}^{+}.

The detector performance study described in this thesis is devoted to the improvement of the agreement in the VELO hit resolution between data and simulation. The presented method uses the hit resolutions from the data to generate the hit residuals in the simulation. Subsequently, the adjustment of the charge on the strips to match the generated residual was performed and implemented as an algorithm used in the BRUNEL application, which is used to transform the hits in the LHCb detector to reconstructed objects. It is shown that the resolutions of the 2- and 3-strip clusters in the corrected simulation agree with the corresponding resolutions in the data. However, the proposed method is not applicable to 1-strip clusters, therefore a strategy was outlined to correct the fractions of clusters of different sizes as a function of the distance between the hit and the nearest strip, in bins of the projected angle and strip pitch. The correction of charge that was demonstrated for 2- and 3-strip clusters can then be applied after the adjustment of the cluster sizes.

The main analysis discussed in this thesis is devoted to a search for the doubly charmed baryon Ξ_{cc}^{+} in the $\Xi_{c}^{+}\pi^{-}\pi^{+}$ final state. Even though there were previous searches for the Ξ_{cc}^{+} baryon performed by different experiments, as discussed in Section 1.3.2, the analysis described in this thesis is the first search for the Ξ_{cc}^{+} baryon in this particular final state. Since the Ξ_{cc}^{+} baryon has not been observed before, the analysis was treated as blinded until all of its aspects were defined and approved by the corresponding analysis review committee at the LHCb collaboration. All studies were therefore performed without examination of the invariant-mass spectrum from 3.3 to 3.8 GeV, so every aspect had to be carefully checked and evaluated before the final decision for unblinding took place. In particular, an extensive outline of the analysis strategy, the candidate selection, determination of the relative selection efficiencies and evaluation of the relevant systematic uncertainties for both the observation and non-observation case, were developed or performed before unblinding. The search for the $\Xi_{cc}^{+} \to \Xi_{c}^{+}\pi^{-}\pi^{+}$ decays is based on the data collected in 2016–2018 at a centre-of-mass energy of 13 TeV, corresponding to about 5.4 fb^{-1} of integrated luminosity. The analysis is now published and can be found in reference [1].

After unblinding, no significant signal of the Ξ_{cc}^{+} baryon is observed in the $\Xi_{c}^{+}\pi^{-}\pi^{+}$ final state. A minimum p-value of 0.0108 (0.0024) at a mass of 3617 (3452) MeV/c^2 corresponding to local significance of 2.3 σ (2.8 σ) is evaluated for the default (extended) trigger set in the invariant-mass range from 3400 to 3800 MeV/c^2. The p-values are also evaluated for the $\Xi_{cc}^{+}\to\Xi_c(2645)^0\pi^+$ decay, which is reconstructed in the same final state, but proceeds through the intermediate resonance $\Xi_c(2645)^0$, however there is no evidence for this resonant decay either, as the evaluated local significance is 2.2 σ for both trigger sets. A combined mass fit with the $\Lambda_c^+K^-\pi^+$ final state is performed using the extended trigger set for the $\Xi_{cc}^{+}\to\Xi_c^+\pi^-\pi^+$ decay. The evaluated significances for the combination of the two channels are 4.0 σ for the local and 2.9 σ for the global significance, including systematic uncertainties. The global significance is evaluated in the invariant-mass range from 3500 to 3700 MeV/c^2. The simultaneous fit to the two spectra is performed, for which the minimum p-value is found at a mass of 3623.0 ± 1.4 MeV/c^2, where the uncertainty is only statistical as no mass measurement is performed due to the lack of a significant observation of the Ξ_{cc}^{+} baryon. The best-fit mass value is consistent with the mass of the isospin partner Ξ_{cc}^{++}, which was previously measured to be $3621.55 \pm 0.23\,(\text{stat}) \pm 0.30\,(\text{syst})$ MeV/c^2 [78]. A complete set of the systematic uncertainties for a potential mass measurement of the Ξ_{cc}^{+} baryon were evaluated before unblinding in case a significant signal would have been observed. However, since no significant signal was observed, they were not used in any of the final results.

Since no significant signal of the Ξ_{cc}^{+} baryon is found, upper limits are set on R, which is the ratio of production cross-section times branching fraction with respect to the already observed $\Xi_{cc}^{++}\to\Xi_c^+\pi^+$ decay, in the rapidity range from 2.0 to 4.5 and the transverse momentum range from 2.5 to 25 GeV/c. The upper limits are determined as a function of the assumed Ξ_{cc}^{+} mass in the invariant-mass range from 3400 to 3800 MeV/c^2, and for four different lifetime hypotheses of the Ξ_{cc}^{+} baryon, namely 40, 80, 120, and 160 fs, since the mass and lifetime of the Ξ_{cc}^{+} baryon are *a priori* unknown. For the Ξ_{cc}^{+} lifetime hypothesis of 80 fs, the evaluated upper limit on R varies between 2 and 5 at 95% CL. For the mass at which the minimum p-value is found in the combined fit with the $\Lambda_c^+K^-\pi^+$ final state, and for the Ξ_{cc}^{+} lifetime of 80 fs, the corresponding upper limit is

$$R < 4.0\ (4.7)\ \text{at}\ 90\%\ (95\%)\ \text{CL}.$$

The evaluated upper limits are not contradictory to any known theory predictions. As there are no direct branching fraction predictions for the $\Xi_{cc}^{+}\to\Xi_c^+\pi^-\pi^+$ decay, only the $\Xi_{cc}^{+}\to\Xi_c^+\rho^0$ decay, which is reconstructed in the $\Xi_c^+\pi^-\pi^+$ final state, is considered in the following comparison. The branching fraction of the $\Xi_{cc}^{+}\to\Xi_c^+\rho^0$ decay with respect to the $\Xi_{cc}^{++} \to \Lambda_c^+ K^- \pi^+ \pi^+$ decay is predicted to be 0.04 in reference [91], where the ratio of the Ξ_{cc}^+ and Ξ_{cc}^{++} lifetimes is considered to be 0.3, and it is estimated to be between 0.04 and 1.4 in reference [93] for the Ξ_{cc}^+ lifetime of 45 fs and the Ξ_{cc}^{++} lifetime of 256 fs. The ratio of branching fractions between the already observed $\Xi_{cc}^+ \to (\Xi_c^+ \to pK^-\pi^+)\pi^-\pi^+$ and $\Xi_{cc}^{++} \to (\Lambda_c^+ \to pK^-\pi^+)K^-\pi^+\pi^+$ decays was measured by the LHCb collaboration to be $0.035 \pm 0.009\,(\text{stat}) \pm 0.003\,(\text{syst})$ [103]. Using the measured values of the branching fractions for the $\Xi_c^+ \to pK^-\pi^+$ and $\Lambda_c^+ \to pK^-\pi^+$ decays [11], the upper limit on the ratio of branching fraction between the $\Xi_{cc}^+ \to \Xi_c^+ \pi^- \pi^+$ and $\Xi_{cc}^{++} \to \Lambda_c^+ K^- \pi^+ \pi^+$ decays is estimated to be 0.16. This is consistent with the predicted values, and more data are required in order to improve the limit.

9.2. Future prospects

As was mentioned in Section 2.13, the upgraded LHCb detector [185] that has started its Run 3 operation this year, uses a fully software-based trigger [186]. Consequently, almost all of the trigger selections needed to be implemented as Turbo, TurboSP, or Turbo++ to cope with the given bandwidth of the trigger system. This is particularly relevant for charm hadrons, which are vastly produced at LHCb. The candidates that are not saved by the trigger system are however lost forever. As not all of the decays of the hadrons can be predicted and placed in the software trigger beforehand, as well as there might be various unpredicted exotic hadrons, inclusive triggers play an important role to observe new hadrons or decay modes. It is therefore important to consider some of the decays of charmed baryons to be implemented as TurboSP or Turbo++, to allow for various unforeseen spectroscopy studies. The rate of the Turbo++ trigger line for the $\Xi_c^0 \to pK^-K^-\pi^+$ decay discussed in Chapter 3 would be however insufficient in the upgraded trigger conditions. Various studies using the simulation samples have shown that TurboSP is a preferred choice for charmed baryon decays in order to accommodate the bandwidth and event size requirements of the upgraded trigger system [164]. However, the selections might be tuned during Run 3, once the real data-taking conditions are evaluated, and a sufficiently large efficiency of the corresponding trigger selections is achieved.

Regarding the VELO-hit resolution study described in Chapter 4, its future prospect was already extensively discussed in the corresponding chapter. Since agreement in the resolutions between the data and simulation was not achieved when including 1-strip clusters, future corrections of the cluster sizes are desired, for which a strategy outlined in Section 4.3.1 can be used. It is expected that the proposed additional correction of the fractions of clusters of different sizes, with a subsequent correction of charge that was demonstrated for 2- and 3-strip clusters, would improve the overall agreement in the hit resolution, which would lead to a consistent evaluation of the displacement variables in data and simulation. As there are still many analyses being performed using Run 2 data, it is important to improve the agreement in these commonly used variables, such as χ^2_{IP}, for which a consistent estimation of the hit resolution in the data and simulation is needed. The upgraded VELO detector is a hybrid pixel detector [220], therefore it is not possible to use the same procedure as developed for the silicon strip VELO detector used in Run 1 and Run 2, in case a similar issue would be encountered in the future. The pixel detector has a binary readout scheme, therefore a redistribution of the collected charge cannot be performed. However, the proposed transformation of the cluster size can be potentially adapted in case cluster-size frequencies are different between the data and simulation once the radiation damage of the VELO detector is evident.

The Ξ_{cc}^{+}, Ω_{cc}^{+}, and Ω_{ccc}^{++} baryons are the only baryons from the SU(4) 20-plets that remain unobserved. Even though it is not an area where physics beyond the SM is expected, the studies of doubly charmed baryons are important for a better understanding of QCD and evaluation of its theoretical predictions, which are based on different calculation techniques, as discussed in Section 1.2.2. The doubly charmed baryons, and even more generally the doubly heavy baryons, provide a different environment to study the QCD dynamics in baryons than for baryons with none or only one heavy quark. Given the unprecedented data samples of charm hadrons collected by particle experiments in the last few years, especially at LHCb, it is intriguing that it was not possible to observe these ground-state baryons. This is particularly true for the Ξ_{cc}^{+} baryon, since its isospin partner Ξ_{cc}^{++} was observed in 2017 at LHCb, and they are expected to have the same production cross-sections. Currently, the most plausible explanation for the lack of an observation is a much shorter lifetime of the Ξ_{cc}^{+} baryon with respect to its isospin partner, which is predicted by the theory to be about 2–4 times shorter, as it is experimentally more challenging to search for such a short-lived state. However, the upgraded LHCb detector [185] will allow to collect much larger data sample than already recorded in Run 1 and Run 2. It is expected that the doubly charmed baryon Ξ_{cc}^{+}, as well as the Ω_{cc}^{+} baryon, will be found once the data are collected and analysed in the next few years.

Moreover, before sufficient data samples are processed in Run 3, there are still other decay modes that can be analysed in order to search for the Ξ_{cc}^{+} baryon using the data already collected by the LHCb detector in the previous years. There are software trigger lines that were in place during Run 2 data taking specifically to search for doubly charmed baryons, for example in the $\Xi_{cc}^{+} \to \Xi_{c}^{0}\pi^{+}$ or $\Xi_{cc}^{+} \to D^{+}pK^{-}$ decays. Since the former might have a large branching fraction based on some theory predictions [94, 218], and the latter is experimentally more clean due to the relatively long lifetime of the D^{+} meson, we might see a significant signal of the Ξ_{cc}^{+} baryon from LHCb even before its Run 3 data are analysed, in particular when combined with the previous searches in the $\Xi_{c}^{+}\pi^{-}\pi^{+}$ and $\Lambda_{c}^{+}K^{-}\pi^{+}$ final states. Due to limited and uncertain theory predictions for the branching fractions of the doubly charmed baryon decays, there might be some decay modes with a higher branching fraction that we are not aware of yet. Therefore it is important to study more decay modes, if possible. The analysts should not be discouraged by previous unsuccessful searches for the Ξ_{cc}^{+} baryon, as null results are also important to evaluate potential future searches and their limitations, and the upper limit on the ratio of branching fractions are relevant to compare with theoretical calculations, to evaluate if there are no discrepancies with the corresponding theory expectations.

It is important to note that observing a particle is just a beginning. Without any doubt, it is surely very exciting to observe a new hadron that has not been observed before. Even more so for species that are difficult to find and that have an intriguing history of searches for them, such as the Ξ_{cc}^{+} baryon. However, to confront countless theoretical predictions on their properties, such as masses, lifetimes, production cross-sections, or branching fractions, precise measurements have to be performed once these states are observed. The excited states make also a very interesting area to confront theoretical predictions. To perform these studies precisely, a large data sample is essential in order for a measurement not to be statistically limited. It is clear that the upgraded LHCb detector will provide a large data sample to study the already observed Ξ_{cc}^{++} baryon and its excited states, which will provide more insight into doubly charmed baryons.

I am an optimist and I believe in a better future for the doubly charmed baryon Ξ_{cc}^{+}, and also for its doubly and triply charmed friends, the Ω_{cc}^{+} and Ω_{ccc}^{++} baryons. A combination of the excellent LHCb detector (both the original and the upgraded versions) and its efficient trigger system, an unprecedented data sample of charm hadrons that will be collected by LHCb in Run 3, quickly developing analysis techniques and methods, and brilliant minds working on these searches, makes me confident that we can expect exciting discoveries in this area in the near future. Stay tuned, because I surely will.

Appendix A.

Comparison of 2016, 2017 and 2018 data and simulation

The distributions of the Ξ_{cc}^{+} and Ξ_{c}^{+} kinematic variables after the HLT2 and pre-selection requirements applied to the WSM, WSP, SB and simulation data are shown in Figures A.1, A.2, A.3 and A.4, respectively.

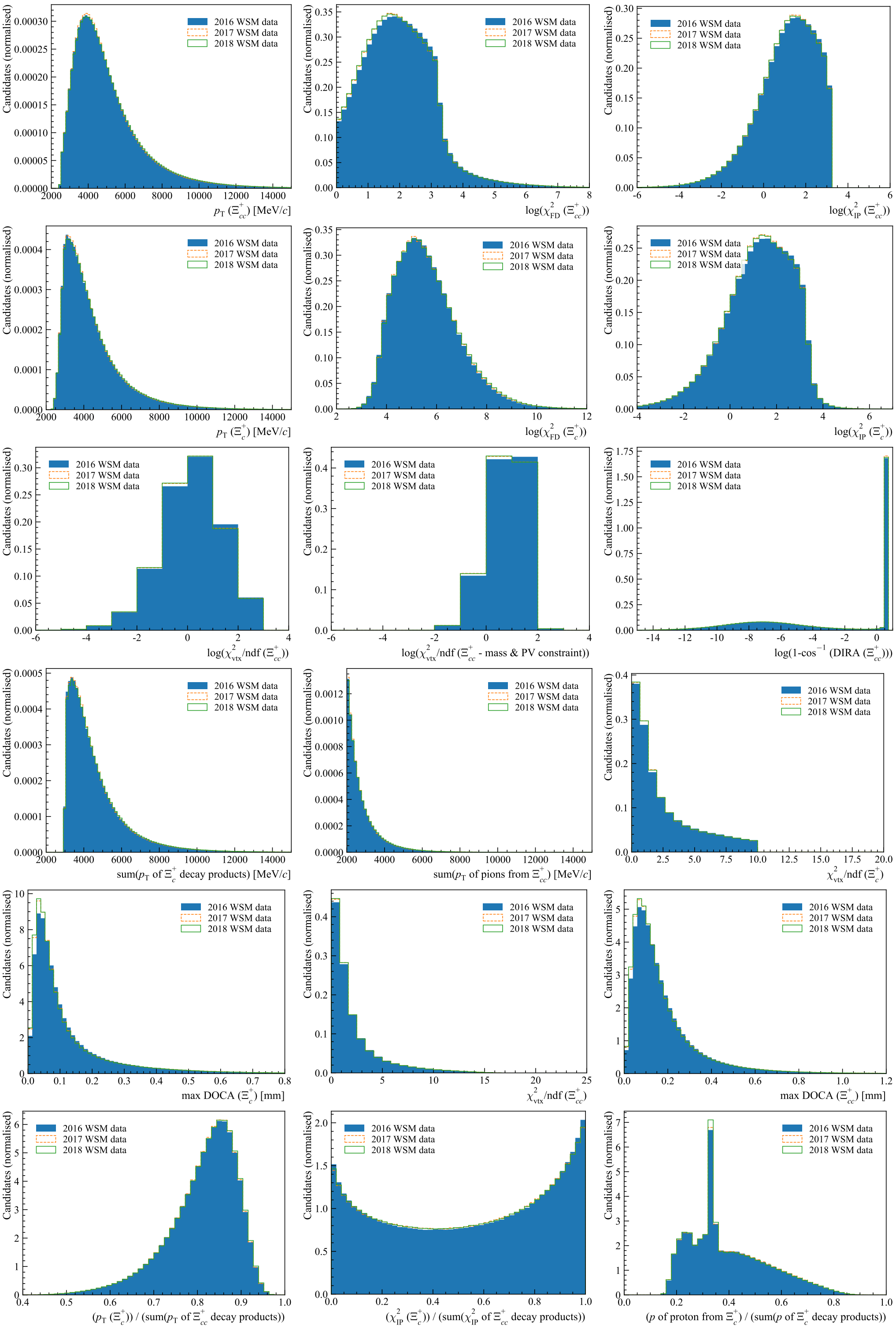

Figure A.1.: Comparison of distributions for several kinematic variables for 2016 (blue area), 2017 (orange dashed line) and 2018 (green solid line) WSM data for the $\Xi_{cc}^{+} \to \Xi_c^{+} \pi^{-} \pi^{+}$ decay after the pre-selections cuts are applied for the default trigger set.

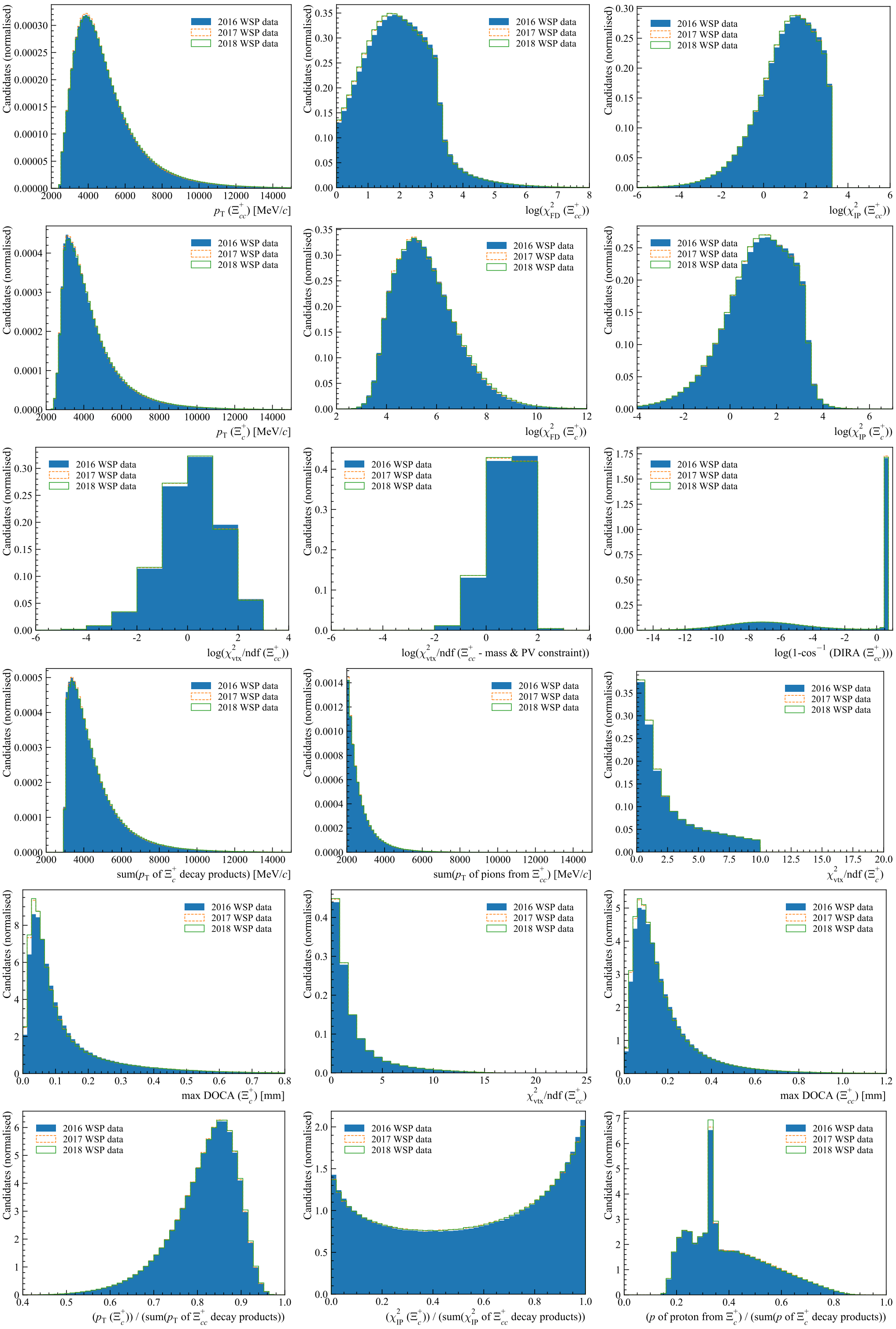

Figure A.2.: Comparison of distributions for several kinematic variables for 2016 (blue area), 2017 (orange dashed line) and 2018 (green solid line) WSP data for the $\Xi_{cc}^{+} \to \Xi_{c}^{+}\pi^{-}\pi^{+}$ decay after the pre-selections cuts are applied for the default trigger set.

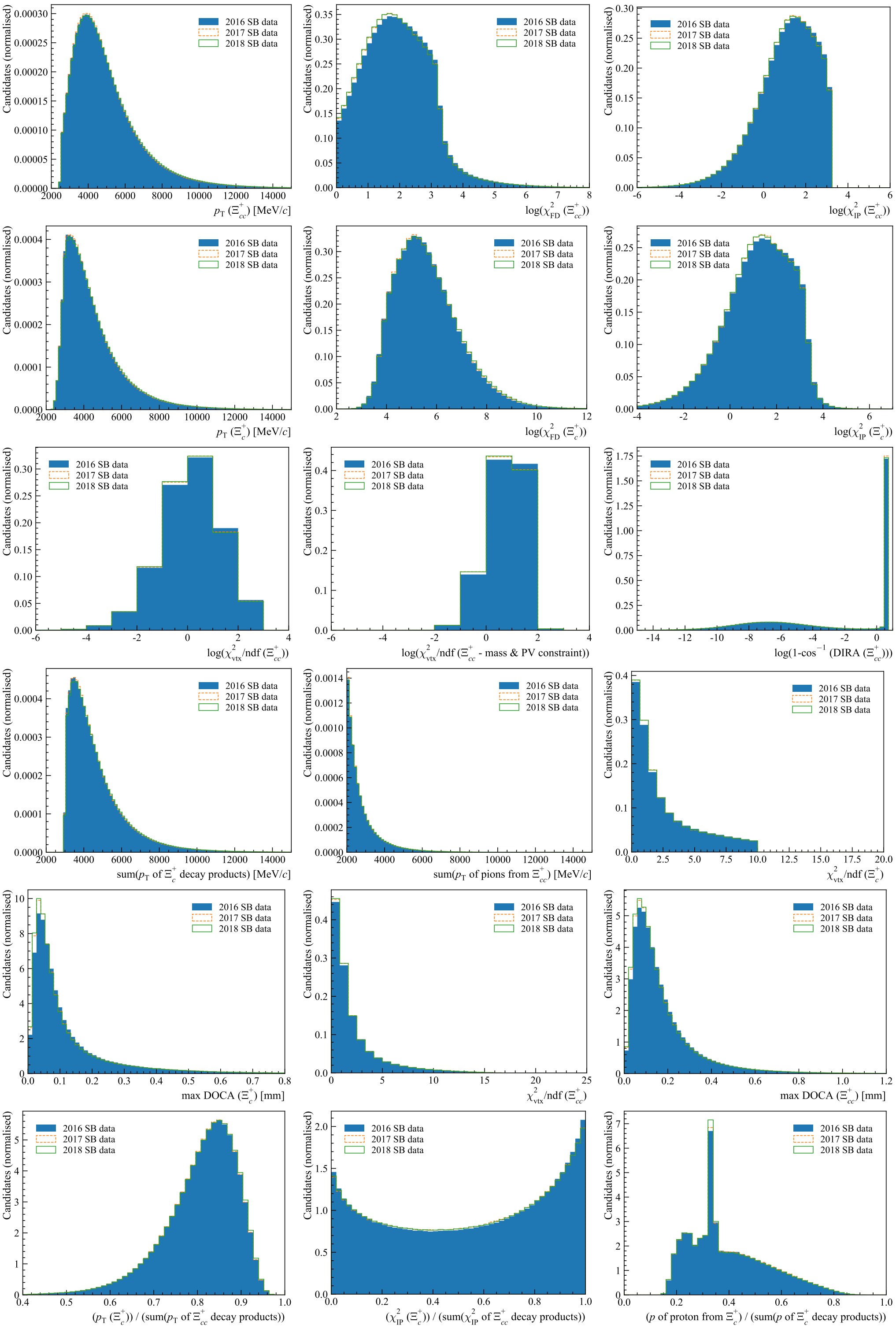

Figure A.3.: Comparison of distributions for several kinematic variables for 2016 (blue area), 2017 (orange dashed line) and 2018 (green solid line) SB data for the $\Xi_{cc}^+ \to \Xi_c^+ \pi^- \pi^+$ decay after the pre-selections cuts are applied for the default trigger set.

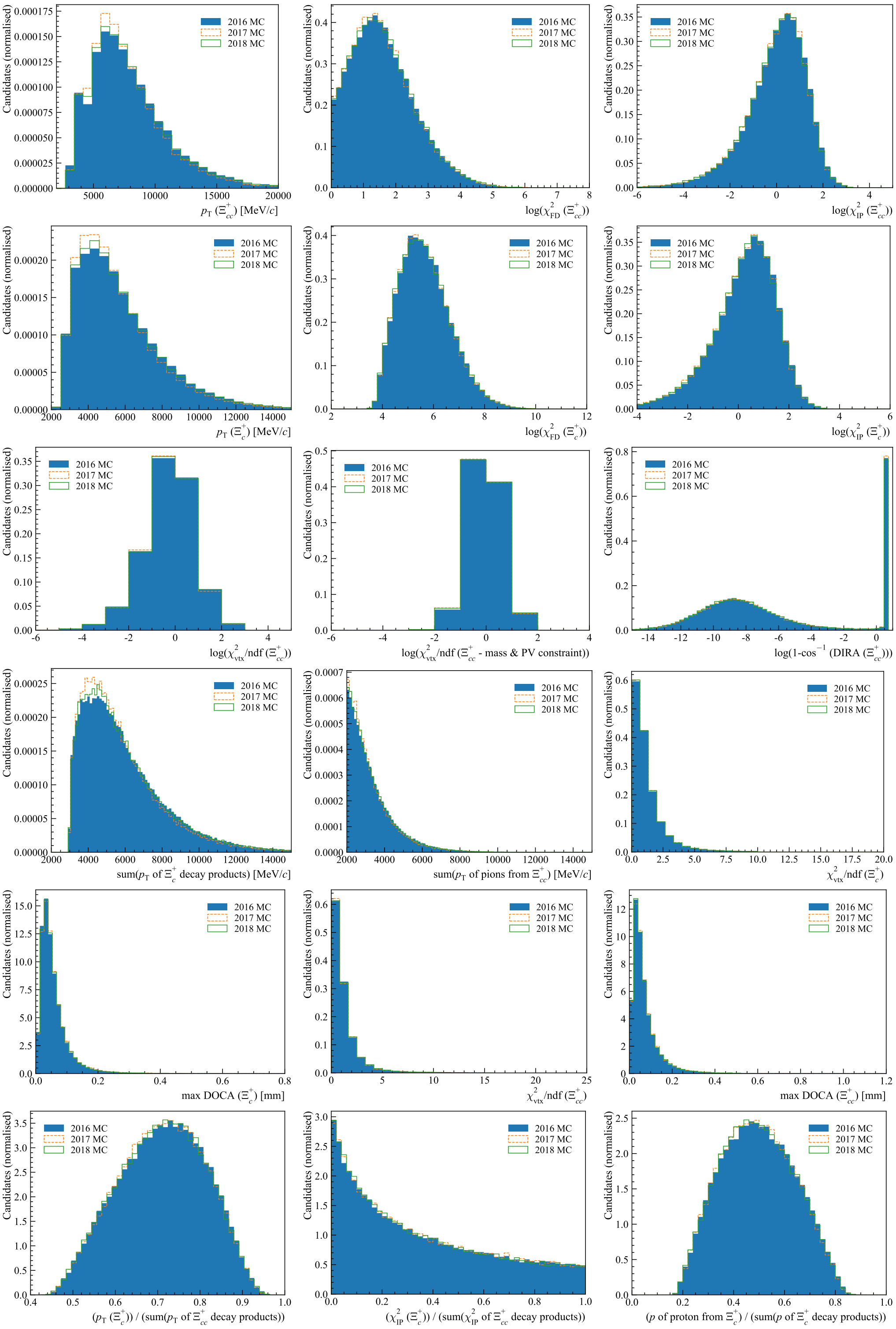

Figure A.4.: Comparison of distributions for several kinematic variables for 2016 (blue area), 2017 (orange dashed line) and 2018 (green solid line) simulation for the $\Xi_{cc}^+ \to \Xi_c^+ \pi^- \pi^+$ decay after the pre-selections cuts are applied for the default trigger set.

Appendix B.

Extra material for the MVA training of the signal channel

B.1. MVA response of different classifiers for simulation and data samples

The MVA response distributions of different MVA classifiers for the simulation and WSM data for the signal channel samples for each year of data taking are shown in Figure B.1.

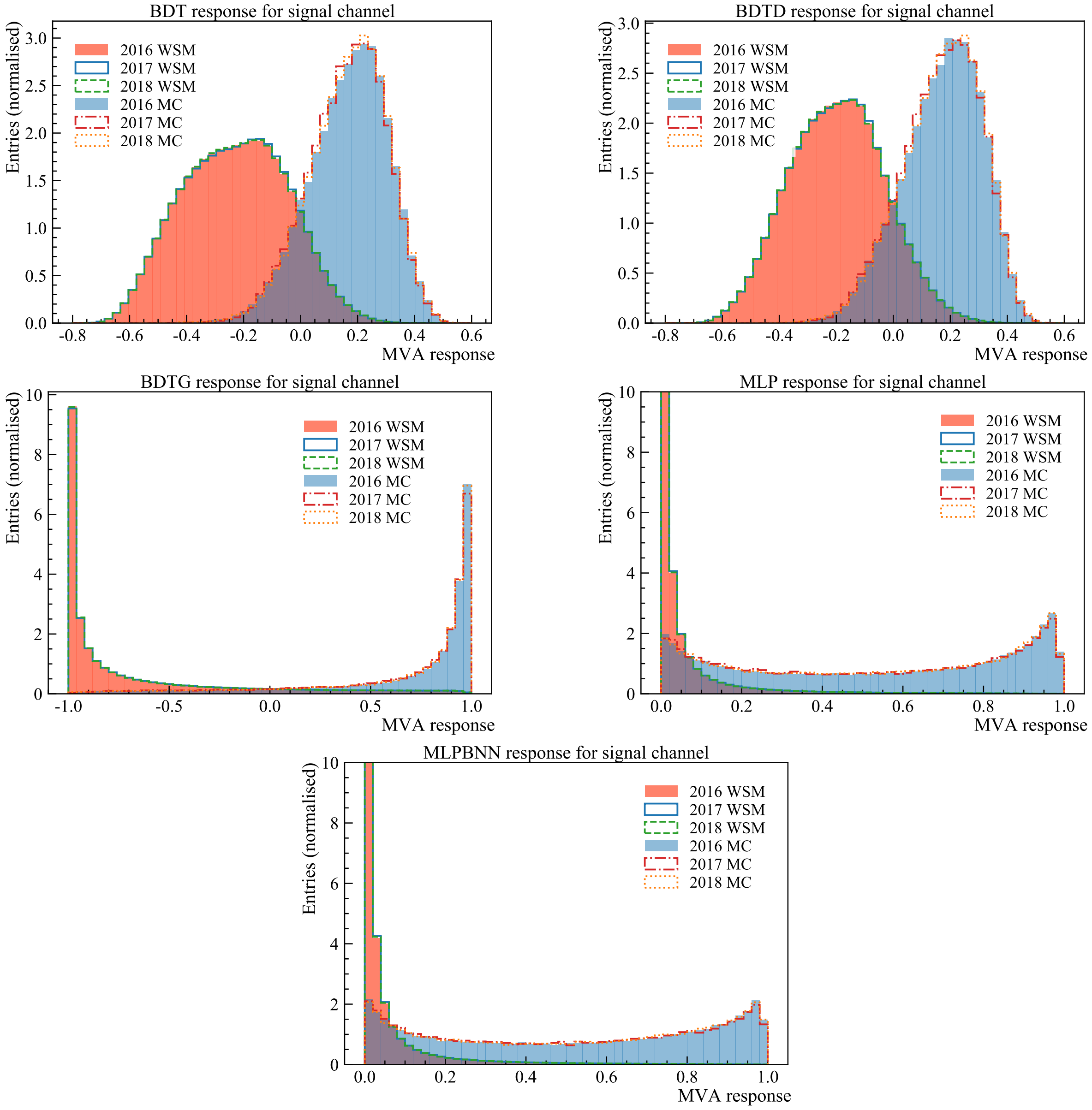

Figure B.1.: Distribution of the MVA response for different classifiers for the simulation and WSM signal channel samples for each year of data taking.

B.2. MVA variables for the signal channel after the optimal MVA cut

Figure B.2 shows the distributions of the final set of variables used in the MVA training for the $\Xi_{cc}^{+}\to\Xi_{c}^{+}\pi^{-}\pi^{+}$ decay mode after the optimal MVA cut (MLP > 0.905) is applied.

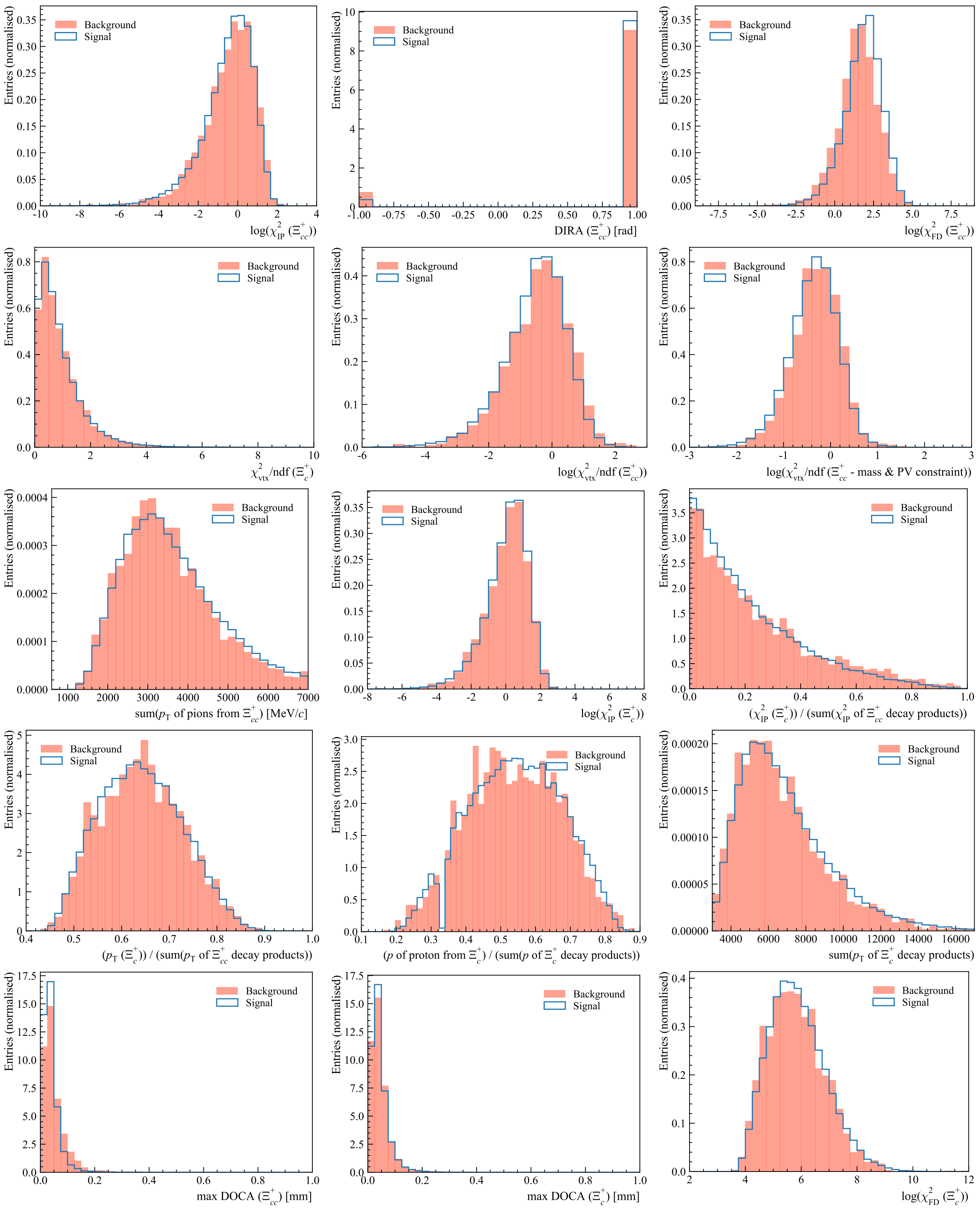

Figure B.2.: Distributions of the final set of 15 variables for the $\Xi_{cc}^{+}\to\Xi_c^{+}\pi^{-}\pi^{+}$ channel used in the MVA training for signal (blue area) and background (red dashed area) after the optimal MVA cut is applied for the default trigger set.

Appendix C.

Extra material for the MVA training of the normalisation channel

C.1. Distribution of the MVA variables

Figure C.1 shows the distributions of the final set of variables used in the MVA training of the normalisation channel.

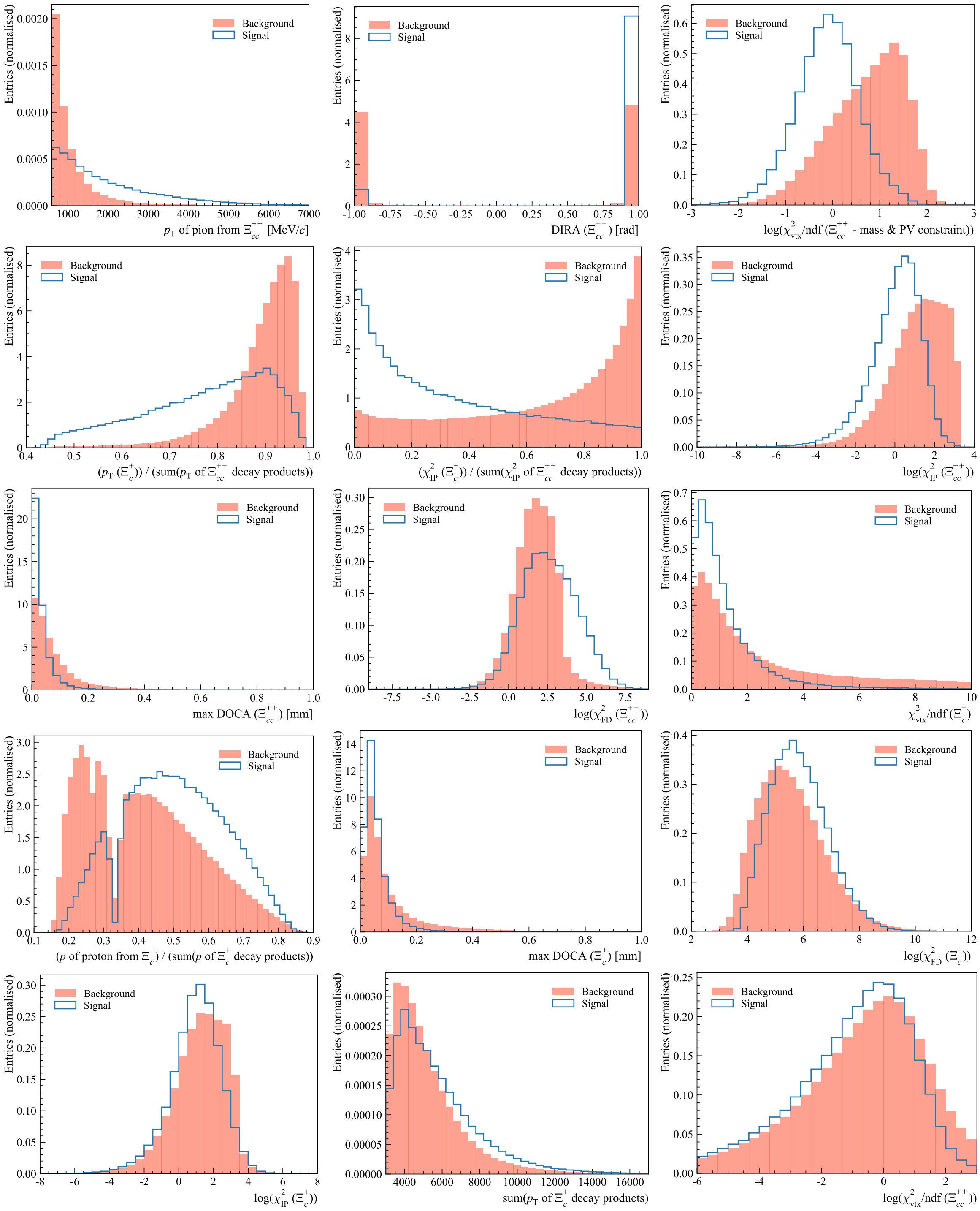

Figure C.1.: Distributions of the final set of 15 variables used in the MVA training of the normalisation channel for the signal sample (blue line) and the background (red area) represented by the WSM sample, ordered by their separation power as shown in Table 6.22.

C.2. Correlation matrices for the MVA variables

Figures C.2 and C.3 show the correlation matrices for the final set of variables used in the MVA training of the normalisation channel.

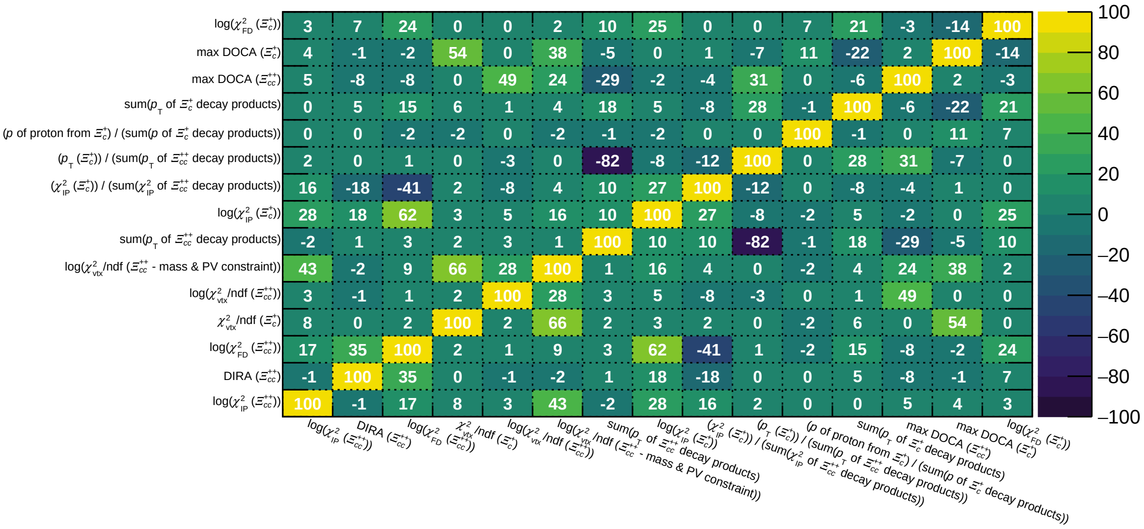

	log(χ^2_{IP} (Ξ_{cc}^{++}))	DIRA (Ξ_{cc}^{++})	log(χ^2_{FD} (Ξ_{cc}^{++}))	χ^2_{vtx}/ndf (Ξ_c^+)	log(χ^2_{vtx}/ndf (Ξ_{cc}^{++}))	log(χ^2_{vtx}/ndf (Ξ_{cc}^{++} - mass & PV constraint))	sum(p_{T} of Ξ_{cc}^{++} decay products)	log(χ^2_{IP} (Ξ_c^+))	(χ^2_{IP} (Ξ_c^+)) / (sum(χ^2_{IP} of Ξ_{cc}^{++} decay products))	(p_{T} (Ξ_c^+)) / (sum(p_{T} of Ξ_{cc}^{++} decay products))	(p of proton from Ξ_c^+) / (sum(p of Ξ_c^+ decay products))	sum(p_{T} of Ξ_c^+ decay products)	max DOCA (Ξ_{cc}^{++})	max DOCA (Ξ_c^+)	log(χ^2_{FD} (Ξ_c^+))
log(χ^2_{FD} (Ξ_c^+))	3	7	24	0	0	2	10	25	0	0	7	21	-3	-14	100
max DOCA (Ξ_c^+)	4	-1	-2	54	0	38	-5	0	1	-7	11	-22	2	100	-14
max DOCA (Ξ_{cc}^{++})	5	-8	-8	0	49	24	-29	-2	-4	31	0	-6	100	2	-3
sum(p_{T} of Ξ_c^+ decay products)	0	5	15	6	1	4	18	5	-8	28	-1	100	-6	-22	21
(p of proton from Ξ_c^+) / (sum(p of Ξ_c^+ decay products))	0	0	-2	-2	0	-2	-1	-2	0	0	100	-1	0	11	7
(p_{T} (Ξ_c^+)) / (sum(p_{T} of Ξ_{cc}^{++} decay products))	2	0	1	0	-3	0	-82	-8	-12	100	0	28	31	-7	0
(χ^2_{IP} (Ξ_c^+)) / (sum(χ^2_{IP} of Ξ_{cc}^{++} decay products))	16	-18	-41	2	-8	4	10	27	100	-12	0	-8	-4	1	0
log(χ^2_{IP} (Ξ_c^+))	28	18	62	3	5	16	10	100	27	-8	-2	5	-2	0	25
sum(p_{T} of Ξ_{cc}^{++} decay products)	-2	1	3	2	3	1	100	10	10	-82	-1	18	-29	-5	10
log(χ^2_{vtx}/ndf (Ξ_{cc}^{++} - mass & PV constraint))	43	-2	9	66	28	100	1	16	4	0	-2	4	24	38	2
log(χ^2_{vtx}/ndf (Ξ_{cc}^{++}))	3	-1	1	2	100	28	3	5	-8	-3	0	1	49	0	0
χ^2_{vtx}/ndf (Ξ_c^+)	8	0	2	100	2	66	2	3	2	0	-2	6	0	54	0
log(χ^2_{FD} (Ξ_{cc}^{++}))	17	35	100	2	1	9	3	62	-41	1	-2	15	-8	-2	24
DIRA (Ξ_{cc}^{++})	-1	100	35	0	-1	-2	1	18	-18	0	0	5	-8	-1	7
log(χ^2_{IP} (Ξ_{cc}^{++}))	100	-1	17	8	3	43	-2	28	16	2	0	0	5	4	3

Figure C.2.: Correlation matrix for the MVA variables for the signal sample of the normalisation channel. The linear correlation coefficients in the matrix are given in %.

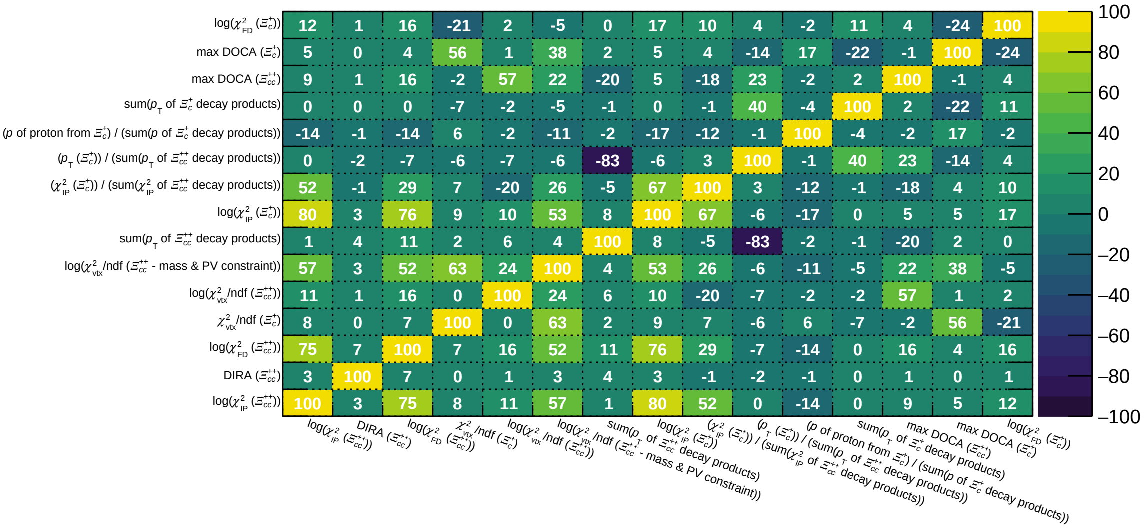

	log(χ^2_{IP} (Ξ_{cc}^{++}))	DIRA (Ξ_{cc}^{++})	log(χ^2_{FD} (Ξ_{cc}^{++}))	χ^2_{vtx}/ndf (Ξ_c^+)	log(χ^2_{vtx}/ndf (Ξ_{cc}^{++}))	log(χ^2_{vtx}/ndf (Ξ_{cc}^{++} - mass & PV constraint))	sum(p_{T} of Ξ_{cc}^{++} decay products)	log(χ^2_{IP} (Ξ_c^+))	(χ^2_{IP} (Ξ_c^+)) / (sum(χ^2_{IP} of Ξ_{cc}^{++} decay products))	(p_{T} (Ξ_c^+)) / (sum(p_{T} of Ξ_{cc}^{++} decay products))	(p of proton from Ξ_c^+) / (sum(p of Ξ_c^+ decay products))	sum(p_{T} of Ξ_c^+ decay products)	max DOCA (Ξ_{cc}^{++})	max DOCA (Ξ_c^+)	log(χ^2_{FD} (Ξ_c^+))
log(χ^2_{FD} (Ξ_c^+))	12	1	16	-21	2	-5	0	17	10	4	-2	11	4	-24	100
max DOCA (Ξ_c^+)	5	0	4	56	1	38	2	5	4	-14	17	-22	-1	100	-24
max DOCA (Ξ_{cc}^{++})	9	1	16	-2	57	22	-20	5	-18	23	-2	2	100	-1	4
sum(p_{T} of Ξ_c^+ decay products)	0	0	0	-7	-2	-5	-1	0	-1	40	-4	100	2	-22	11
(p of proton from Ξ_c^+) / (sum(p of Ξ_c^+ decay products))	-14	-1	-14	6	-2	-11	-2	-17	-12	-1	100	-4	-2	17	-2
(p_{T} (Ξ_c^+)) / (sum(p_{T} of Ξ_{cc}^{++} decay products))	0	-2	-7	-6	-7	-6	-83	-6	3	100	-1	40	23	-14	4
(χ^2_{IP} (Ξ_c^+)) / (sum(χ^2_{IP} of Ξ_{cc}^{++} decay products))	52	-1	29	7	-20	26	-5	67	100	3	-12	-1	-18	4	10
log(χ^2_{IP} (Ξ_c^+))	80	3	76	9	10	53	8	100	67	-6	-17	0	5	5	17
sum(p_{T} of Ξ_{cc}^{++} decay products)	1	4	11	2	6	4	100	8	-5	-83	-2	-1	-20	2	0
log(χ^2_{vtx}/ndf (Ξ_{cc}^{++} - mass & PV constraint))	57	3	52	63	24	100	4	53	26	-6	-11	-5	22	38	-5
log(χ^2_{vtx}/ndf (Ξ_{cc}^{++}))	11	1	16	0	100	24	6	10	-20	-7	-2	-2	57	1	2
χ^2_{vtx}/ndf (Ξ_c^+)	8	0	7	100	0	63	2	9	7	-6	6	-7	-2	56	-21
log(χ^2_{FD} (Ξ_{cc}^{++}))	75	7	100	7	16	52	11	76	29	-7	-14	0	16	4	16
DIRA (Ξ_{cc}^{++})	3	100	7	0	1	3	4	3	-1	-2	-1	0	1	0	1
log(χ^2_{IP} (Ξ_{cc}^{++}))	100	3	75	8	11	57	1	80	52	0	-14	0	9	5	12

Figure C.3.: Correlation matrix for the MVA variables for the background sample of the normalisation channel. The linear correlation coefficients in the matrix are given in %.

C.3. Overtraining check

The overtraining checks for all used MVA classifiers for the normalisation channel are shown in Figure C.4. The MVA response distributions of different MVA classifiers for the simulation and WSM data for the signal channel samples for each year of data taking are shown in Figure C.5.

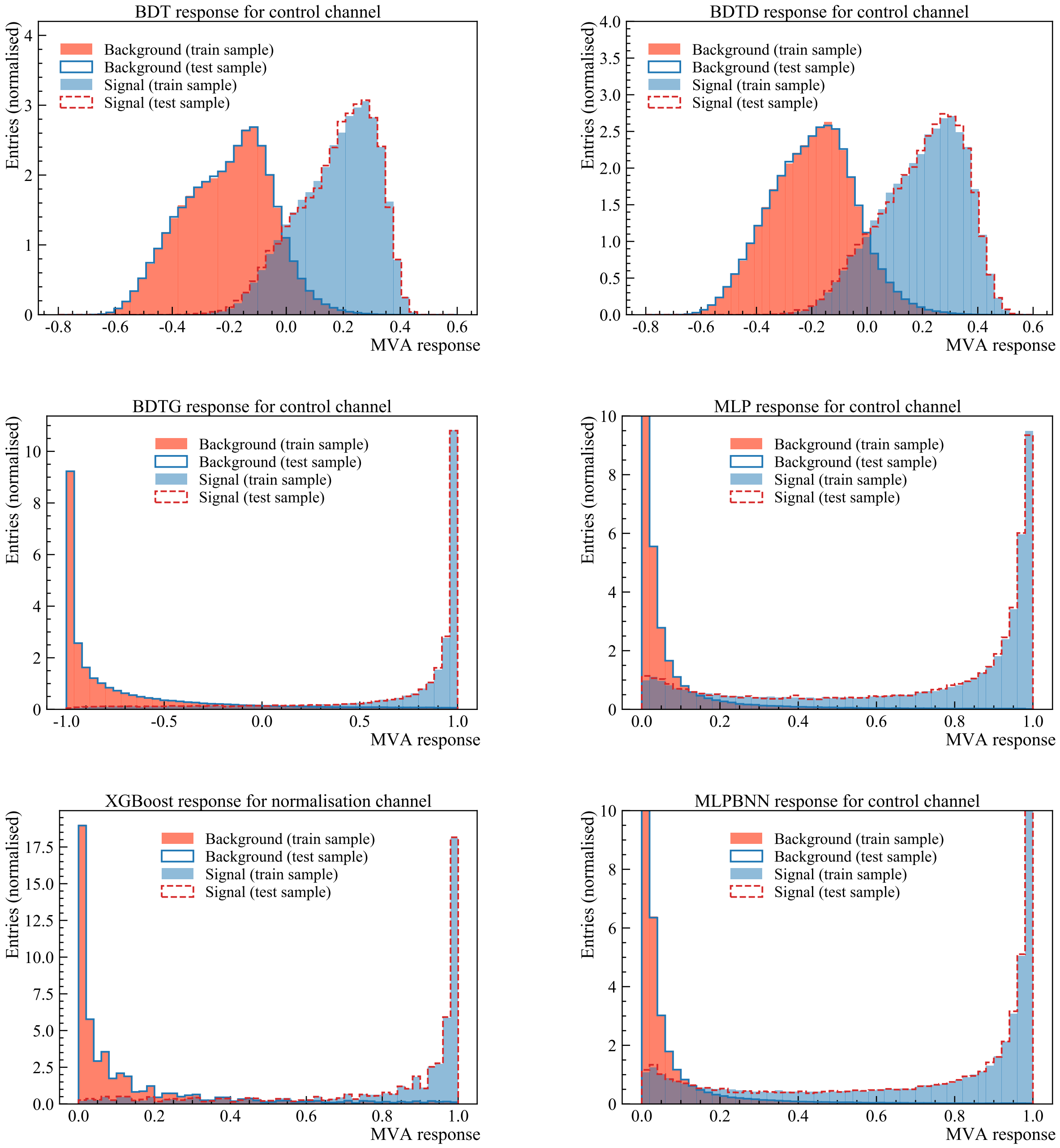

Figure C.4.: Overtraining plots for different MVA classifiers for the normalisation channel.

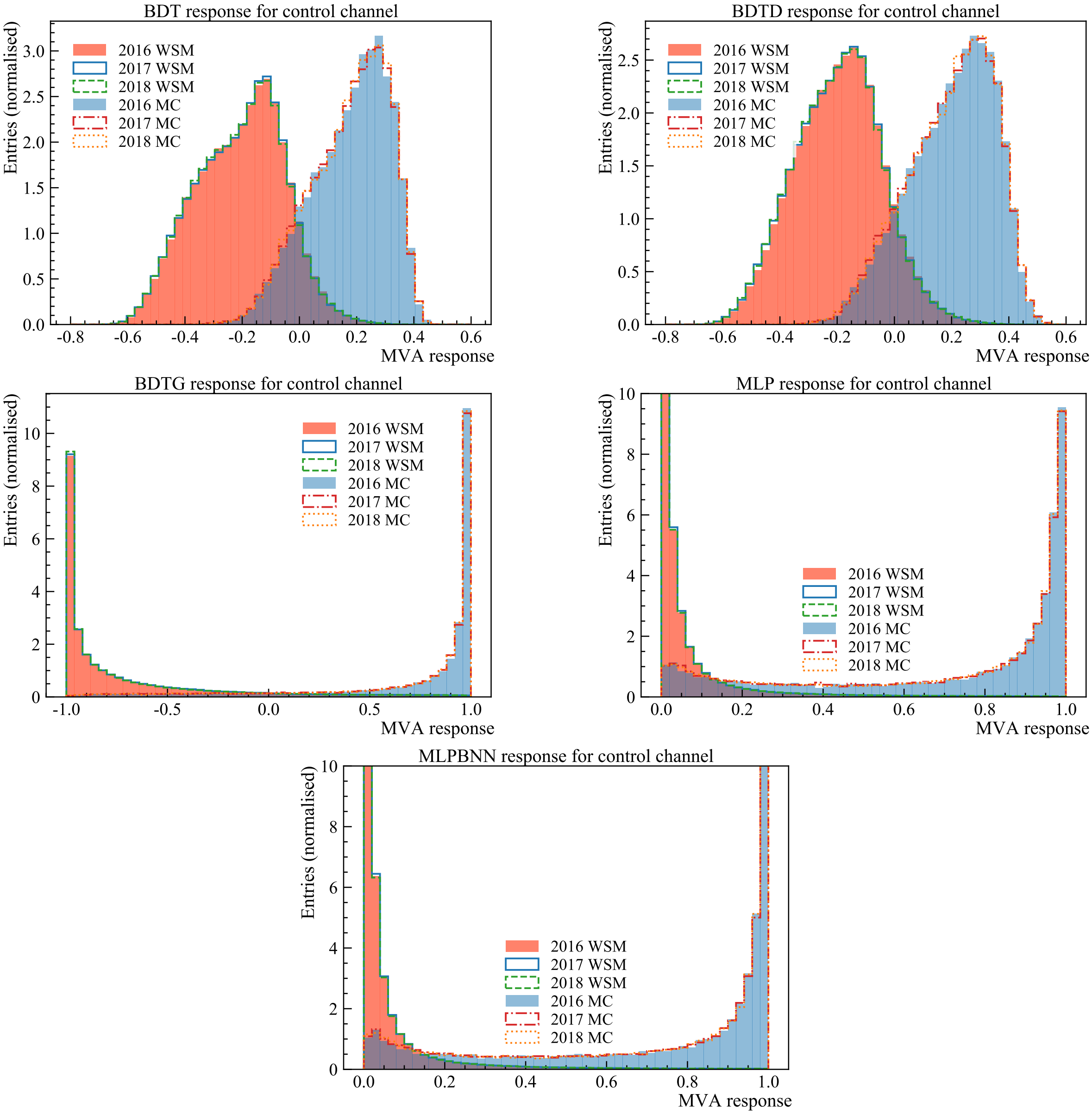

Figure C.5.: Distribution of the MVA response for different classifiers for the simulation and WSM normalisation channel samples for each year of data taking.

C.4. ROC curves

Figure C.6 shows the ROC curve for various TMVA methods used for the normalisation channel.

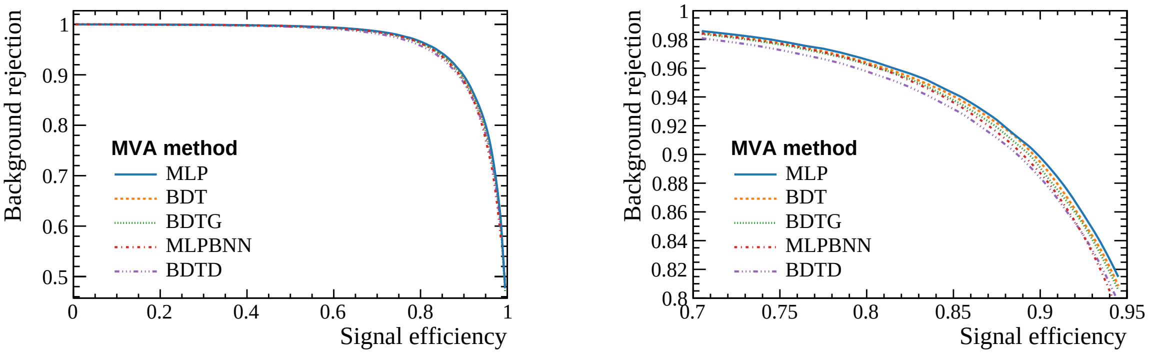

Figure C.6.: ROC curve representing a background rejection versus signal efficiency for tested TMVA classifiers (zoomed on the right) for the normalisation channel.

C.5. Punzi FoM

The Punzi FoM for the different MVA classifiers as a function of the MVA threshold of the normalisation channel for the default and extended trigger sets can be found in Figures C.7 and C.8, respectively.

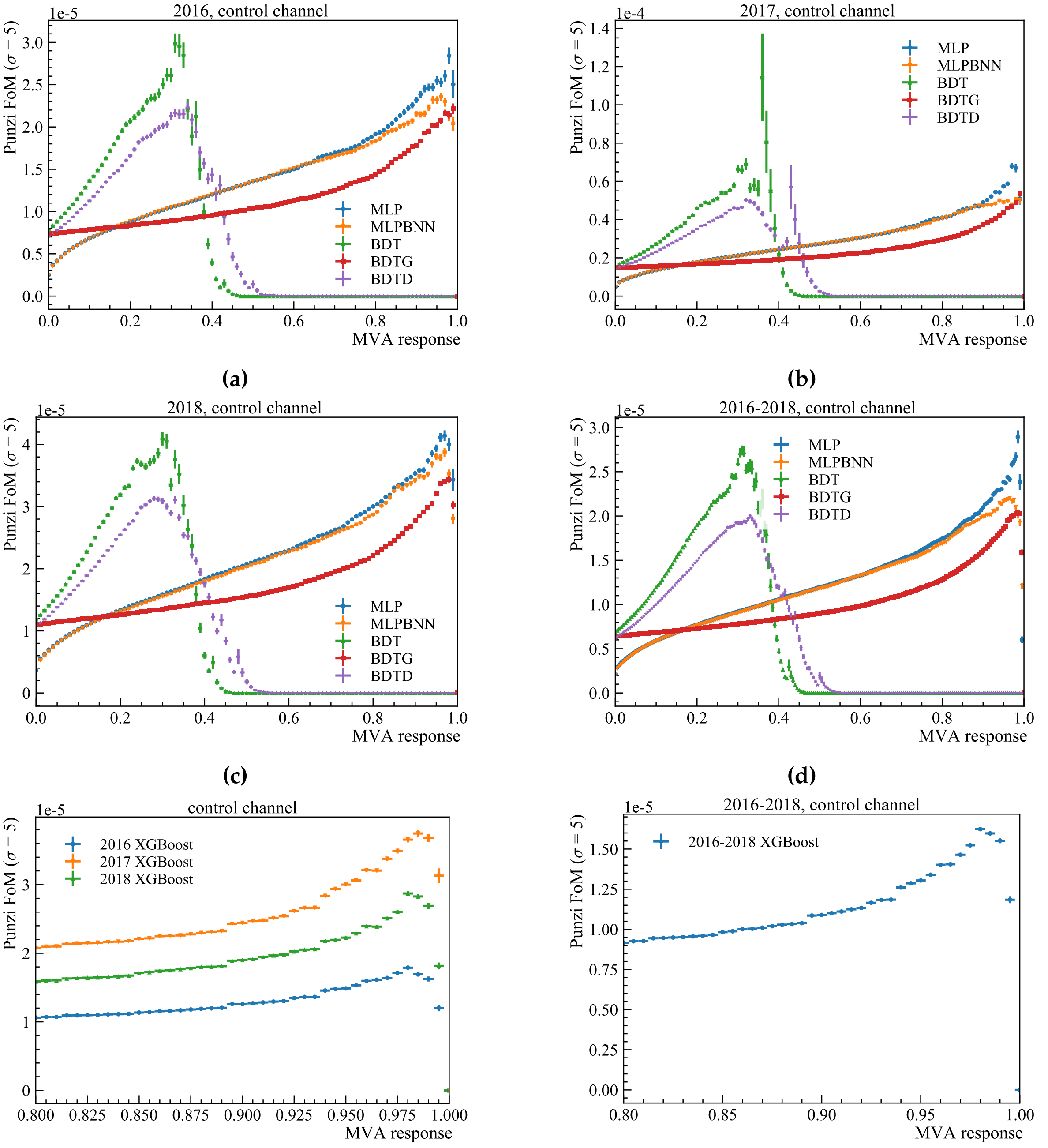

(a)

(b)

(c)

(d)

(e)

(f)

Figure C.7.: Punzi FoM for the normalisation channel for different MVA classifiers from the (a, b, c, d) TMVA package and for the (d, e) XGBoost method evaluated for (a, b, c, e) each year separately and for (d, f) all years combined for the default trigger.

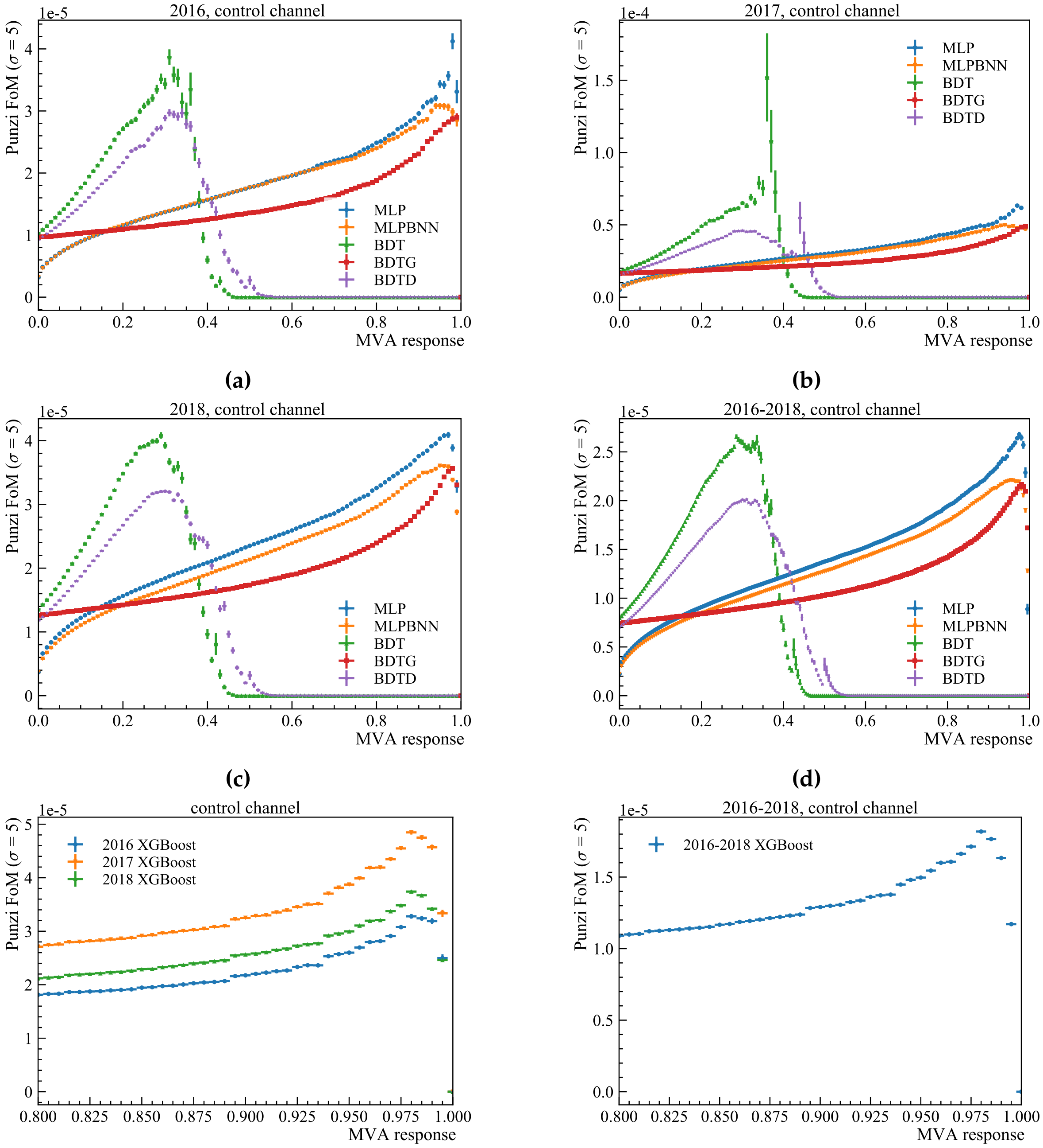

(a) **(b)**

(c) **(d)**

(e) **(f)**

Figure C.8.: Punzi FoM for different MVA classifiers from the (a, b, c, d) TMVA package and for the (d, e) XGBoost method evaluated for (a, b, c, e) each year separately and for (d, f) all years combined for the extended trigger set.

List of figures

List of tables

Bibliography

[1] LHCb collaboration, R. Aaij *et al.*, *Search for the doubly charmed baryon Ξ_{cc}^{+} in the $\Xi_{c}^{+}\pi^{-}\pi^{+}$ final state*, JHEP **12** (2021) 107, `arXiv:2109.07292`. (Cited pages: ix, 31, and 223.)

[2] S. Weinberg, *The Quantum theory of fields. Vol. 1: Foundations*, Cambridge University Press, 2005. (Cited page: 4.)

[3] M. E. Peskin and D. V. Schroeder, *An Introduction to quantum field theory*, Addison-Wesley, Reading, USA, 1995. (Cited page: 4.)

[4] Super-Kamiokande collaboration, Y. Fukuda *et al.*, *Evidence for oscillation of atmospheric neutrinos*, Phys. Rev. Lett. **81** (1998) 1562, `arXiv:hep-ex/9807003`. (Cited page: 5.)

[5] SNO collaboration, Q. R. Ahmad *et al.*, *Direct evidence for neutrino flavor transformation from neutral current interactions in the Sudbury Neutrino Observatory*, Phys. Rev. Lett. **89** (2002) 011301, `arXiv:nucl-ex/0204008`. (Cited page: 5.)

[6] K. Assamagan *et al.*, *Upper limit of the muon-neutrino mass and charged pion mass from momentum analysis of a surface muon beam*, Phys. Rev. **D53** (1996) 6065. (Cited page: 5.)

[7] ALEPH collaboration, R. Barate *et al.*, *An upper limit on the tau-neutrino mass from three-prong and five-prong tau decays*, Eur. Phys. J. **C2** (1998) 395. (Cited page: 5.)

[8] KATRIN collaboration, M. Aker *et al.*, *Direct neutrino-mass measurement with sub-electronvolt sensitivity*, Nature Phys. **18** (2022) 160, `arXiv:2105.08533`. (Cited page: 5.)

[9] N. Cabibbo, *Unitary symmetry and leptonic decays*, Phys. Rev. Lett. **10** (1963) 531. (Cited page: 9.)

[10] M. Kobayashi and T. Maskawa, *CP-violation in the renormalizable theory of weak*

interaction, Prog. Theor. Phys. **49** (1973) 652. (Cited pages: 9 and 10.)

[11] Particle Data Group, P. A. Zyla *et al.*, *Review of particle physics*, Prog. Theor. Exp. Phys. **2020** (2020) 083C01. (Cited pages: 10, 12, 16, 17, 18, 23, 24, 27, and 225.)

[12] Muon g-2 collaboration, B. Abi and others. *Measurement of the positive muon anomalous magnetic moment to 0.46 ppm*, Phys. Rev. Lett. **126** (2021) 141801. (Cited page: 11.)

[13] Muon g-2 collaboration, G. W. Bennett *et al.*, *Final report of the muon E821 anomalous magnetic moment measurement at BNL*, Phys. Rev. **D73** (2006) 072003, `arXiv:hep-ex/0602035`. (Cited page: 11.)

[14] W. Altmannshofer and P. Stangl, *New physics in rare B decays after Moriond 2021*, Eur. Phys. J. **C81** (2021) 952, `arXiv:2103.13370`. (Cited page: 12.)

[15] LHCb collaboration, R. Aaij *et al.*, *Test of lepton universality in beauty-quark decays*, `arXiv:2103.11769`, to appear in Nature Physics. (Cited pages: 12 and 38.)

[16] CDF collaboration, T. Aaltonen *et al.*, *High-precision measurement of the W boson mass with the CDF II detector*, Science **376** (2022) 170, `arXiv:https://www.science.org/doi/pdf/10.1126/science.abk1781`. (Cited page: 12.)

[17] D0 collaboration, V. M. Abazov *et al.*, *Measurement of the W boson mass with the D0 detector*, Phys. Rev. Lett. **108** (2012) 151804, `arXiv:1203.0293`. (Cited page: 12.)

[18] ALEPH, DELPHI, L3, OPAL, LEP Electroweak collaboration, S. Schael *et al.*, *Electroweak measurements in electron-positron collisions at W-boson-pair energies at LEP*, Phys. Rept. **532** (2013) 119, `arXiv:1302.3415`. (Cited page: 12.)

[19] ATLAS collaboration, M. Aaboud *et al.*, *Measurement of the W-boson mass in pp collisions at $\sqrt{s} = 7$ TeV with the ATLAS detector*, Eur. Phys. J. **C78** (2018) 110, `arXiv:1701.07240`, [Erratum: Eur.Phys.J.C 78, 898 (2018)]. (Cited page: 12.)

[20] LHCb collaboration, R. Aaij *et al.*, *Measurement of the W boson mass*, JHEP **01** (2022) 036, `arXiv:2109.01113`. (Cited page: 12.)

[21] M. Gell-Mann, *A schematic model of baryons and mesons*, Phys. Lett. **8** (1964) 214. (Cited page: 13.)

[22] G. Zweig, *An SU_3 model for strong interaction symmetry and its breaking; Version 1* CERN-TH-401, CERN, Geneva, 1964. (Cited page: 13.)

[23] R. Slansky, *Group theory for unified model building*, Physics Reports **79** (1981) 1. (Cited page: 16.)

[24] K. G. Wilson, *Confinement of quarks*, Phys. Rev. **D10** (1974) 2445. (Cited page: 18.)

[25] N. Isgur and M. B. Wise, *Weak decays of heavy mesons in the static quark approximation*, Physics Letters **B232** (1989) 113. (Cited page: 19.)

[26] E. Eichten and B. R. Hill, *An effective field theory for the calculation of matrix elements involving heavy quarks*, Phys. Lett. **B234** (1990) 511. (Cited page: 19.)

[27] H. Georgi, *An effective field theory for heavy quarks at low-energies*, Phys. Lett. **B240** (1990) 447. (Cited page: 19.)

[28] B. Grinstein, *The static quark effective theory*, Nucl. Phys. **B339** (1990) 253. (Cited page: 19.)

[29] A. F. Falk, M. Neubert, and M. Luke, *The residual mass term in the heavy quark effective theory*, Nuclear Physics **B388** (1992) 363. (Cited page: 19.)

[30] M. A. Shifman, A. I. Vainshtein, and V. I. Zakharov, *QCD and resonance physics. Theoretical foundations*, Nuclear Physics **B147** (1979) 385. (Cited page: 19.)

[31] M. Neubert, *Heavy-quark symmetry*, Physics Reports **245** (1994) 259. (Cited page: 19.)

[32] P. Colangelo and A. Khodjamirian, *QCD sum rules, a modern perspective*, doi: 10.1142/9789812810458$_0$033 `arXiv:hep-ph/0010175`. (Cited page: 20.)

[33] S. P. Baranov, *Production of doubly flavored baryons in pp, ep, and $\gamma\gamma$ collisions*, Phys. Rev. **D54** (1996) 3228. (Cited pages: 21 and 22.)

[34] A. V. Berezhnoy, V. V. Kiselev, A. K. Likhoded, and A. I. Onishchenko, *Doubly charmed baryon production in hadronic experiments*, Phys. Rev. **D57** (1998) 4385, `arXiv:hep-ph/9710339`. (Cited pages: 21, 22, and 30.)

[35] V. V. Kiselev and A. K. Likhoded, *Baryons with two heavy quarks*, Phys. Usp. **45** (2002) 455, `arXiv:hep-ph/0103169`. (Cited pages: 21, 22, 23, 24, 25, 27, 30, and 98.)

[36] V. Braguta, V. Kiselev, and A. E. Chalov, *Pair production of doubly heavy diquarks*, Phys. Atom. Nuclei **65** (2002) 1537. (Cited pages: 21 and 22.)

[37] J. P. Ma and Z. G. Si, *Factorization approach for inclusive production of doubly heavy baryon*, Phys. Lett. **B568** (2003) 135, `arXiv:hep-ph/0305079`. (Cited pages: 21, 22, and 30.)

[38] C.-H. Chang, C.-F. Qiao, J.-X. Wang, and X.-G. Wu, *Estimate of the hadronic production of the doubly charmed baryon Ξ_{cc} in the general-mass variable-flavor-number scheme*, Phys. Rev. **D73** (2006) 094022. (Cited pages: 21, 22, 30, 89, and 207.)

[39] C.-H. Chang, J.-P. Ma, C.-F. Qiao, and X.-G. Wu, *Hadronic production of the doubly charmed baryon Ξ_{cc} with intrinsic charm*, J. Phys. **G34** (2007) 845, `arXiv:hep-ph/0610205`. (Cited pages: 21, 22, and 30.)

[40] J.-W. Zhang *et al.*, *Hadronic production of the doubly heavy baryon Ξ_{bc} at LHC*, Phys. Rev. **D83** (2011) 034026, `arXiv:1101.1130`. (Cited pages: 21, 22, and 30.)

[41] G. T. Bodwin, E. Braaten, and G. P. Lepage, *Rigorous QCD analysis of inclusive annihilation and production of heavy quarkonium*, Phys. Rev. **D51** (1995) 1125, `arXiv:hep-ph/9407339`, [Erratum: Phys.Rev.D 55, 5853 (1997)]. (Cited pages: 22 and 98.)

[42] A. V. Berezhnoy, A. K. Likhoded, and A. V. Luchinsky, *Doubly heavy baryons at the LHC*, Phys. Rev. **D98** (2018) 113004, `arXiv:1809.10058`. (Cited page: 22.)

[43] L. Liu, H.-W. Lin, K. Orginos, and A. Walker-Loud, *Singly and doubly charmed J=1/2 baryon spectrum from lattice QCD*, Phys. Rev. **D81** (2010) 094505, `arXiv:0909.3294`. (Cited pages: 23 and 24.)

[44] R. A. Briceno, H.-W. Lin, and D. R. Bolton, *Charmed-baryon spectroscopy from lattice QCD with $N_f = 2+1+1$ flavors*, Phys. Rev. **D86** (2012) 094504, `arXiv:1207.3536`. (Cited pages: 23 and 24.)

[45] S. Durr, G. Koutsou, and T. Lippert, *Meson and Baryon dispersion relations with Brillouin fermions*, Phys. Rev. D **86** (2012) 114514, `arXiv:1208.6270`. (Cited pages: 23 and 24.)

[46] PACS-CS collaboration, Y. Namekawa *et al.*, *Charmed baryons at the physical point in 2+1 flavor lattice QCD*, Phys. Rev. **D87** (2013) 094512, `arXiv:1301.4743`. (Cited pages: 23 and 24.)

[47] C. Alexandrou *et al.*, *Baryon spectrum with $N_f = 2 + 1 + 1$ twisted mass fermions*, Phys. Rev. **D90** (2014) 074501, `arXiv:1406.4310`. (Cited pages: 23 and 24.)

[48] M. Padmanath, R. G. Edwards, N. Mathur, and M. Peardon, *Spectroscopy of triply-charmed baryons from lattice QCD*, Phys. Rev. **D90** (2014) 074504, `arXiv:1307.7022`. (Cited pages: 23 and 24.)

[49] Z. S. Brown, W. Detmold, S. Meinel, and K. Orginos, *Charmed bottom baryon spectroscopy from lattice QCD*, Phys. Rev. **D90** (2014) 094507, `arXiv:1409.0497`. (Cited pages: 23 and 24.)

[50] P. Pérez-Rubio, S. Collins, and G. S. Bali, *Charmed baryon spectroscopy and light flavor symmetry from lattice QCD*, Phys. Rev. **D92** (2015) 034504, `arXiv:1503.08440`. (Cited pages: 23 and 24.)

[51] C. Alexandrou and C. Kallidonis, *Low-lying baryon masses using $N_f = 2$ twisted mass clover-improved fermions directly at the physical pion mass*, Phys. Rev. **D96** (2017) 034511, `arXiv:1704.02647`. (Cited pages: 23 and 24.)

[52] M. Karliner and J. L. Rosner, *Baryons with two heavy quarks: Masses, production, decays, and detection*, Phys. Rev. **D90** (2014) 094007, `arXiv:1408.5877`. (Cited pages: 23, 24, and 25.)

[53] D. B. Lichtenberg, R. Roncaglia, and E. Predazzi, *Mass sum rules for singly and doubly heavy flavored hadrons*, Phys. Rev. **D53** (1996) 6678, `arXiv:hep-ph/9511461`. (Cited pages: 23 and 24.)

[54] J. Zhang and M. Huang, *Doubly heavy baryons in QCD sum rules*, Phys. Rev. **D78** (2008) 094007, `arXiv:0810.5396`. (Cited pages: 23 and 24.)

[55] Z.-G. Wang, *Analysis of the $\frac{1}{2}^+$ doubly heavy baryon states with QCD sum rules*, Eur. Phys. J. **A45** (2010) 267, `arXiv:1001.4693`. (Cited pages: 23 and 24.)

[56] H. Chen *et al.*, *Establishing low-lying doubly charmed baryons*, Phys. Rev. **D96** (2017) 031501, `arXiv:1707.01779`. (Cited pages: 23 and 24.)

[57] Z.-G. Wang, *Analysis of the doubly heavy baryon states and pentaquark states with QCD sum rules*, Eur. Phys. J. **C78** (2018) 826, `arXiv:1808.09820`. (Cited pages: 23 and 24.)

[58] J. G. Korner, M. Kramer, and D. Pirjol, *Heavy baryons*, Prog. Part. Nucl. Phys. **33** (1994) 787, `arXiv:hep-ph/9406359`. (Cited pages: 23 and 24.)

[59] D. He *et al.*, *Evaluation of spectra of baryons containing two heavy quarks in bag model*, Phys. Rev. **D70** (2004) 094004, `arXiv:hep-ph/0403301`. (Cited pages: 23 and 24.)

[60] D. Ebert, R. N. Faustov, V. O. Galkin, and A. P. Martynenko, *Mass spectra of doubly heavy baryons in the relativistic quark model*, Phys. Rev. **D66** (2002) 014008, `arXiv:hep-ph/0201217`. (Cited pages: 23 and 24.)

[61] S. Fleck and J.-M. Richard, *Baryons with double charm*, Prog. Theor. Phys. **82** (1989) 760. (Cited pages: 23, 24, and 25.)

[62] B. O. Kerbikov, M. I. Polikarpov, and L. V. Shevchenko, *Multiquark masses and wave functions through a modified green function Monte Carlo method*, Nucl. Phys. **B331** (1990) 19. (Cited pages: 23 and 24.)

[63] S. Chernyshev, M. A. Nowak, and I. Zahed, *Heavy hadrons and QCD instantons*, Phys. Rev. **D53** (1996) 5176. (Cited pages: 23 and 24.)

[64] C. Itoh, T. Minamikawa, K. Miura, and T. Watanabe, *Doubly charmed baryon masses and quark wave functions in baryons*, Phys. Rev. **D61** (2000) 057502. (Cited pages: 23 and 24.)

[65] S. S. Gershtein, V. V. Kiselev, A. K. Likhoded, and A. I. Onishchenko, *Spectroscopy of doubly heavy baryons*, Phys. Rev. **D62** (2000) 054021. (Cited pages: 23 and 24.)

[66] N. Mathur, R. Lewis, and R. M. Woloshyn, *Charmed and bottom baryons from lattice nonrelativistic QCD*, Phys. Rev. **D66** (2002) 014502. (Cited pages: 23 and 24.)

[67] W. Roberts and M. Pervin, *Heavy baryons in a quark model*, Int. J. Mod. Phys. **A23** (2008) 2817, `arXiv:0711.2492`. (Cited pages: 23 and 24.)

[68] A. Valcarce, H. Garcilazo, and J. Vijande, *Towards an understanding of heavy baryon spectroscopy*, Eur. Phys. J. **A37** (2008) 217. (Cited pages: 23 and 24.)

[69] T. M. Aliev, K. Azizi, and M. Savci, *Doubly heavy spin–1/2 baryon spectrum in QCD*, Nucl. Phys. **A895** (2012) 59, `arXiv:1205.2873`. (Cited pages: 23 and 24.)

[70] M. Padmanath, R. G. Edwards, N. Mathur, and M. Peardon, *Spectroscopy of doubly-charmed baryons from lattice QCD*, Phys. Rev. **D91** (2015) 094502, `arXiv:1502.01845`. (Cited pages: 23 and 24.)

[71] Z.-F. Sun, Z.-W. Liu, X. Liu, and S.-L. Zhu, *Masses and axial currents of the doubly charmed baryons*, Phys. Rev. **D91** (2015) 094030, `arXiv:1411.2117`. (Cited pages:

23 and 24.)

[72] K.-W. Wei, B. Chen, and X.-H. Guo, *Masses of doubly and triply charmed baryons*, Phys. Rev. **D92** (2015) 076008, `arXiv:1503.05184`. (Cited pages: 23 and 24.)

[73] Z.-F. Sun and M. J. Vicente Vacas, *Masses of doubly charmed baryons in the extended on-mass-shell renormalization scheme*, Phys. Rev. **D93** (2016) 094002, `arXiv:1602.04714`. (Cited pages: 23 and 24.)

[74] Y. Liu and I. Zahed, *Heavy and strange holographic baryons*, Phys. Rev. **D96** (2017) 056027, `arXiv:1705.01397`. (Cited pages: 23 and 24.)

[75] C.-W. Hwang and C.-H. Chung, *Isospin mass splittings of heavy baryons in heavy quark symmetry*, Phys. Rev. **D78** (2008) 073013. (Cited page: 23.)

[76] S. J. Brodsky, F. Guo, C. Hanhart, and U. Meißner, *Isospin splittings of doubly heavy baryons*, Phys. Lett. **B698** (2011) 251, `arXiv:1101.1983`. (Cited pages: 23 and 28.)

[77] M. Karliner and J. L. Rosner, *Isospin splittings in baryons with two heavy quarks*, Phys. Rev. **D96** (2017) 033004. (Cited page: 23.)

[78] LHCb collaboration, R. Aaij *et al.*, *Precision measurement of the* Ξ_{cc}^{++} *mass*, JHEP **02** (2020) 049, `arXiv:1911.08594`. (Cited pages: 24, 29, 88, 112, 142, 160, 162, 163, and 224.)

[79] LHCb collaboration, R. Aaij *et al.*, *Observation of the doubly charmed baryon* Ξ_{cc}^{++}, Phys. Rev. Lett. **119** (2017) 112001, `arXiv:1707.01621`. (Cited pages: 24, 28, 29, and 38.)

[80] W. Wang, F. Yu, and Z. Zhao, *Weak decays of doubly heavy baryons: the* $1/2 \to 1/2$ *case*, Eur. Phys. J. **C77** (2017) 781, `arXiv:1707.02834`. (Cited page: 25.)

[81] B. Guberina, B. Melić, and H. Štefančić, *Inclusive decays and lifetimes of doubly charmed baryons*, Eur. Phys. J. **C9** (1999) 213, `arXiv:hep-ph/9901323`. (Cited page: 25.)

[82] V. V. Kiselev, A. K. Likhoded, and A. I. Onishchenko, *Lifetimes of doubly charmed baryons:* Ξ_{cc}^{+} *and* Ξ_{cc}^{++}, Phys. Rev. **D60** (1999) 014007, `arXiv:hep-ph/9807354`. (Cited pages: 25 and 98.)

[83] A. K. Likhoded and A. I. Onishchenko, *Lifetimes of doubly heavy baryons*, `arXiv:hep-ph/9912425`. (Cited pages: 25 and 98.)

[84] A. V. Berezhnoy and A. K. Likhoded, *Doubly heavy baryons*, Phys. Atom. Nucl. **79** (2016) 260. (Cited page: 25.)

[85] C. Chang, T. Li, X. Li, and Y. Wang, *Lifetime of doubly charmed baryons*, Commun. Theor. Phys. **49** (2008) 993, `arXiv:0704.0016`. (Cited pages: 25 and 98.)

[86] H.-Y. Cheng and Y.-L. Shi, *Lifetimes of Doubly Charmed Baryons*, Phys. Rev. **D98** (2018) 113005, `arXiv:1809.08102`. (Cited pages: 25 and 26.)

[87] M. A. Shifman and M. B. Voloshin, *Preasymptotic Effects in Inclusive Weak Decays of Charmed Particles*, Sov. J. Nucl. Phys. **41** (1985) 120. (Cited page: 25.)

[88] M. B. Voloshin, *Spectator effects in semileptonic decay of charmed baryons*, Physics Letters B **385** (1996) 369. (Cited page: 25.)

[89] N. Bilic, B. Guberina, and J. Trampetic, *Pauli Interference Effect in D+ Lifetime*, Nucl. Phys. B **248** (1984) 261. (Cited page: 25.)

[90] R.-H. Li *et al.*, *Doubly-heavy baryon weak decays: $\Xi_{bc}^{0} \to pK^{-}$ and $\Xi_{cc}^{+} \to \Sigma_{c}^{++}(2520)K^{-}$*, Phys. Lett. **B767** (2017) 232, `arXiv:1701.03284`. (Cited page: 27.)

[91] F. Yu *et al.*, *Discovery potentials of doubly charmed baryons*, Chin. Phys. **C42** (2018) 051001, `arXiv:1703.09086`. (Cited pages: 27, 30, and 225.)

[92] Y.-J. Shi, W. Wang, Y. Xing, and J. Xu, *Weak decays of doubly heavy baryons: multi-body decay channels*, Eur. Phys. J. **C78** (2018) 56, `arXiv:1712.03830`. (Cited page: 27.)

[93] L.-J. Jiang, B. He, and R.-H. Li, *Weak decays of doubly heavy baryons: $\mathcal{B}_{cc} \to \mathcal{B}_{c}V$*, Eur. Phys. J. **C78** (2018) 961, `arXiv:1810.00541`. (Cited pages: 27 and 225.)

[94] N. Sharma and R. Dhir, *Estimates of W-exchange contributions to Ξ_{cc} decays*, Phys. Rev. **D96** (2017) 113006, `arXiv:1709.08217`. (Cited pages: 27, 190, and 227.)

[95] SELEX collaboration, M. Mattson *et al.*, *First observation of the doubly charmed baryon Ξ_{cc}^{+}*, Phys. Rev. Lett. **89** (2002) 112001, `arXiv:hep-ex/0208014`. (Cited pages: 27 and 88.)

[96] SELEX collaboration, A. Ocherashvili *et al.*, *Confirmation of the double charm baryon $\Xi_{cc}^{+}(3520)$ via its decay to $pD^{+}K^{-}$*, Phys. Lett. **B628** (2005) 18, `arXiv:hep-ex/0406033`. (Cited page: 27.)

[97] BaBar collaboration, B. Aubert *et al.*, *Search for doubly charmed baryons* Ξ_{cc}^{+} *and* Ξ_{cc}^{++} *in BABAR*, Phys. Rev. **D74** (2006) 011103, `arXiv:hep-ex/0605075`. (Cited page: 28.)

[98] Belle collaboration, R. Chistov *et al.*, *Observation of new states decaying into* $\Lambda_c^+ K^- \pi^+$ *and* $\Lambda_c^+ K_S^0 \pi^-$, Phys. Rev. Lett. **97** (2006) 162001, `arXiv:hep-ex/0606051`. (Cited page: 28.)

[99] S. P. Ratti *et al.*, *New results on c-baryons and a search for cc-baryons in FOCUS*, Nucl. Phys. Proc. Suppl. **115** (2003) 33. (Cited page: 28.)

[100] LHCb collaboration, R. Aaij *et al.*, *Search for the doubly charmed baryon* Ξ_{cc}^{+}, JHEP **12** (2013) 090, `arXiv:1310.2538`. (Cited page: 28.)

[101] LHCb collaboration, R. Aaij *et al.*, *Search for the doubly charmed baryon* Ξ_{cc}^{+}, Sci. China Phys. Mech. Astron. **63** (2020) 221062, `arXiv:1909.12273`. (Cited pages: 28, 92, 175, and 179.)

[102] LHCb collaboration, R. Aaij *et al.*, *Measurement of the lifetime of the doubly charmed baryon* Ξ_{cc}^{++}, Phys. Rev. Lett. **121** (2018) 052002, `arXiv:1806.02744`. (Cited pages: 28 and 213.)

[103] LHCb collaboration, R. Aaij *et al.*, *First observation of the doubly charmed baryon decay* $\Xi_{cc}^{++} \to \Xi_c^+ \pi^+$, Phys. Rev. Lett. **121** (2018) 162002, `arXiv:1807.01919`. (Cited pages: 28, 142, and 225.)

[104] LHCb collaboration, R. Aaij *et al.*, *A search for* $\Xi_{cc}^{++} \to D^+ p K^- \pi^+$ *decays*, JHEP **10** (2019) 124, `arXiv:1905.02421`. (Cited page: 29.)

[105] LHCb collaboration, R. Aaij *et al.*, *Measurement of* Ξ_{cc}^{++} *production in pp collisions at* $\sqrt{s} = 13\,\text{TeV}$, Chin. Phys. **C44** (2020) 022001, `arXiv:1910.11316`. (Cited page: 29.)

[106] S. J. Brodsky, S. Groote, and S. Koshkarev, *Resolving the SELEX–LHCb double-charm baryon conflict: the impact of intrinsic heavy-quark hadroproduction and supersymmetric light-front holographic QCD*, Eur. Phys. J. **C78** (2018) 483, `arXiv:1709.09903`. (Cited page: 29.)

[107] LHCb collaboration, R. Aaij *et al.*, *Search for the doubly charmed baryon* Ω_{cc}^{+}, Sci. China Phys. Mech. Astron. **64** (2021) 101062, `arXiv:2105.06841`. (Cited page: 30.)

[108] O. S. Brüning *et al.*, *LHC Design Report*, CERN Yellow Reports: Monographs, CERN, Geneva, 2004. (Cited page: 32.)

[109] C. Wyss, *LEP design report, v.3: LEP2*, CERN, Geneva, 1996. Vol. 1-2 publ. in 1983-84. (Cited page: 33.)

[110] ATLAS collaboration, G. Aad *et al.*, *The ATLAS Experiment at the CERN Large Hadron Collider*, JINST **3** (2008) S08003. (Cited page: 33.)

[111] ALICE collaboration, K. Aamodt *et al.*, *The ALICE experiment at the CERN LHC*, JINST **3** (2008) S08002. (Cited page: 33.)

[112] CMS collaboration, S. Chatrchyan *et al.*, *The CMS Experiment at the CERN LHC*, JINST **3** (2008) S08004. (Cited page: 33.)

[113] LHCb collaboration, A. A. Alves Jr. *et al.*, *The LHCb detector at the LHC*, JINST **3** (2008) S08005. (Cited pages: 33, 36, 41, 42, 44, 45, 46, and 47.)

[114] ATLAS collaboration, G. Aad *et al.*, *Observation of a new particle in the search for the Standard Model Higgs boson with the ATLAS detector at the LHC*, Phys. Lett. B **716** (2012) 1, `arXiv:1207.7214`. (Cited page: 33.)

[115] CMS collaboration, S. Chatrchyan *et al.*, *Observation of a new boson at a mass of 125 GeV with the CMS experiment at the LHC*, Phys. Lett. B **716** (2012) 30, `arXiv:1207.7235`. (Cited page: 33.)

[116] TOTEM collaboration, G. Anelli *et al.*, *The TOTEM experiment at the CERN Large Hadron Collider*, JINST **3** (2008) S08007. (Cited page: 33.)

[117] LHCf collaboration, O. Adriani *et al.*, *The LHCf detector at the CERN Large Hadron Collider*, JINST **3** (2008) S08006. (Cited page: 33.)

[118] MoEDAL collaboration, B. Acharya *et al.*, *The physics programme of the MoEDAL experiment at the LHC*, Int. J. Mod. Phys. A **29** (2014) 1430050, `arXiv:1405.7662`. (Cited page: 33.)

[119] FASER collaboration, A. Ariga *et al.*, *FASER: ForwArd Search ExpeRiment at the LHC*, `arXiv:1901.04468`. (Cited page: 33.)

[120] E. Mobs, *The CERN accelerator complex - August 2018. Complexe des accélérateurs du CERN - Août 2018*, `http://cds.cern.ch/record/2636343`, 2018. (Cited page: 34.)

[121] LHCb collaboration, R. Aaij *et al.*, *LHCb detector performance*, Int. J. Mod. Phys. **A30** (2015) 1530022, `arXiv:1412.6352`. (Cited pages: 36 and 46.)

[122] R. Lindner, *LHCb layout*, `http://cds.cern.ch/record/1087860`, 2008. LHCb Collection. (Cited page: 37.)

[123] LHCb collaboration, R. Aaij *et al.*, *Observation of CP violation in two-body B_s^0-meson decays to charged pions and kaons*, JHEP **03** (2021) 075, `arXiv:2012.05319`. (Cited page: 38.)

[124] LHCb collaboration, R. Aaij *et al.*, *Measurement of the CP-violating phase ϕ_s from $B_s^0 \to J/\psi \pi^+\pi^-$ decays in 13 TeV pp collisions*, Phys. Lett. **B797** (2019) 134789, `arXiv:1903.05530`. (Cited page: 38.)

[125] LHCb collaboration, R. Aaij *et al.*, *Updated measurement of time-dependent CP-violating observables in $B_s^0 \to J/\psi K^+K^-$ decays*, Eur. Phys. J. **C79** (2019) 706, Erratum ibid. **C80** (2020) 601, `arXiv:1906.08356`. (Cited page: 38.)

[126] LHCb collaboration, R. Aaij *et al.*, *Observation of CP violation in charm decays*, Phys. Rev. Lett. **122** (2019) 211803, `arXiv:1903.08726`. (Cited page: 38.)

[127] LHCb collaboration, R. Aaij *et al.*, *Measurement of the $B_s^0 \to \mu^+\mu^-$ decay properties and search for the $B^0 \to \mu^+\mu^-$ and $B_s^0 \to \mu^+\mu^-\gamma$ decays*, Phys. Rev. **D105** (2022) 012010, `arXiv:2108.09283`. (Cited page: 38.)

[128] LHCb collaboration, R. Aaij *et al.*, *Branching fraction measurements of the rare $B_s^0 \to \phi\mu^+\mu^-$ and $B_s^0 \to f_2'(1525)\mu^+\mu^-$ decays*, Phys. Rev. Lett. **127** (2021) 151801, `arXiv:2105.14007`. (Cited page: 38.)

[129] LHCb collaboration, R. Aaij *et al.*, *Observation of five new narrow Ω_c^0 states decaying to $\Xi_c^+K^-$*, Phys. Rev. Lett. **118** (2017) 182001, `arXiv:1703.04639`. (Cited page: 38.)

[130] LHCb Collaboration, R. Aaij *et al.*, *List of hadrons observed at the LHC*, `https://cds.cern.ch/record/2749030`, 2021. (Cited pages: 38 and 39.)

[131] LHCb collaboration, R. Aaij *et al.*, *Observation of $J/\psi p$ resonances consistent with pentaquark states in $\Lambda_b^0 \to J/\psi pK^-$ decays*, Phys. Rev. Lett. **115** (2015) 072001, `arXiv:1507.03414`. (Cited page: 39.)

[132] LHCb collaboration, R. Aaij *et al.*, *Observation of a narrow pentaquark state, $P_c(4312)^+$, and of two-peak structure of the $P_c(4450)^+$*, Phys. Rev. Lett. **122** (2019)

222001, arXiv:1904.03947. (Cited page: 39.)

[133] LHCb collaboration, R. Aaij *et al.*, *Observation of new resonances decaying to* $J/\psi K^+$ *and* $J/\psi\phi$, Phys. Rev. Lett. **127** (2021) 082001, arXiv:2103.01803. (Cited page: 39.)

[134] LHCb collaboration, R. Aaij *et al.*, *Observation of an exotic narrow doubly charmed tetraquark*, arXiv:2109.01038, submitted to journal. (Cited page: 39.)

[135] LHCb collaboration, R. Aaij *et al.*, *Measurement of the b-quark production cross-section in 7 and 13 TeV pp collisions*, Phys. Rev. Lett. **118** (2017) 052002, Erratum ibid. **119** (2017) 169901, arXiv:1612.05140. (Cited page: 40.)

[136] LHCb collaboration, R. Aaij *et al.*, *Measurements of prompt charm production cross-sections in pp collisions at* $\sqrt{s}$ *=13 TeV*, JHEP **03** (2016) 159, Erratum ibid. **09** (2016) 013, Erratum ibid. **05** (2017) 074, arXiv:1510.01707. (Cited pages: 40 and 61.)

[137] LHCb collaboration, *LHCb operations plots*, https://lbgroups.cern.ch/online/OperationsPlots/index.htm. LHCb Collection. (Cited page: 41.)

[138] LHCb collaboration, *LHCb VELO (VErtex LOcator): Technical Design Report*, CERN-LHCC-2001-011, 2001. (Cited page: 40.)

[139] R. Aaij *et al.*, *Performance of the LHCb Vertex Locator*, JINST **9** (2014) P09007, arXiv:1405.7808. (Cited pages: 40, 72, 73, and 77.)

[140] S. Löchner and M. Schmelling, *The Beetle Reference Manual - chip version 1.3, 1.4 and 1.5*, LHCb-2005-105, CERN-LHCb-2005-105, CERN, Geneva, 2006. (Cited page: 41.)

[141] R. Aaij *et al.*, *Performance of the LHCb trigger and full real-time reconstruction in Run 2 of the LHC*, JINST **14** (2019) P04013, arXiv:1812.10790. (Cited pages: 42, 49, 50, 51, 52, 63, 64, and 195.)

[142] LHCb collaboration, *LHCb RICH: Technical Design Report*, CERN-LHCC-2000-037, 2000. (Cited page: 43.)

[143] M. Adinolfi *et al.*, *Performance of the LHCb RICH detector at the LHC*, Eur. Phys. J. **C73** (2013) 2431, arXiv:1211.6759. (Cited page: 43.)

[144] P. A. Čerenkov, *Visible radiation produced by electrons moving in a medium with velocities exceeding that of light*, Phys. Rev. **52** (1937) 378. (Cited page: 43.)

[145] M. Alemi *et al.*, *First operation of a hybrid photon detector prototype with electrostatic cross-focussing and integrated silicon pixel readout*, Nucl. Instrum. Methods Phys. Res. A **449** (2000) 48. (Cited page: 44.)

[146] LHCb collaboration, *LHCb outer tracker: Technical Design Report*, CERN-LHCC-2001-024, 2001. (Cited page: 45.)

[147] LHCb collaboration, *LHCb inner tracker: Technical Design Report*, CERN-LHCC-2002-029, 2002. (Cited page: 45.)

[148] R. Arink *et al.*, *Performance of the LHCb Outer Tracker*, JINST **9** (2014) P01002, `arXiv:1311.3893`. (Cited page: 45.)

[149] P. d'Argent *et al.*, *Improved performance of the LHCb Outer Tracker in LHC Run 2*, JINST **12** (2017) P11016, `arXiv:1708.00819`. (Cited page: 45.)

[150] LHCb Silicon Tracker Group, C. Abellan Beteta *et al.*, *Monitoring radiation damage in the LHCb Tracker Turicensis*, JINST **15** (2020) P08016, `arXiv:1809.05063`. (Cited page: 45.)

[151] LHCb collaboration, *LHCb magnet: Technical Design Report*, CERN-LHCC-2000-007, 2000. (Cited page: 46.)

[152] LHCb collaboration, *LHCb calorimeters: Technical Design Report*, CERN-LHCC-2000-036, 2000. (Cited page: 47.)

[153] C. Abellan Beteta *et al.*, *Calibration and performance of the LHCb calorimeters in Run 1 and 2 at the LHC*, `arXiv:2008.11556`, submitted to JINST. (Cited pages: 47 and 48.)

[154] LHCb collaboration, *LHCb muon system: Technical Design Report*, CERN-LHCC-2001-010, 2001. (Cited page: 48.)

[155] A. A. Alves Jr. *et al.*, *Performance of the LHCb muon system*, JINST **8** (2013) P02022, `arXiv:1211.1346`. (Cited page: 48.)

[156] K. Carvalho Akiba *et al.*, *The HeRSCheL detector: high-rapidity shower counters for LHCb*, JINST **13** (2018) P04017, `arXiv:1801.04281`. (Cited page: 49.)

[157] M. G. Albrow, T. D. Coughlin, and J. R. Forshaw, *Central exclusive particle production at high energy hadron colliders*, Prog. Part. Nucl. Phys. **65** (2010) 149, `arXiv:1006.1289`. (Cited page: 49.)

[158] R. Aaij *et al.*, *The LHCb trigger and its performance in 2011*, JINST **8** (2013) P04022, `arXiv:1211.3055`. (Cited pages: 49 and 51.)

[159] LHCb Collaboration, R. Aaij *et al.*, *LHCb trigger plots and diagrams*, `https://twiki.cern.ch/twiki/bin/view/LHCb/LHCbTriggerConferenceDiagramsPlots`. (Cited page: 50.)

[160] A. Gulin, I. Kuralenok, and D. Pavlov, *Winning the transfer learning track of yahoo!'s learning to rank challenge with yetirank*, in *Proceedings of the Learning to Rank Challenge*, 63–76, 2011. Available at `https://proceedings.mlr.press/v14/gulin11a.html`. (Cited pages: 52 and 64.)

[161] R. Aaij *et al.*, *Tesla: an application for real-time data analysis in High Energy Physics*, Comput. Phys. Commun. **208** (2016) 35, `arXiv:1604.05596`. (Cited page: 53.)

[162] LHCb collaboration, *Computing Model of the Upgrade LHCb experiment*, CERN-LHCC-2018-014, 2018. (Cited page: 53.)

[163] T. Likhomanenko *et al.*, *LHCb topological trigger reoptimization*, J. Phys. Conf. Ser. **664** (2015) 082025, `arXiv:1510.00572`. (Cited page: 53.)

[164] R. Aaij *et al.*, *A comprehensive real-time analysis model at the LHCb experiment*, JINST **14** (2019) P04006, `arXiv:1903.01360`. (Cited pages: 53 and 225.)

[165] LHCb collaboration, R. Aaij *et al.*, *Measurement of the track reconstruction efficiency at LHCb*, JINST **10** (2015) P02007, `arXiv:1408.1251`. (Cited pages: 54 and 209.)

[166] D. Hutchcroft, *VELO Pattern Recognition* , CERN, Geneva, 2007. (Cited page: 54.)

[167] O. Callot and S. Hansmann-Menzemer, *The Forward Tracking: Algorithm and Performance Studies*, . (Cited page: 55.)

[168] M. Needham and J. Van Tilburg, *Performance of the track matching*, . (Cited page: 55.)

[169] M. Needham, *Performance of the track matching*, . (Cited page: 55.)

[170] O. Callot and M. Schiller, *PatSeeding: A standalone track reconstruction algorithm*, . (Cited page: 55.)

[171] R. E. Kalman and Others, *A new approach to linear filtering and prediction problems*, Journal of basic Engineering **82** (1960) 35. (Cited pages: 55 and 73.)

[172] R. Frühwirth, *Application of Kalman filtering to track and vertex fitting*, Nuclear Instruments and Methods in Physics Research Section A: Accelerators, Spectrometers, Detectors and Associated Equipment **262** (1987) 444. (Cited pages: 55 and 73.)

[173] LHCb Collaboration, R. Aaij *et al.*, *Muon track reconstruction efficiency at LHCb*, `https://cds.cern.ch/record/2718525`, 2020. (Cited page: 56.)

[174] R. Brun and F. Rademakers, *ROOT: An object oriented data analysis framework*, Nucl. Instrum. Meth. **A389** (1997) 81. (Cited pages: 57, 67, 118, and 162.)

[175] M. Clemencic *et al.*, *The LHCb simulation application, Gauss: Design, evolution and experience*, J. Phys. Conf. Ser. **331** (2011) 032023. (Cited pages: 57 and 58.)

[176] T. Sjöstrand, S. Mrenna, and P. Skands, *A brief introduction to PYTHIA 8.1*, Comput. Phys. Commun. **178** (2008) 852, `arXiv:0710.3820`. (Cited page: 57.)

[177] T. Sjöstrand, S. Mrenna, and P. Skands, *PYTHIA 6.4 physics and manual*, JHEP **05** (2006) 026, `arXiv:hep-ph/0603175`. (Cited page: 57.)

[178] I. Belyaev *et al.*, *Handling of the generation of primary events in Gauss, the LHCb simulation framework*, J. Phys. Conf. Ser. **331** (2011) 032047. (Cited page: 57.)

[179] C.-H. Chang, J.-X. Wang, and X.-G. Wu, *GENXICC2.0: An upgraded version of the generator for hadronic production of double heavy baryons* Ξ_{cc}, Ξ_{bc} *and* Ξ_{bb}, Comput. Phys. Commun. **181** (2010) 1144, `arXiv:0910.4462`. (Cited pages: 57 and 97.)

[180] D. J. Lange, *The EvtGen particle decay simulation package*, Nucl. Instrum. Meth. **A462** (2001) 152. (Cited page: 57.)

[181] N. Davidson, T. Przedzinski, and Z. Was, *PHOTOS interface in C++: Technical and physics documentation*, Comp. Phys. Comm. **199** (2016) 86, `arXiv:1011.0937`. (Cited page: 58.)

[182] Geant4 collaboration, J. Allison *et al.*, *Geant4 developments and applications*, IEEE Trans. Nucl. Sci. **53** (2006) 270. (Cited page: 58.)

[183] Geant4 collaboration, S. Agostinelli *et al.*, *Geant4: A simulation toolkit*, Nucl. Instrum. Meth. **A506** (2003) 250. (Cited page: 58.)

[184] D. Müller, M. Clemencic, G. Corti, and M. Gersabeck, *ReDecay: A novel approach to speed up the simulation at LHCb*, Eur. Phys. J. **C78** (2018) 1009, `arXiv:1810.10362`.

(Cited page: 58.)

[185] LHCb collaboration, *Framework TDR for the LHCb Upgrade: Technical Design Report*, CERN-LHCC-2012-007, 2012. (Cited pages: 59, 190, 225, and 226.)

[186] LHCb collaboration, *LHCb Trigger and Online Upgrade Technical Design Report*, CERN-LHCC-2014-016, 2014. (Cited pages: 59, 71, and 225.)

[187] LHCb collaboration, *Letter of Intent for the LHCb Upgrade*, CERN-LHCC-2011-001, LHCC-I-018, 2011. (Cited page: 59.)

[188] Particle Data Group, M. Tanabashi *et al.*, *Review of particle physics*, Phys. Rev. **D98** (2018) 030001, and 2019 update. (Cited pages: 63, 94, 98, 100, 102, 158, 185, and 190.)

[189] R. Aaij *et al.*, *Selection and processing of calibration samples to measure the particle identification performance of the LHCb experiment in Run 2*, Eur. Phys. J. Tech. Instr. **6** (2019) 1, `arXiv:1803.00824`. (Cited pages: 66, 109, and 195.)

[190] A. Hoecker *et al.*, *TMVA 4 — Toolkit for Multivariate Data Analysis with ROOT. Users Guide.*, `arXiv:physics/0703039`. (Cited pages: 67 and 118.)

[191] L. Breiman, J. H. Friedman, R. A. Olshen, and C. J. Stone, *Classification and regression trees*, Wadsworth international group, Belmont, California, USA, 1984. (Cited pages: 67 and 119.)

[192] V. V. Gligorov and M. Williams, *Efficient, reliable and fast high-level triggering using a bonsai boosted decision tree*, JINST **8** (2013) P02013, `arXiv:1210.6861`. (Cited page: 67.)

[193] J. L. Hodges, *The significance probability of the Smirnov two-sample test*, Arkiv för Matematik **3** (1958) 469. (Cited pages: 68 and 124.)

[194] M. Smith, *Measurement of indirect CP violation in charm at LHCb*, PhD thesis, University of Manchester, 2015, CERN-THESIS-2015-377. (Cited pages: 73 and 77.)

[195] W. D. Hulsbergen, *A study of track reconstruction and massive dielectron production in HERA-B*, PhD thesis, Amsterdam University, 2002, PRINT-2004-010. (Cited page: 77.)

[196] LHCb collaboration, R. Aaij *et al.*, *First branching fraction measurement of the sup-*

pressed decay $\Xi_c^0 \to \pi^- \Lambda_c^+$, Phys. Rev. **D102** (2020) 071101(R), `arXiv:2007.12096`. (Cited page: 87.)

[197] Belle collaboration, Y. B. Li *et al.*, *First measurements of absolute branching fractions of the* Ξ_c^+ *baryon at Belle*, Phys. Rev. **D100** (2019) 031101, `arXiv:1904.12093`. (Cited page: 87.)

[198] LHCb collaboration, R. Aaij *et al.*, *Precision measurement of the mass and lifetime of the* Ξ_b^0 *baryon*, Phys. Rev. Lett. **113** (2014) 032001, `arXiv:1405.7223`. (Cited page: 107.)

[199] W. D. Hulsbergen, *Decay chain fitting with a Kalman filter*, Nucl. Instrum. Meth. **A552** (2005) 566, `arXiv:physics/0503191`. (Cited pages: 108 and 158.)

[200] L. Anderlini *et al.*, *Computing strategy for PID calibration samples for LHCb Run 2*, CERN, Geneva, LHCb-PUB-2016-020, 2016. (Cited page: 109.)

[201] A. Powell *et al.*, *Particle identification at LHCb*, PoS **ICHEP2010** (2010) 020, LHCb-PROC-2011-008. (Cited pages: 109 and 195.)

[202] L. Anderlini *et al.*, *The PIDCalib package*, LHCb-PUB-2016-021, 2016. (Cited pages: 109 and 195.)

[203] A. Rogozhnikov, *Reweighting with Boosted Decision Trees*, J. Phys. Conf. Ser. **762** (2016) 012036, `arXiv:1608.05806`, `https://github.com/arogozhnikov/hep_ml`. (Cited page: 112.)

[204] M. Pivk and F. R. Le Diberder, *sPlot: A statistical tool to unfold data distributions*, Nucl. Instrum. Meth. **A555** (2005) 356, `arXiv:physics/0402083`. (Cited page: 112.)

[205] LHCb collaboration, R. Aaij *et al.*, *Measurements of the* Λ_b^0, Ξ_b^-, *and* Ω_b^- *baryon masses*, Phys. Rev. Lett. **110** (2013) 182001, `arXiv:1302.1072`. (Cited page: 118.)

[206] LHCb collaboration, R. Aaij *et al.*, *Precision measurement of D meson mass differences*, JHEP **06** (2013) 065, `arXiv:1304.6865`. (Cited pages: 118 and 185.)

[207] J. H. Friedman, *Greedy function approximation: A gradient boosting machine*, Ann. Statist. **29** (2001) 1189. (Cited page: 119.)

[208] Y. Freund and R. E. Schapire, *A decision-theoretic generalization of on-line learning and an application to boosting*, J. Comput. Syst. Sci. **55** (1997) 119. (Cited page:

119.)

[209] S. Haykin, *Neural networks: a comprehensive foundation, 2nd ed*, New York: Macmillan College Publishing, 1998. (Cited page: 119.)

[210] T. Chen and C. Guestrin, *XGBoost: A Scalable Tree Boosting System*, in *Proceedings of the 22nd ACM SIGKDD International Conference on Knowledge Discovery and Data Mining*, KDD '16, (New York, NY, USA), 785–794, ACM, 2016. (Cited page: 119.)

[211] G. Punzi, *Sensitivity of searches for new signals and its optimization*, eConf **C030908** (2003) MODT002, `arXiv:physics/0308063`. (Cited page: 124.)

[212] T. Skwarnicki, *A study of the radiative cascade transitions between the Upsilon-prime and Upsilon resonances*, PhD thesis, Institute of Nuclear Physics, Krakow, 1986, DESY-F31-86-02. (Cited pages: 142 and 158.)

[213] S. S. Wilks, *The large-sample distribution of the likelihood ratio for testing composite hypotheses*, Ann. Math. Stat. **9** (1938) 60. (Cited pages: 143, 162, and 166.)

[214] LHCb collaboration, R. Aaij *et al.*, *Observation of the doubly charmed baryon decay* $\Xi_{cc}^{++} \to \Xi_c^{\prime +}\pi^+$, JHEP **05** (2022) 038, `arXiv:2202.05648`. (Cited pages: 161, 162, and 163.)

[215] G. Cowan, K. Cranmer, E. Gross, and O. Vitells, *Asymptotic formulae for likelihood-based tests of new physics*, Eur. Phys. J. **C71** (2011) 1554, `arXiv:1007.1727`, [Erratum: Eur. Phys. J. **C73** (2013) 2501]. (Cited pages: 165 and 166.)

[216] E. Gross and O. Vitells, *Trial factors for the look elsewhere effect in high energy physics*, Eur. Phys. J. **C70** (2010) 525, `arXiv:1005.1891`. (Cited pages: 168 and 169.)

[217] L. Jost, *Combining Significance Levels from Multiple Experiments or Analyses*, `http://www.loujost.com/Statistics%20and%20Physics/Significance%20Levels/CombiningPValues.htm`. (Cited page: 176.)

[218] H.-Y. Cheng, G. Meng, F. Xu, and J. Zou, *Two-body weak decays of doubly charmed baryons*, Phys. Rev. **D101** (2020) 034034, `arXiv:2001.04553`. (Cited pages: 190 and 227.)

[219] A. L. Read, *Modified frequentist analysis of search results (The CL(s) method)*, in *Workshop on Confidence Limits*, 81–101, 2000. CERN-OPEN-2000-205. (Cited pages: 215 and 216.)

[220] LHCb collaboration, *LHCb VELO Upgrade Technical Design Report*, CERN-LHCC-2013-021, 2013. (Cited page: 226.)